gem

November 30, 1991

SSCL-SR-1184
GEM TN-92-49

GEM Letter of Intent

November 30, 1991

Contact Persons

Barry Barish
Caltech
HEP 256-48
Pasadena, CA 91125
818/356-6684
Barish@Cithex.Bitnet

William Willis
Nevis Laboratory
Columbia University
P.O. Box 137
Irvington, NY 10533
914/591-8100, ext. 208
Willis@Nevis.Bitnet

Prepared in collaboration with the Superconducting Super Collider Laboratory, operated by the Universities Research Association Inc, for the Department of Energy under Contract No. DE-AC35-89ER40486.

GEM Collaborators

Adelphi University: R. Steiner

Universidad de los Andes: J. P. Negret

University of Arizona: G. E. Forden, J. P. Rutherfoord, L. Shaver, M. A. Shupe

Beijing Glass Research Institute: G. Chen, Z.Z. Dai, X.Y. Dong, Y.C. Gao, T.Z. Li, G.T. Liu, Z.Q. Liu, S.Q. Man, S.X. Ren, Z.L. Su, Y.T. Wang, O. Wen, H. Xiao, H.Z. Yang, F.C. Zhang, F.Y. Zhang, J. Zhang, J.Q. Zhang, Y.N. Zheng

Beijing University, China: D. Jiang, C. Lai, H. Liu, S. Xia, Y. Ye

Institute of High Energy Physics, Beijing: W. Gu, Y. Gu, Y. Guo, Y. Huang, J. Li, C. Mao, H. Sheng, R. Xu, D. Zhang, B. Zhuang

Boston University: S. P. Ahlen, E. Booth, R. Carey, S. Dye, M. Golden, T. Hazen, D. Higby, T. Johnson, K. D. Lane, A. Marin, J. P. Miller, D. Osborne, B. L. Roberts, J. Shank, J. L. Stone, L. R. Sulak, D. Warner, J. S. Whitaker, R. J. Wilson, W. A. Worstell, B. Zhou

Brookhaven National Laboratory: M. S. Atiya, I-H. Chiang, B. Gibbard, H. Gordon, J. S. Haggerty, S. Kahn, H. W. Kraner, P. Kroon, D. Lissauer, L. S. Littenberg, H. Ma, D. Makowiecki, M. J. Murtagh, P. O'Connor, L. Paffrath, F. E. Paige, V. A. Polychronakos, S. Protopopescu, V. Radeka, D. C. Rahm, S. Rankowitz, P. Rehak, S. Rescia, L. Rogers, N. P. Samios, D. Stephani, I. Stumer, H. Takai, M. J. Tannenbaum, C. L. Woody, S. P. Yamin

Brown University: M. Widgoff

Bucharest University: C. Besliu

Institute of Atomic Physics, Bucharest: A. Aculai, C. Blaj, H. Bozdog, L. Butacu, M. Ciobanu, A. Dorobantu, D. Ighicianu, G. Pascovici, V. Popa, G. Radulescu, D. Spanu, C. Stan-Sion, V. Valeanu, K. Zimmer

University of California - San Diego: J. G. Branson, W. Brower, H. E. G. Kobrak, R. Masek, H.P. Paar, R. A. Swanson, M. Sivertz

California Institute of Technology: B. C. Barish, G. Gratta, M. Gruenewald, D. Kirkby, W. Lu, R. Mount, H. B. Newman, S. Shevchenko, X. Shi, Z. Y. Wei, H. Yamamoto, R.Y. Zhu

Carnegie-Mellon University: M. J. Clemen, R. Edelstein, A. Engler, T. Ferguson, R. W. Kraemer, J. S. Russ, R. B. Sutton, H. Vogel

Changwon National College, Korea: C.H. Hahn

Chonnam National University, Korea: H.I. Jang, J.Y. Kim, T.I. Kim, I.T. Lim, M.Y. Pac

CINVESTAV, Mexico: H. Castilla-Valdez, G. Herrera-Corral

Columbia University: Y. Au, E. Aprile, A. Bolotnikov, T. Bolton, D. Chen, M. Leltchouk, M. Moulsen, R. Mukherjee, J. Parsons, P. C. Rowson, M. Seman, M. Shaevitz, W. Sippach, W. Willis

University of Delhi South Campus: V. Kapoor, R. K. Shivpuri

Draper Laboratory: F. Ayer, C. Elder, T. Hamilton, M. Hansberry, F. Nimblett, D. Sullivan, E. Womble

Drexel University: C. Lane

Joint Institute for Nuclear Research, Dubna: G.D. Alekseev, A.V. Bannikov, L.S. Barabash, S.A. Baranov, D.A. Belosludtsev, Yu. E. Bonyushkin, V. N. Bychkov, G.A. Chelkov, Yu. V. Ershov, V. Frolov, I.A. Golutvin, N.V. Gorbunov, Yu. A. Gornushkin, V.A. Kalinnikov, M.N. Kapishin, A.G. Karev, V.Yu. Karzhavin, M. Yu. Kazarinov, V. D. Kekelidze, S. V. Khabarov, V.S. Khabarov, B.A. Khomenko, N. N. Khovansky, Yu.T. Kiryushin, O. Klimov, A.V. Korytov, V.M. Kotov, Z.V. Krumstein, P.A. Kulinich, G.A. Kvirikashvili, V.N. Lysiakov, A.L. Lyubin, A.V. Makhankov, V.L. Malyshev, Yu.P. Merekov, S.A. Movchan, A.A. Nozdrin, A.K. Odishvili, A.G. Olshevski, V.D. Peshekhonov, Yu.P. Petukhov, A.A. Popov, D. Pose, T. Predo, T.G. Progulova, V.A. Sashin, Yu.V. Sedykh, S.Yu. Selyunin, D.A. Smolin, V.N. Spaskov, G.T. Tatishvili, L.G. Tkatchev, V.V. Tokmenin, L.S. Vertogradov, A.V. Vishnevsky, V.S. Yamburenko, A. I. Zinchenko

Fairfield University: D. R. Winn

Universidad de Guanajuato, Mexico: A. Gonzalez, A. Morelos, G. Moreno, L. Villasenor

Gunsan National University, Korea: J.Y. Ryu

Gyeongsang National University, Korea: K.S. Chung, S. H. Chung, I. G. Park, J. S. Song, C.S. Yoon

Universität Hamburg: E. Fretwurst, G. Lindstroem, V. Riech

Harvard University: E. Carlson, E. H. Simmons

University of Science and Technology of China, Hefei: Z. H. Bian, M. F. Cai, Y. M. Fang, R. D. Han, L. Y. Hao, X. S. Lin, B. A. Liu, W. Mei, Q. C. Shi, H. M. Wang, Z. M. Wang, S. L. Wu, S. L. Xing, J. H. Xu, X. L. Xu, K. Z. Xu, B. X. Yang, B. J. Ye, X. Q. Yu, J. Zhang, Y. Z. Zhou

University of Houston: K. Lau, B. W. Mayes, L. Pinsky, J. Pyrlik, R. Weinstein

University of Iowa: N. Akchurin, D. Kadrmas, K. Langland, E. R. McCliment, Y. Meurice, F. Olchowski, Y. Onel, M. Reno, V. Rodgers

Indiana University: E. D. Alyea, C. Bower, M. Gephard, R. M. Heinz, S. Mufson, J. Musser, S. Nutter, J. Pitts

Korea University: S. D. Chang, B.G. Cheon, J. H. Cho, C. O. Kim, T.Y. Kim, S. B. Lee, S.W. Nam

Kurchatov Institute of Atomic Energy: M. A. Vasiliev

Lawrence Livermore National Laboratory: E. Ables, R. Bionta, J. M. Bowers, H. C. Britt, M. H. Capell, A. K. Chargin, G. A. Deis, O. D. Fackler, J. Heim, C. Johnson, M. Lowry, C. F. McConaghy, M. Mugge, K. M. Skulina, K. VanBibber, T. J. Wenaus, S. Wineman, C. R. Wuest

Lebedev Physical Institute: V. Tikhomirov

Los Alamos National Laboratory: R. Barber, J. G. Boissevain, M. Brooks, D. Brown, T. Coan, R. M. Farber, S. F. Hahn, J. Kapustinsky, W. W. Kinnison, K. S. Lackner, A. S. Lapedes, D. M. Lee, W. B. Maier, G. B. Mills, G. H. Sanders, D. Sharp, B. Smith, W. F. Sommer, W. E. Sondheim

Louisiana State University: R. McNeil

Marshall Space Flight Center: K.H. Moom

Martin Marietta Astronautics: J. Coulson, N. J. DiGiacomo, B. Easom, K. Killian, L. Mason

Massachusetts Institute of Technology: P. Burrows, W. Busza, Y-H. Chang, M. Chen, H. Ding, J. I. Friedman, M. P.J. Gaudreau, E. D. Hafen, P. Haridas, J. Kelsey, H. Kendall, V. Lebedenko, D.B. Montgomery, L. S. Osborne, I. A. Pless, L. Randall, L. Rosenson, R. Shuvalov, J. D. Sullivan, S. Sumorok, F. E. Taylor, R. Verdier, B. Wadsworth, X. J. Yan, X. Zhang

University of Michigan: D. Levin, S. McKee, G. Tarlé, A. Tomasch

Michigan State University: M. A. Abolins, C. Bromberg, R. J. Miller

University of Mississippi: L. M. Cremaldi, B. Moore, J. J. Reidy

Institute for Theoretical and Experimental Physics, Moscow: V. Balagura, A. Bolozdynya, Y. Efremenko, A. Golutvin, P. Gorichev, L. Gusev, Yu. Kamyshkov, I. Korolko, A. Koutchenkov, A. Kovalenko, L. Laptin, V. Lebedenko, P. Murat, V. Nagovitsin, A. Nepejpivo, A. Ostapchuk, F. Ratnikov, A. Savin, S. Shevchenko, K.Shmakov, I. Tikhomirov, V. Tchernyshev, V. Tchistilin, V.A. Vinogradov

Institute of Nuclear Physics, Novosibirsk: L. Barkov, D. Grigoriev, B. Khazin, S. Klimenko, E. Kuraev, M. Leltchouk, V. Malyshev, A. Maslennikov, S. Redin, Yu. Shatunov, E. Solodov, A. Onuchin, V. Panin, S. Peleganchuk, V. Sidorov, Yu. Tikhonov

Institute of Nuclear Problems, Minsk: M. Baturitsky, A. Degtiarev, A. Kubasov, V. Mikhailov, V. Shuljak, N. Shumeiko

Moscow Engineering Physics Institute: V. Grigoriev, P. Nevski, M. Potekhin, A. Sumarokov, V. Tcherniatin, A. Vanyashin

Moscow State University: A. A. Arodzero, G. Bashindzhagyan, P. F. Ermolov, Yu. V. Fisyak, A. N. Larichev, M. M. Merkin, V. S. Murzin, N. A. Sotnikova, A. G. Voronin, S. A. Zotkin, V. Yu. Zhukov

National Teacher's University, Korea: S. N. Kim

Northwestern University: D. Buchholz, B. Gobbi, H. Schellman

Oak Ridge National Laboratory: M. L. Bauer, S. Chae, H. O. Cohn, C. Eberle, Yu. Kamyshkov, J. Moore, F. Plasil, K. Read, M. Rennich, R. A. Todd, K. Young

University of Oregon: J. E. Brau, R. Frey, K. Furuno, D. M. Strom, C.J. Zeitlin

University of Pittsburgh: W. Cleland, E. Stern

Princeton University: P. Denes, M. Ito, D. Marlow

Riken Institute: M. Suzuki, T. Takahashi

University of Rochester: T. Ferbel, G. Fanourakis, M. Zielinski

Rutgers University: P. Jacques, M. Kalelkar, R. J. Plano, P. Stamer, G. B. Word

St. Petersburg Nuclear Physics Institute: V.T. Gratchev, A.G. Krivshich, O.E. Prokofiev, V.M. Samsonov, V.V. Sarantsev, N. K. Terentyev

Saitama University: K. Masuda, E. Shibamura

Universidade de São Paulo: O. P. Eboli, C. O. Escobar, P. Gouffon, M. Luksys, S. F. Novaes

Shanghai Institute of Ceramics: X.L. Fang, P.X. Gu, J.K. Guo, G.Q. Hu, S.K. Hua, Z. D. Ji, P.J. Li, D.Z. Shen, G.S. Shen, E.W. Shi, W.T. Su, Z.Y. Wei, Y.Y. Xie, L. Xu, Z.L. Xue, D.S. Yan, Z.W. Yin, X.L. Yuan, G. M. Zhao, Y.L. Zhao, W.Z. Zhong, R.M. Zhou

Shanghai Institute of Nuclear Research: J. Bao, D. Cao, S. Chen, D. Jiang, X. P. Li, S. Lin, H. Liu, T. Rong, L.R. Shen, K. Sheng, H. Wan, F. H. Yu, W. H. Zheng, D. Zhu, F. Zhu

Sookmyeong Women's University: J.N. Park

University of South Carolina: C. Rosenfeld, J. R. Wilson

Southern Methodist University: F. Olness, R. Stroynowski, V. Teplitz

SSC Laboratory: L. R. Cormell, P. Dingus, M. Harris, J. Kuzminski, A. W. Maschke, W. K. McFarlane, N. Mehta, R. Meinke, G. Mitselmakher, K. Morgan, B. Parker, L.A. Roberts, B. Scipioni, R. Soundranayagam, F. Stocker, J. Thomas, A. Vaniachine, L. Villasenor, G. P. Yost

State University of New York at Albany: M. S. Alam, I.J. Kim, Z.C. Ling, B. Nemati, J.O'Neill, H. Severini, C.R. Sun

State University of New York at Stony Brook: R. Engelmann, C.K. Jung, M. D. Marx, R. L. McCarthy, M. Mohammadi, M. Rijssenbeek, C. Yanagisawa

Syracuse University: G. C. Fox, W. Furmanski, T. Haupt

Technion - Israel Institute of Technology: J. Goldberg

Tbilisi State University: N. S. Amaglobeli, W. P. Dzhordzhadze, A. J. Mchedlishvili, D. A. Mzavia, R. G. Shanidze, F. G. Tkebuchava

Tel Aviv University: G. Alexander, A. Beck, G. Bella, O. Benary, I. Cohen, E. Etzion, R. Heifetz, Y. Oren, N. Paz

University of Tennessee: S. Berridge, W. M. Bugg, Y.C. Du, R. Kroeger, I. Tsveybak, A. Weidemann

Temple University: S. H. Kettell, W. K. McFarlane

University of Texas at Austin: C. C. Allen, G. W. Hoffmann, K. Lang, M. R. Marcin, J. L. Ritchie

Texas A&M University: C. Gagliardi, G. Glass, R. Tribble, R. C. Webb

Tongji University, China: L. Y. Chen, J. Du, M. Gu, J. Wang, L. M. Wang, X. Wu, K. H. Xiang

Tsinghua University, China: J. An, K. Kang, Y. Lin, G. Liu, D. Mai, W. Ni, R. Shang, J. Wang, S. Xu, Z. Xu, J. Zhang

Vanderbilt University: R. S. Panvini, J. P. Venuti

Vassar College: C. Schwarz

Waseda University: T. Doke, A. Hitachi, N. Ishida, T. Kashiwagi, J. Kikuchi

University of Washington: V. Cook, J. Eisenberg, D. Forbush, P.M. Mockett, S. Sutlief, F. Toeus

Washington University: J. Beatty, W. Binns, D. Crary, D. Ficenec, J. Klarmann

Wonkwang University: S.Y. Bahk

Yale University: R. K. Adair, C. Baltay, R. Ben-David, W. Emmett, H. Kasha, S. L. Manly, S. Sen, J. Turk

TABLE OF CONTENTS

1

Introduction

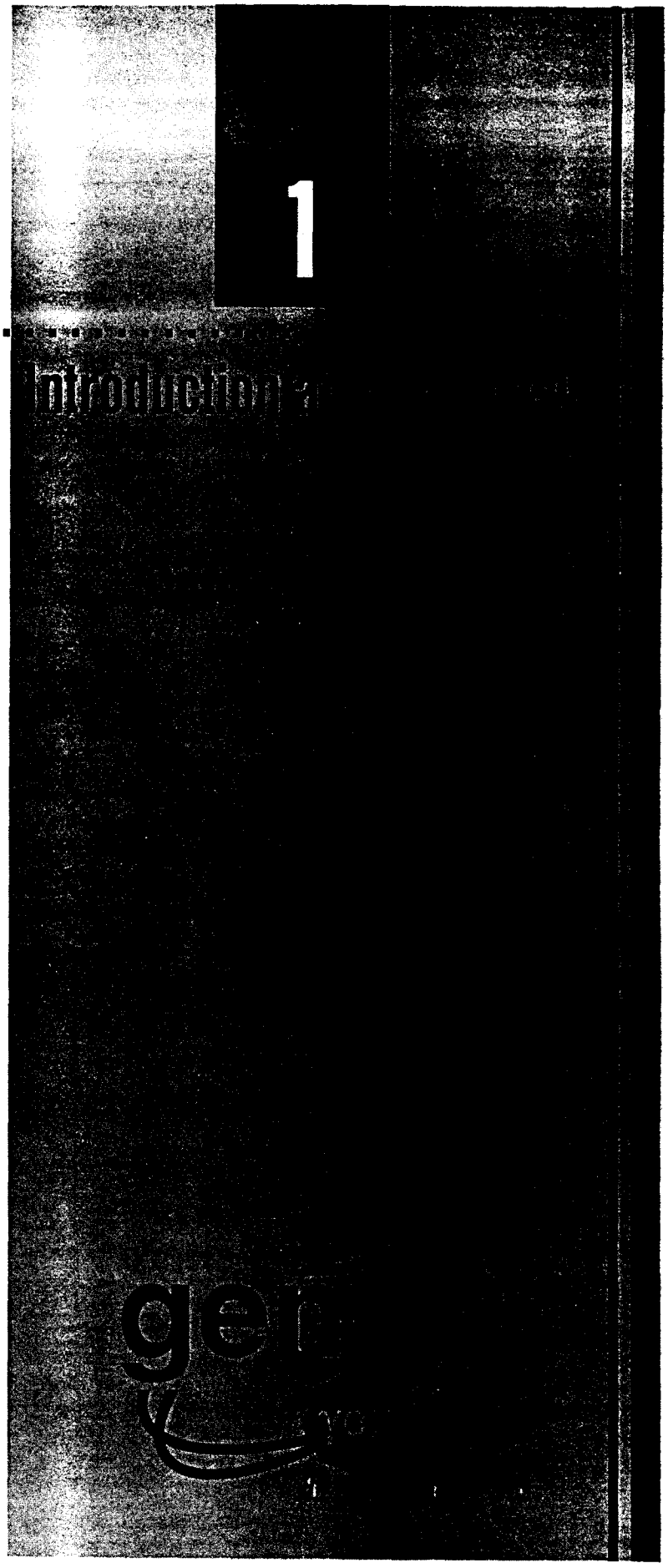

GEM

DETECTOR ISO SECTION (LAr OPTION)

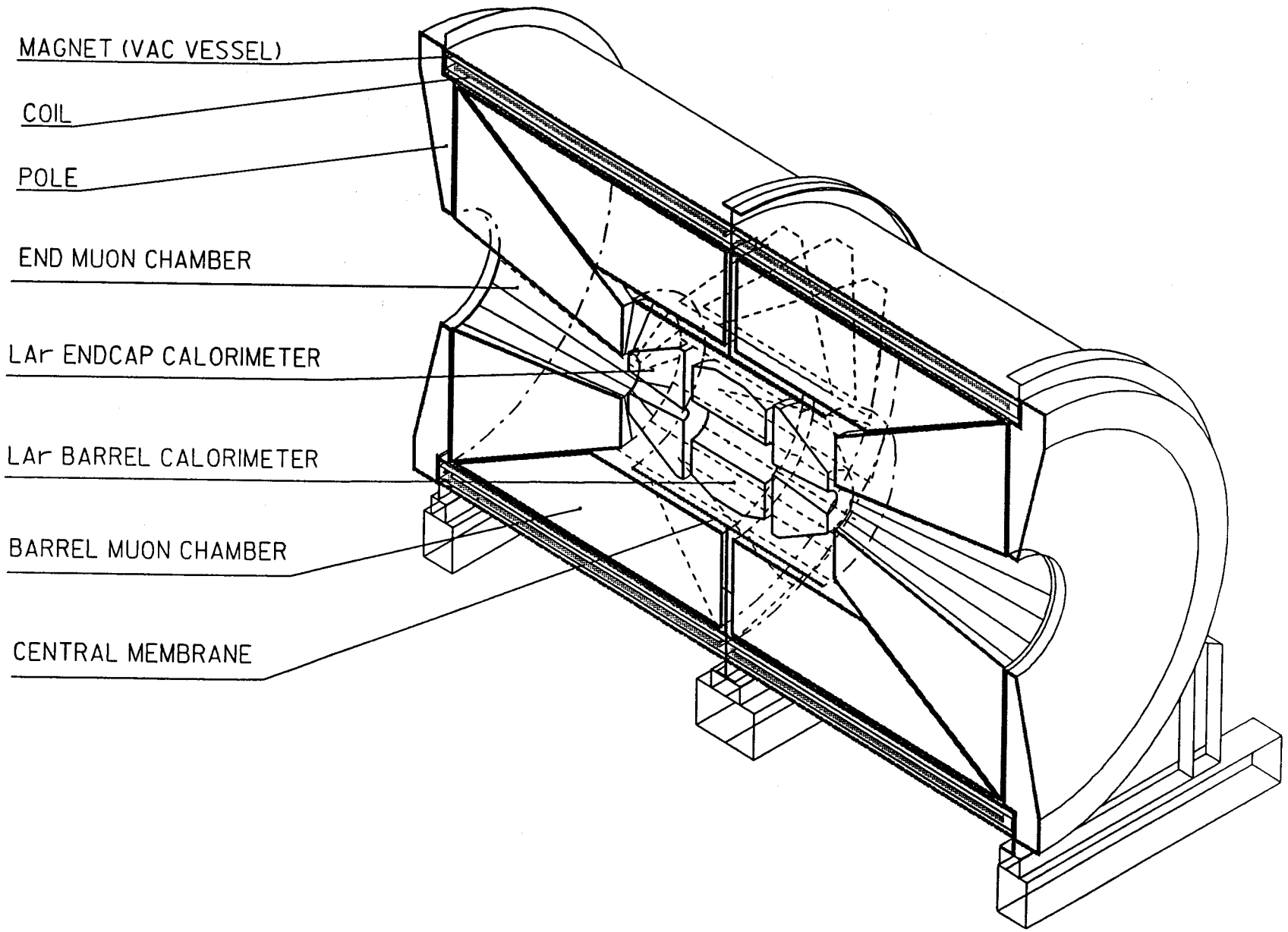

1.0 INTRODUCTION AND OVERVIEW

The construction of the Superconducting Super Collider offers an unprecedented increase in the energy available to reveal new aspects of the structure of matter. It has long been known that collisions with a small distance between two constituents in the incident protons are associated with the production of particles with large momenta transverse to the incoming protons, and that the characterisics of such collsions are controlled by the fundamental strong and electroweak interactions. This fact underlies the discovery of the $W^{\pm}$and Z^0 bosons at the SPS Collider at CERN and the continuing search for the top quark at the Tevatron Collider at Fermilab. With its much greater energy and luminosity the SSC will greatly extend such measurements. There are strong theoretical reasons to believe that this will lead to an understanding of the origin of the $W^{\pm}$and Z^0 masses, perhaps through the discovery of the predicted Higgs particle. It may also lead to an explanation of the quark and lepton masses, to the discovery of new and striking symmetries, such as the existence of supersymmetric particles—a whole world of particles mirroring the familiar particles but with different spin and higher masses, or to the discovery of completely new interactions.

In the realm of such short-distance collisions the particles of interest are not the mesons and nucleons but rather the particles which directly participate in the fundamental interactions. These are charged leptons — electrons, muons and taus; uncharged neutrinos; photons; $W^{\pm}$ and Z^0 bosons, which are detected by their decays into leptons; and quarks and gluons, which are not detected directly but reveal themselves as "jets" of many mesons and nucleons in a narrow cone. To study short-distance collisions at the SSC it is advantageous to design a detector which measures charged leptons, photons and jets, but largely ignores individual mesons and nucleons. This allows more freedom to concentrate on the most accurate possible measurement of the fundamental particles, and to adopt detection strategies which enable operation at a very high rate of collisions, as high as the billion per second which the SSC should reach after some development.

This document describes an experiment which has been designed on these principles. GEM stands for Gammas (photons), Electrons and Muons. Precise measurement of these will be the main emphasis of the detector, though jets will be measured as well. By finding how much transverse energy is missing in the collision, it will be possible to deduce the presence of energetic neutrinos.

Photons and electrons will both be accurately measured by the same device—an electromagnetic calorimeter. The intention is to measure the energy of high energy electrons and photons to an accuracy of better than one percent, while determining their position to about one millimeter. This opens up the possibility of discovery of the Higgs particles in the low mass region, around 80 to 140 Gev, where the decay into two photons is the only mode with a reasonably favorable signal-to-background ratio. GEM will excel at this difficult task. The precise energy measurement of electrons plays a vital role as well in the discovery of more-massive Higgs by the decay first into two Z particles, which yield four charged leptons. The background is more favorable in this case, but the rate is low and the discovery must be made with a small number of events. Such precision might

also be useful in the search for many other hypothetical particles.

To obtain this performance in the electromagnetic calorimeter, there is an ongoing program of research and development exploring the most promising techniques for giving the highest resolution in this range of energy. A relatively small tracking volume has been accepted in order to minimize the overall size of the calorimeter, which thereby gives greater freedom in choosing detector technologies and mechanical structures. A study of the many possible technologies has yielded two strong candidates which will give the best and most cost effective performance. These two technologies are noble-liquid ionization detectors and barium fluoride crystal scintillators. The goal is to make this important choice within one year.

Hadronic calorimetry is given less emphasis in GEM but is still important. It is needed to help identify photons, to search for possible substructure of quarks by looking for deviations from the predicted rates for jets, to contribute to the search for Higgs by detecting the decay of Z^0s to jets, and to detect neutrinos or other non-interacting particles by measurement of missing transverse energy. In the central region scintillating-fiber hadron calorimetry would be used with the barium fluoride electromagnetic calorimeter option or liquid ionization hadron calorimetry with the liquid ionization electromagnetic calorimetry option. The methods of extension of the calorimetry to the most forward angles is still under study.

The GEM design for muon measurement relies on tracking in a magnetic field outside the calorimeter, which is made sufficiently thick that the muon tracking is well-shielded from the high particle flux from the interaction point. Hence, it should work well even at the highest collision rates possible at the SSC. High precision on the muon momentum is attained by measuring the curvature in a magnetic volume. The track length will be about 5 m. Track detectors of high point accuracy and stable alignment which are relatively insensitive to the magnitude and direction of the magnetic field have been chosen. This gives more flexibility which is particularly important in the forward direction. Here, the choice of a detector relying on charge interpolation on cathode strips allows a convenient mechanical design. Such a design would adapt very well to the problems of rapidly varying density of background muons and required trigger granularity. An important consideration, particularly in the "barrel" region where most of the tracking detector area is found, is the choice of a detector which achieves approximately the desired tracking accuracy in a single measurement rather than by averaging many measurements.

The cost of the total system of magnet and tracking detectors within this strategy has been studied, with a performance goal for muon momentum measurement of 5% at 90° for muons of 500 GeV/c. A minimum has been found at fields near 0.8 T and the chosen magnet size. The cost of the magnet itself is dominated by conventional structures, since rather little superconductor is required. There are a number of advantages in a magnet with iron only in the poles which fill the

ends of the solenoid. The magnet is then relatively light compared to the many thousand tons which would be required for a return yoke, saving many months of installation time and a major cost as well. This also provides a useful region outside the coil in which, at some future time, additional tracking could be placed to yield a substantial improvement in accuracy at high muon momenta. The requirements for working in the fringe field of such a magnet have been studied, and will be summarized in section 2.2.

The measurement of particle momentum in a solenoidal field degrades rapidly at forward angles. The feasibility of improving the measurement for angles in the 10 to 30 degree range by adding iron cones to the poles is being studied, since potential improvements of more than a factor of two are possible.

The goals of tracking particles in the central volume inside the GEM detector have been carefully analyzed. The performance will inevitably be limited by the relatively small magnetic field and radius provided in the design, but there are compensating advantages for particle tracking itself. The number of tracks which curl up inside the tracking detectors is relatively small, reducing the load on pattern recognition. The small size of the detector structures gives a possibility of achieving a small amount of material and a low number of conversions of photons to electron pairs near the beam pipe. The current design of the tracker provides unambiguous three-dimensional space points. All of these things are important, given the aim of retaining tracking capability at very high collision rates. The details of the design are still evolving. Section 2.5 relates the present status of these studies.

The trigger system must cope with the succession of beam crossings every 16 ns with more than one event in each crossing. When a trigger is derived from one detector system, it is important that the data in other detector systems should be recorded in a way which allows the correlation to the same beam crossing. The trigger must be available quickly and the resulting strobe must be distributed back to the detector-mounted electronics in only a few microseconds so that the data buffers can be of the minimum length. Satisfactory solutions to these demands have been identified in a multilevel trigger system.

A great deal of engineering, and research and development must be accomplished in the year between the submission of the Letter of Intent and the Technical Proposal. The necessary work is briefly described here, and in greater detail in a series of proposals. The engineering is underway to give a preliminary cost estimate within less than two months, which will allow for design refinement to help maintain a total cost within the stated guideline of 500 M$.

The management of GEM has evolved since the collaboration was formed in June of 1991. The collaboration includes physicists who were working with L*, EMPACT, or TEXAS, and many who were new to the SSC program. An interim management scheme was adopted in the July meeting to carry through to the preparation of this Letter of Intent. A more formal plan is now being set up to allow GEM to proceed on to the next phase. An important goal of the collaboration is

the creation of a truly international framework for this experiment. Very extensive contacts have been established in many countries around the world and a large number of physicists from different countries have been invited to visit the SSC Laboratory. The leadership of the collaboration has already visited institutes in several countries and will continue to seek a very broad participation in GEM. Plans have also been made to include physicists from the international community in all levels of the management.

2

2.1

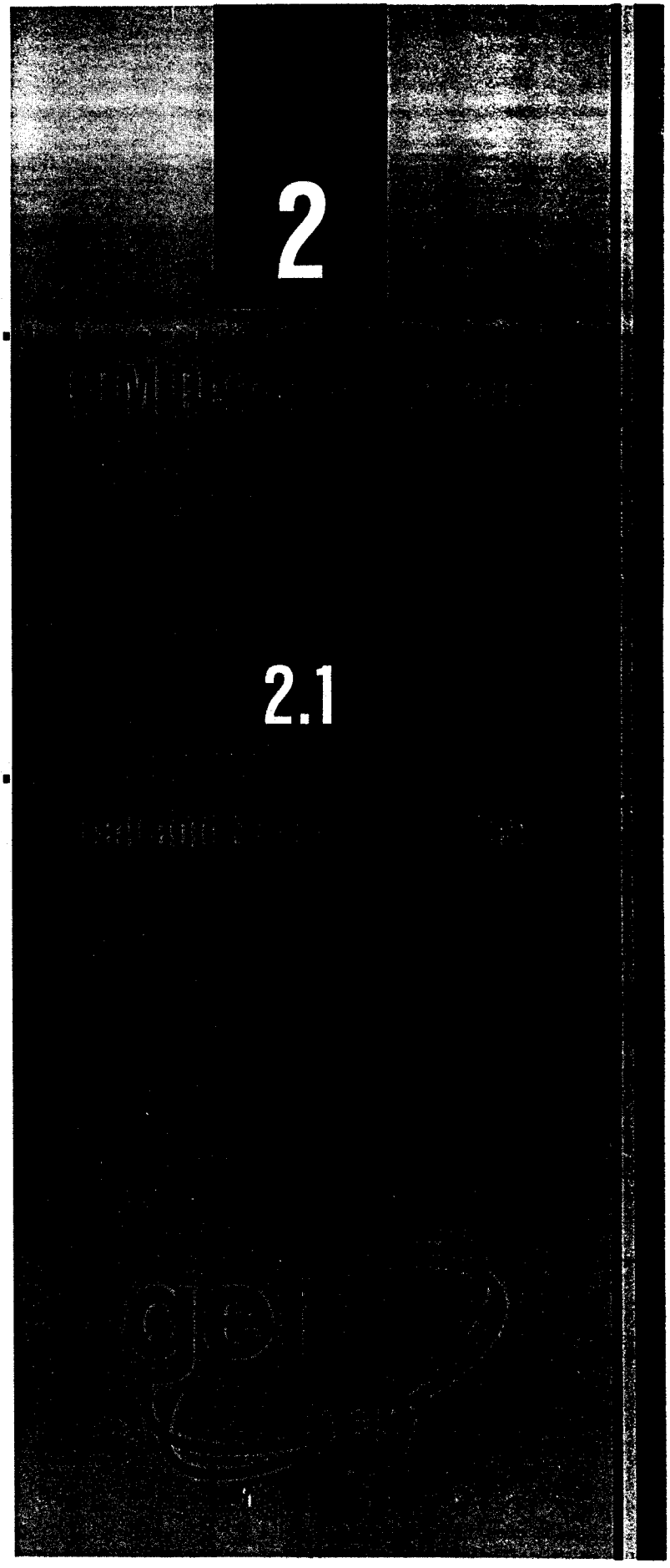

GEM'S EXPERIMENTAL HALL

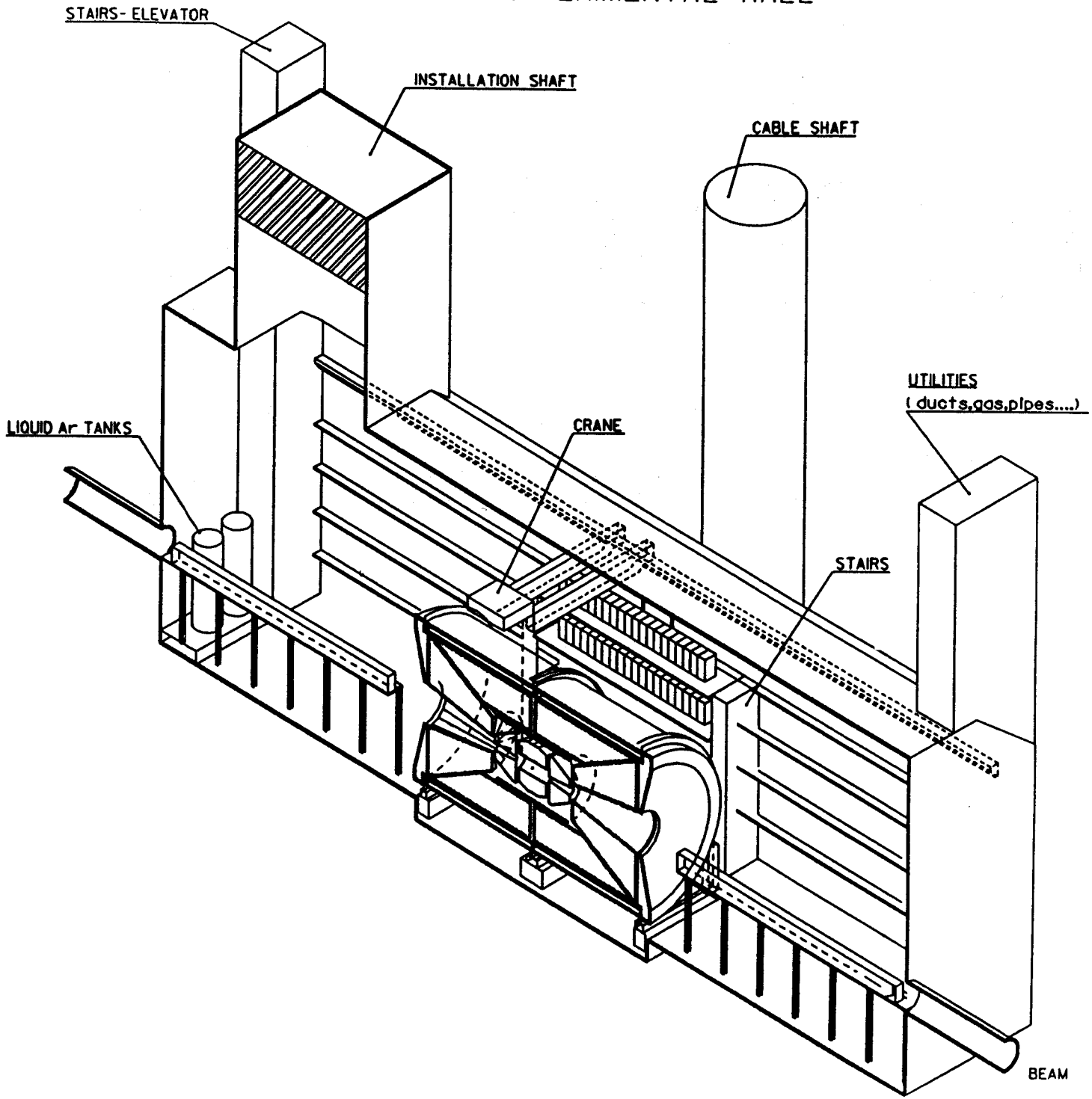

2.0 GEM DETECTORS

2.1 Detector Hall and Surface Facilities

Since the submission of the Expression of Interest (EOI), the conceptual design of the underground detector hall and surface facilities has undergone considerable study and revision. The design of a 26 m wide caverned hall at IR1, which had been the favored option by the architect/engineer firm PB/MK, has now been rejected based upon the results of geotechnical studies. A new design concept for a cut-and-cover hall at the East Campus site IR5 is under early study. A goal of this new study is the definition of the date upon which the underground hall will be available for detector component installation. Similarly, the definition of the required surface facilities is undergoing revision. The most significant issue related to the surface facilities is the need for the magnet coil fabrication hall early in 1993.

The original West Campus sites for GEM and SDC were located in Austin chalk, above a base of Eagleford shale. The stability of Austin chalk led to a recommendation that the smaller GEM detector be accommodated in a caverned hall with a maximum span of 26 m. This was the basis of the EOI design, and this concept placed no limitations on the detector and offered construction schedule advantages over the cut-and-cover construction method. A concern, at that time, was the poor stability of the underlying Eagleford shale.

Following additional geotechnical studies, PB/MK reported that the West Campus sites offered unacceptable foundation risks for the proposed major detectors, as the Eagleford shale reached maximum elevation in the detector site vicinities. The SSC Laboratory reviewed the recommendations and consulted with its own Physics Research and Conventional Construction Divisions, and with the SDC and GEM collaborations. This has resulted in a decision to relocate both major detectors on the East Campus where the Austin chalk offers superior foundation stability. The SSC Laboratory decision has been transmitted to the Department of Energy for approval of this project change. Pending this approval, both detector sites are now being planned at the conceptual level for the East Campus and mobilization for comprehensive geotechnical studies has begun. It is not known at this time whether the relocation will result in modified facility costs or delayed availability of the underground halls. These issues are being studied carefully by PB/MK.

The superior geologic characteristics at the East Campus promise several advantages for GEM. The hall can now be excavated by the cut-and-cover technique, which may permit greater hall width. This entails a small cost penalty which will not be accepted without offsetting technical advantages. The cut-and-cover technique permits additional installation shafts over the hall, within the excavation area, as these shafts require only emplacement of the shaft walls prior to the backfill, which would be reduced by the shaft volumes. Multiple shafts may offer significant installation and maintenance flexibility. This may reduce the required installation period. Hall width choices are permitted which may include the

volumes for forward electronics racks and underground cryogenic equipment for the magnet and cryogenic calorimeter options. These possibilities are under vigorous study by the SSC Laboratory, PB/MK, and GEM. The figure on the divider page shows a cutaway of the single-shaft cut-and-cover hall concept now being studied. It should be noted that prior to the decision to relocate the detector halls, the GEM collaboration, working with the SSC Laboratory, completed the version of the document specifying [1] the facility requirements. As these requirements are not site specific, they are guiding the East Campus design study.

Selection of the specific sites at the East Campus for GEM and SDC will depend upon the detailed geologic characteristics discovered during geotechnical studies. Each detector has distinct support concepts and floor stability requirements. The current concept for the SDC hall has a wider span. The difficulty of excavating the wider hall in the Taylor marl layers at IR5 has resulted in a preference for the SDC hall to be constructed at IR8. The slightly greater depth of the IR5 site provides the option of reduced return flux at the surface from the GEM solenoid. For these reasons, current planning assumes location of GEM at IR5, and SDC at IR8.

Figure 2.1-1 shows the current layout concept for surface facilities at the IR5 site. The halls are arranged so that transport of the large coil and calorimeter assemblies is over a very short distance to the headhouse area through which they will be lowered into the hall. The magnet fabrication schedule is very tight. A critical milestone is the availability of the surface hall for magnet coil fabrication. This hall is required in September 1993. Since this hall is located just outside the excavation region for the underground facility, no interference is expected in the two schedules.

However, it is a major current concern that the required change control procedures, which will ratify the decision to move the major detectors to the East Campus, will delay Title I design of the magnet fabrication hall. This could result in insufficient time to fabricate the magnet, install and test it, and complete the detector installation prior to the 1999 commencement of the physics program. The GEM collaboration is working closely with the SSC Laboratory, PB/MK, and the DOE area office, to facilitate rapid decisions on the critical issues identified in this chapter.

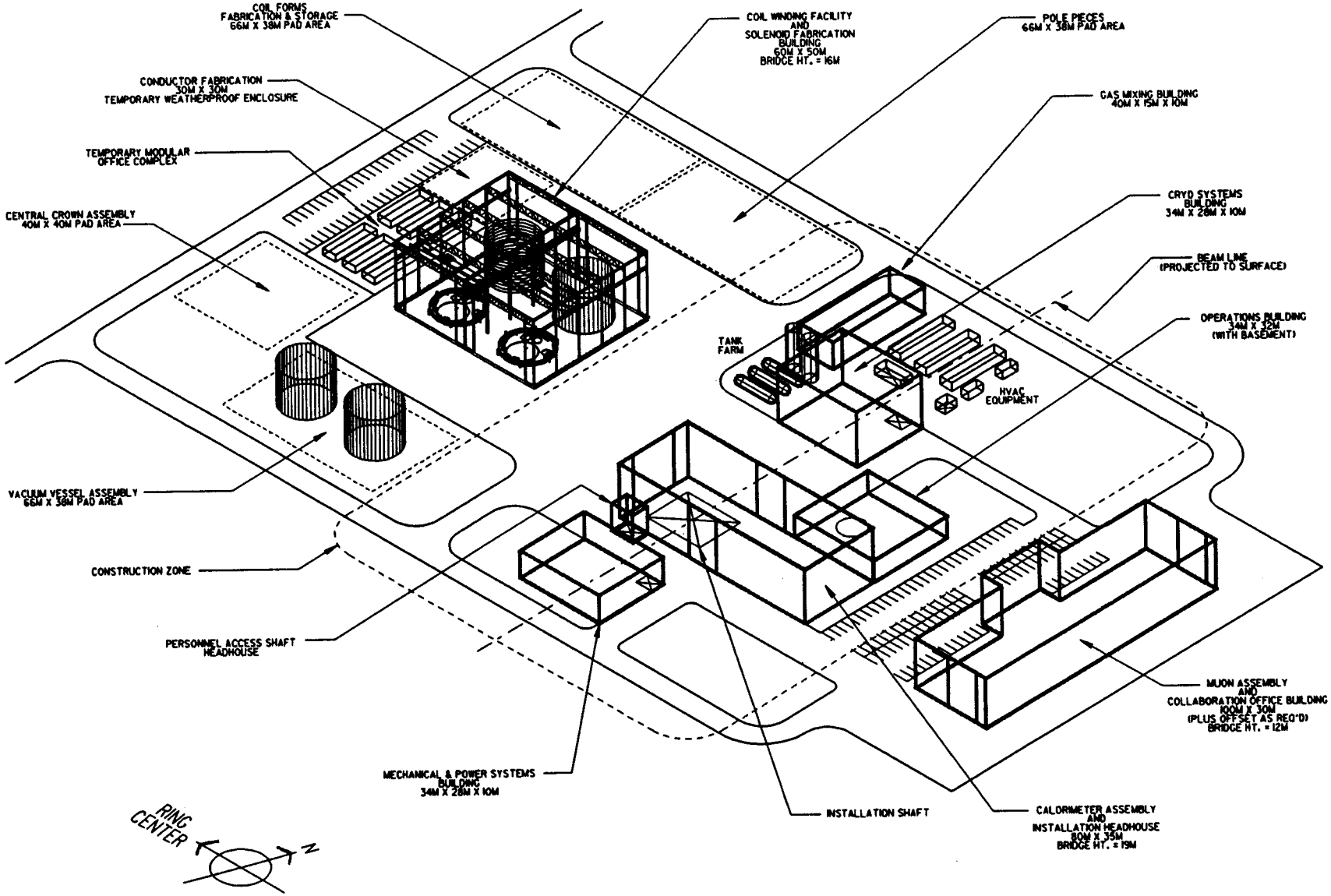

GEM SURFACE FACILITIES

Figure 2.1-1 GEM Surface Facilities Conceptual View

[1] Element specification for the Gamma, Electron, Muon Detector Collaboration (GEM) Experimental Facilities (User Requirements), GCT-000001, November 6, 1991.

2

2.2

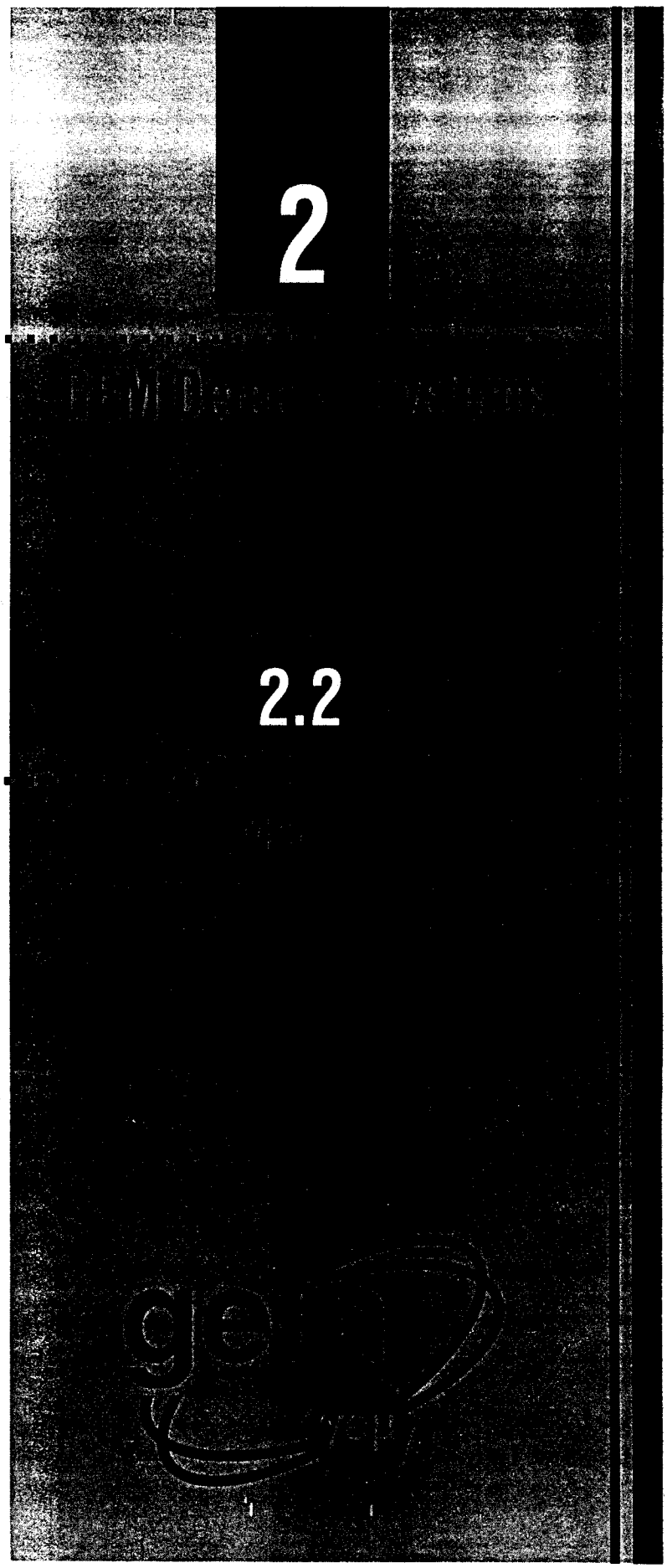

GEM MAGNET

WITH THICK POLE PIECES

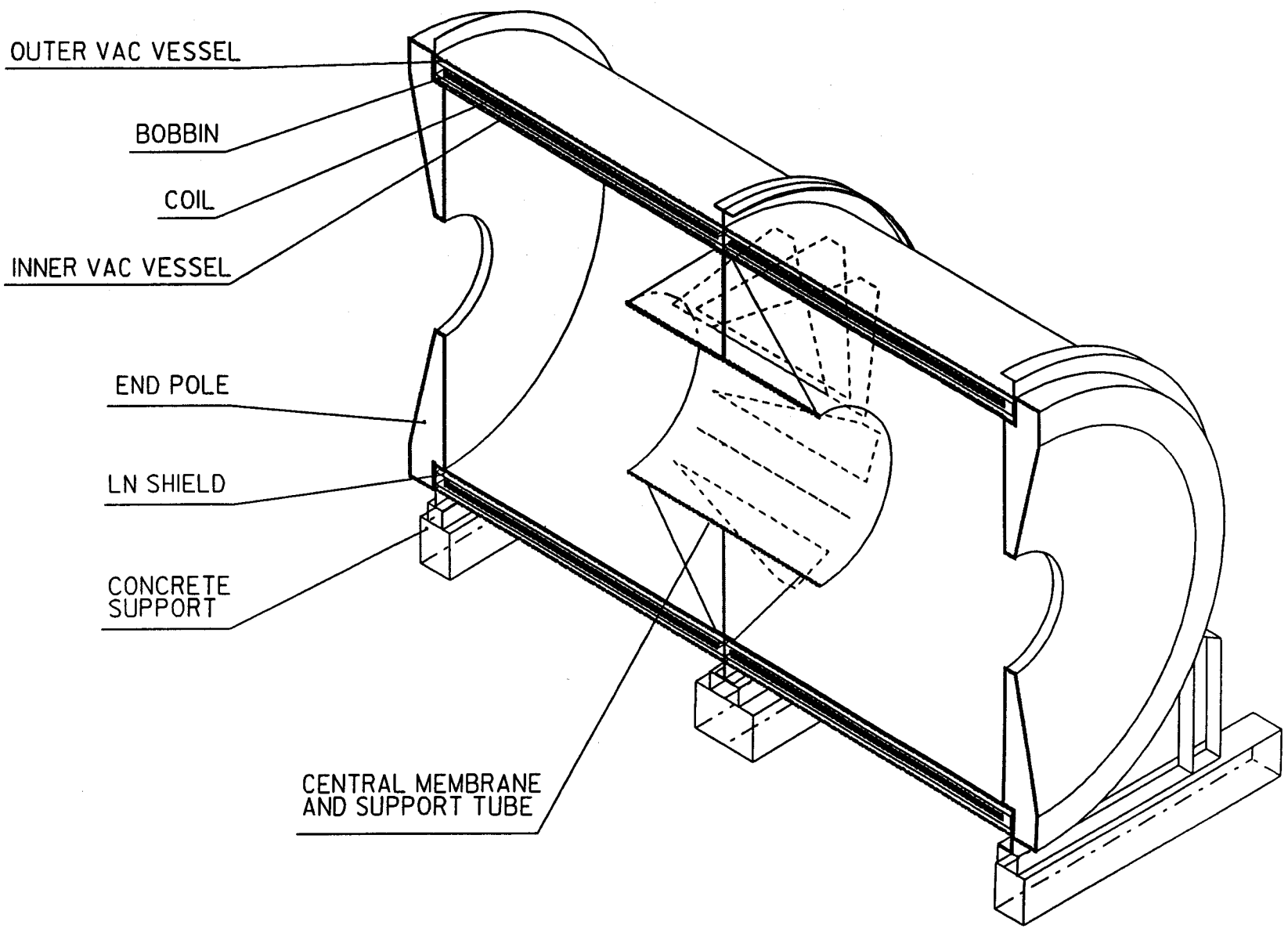

2.2 Magnet

The physics goals of the GEM experiment include, among others, high resolution measurements of the muons emitted at large transverse momentum in proton - proton collisions. The aim of the design concept is to have 5% momentum resolution for 500 GeV muons at 90 degrees assuming 100 micron measurement errors and no vertex constraint. Such resolution should be achieved over a broad central region of rapidity in order to provide sufficient acceptance for multimuon events. In addition, it is desirable to avoid placing material in front of the calorimeters which would reduce their performance. These requirements lead to the concept of a large aperture solenoidal magnet with muon tracking stations inside the uniform magnetic field.

The GEM Collaboration is proposing a large superconducting solenoid with field shaping iron end poles. Within this concept, the design has not yet been optimized either for the field or for the radius, but the proposed magnet could have a field of 0.8 T, an outside diameter of 20.4 m, an inner diameter available for tracking and calorimetry of 16.6 m, and a pole-to-pole inside length of 29 m. Other relevant parameters are: total stored energy of 2.04 GJ, operating current of 52.5 kA, discharge time of about 2 hours and an emergency discharge time of about 5 min. A list of parameters is given in table 2.2-1; the schematic drawing of the magnet is shown in figure 2.2-1. The corresponding resolution of the muon measurement expected for this baseline request and muon system performance described in the next section is shown in figure 2.2-2.

The design team comprises magnet designers and engineers from the MIT Plasma Fusion Center, Lawrence Livermore National Laboratory and National High Magnetic Field Laboratory (Florida). In addition all aspects of the design have been scrutinized by the GEM Magnet Technical Panel convened by the SSCL to study issues related to the feasibility of the technical concept, the cost estimate, the proposed schedule and operational issues. The membership of the panel included national and international magnet design experts as well as representatives of major industrial firms. The Panel found the concept of the GEM magnet to be feasible, the cost estimate to be credible and the construction schedule tight but possible. All recommendations of the panel are incorporated in the present design.

Table 2.2-1 Major Parameters List

1.	Central induction	0.80 T
2.	Mean radius of windings	8.9 m
3.	Outer radius of outer cryostat vessel	9.45 m
4.	Inner radius of inner cryostat vessel	8.40 m
5.	Coil length, end-to-end (per half)	14.44 m
6.	Cryostat vessel length	30.0 m
7.	Conductor length (total)	24 km
8.	Number of turns	408
9.	Total mass of coil windings (per half)	238 t
10.	Total mass of cryostat vessel (each half)	717 t
11.	Total mass of iron end pole (each)	2950 t
12.	Radial pressure on windings	255 kPa
13.	Inductance	1.47 H
14.	Number of ribs per coil assembly	3
15.	Central membrane maximum Z	0.025 m
16.	Winding minimum Z	0.25 m
17.	Axial force on poles	63.5×10^6 N
18.	Axial force on conductor	27.9×10^6 N
19.	Magnet axis height above hall floor	13.0 m

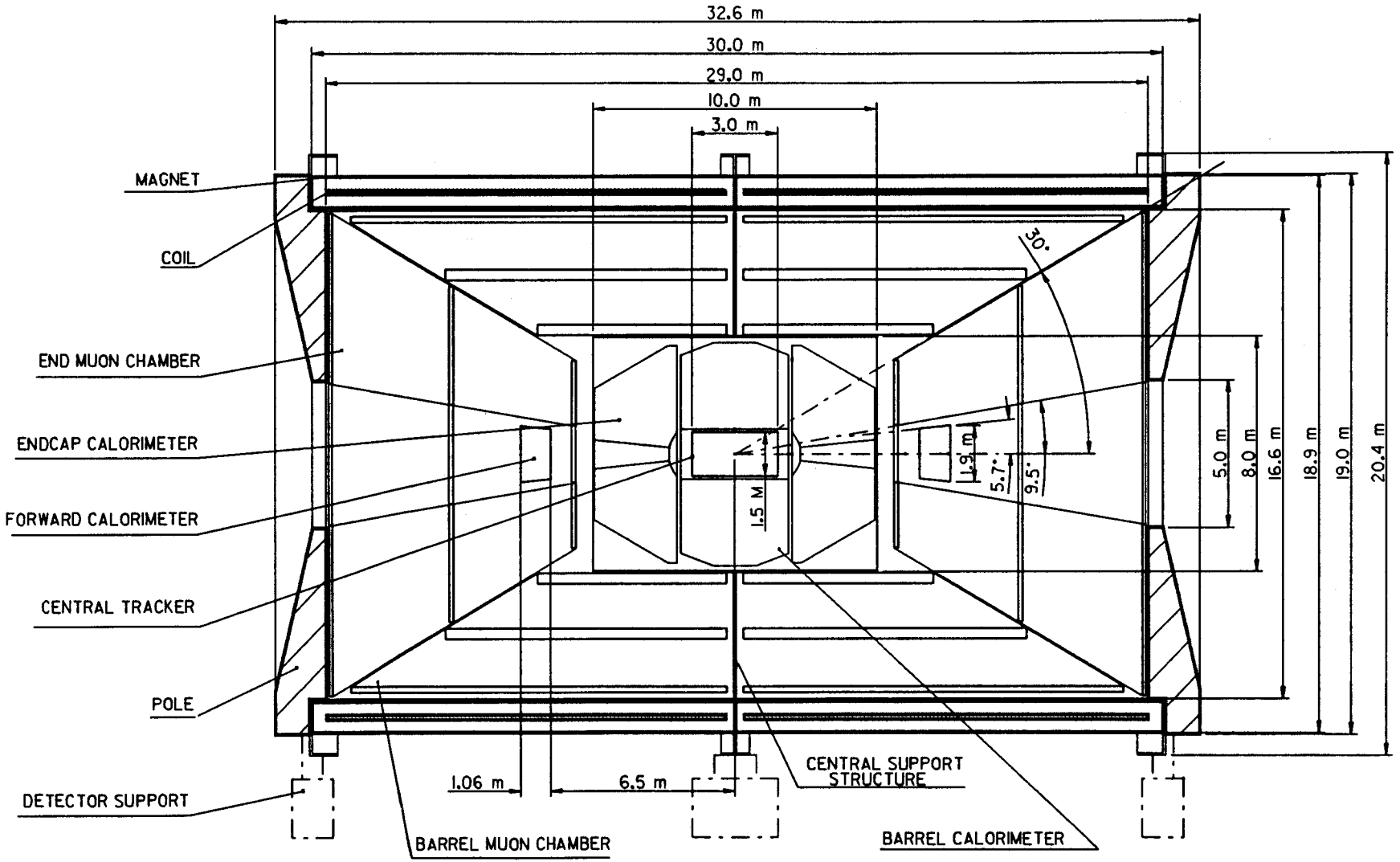

Figure 2.2-1 Schematic Drawing of the Magnet

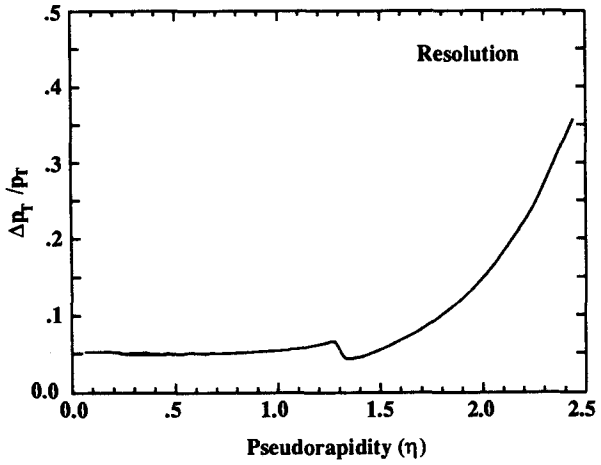

Figure 2.2-2 Momentum resolution of muons with p_T = 500 GeV as function of the pseudorapidity

The magnet will be constructed from two independent sets of single layer windings. The coil will be wound on the inner side of the 5 cm thick bobbin. The bobbin will be constructed in 24 separate cylindrical sections, 1.2 m long each. Each section will be wound separately. The winding will be surrounded by a liquid nitrogen radiation shield. Details of the assembly are shown in figure 2.2-3. The coil assemblies will be supported within the vacuum vessel by titanium rods connecting to both the 4 K coil assembly at one end and to the ambient temperature vacuum vessel at the other end. Support against gravity will be provided by a system of 16 titanium rods oriented roughly tangentially to the bobbin and connected to each end of the bobbin. This arrangement distributes the loads over 8 support points, and minimizes localized stress. Furthermore, the supports allow some axial and radial freedom to accommodate cooldown motion. Support against the axial Lorentz force on the coil will be provided by a set of 16 axially oriented rods providing a tensile preload and preventing any buckling problems.

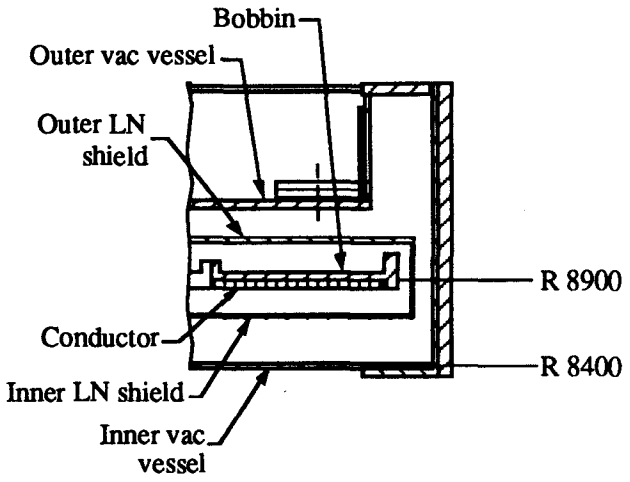

Figure 2.2-3 Details of the magnet coil assembly (dimensions in mm)

The mechanical structure will have a central support membrane sandwiched between the two halves. The membrane will provide structural support for the cryostat as well as a support for the muon chambers. The membrane will also support a tube containing calorimeters and the central tracker.

The cooling for the magnet coil will be obtained by the natural convection flow provided by the thermal syphon method. The tubing attached to the outside of the coil bobbin will be connected to headers on the top and bottom to promote free convection. The system can handle all heat loads including thermal radiation, cold mass support conduction and heating in the area of conductor joints. A separate low-flow loop will provide liquid helium to the conductor itself, but this helium will be used only for stabilization, not for cooling. The refrigeration system will be patterned on that of the accelerator.

There are several proposed conductor designs. All of them include standard niobium-titanium conductor with either copper or aluminium stabilizer. The designs differ in the liquid helium cooling arrangements ranging from a passive to a forced flow scheme. The choice of the conductor will be made based on its stability and the manufacturing scheme. A high priority R&D program of conductor development and tests will be initiated in the next few months. The design and costing is based at present on a high stability "cable-in-conduit" conductor with copper stabilizer.

The total cost of the magnet and its mechanical support system is estimated to be 104.7 M$ including contingency. The breakdown of the cost estimate for major subcomponents is given in table 2.2-2.

Table 2.2-2 Cost estimates for magnet subcomponents in k$

		Cost Estimate	Contingency
1.	Magnet R&D	4871	0
2.	Preliminary Design	4903	0
3.	Coil assemblies	36446	10255
4.	Poles and support	14874	3138
5.	Central detector support	4095	983
6.	Power/protection	832	136
7.	Cryogenics	8680	1418
8.	Vacuum	856	97
9.	Controls	285	51
10.	Installation	6925	1799
11.	Management	3552	568
Total		86319	18445
Grand total			104764

The iron magnet poles serve as field shaping components and not as a flux return. In the proposed design, there will be a fringe magnetic field in the experimental hall, access shafts and on the earth's surface immediately above the interaction region. The fringe field and the corresponding forces on ferromagnetic components has been calculated at all points in the hall, access shafts and on the surface using full two-dimensional, axisymmetric, finite element programs developed for plasma fusion confinement calculations. The field in the underground area will range from about 0.2 T close to the magnet poles to ~0.02 T at the end of the experimental hall. All the forces on the structural components of the hall, including crane rails and supporting structure appears to be small except in the immediate vicinity of the poles. The surface field will have a maximum of about 40 gauss immediately above the detector and the 5 gauss perimeter will extend over an oval area of about 200 by 180 m. This field will require local shielding of operation and control areas on the surface and institution of special operational procedures for the GEM experiment. These procedures, described in [1], will be based on experiences gained at other large magnet facilities with unconstrained fields (MRI hospital installations, plasma fusion facilities, FNAL 15' Bubble Chamber etc.). They will include restricting access to the detector when the magnet is on, securing ferromagnetic objects in the hall, etc. Local shielding of specialized equipment may be needed, although most of the problems associated with equipment working in a magnetic field can be minimized by the choice of less sensitive components and alignment with respect to the field lines. The surface area affected by the magnetic field will be inaccessible to the public. A proposal to shield the surface with a 15 cm thick iron plate appears to be a possible and cost

effective backup scheme. Complete discussion of fringe field related issues can be found in [1].

The magnet represents a critical path item in the GEM detector construction schedule. The experiment has to be completed at the beam turn-on time. The construction schedule derived with this constraint requires that the magnet should be manufactured, assembled and tested in the experimental hall before the end of September 1996. Rapid progress mandated by such an aggressive construction schedule requires timely completion of the engineering design studies and an early decision on the manufacturing scheme. In particular, intensive studies of the conductor and its stabilizer and of the winding scheme and the associated tooling are part of the FY92 R&D proposal. The engineering studies planned for the coming year include completion of preliminary design and specifications for mechanical supports, cryogenic, power supplies and power protection systems and for the magnet control and monitoring systems. The R&D program includes study leading to the choice of the conductor design, development and test, in conjunction with industrial partners, of a sample length of the conductor and development of a technique for making conductor joints. It includes also design and development of specialized tooling for conductor manufacturing and winding. Detailed engineering models [1] of the magnet and of the muon system will allow for optimization of the design with respect to the cost, size, and field value.

Because of its size, the proposed magnet will have to be constructed on site at the SSC Laboratory. A manufacturing plan calls for construction of two halves of the coil and the associated cryogenic systems in the surface building situated near the interaction region, and a complete assembly and test of the magnet in the underground hall. This plan requires the availability of the surface fabrication hall in 1993 and early definition and implementation of procurement strategy.

Additional design work on the improvement of the momentum resolution at larger values of rapidity has been initiated as well. The most promising option is to modify the shape of the iron pole to concentrate magnetic field flux at small angles. More detailed discussion of such options is given in the next section. All the options studied preserve the capability of the GEM detector for further improvements of muon momentum resolution by addition of muon chambers outside of the magnet coil.

---

[1] Considerations Leading to the Choice of Open Field Magnet, GEM Note No. GEM TN-91-30.

2

2.3

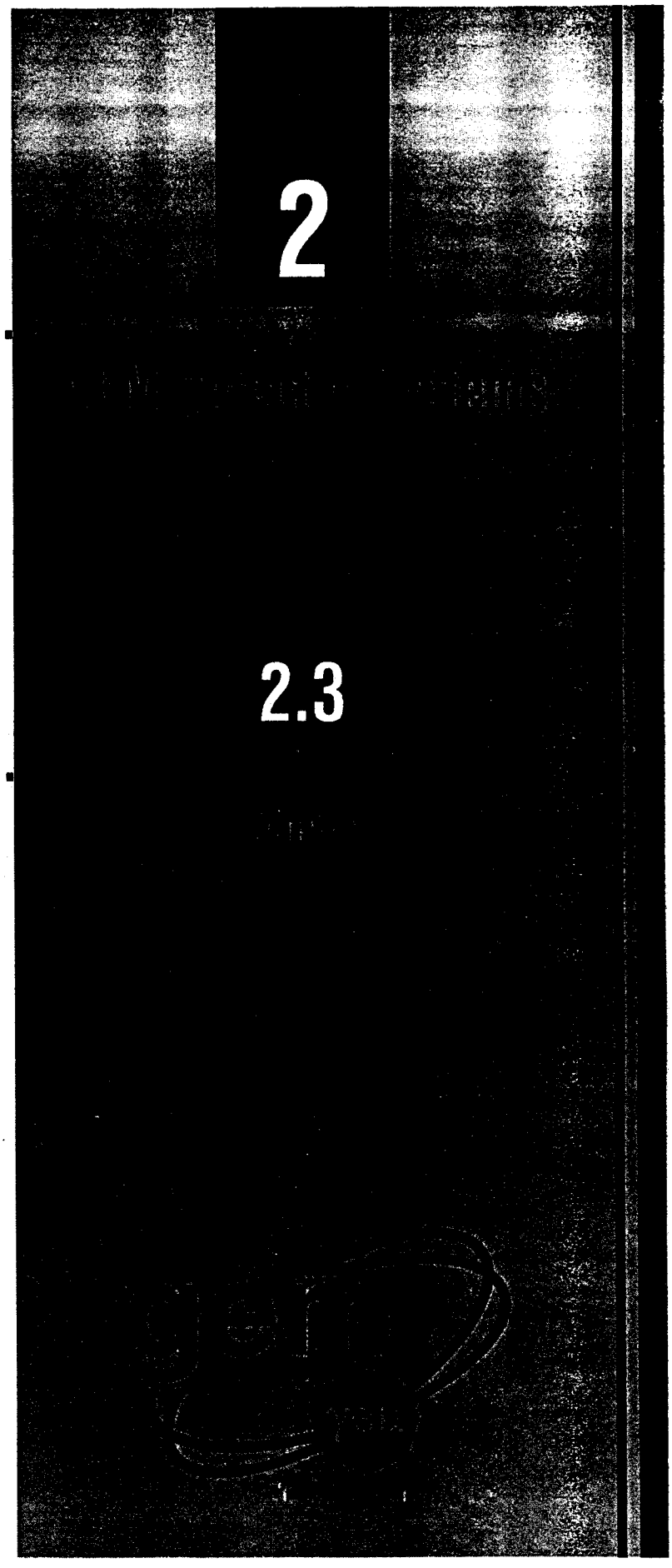

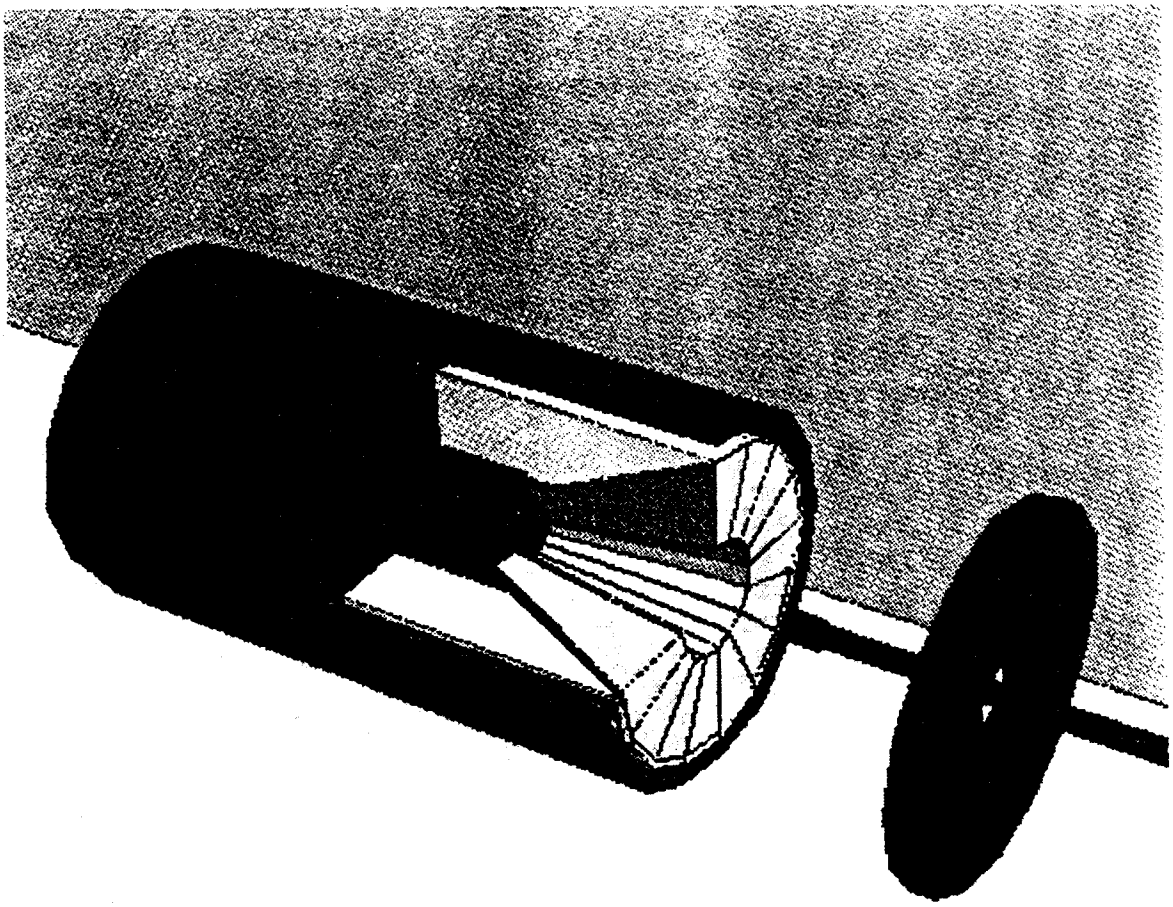

GEM Muon Subsystem

2.3 Muons

2.3.1 Introduction

The detection and momentum analysis of muons provide important access to rare and potentially important physics at the SSC. Reactions where the muon system is essential include: Higgs scalar production, production of new heavy Z bosons, gauge boson scattering, the high mass Drell-Yan process, technicolor, and supersymmetry. The expectation is that all of these processes, if real, will occur at a low rate.

To access this important physics, the GEM Muon System will furnish the following:

(1) muon identification,

(2) charge assignment,

(3) p_T trigger - both Levels 1 and 2,

(4) beam crossing time marker, and

(5) muon momentum determination from a few GeV/c to a few TeV/c.

Muons are unique in their great penetrating power, providing a distinct advantage in carrying out searches for new physics at the SSC. With sufficient material in the electromagnetic and hadron calorimeters, particle rates in the muon system are low enough to enable triggering and momentum measurements to be made reliably with luminosities at the $10^{34}\,cm^{-2}\,s^{-1}$ level. The GEM muon system will detect muons with 98% solid angle coverage and with high precision measurements of the momenta.

Our design goal of a muon system with large background rejection and good momentum resolution, which can be triggered selectively on large transverse momentum, requires that the detection elements be placed outside the hadron calorimeter. Figure 2.3-1 shows a schematic of the GEM muon system. Chambers are located in three superlayers between the calorimeter and the magnetic coil or endplate in both the central and

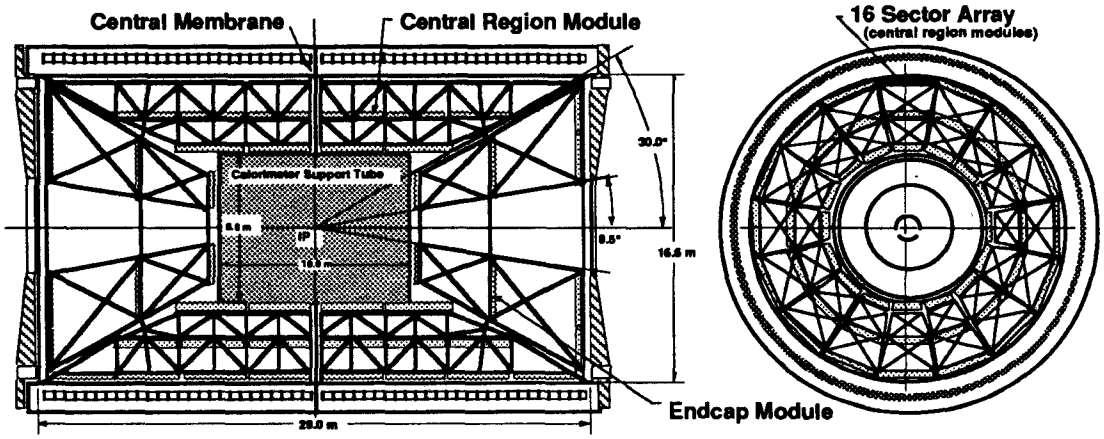

Figure 2.3-1 Overview of the GEM Muon System. The dimensions of the large solenoidal magnet are indicated. Shown are the placement of the muon chambers in both side and end view

endcap regions. The amount of material within the muon tracking system is kept to a minimum so that multiple scattering is small. A trigger based on transverse momentum of the muon is generated by trigger chambers located in each of the three superlayers.

The following table summarizes the baseline design of the GEM Muon System.

Table 2.3-1 Configuration of GEM Muon System

Dimensions of system:		
Length of magnet		29 m
Inside diameter of magnet		16.6 m
Uniform magnetic field		0.8 T
Calorimeter length		10 m
Calorimeter diameter		8 m
Calorimeter thickness at 90 degrees		12 λ
General characteristics of muon chambers:		
Intrinsic single layer resolution		100 μm
Layer-to-layer within a superlayer		25 μm
Superlayer-to-superlayer		50 μm
Global alignment systematics		200 μm
An 8 layer superlayer is <10% X_o		
Barrel region:		
Angle region: 30° to 90° ($1.32>\eta>0$)		
For momentum reconstruction and Level. 2 trigger:		
Three superlayers:	Bend plane	8-8-4 layers
	Nonbend plane	2-4-4 layers
Channel segmentation		3 cm
Channel count:	Bend plane	133 k
	Nonbend plane	25 k
For Level 1 trigger:		
Three superlayers:	Bend plane	2-2-2 layers
	Nonbend plane	2-2-2 layers
Channel count:	Bend plane	18 k
	Nonbend plane	21 k
Endcaps:		
Angle region: 10° to 30° ($2.44>\eta>1.32$)		
For momentum reconstruction and Level 1 & 2 trigger:		
Three superlayers:	Bend plane	4-4-3 layers
	Nonbend plane	2-2-2 layers
Channel segmentation		5 mm
Channel count:	Bend plane	231 k
	Nonbend plane	21 k

Momenta are reconstructed by measuring the sagitta S(m) given by $S = 0.3\ B\ L^2/8p$ for a trajectory at 90° to the beam, where L (m) is the length of magnetic field B (T) traversed, and p (GeV/c) is the momentum. In order to achieve good momentum resolution, the sagitta S (m) must be made as large as practically possible. Thus, $B \cdot L^2$ is the term to maximize and a large radius magnet of moderate field can provide a cost effective high resolution muon system.

2.3.2 Design Criteria

Various studies have been done to determine the technology independent specifications for the GEM muon system based on physics criteria.

(a) Momentum resolution. It is convenient to parameterize the muon momentum resolution, $dp/p = [(ap)^2 + b^2]^{1/2}$. The term b, dependent on multiple scattering in the middle module and pseudorapidity, limits the resolution at low momentum. The term a, which depends primarily on pseudorapidity, is determined by systematic alignment errors and module spatial resolution. This term limits high momentum measurements.

The low momentum specification for the measurement resolution comes from consideration of the intermediate mass Higgs search ($140 < M_H < 180$ GeV/c^2) through the process $H \rightarrow ZZ^* \rightarrow 4$ muons, which is expected to have a very small line width. To achieve clean detection of the Higgs and an estimate of its width, $b < 1\%$ is required. Thus the number of

radiation lengths in the middle superlayer must be < 10%. Figure 2.3-2 illustrates the point.

For large momentum, the most stringent constraint for resolution arises from the requirement of being able to assign charge to each of the two muons from the decay of a high mass Z′ so that accurate measurements of the forward/backward asymmetry can be made. As statistics limit Z′ searches even at the highest luminosity, only a small fraction of decay muons should be allowed to have charge misidentified, implying $dp/p < 30\%$ for about 3σ confidence level charge assignment. The heaviest Z′ accessible at the SSC has a mass of about 6 TeV/c^2, implying that $a = dp/p^2 = 1.0\times10^{-4}$ GeV^{-1}.

Several factors contribute to the momentum resolution in an actual system. There is the intrinsic muon chamber spatial resolution, the alignment errors, the multiple scattering smearing, and the precision of the B-field. Given the baseline design outlined in table 2.3-1, the momentum resolution as a function of angle and momentum for the baseline muon system is shown in figure 2.3-3. At 90° $dp/p = 4.5\%$ for $p =$ 500 GeV/c. With the parameters tabulated, it has been found that over most of the momentum range, the resolution is limited by the spatial resolution of the tracking chambers. Note that the muon charge can be determined to better than the 3 σ level for $p < 4$ TeV/c.

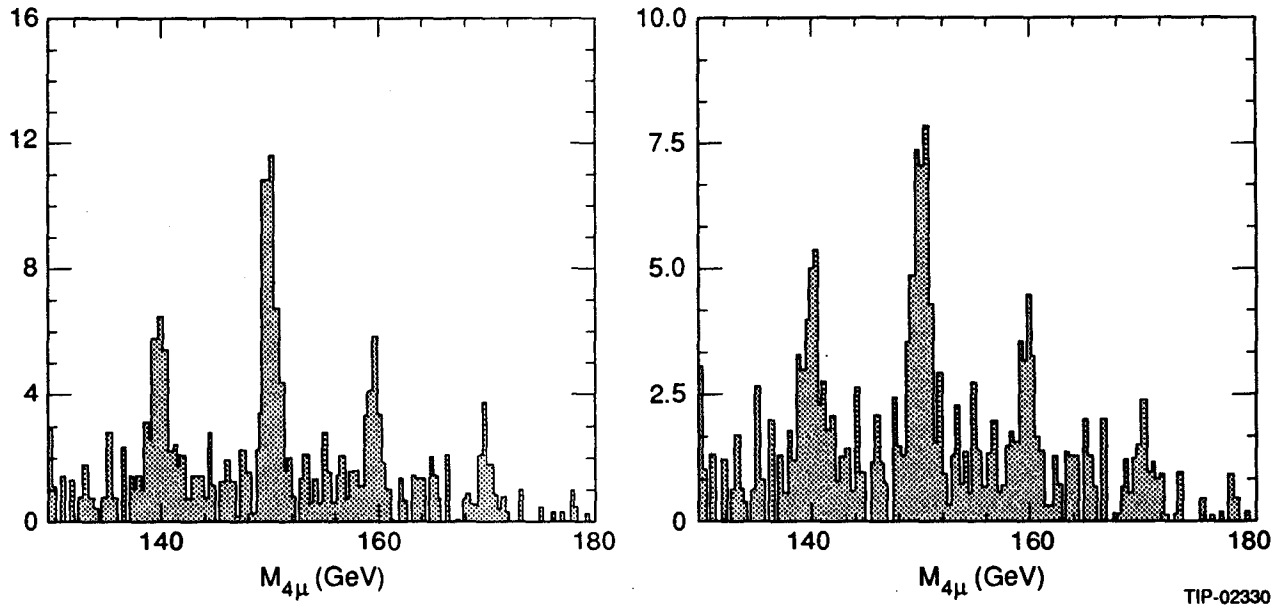

Figure 2.3-2 The reconstructed Higgs mass distribution for several values of mass is shown for two resolutions of the muon system, quantified by the number of radiation lengths in the middle superlayer. 1% on left, 10% right

Various improvements of the momentum resolution at high energies and in the forward direction can be effected at relatively low cost. Among the enhancements being considered are the addition of tracking chambers external to the magnet and B-field shaping in the forward direction. Furthermore, the reconstruction of the muon trajectory can be constrained to go through the primary interaction vertex leading to increased resolution. Figure 2.3-4a shows the enhanced performance if another superlayer consisting of three layers of chambers is placed 3 m outside the

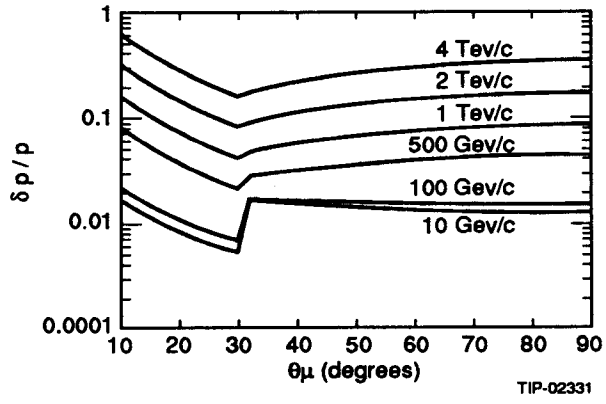

Figure 2.3-3 The muon momentum resolution of the baseline system is shown versus polar angle

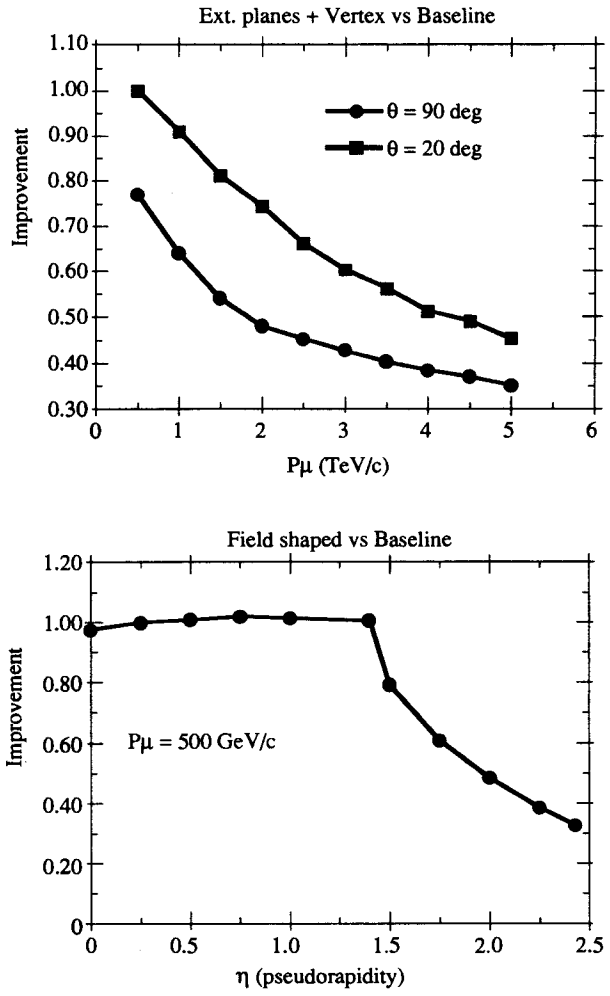

Figure 2.3-4 (a) The improvement of the momentum resolution by the addition of a vertex constraint and external muon planes is shown for two muon polar angles as a function of muon momentum. (b) For a 500 GeV/c muon the improvement of the momentum resolution by shaping the B-field in the forward direction is given as a function of pseudorapidity

magnet, and if the vertex is constrained transversely by 200 μm. The effect of shaping the B-field by increasing the radial component in the forward direction is shown in figure 2.3-4b. While it is believed that the baseline performance is quite good, evaluations are being done in terms of cost versus benefit.

(b) Rapidity coverage. To obtain good statistics for the Higgs to 4 muon channel (either through ZZ* or ZZ) a large solid angle (i.e., pseudorapidity) coverage for the muon chambers is required. For detection of the Higgs the goal is to maximize $N(\sigma) = N(\text{Signal})/\sqrt{N(\text{Background})}$. From the studies of Higgs production and detection, it has been found that $N(\sigma)$ is roughly

constant, having a value of about 6, for muons out to a rapidity of about 2.5. And a rapidity coverage of $-2.5 < \eta < 2.5$ provides about 90% acceptance for a 4 TeV/c^2 Z′ and even greater acceptance for a heavier Z′. (See figure 2.3-5.)

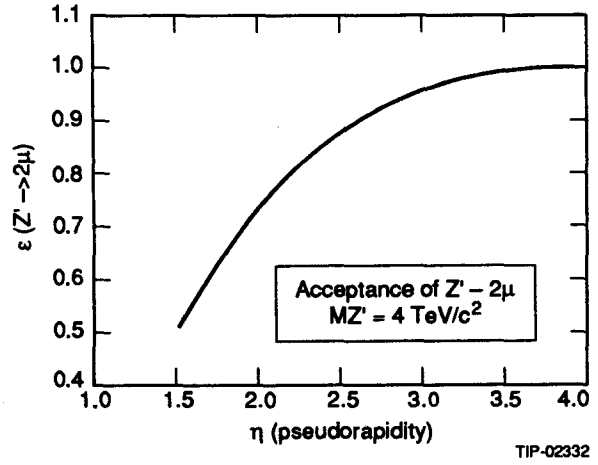

Figure 2.3-5 The acceptance of a 4 TeV/c^2 Z′ as a function of pseudorapidity

(c) Chamber Occupancy. The design goal limits the occupancy at $\mathcal{L} = 10^{34}$ cm^{-2} s^{-1} below a few percent in order to guarantee an unambiguous muon track-finding efficiency of nearly 100%. Figure 2.3-6 shows the muon rate as a function of pseudorapidity, η, for the inner, middle and outer modules, assuming 12 λ in the barrel calorimeter, and 14 λ in the endcap calorimeter. For a 4 m by 3 cm diameter drift tube, with a 3 μs Level 1 trigger delay time, the occupancy would be 1% in the barrel. In the endcap region, the rate increases to about 150 Hz/cm^2 in the inner modules at η = 2.5. For a 1 m long and 5 mm wide cathode strip chamber, and a Level 1 delay time of 3 μs, the occupancy would be less than 3%.

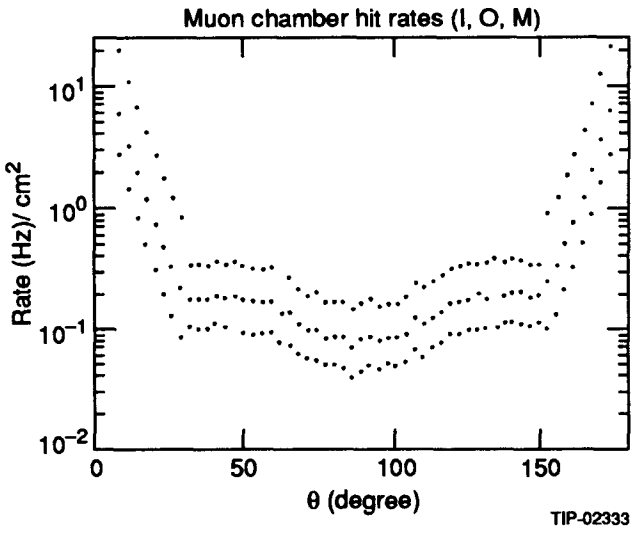

Figure 2.3-6 The muon rate/cm^2 at $\mathcal{L} = 10^{33}$cm^{-2}s^{-1} as a function of pseudorapidity for the three superlayers

Such occupancies are much lower than would be the case for tracking elements located inside of the calorimeter. Benefits of the relatively low rate outside the calorimeter extend to triggering as well. Figure 2.3-7 shows that the rate of muons above 5 GeV/c is a factor 100 lower than the total muon particle rate, implying that the p_T muon trigger is not seriously challenged.

(d) Energy Loss in the Calorimeter. Proper correction of muon energy loss in the calorimeter is very important for high energy muon measurements. As shown in figure 2.3-8, the energy loss spectrum has a significant high energy tail due to radiation processes. One requirement for the calorimeter is the ability to satisfactorily measure this energy loss to permit muon measurement accuracy at the level specified above. Another requirement is that it provide adequate shielding for the muon system. To

preserve a conservative safety margin regarding particle rates in the barrel even at the highest luminosities requires at least 12 λ for the barrel calorimeter.

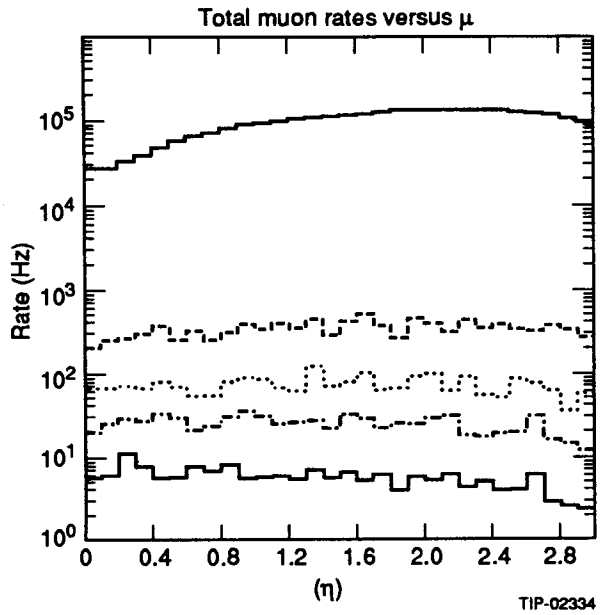

Figure 2.3-7 The total muon rate as a function of pseudorapidity for p_T cuts of 0, 5, 10, 15, 25 GeV/c

2.3.3 Description of Technologies

This section describes the technology options considered for the final design of the GEM muon system. For the barrel region, pressurized drift tubes (PDT) and limited streamer drift tubes (LSDT) are being investigated for the muon momentum reconstruction and Level 2 trigger. In the barrel region the Level 1 trigger and the beam cross tagging will be provided by resistive plate counters (RPC). For the endcaps cathode strip chambers (CSC) operated in the proportional mode seem to be the most attractive candidate technology. These chambers can be adapted to the radial geometry of that region, and will provide both the muon reconstruction as well as the beam tagging and Levels 1 and 2 trigger signals.

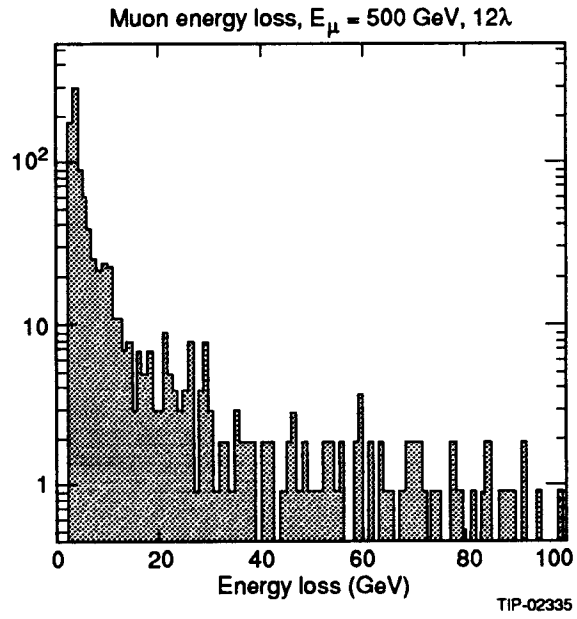

Figure 2.3-8 Energy loss distribution of a 500 GeV/c muon in the calorimeter

(a) Pressurized Drift Tubes. Precise tracking is possible with cylindrical tubes, operated with axes parallel to the magnetic field, due to the simple electric field configuration and the independence of the time-to-distance function on the angle of incidence. The cylindrical geometry of tubes enables improvement of resolution through pressurization as $1/\sqrt{\text{Pressure}}$ by the reduction of the diffusion coefficient, and improved statistics of cluster formation [1].

The GEM PDT's will be aluminum tubes with 300 μm wall thickness, and about 3 cm diameter. A possible configuration of the tubes is for the inner and middle modules each to consist of 8 layers of staggered tubes, and the outer to have 4 staggered layers. The number of radiation lengths in the

central modules would be 8.5% X_0, consistent with the technology independent specifications of the muon system.

The PDT alignment is based on accurate placement of wire ends relative to end plate fiducials. This can be achieved with precision machined reference end plates, and precision fabricated end plugs, pins and ferrules. It is believed that the required precision is achievable by calculating wire position from resonant frequency measurements. Such measurements can be made non-invasively with current-magnetic field excitation, and phase shift analysis. Wire holding through crimp and solder techniques will enable long term stability. Measurements have demonstrated that wire position can be predicted correctly within a few μm. (For 4 m wires tensioned at 80% of the yield strength, the sag will be about 230 μm.) At the sector level, alignment will be achieved with straight-line monitoring techniques such as those used successfully in L3.

(b) Limited Streamer Drift Tubes System. The chambers of this technology are envisaged to be rectangular boxes containing 4 layers of wires, each running through its own U-profiled cathode operated in the limited streamer mode. The positioning of the wires is achieved by supporting them on accurately machined insulating bridges running across the width of the chamber and through slots in the cathode at this support point. The bridge in turn is held against a reference point on the wall of the chamber which can be monitored or aligned from outside. The cathodes are to be made of thin aluminum, possibly coated to minimize secondary electron emission. The cathodes are held in place by a mechanical system separate from the bridges [2].

The chamber design has the flexibility of being made to any length with wire supports at any point of choice to minimize sag, and thus not rely on calculating a large correction. The wires can be laid down in multiples (as is done with Iarocci tubes), inspected, and tested for position and tension before being covered. All chamber parts can be manufactured by state of the art machine shops.

The wires will be operated in limited streamer mode. It has been demonstrated that the combination of large and fast pulses give good drift time measurements [2]. The use of aluminum cathodes makes the tube itself a good transmission line that preserves the rise time of the streamer pulse for drift time measurement and gives a coarse spatial measurement along the wire using instrumentation at both ends of the wire. Because the wires lie in cathodes which are open at the top, instrumented strips can be placed over this open side to obtain a measurement of position orthogonal to the drift time measurement and correlated with it by the common timing signal. In this way an x-y coordinate for each track can be obtained all in one chamber. The chambers have been tested using Laser beams, cosmic rays, and the 0.5 TeV/c beam at Fermilab.

(c) Resistive Plate Counters. Resistive Plate Counters (RPC) work at a uniform electric field of about 40 kV/cm between parallel electrode plates, 2 mm thick, with a resistivity about 10^{11} Ω cm [3]. The electrode plates can be made of plastic phenolic (bakelite) or resistive glass. The field

electrodes are formed by graphite varnish (~ 500 kΩ per square) painted on the outside surface of the 2 mm plates. The readout of the chambers is achieved by means of pick-up strips insulated from the field electrodes by a 0.3 mm thick polyethylene film. The voltage induced is about 0.5 V into 50 Ω with timing characteristics fast enough to tag the 16 ns beam crossings.

RPCs with dimensions up to 0.5 × 0.6 m^2 have been used in many experiments. It is planned that the GEM RPCs will have dimensions of up to 3.3 × 4.0 m^2.

The RPC system will be employed in all three superlayers of the barrel and will completely cover the precision muon measuring components as seen from the interaction point. (See figure 2.3-1.) RPCs will furnish three-dimensional space points for particles passing through the system. Short RPC strips running perpendicular to the magnetic field lines will give the x-coordinate, while long RPC strips running parallel to the magnetic field lines will give the y-coordinate.

The logic for the Level 1 trigger has four components: (1) three-fold coincidence timing in the non-bend plane, (2) straight-line space fit to three points in the non-bend plane, (3) three-fold timing in the bend plane, and (4) three-point sagitta measurement in the bend plane. The signal timing and space-point fitting placed in coincidence with the non-bend plane eliminates most punch-throughs, low energy tracks, and random pick-up noise. Putting the bend plane signals in coincidence with the non-bend plane further reduces the random pick-up noise problem. The sagitta measurement in the bend plane determines the transverse momentum (adjustable from 10 to 100 GeV/c) which activates the trigger.

(d) Cathode Strip Chambers. The high rate environment of the endcap region makes considerable demands on the triggering and tracking technology. Hence, cathode strip chambers (CSC) are being considered. These have a high flexibility in terms of channel segmentation, pattern recognition capability, and trigger speed [4].

The chambers will be deployed in 3 superlayers at z = 6, 10, and 14 m. Each superlayer features modular construction with trapezoidal modules, each of which spans 22.5° of azimuth, resulting in a structure with 16-fold symmetry. The superlayers have modules containing four chambers. In the outermost superlayer only three planes will be instrumented at startup.

Each chamber consists of two cathode planes (only one segmented) with an anode plane between them. The anode wires have a pitch of 2.5 mm and the distance between the cathodes is 5 mm. The precision azimuthal coordinate is obtained by charge interpolation between neighboring strips. Measurements made with this configuration indicate a resolution of order 50 μm per strip, insensitive to anode wire placement, gas gain, pressure, and temperature, and magnetic field nonuniformities.

For a maximum occupancy rate of 10 Hz the total number of channels is 252k. The superlayers closest to the absorber cover a relatively small area. If necessaryt, more planes could be added

for increased pattern recognition with a relatively modest increment in the total channel count.

The spatial resolution of these chambers in the azimuthal direction is limited by the dynamic range of the charge signal referenced to the rms noise, which is proportional to the capacitance of the cathode strip and inversely proportional to the square root of the integration time. In order to operate the chambers at a relatively low gain (~2–3×10^4) the intention is to use an integration time of about 1 μs. Using an analog multiplexer a single ADC can digitize a large number of channels. Monolithic circuits developed for reading out silicon detectors meet the requirements for such a readout system. A parallel branch feeds a discriminator and the resulting signal is used for the formation of the Level 1 trigger.

The logic for the Level 1 trigger in the endcap region roughly follows the scheme used in the barrel, with the following enhancement. The fine segmentation of the trigger elements (5 mm wide strips) permits measurements of local vectors along the muon trajectory. By correlating the local vectors from the second and third superlayers, it will be possible to determine the muon transverse momentum at the first level of the trigger. The radial coordinate (nonbend plane) and the bunch crossing assignment are provided by reading the anode wires.

2.3.4 Mechanical Engineering of the Muon System

The barrel region muon support system is arranged in 16 measurement modules per end as shown in figure 2.3-1. These modules utilize an aluminum truss structure to support the muon chambers. Each module is attached to the endplates of the magnet cryostat, with kinematic hardware.

The support structure design will employ bolted and pinned clevis joints. This design permits the layered assembly of the truss joints to be disassembled and reassembled with accuracy. The maximum deflection will be less than 2 mm in any orientation and the stresses less than 2 kpsi for a central module weight of 10 tons.

The structure of the endcap region will be similar in concept to the central region but will be constructed of lighter cross section tubing appropriate for the 1 ton per module weight expected for the trapezoidal-shaped CSC design. The same 16-fold symmetry of the central region will be translated to the endcap regions and the endcap modules will be attached kinematically to the respective barrel region module structure.

In both regions there will be interface structures between the chambers and the support structure which will direct the support load through the truss nodes. The connection between the chambers and these structures will be flexural elements which permit predictable translation of the chambers in a plane.

Alignment of the muon chambers within a module will be accomplished by means of multiple straight-line monitors, similar to those successfully used to monitor and maintain alignment of the L3 muon system, to an accuracy of 10 μm rms. Actuators will control this alignment either in an automated closed loop or manually. Initial

alignment will be accomplished with precision surveying techniques.

2.3.5 Muon System R&D Plan

In order to design and build the GEM muon system a number of R&D issues have to be resolved. During FY92 there will be a study of the technologies discussed above, with the following specific objectives:

- Design and construct large scale prototypes of each of the technologies discussed above during the winter and spring of '92.
- Compare performance of competing technologies, e.g. PDT and LSDT in the barrel, by the summer of '92. Choose the best technology and concentrate effort leading to a full engineering design. Check that technologies are compatible as an integrated muon system in terms of noise, timing signals, etc.
- Certify that the triggering devices (RPC in barrel and CSC in endcaps) will operate reliably in their respective environments.
- Develop and evaluate chamber alignment scheme.
- Design, construct, and critique a scaled prototype chamber support fixture.

To focus the effort on the final evaluation of the triggering and tracking technologies, as well as study their operation in an integrated muon system, a cosmic rays test rig is envisioned. This setup (named TTR for Texas Test Rig) will be established at the SSCL and will be the central facility of the GEM muon group during the R&D and engineering design phases.

The strategy is to maintain some degree of flexibility during the early stages of the R&D program, keeping in mind that backup solutions should be considered in the event that a particular technology does not work out. The parameters of the technologies described above are nominal, and serious R&D studies are needed to design a practical system. Coordination of the design of the muon system with the evolving GEM detector will be important.

2.3.6 Summary

The design of the GEM Muon System is based on a large solenoid with muon tracking chambers placed outside the hadron calorimeter and inside the magnet coil. In this way, high precision reconstruction of muon tracks is possible, even in the highest rates being envisioned for the SSC. The system will provide a trigger dependent on the transverse momentum of the muons. An active R&D program is envisioned to determine which tracking and triggering technologies will be used and to develop support structures which will satisfy the demanding alignment criteria.

[1] Z. Zhou *et al.*, NIM A287, 439, (1990). S. Ahlen, *et al.*, Part. World 1, 168, (1990), Bing Zhou, *et al.*, IEEE Trans. NS-37, 1564 (1990), A. Tomesch, *et al.*, NIM A241, 265 (1985)

[2] L. S. Osborne *et al.*, Toroidal Spectrometer Group Progress Report, SSC Prog. Rep. No. 218, September 15, 1991

[3] R. Cardarelli *et al.*, NIM A263, 20, (1988), M. Bertino et al., NIM A283, 654, (1989)

[4] R. Debbe *et al.*, BNL-45402, (presented at the Symp. on Det. Res. for SSC, Forth Worth, TX, 1990), B. Yu *et al.*, BNL-44748, (presented at 1990 IEEE Nucl. Sc. Symp. Arlington, VA (1990)

2

2.4

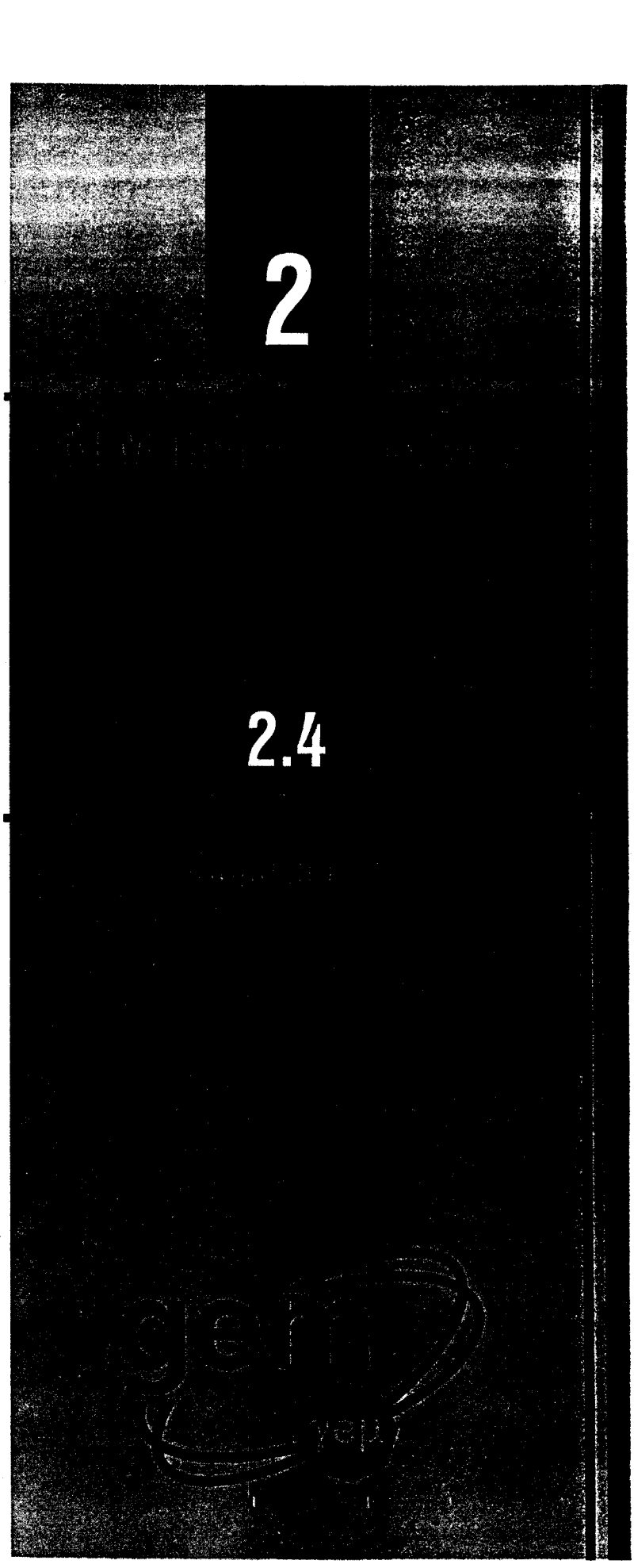

Liquid Argon Calorimeter

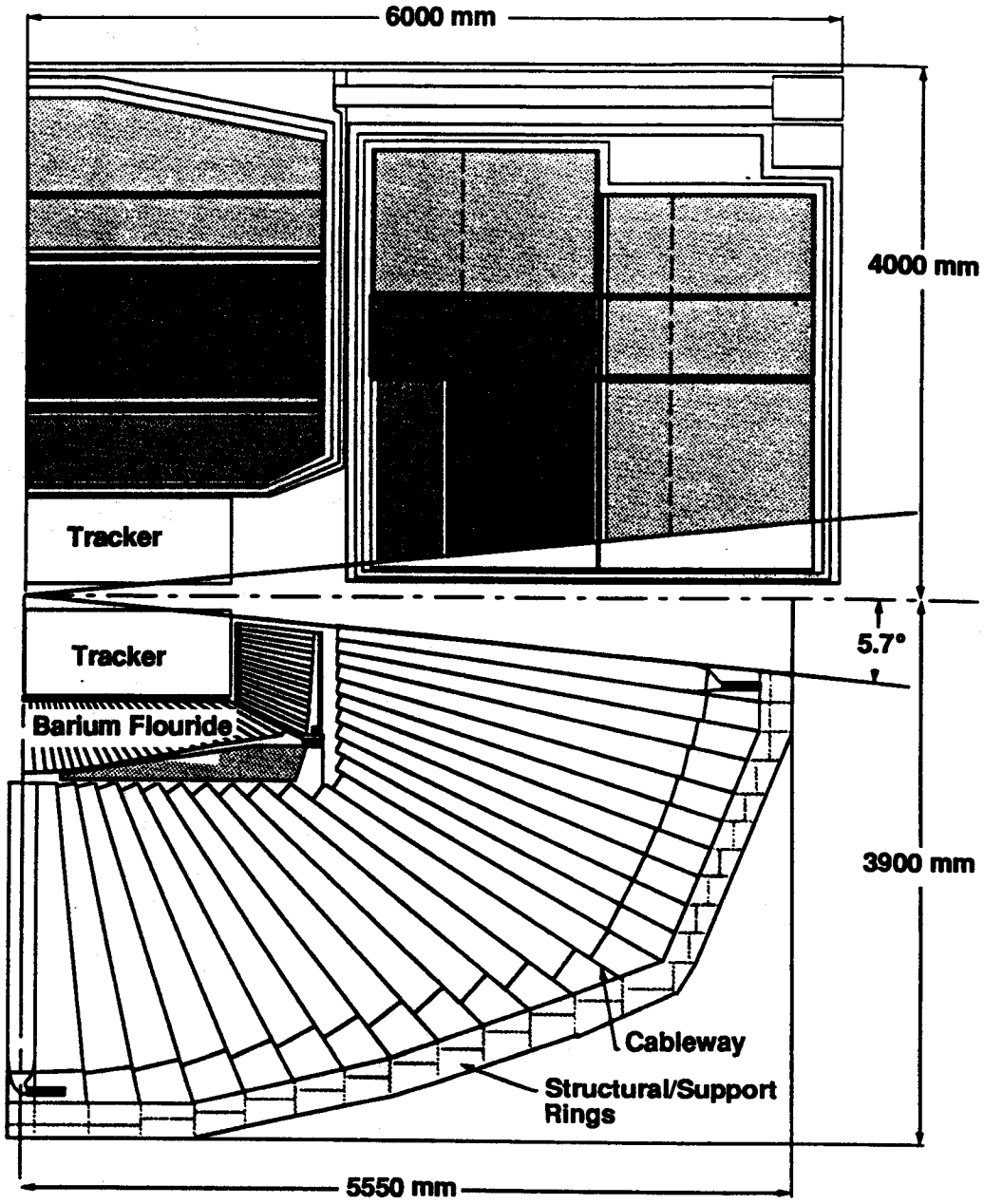

BaF2 with Scintillating Fiber Hadron Calorimeter

2.4 Calorimetry

2.4.1 Introduction

High precision electromagnetic (EM) calorimeters will have unique physics discovery potential at the SSC: in the search for Higgs particles in the mass range between 80 and 180 GeV, and in the search for new physics signatures involving electrons and photons beyond the Standard Model. GEM has thus been designed as a precision lepton and photon detector, where the calorimetry system is the centerpiece of the experiment. One of the principal goals of GEM's experimental design—and its R&D program—is to achieve the best feasible EM resolution, combined with good resolution for hadron jets and missing E_T.

2.4.1.1 BaF_2 with Scintillating Fiber Hadron Calorimeter, and Liquid Argon/Krypton Options

The high resolution, speed, and radiation resistance requirements, and the need to complete the R&D and engineering design of the optimal calorimetry system which fits within the budgetary constraints in 1992, have pointed the way towards two complementary systems:

- BaF_2 crystal high precision EM section, followed by a scintillating fiber hadron calorimeter.
- A Liquid Argon (LAr) calorimeter with a fine sampling accordion [1] EM section, where the EM resolution is improved by the use of Liquid Krypton (LKr) and/or thin plates in the accordion.

The complementary advantages of the two approaches are summarized below.

- BaF_2 Precision Crystal EM; with Scintillating Fiber HCAL
  - Higher intrinsic EM resolution: $\sigma_E/E = (2.0 / \sqrt{E} \oplus 0.5)\%$.
  - High uniformity for the EM section, based on the proven carbon fiber-epoxy composite mechanical support system design used by L3.
  - Higher EM and HCAL speed, resulting in a somewhat higher signal to noise ratio in an isolation cone, when searching for events containing isolated electrons or photons:
  - Effective compensation: the intrinsically non-compensating EM section (e/π response ratio ~ 1.7) can be compensated by adjusting the $e/\pi \approx 1$ in the hadron calorimeter behind the BaF_2. This leads to a small constant term (below 2%) in the resolution for jets.
- Liquid Argon with Accordion EM; Liquid Krypton Option
  - Intrinsic stability resulting from the use of ionization with unity gain and readout of the peak current, leading to ease of calibration.
  - Large systems involving plates have been tested [2], and have demonstrated the requisite resolution and small systematics (below the 0.5% level).
  - Intrinsically radiation resistant.

- Good uniformity and position resolution has been demonstrated in test beam modules.
- Ease of segmentation longitudinally allowing excellent angular resolution for photons.
- Experience in many large systems: SLD, D0, H1, NA34, etc.

2.4.1.2 *GEM Calorimetry: Rationale and Selection Procedure for the Two-Pronged Approach*

Despite the advances on the R&D, conceptual and engineering design, and simulation studies of a full GEM calorimeter made for both systems over the last year, each requires one more year of R&D before the final choice of the system which best meets GEM's physics goals can be made. Some of the principal issues for each system are summarized below.

The BaF_2 system, while providing a potentially large performance gain in energy resolution in the search for new physics, carries with it a higher risk. Production of large radiation hard crystals has not yet been achieved (the target date for a milestone demonstration of large rad-hard crystals is in the third quarter of 1992). In order to assess the risk, a panel of internationally recognized experts on radiation damage in materials in general, and on crystals in particular, is now reviewing the progress towards radiation hardness achieved up until now by SIC and BGRI in China. Following this review — if the level of risk is judged acceptable—the panel is expected to provide expert guidance on the research methods and the scope of the program required to achieve the required radiation hardness, with large scale production scheduled to start in 1993.

The Liquid Argon system has demonstrated stable performance in test beams—with EM resolution for an accordion module[1] at the level of $\sigma_E/E = 10\%/\sqrt{E}$ with a constant term consistent with zero. However, it has yet to demonstrate a resolution of $\sigma_E/E = (7.5/\sqrt{E} \oplus 0.5)\%$ or better, the performance goal set by optimizing sensitivity to the Higgs in the 80–140 GeV mass range at the SSC. In addition to test beam results with liquid krypton and/or a thin-plate accordion module, with the beam incident over a range of angles which is representative of the proposed GEM detector, the overall engineering design for this option will be developed rapidly and in detail over the next several months.

As the R&D proceeds during 1992, test beam results, other performance data, and the detailed engineering design, will be used to carry out a series of full detector simulations. The simulations for each calorimeter option will include a sufficiently detailed representation of the overall GEM detector geometry, its cracks and inactive regions, its readout characteristics, and the principal systematic effects, to objectively compare the two systems. The overall performance of each system in terms of its resolution, uniformity and hermeticity will be completed, and illustrated in terms of a series of physics examples — including Higgs, SUSY, and other new searches for new physics. This process will be finished, and the final GEM calorimetry system will be chosen in time for the submission of the Technical Proposal in the Fall of 1992.

2.4.2 Physics Requirements

2.4.2.1 Electromagnetic Calorimeter

An important potential discovery for the GEM electromagnetic calorimeter (EMC) is the Higgs boson in a mass range between 80 and 180 GeV through its $\gamma\gamma$ and $ZZ^* \rightarrow 4\ell$decay modes [3]. While the 4ℓdecay mode will allow GEM to detect a Higgs with a mass heavier than 140 GeV, the $\gamma\gamma$ decay mode will cover a gap between 140 GeV and the upper limit for Higgs detection at LEP Phase II (80 GeV) [4].

$H \rightarrow \gamma\gamma$ detection places stringent requirements on the overall detector design, especially on the design of the EMC. Because of the small production cross-section (50 to 200 fb) and the narrow decay width (5 to 10 MeV) of the Higgs boson in this mass range, and because of the huge irreducible $\gamma\gamma$ background and QCD jet background, the discovery potential is directly related to the reconstructed $\gamma\gamma$ mass resolution and the ability of the detector to reject background. Note that GEM requires the capability to distinguish photons from electrons with close to 100% efficiency (either from the central tracker or a pre-shower stub detector) so that the electron pair background, which has a rate of 2 Hz at the SSC, may be rejected effectively.

2.4.2.1.1 Energy Resolution

A simple parametrization of the energy resolution of a calorimeter can be expressed as:

$$\frac{\sigma_E}{E} = \frac{a\%}{\sqrt{E}} \oplus b\%$$

where **a** and **b** are two constants and E is the energy being measured. Table 2.4-1 lists the time factor in discovering the Higgs by using the $\gamma\gamma$ decay mode as a function of **a** and **b**, normalized to the BaF_2 resolution goal **a** = 2.0 and **b** = 0.5. A calorimeter with a resolution of **a** = 7.5 or better has a significant advantage over an experiment that does not emphasize EM resolution.

Table 2.4-1 Effect of Energy Resolution: a and b

	a = 2.0	5.0	7.5	10	15
b = .25	0.63	1.2	1.7	2.2	3.3
b = 0.5	1.0	1.4	1.8	2.3	3.4
b = .75	1.4	1.7	2.1	2.6	3.6
b = 1.0	1.8	2.1	2.4	2.9	3.7

2.4.2.1.2 Photon Direction Measurement

Since a photon does not leave a track in the central tracking detector, the photon angle information may be obtained by using: (1) longitudinal sampling in the EMC to measure the direction of the shower (the liquid ionization option easily provides this), and/or (2) correct event vertex tagging by the central tracker to determine the origin of the shower. When running at the SSC design luminosity of $10^{33}\,cm^{-2}s^{-1}$ GEM will find the correct event vertex by selecting the vertex with the largest multiplicity of stiff charged tracks in the angular region covered by the central tracker. Since the vertex *z* resolution (500μm) is better than the position resolution for many of the photons in the EMC, the angular

contribution to the mass resolution is dominated by the position resolution of the calorimeter, however the effect of the position resolution on the intermediate-mass Higgs discovery potential is negligible for a resolution of 2 mm. A good vertex z resolution of less than few mm is very important, if the EMC has no longitudinal segmentation. Without angular information from either of the above techniques, the discovery time for the Higgs would increase by as much as a factor of five.

2.4.2.1.3 Photon Identification and QCD Background Rejection

There are copious π^0's, and thus photons, produced at the SSC. The production cross section of QCD two jet events is 2 mb for $p_T > 20$ GeV and of γ-jet events is 237 nb. A narrow neutral jet with multiple photons would fake an isolated photon. Single photons may also be produced in the parton shower process, which will cause irreducible QCD background. To identify real photons and to reject QCD jet background, an isolation cut, shower shape analysis and a preradiator may be used [5].

One simple isolation analysis requires

$$\sum_{r<R} E_T - E_T^{photon} < (E_T^{cut} + 0.1\, E_T^{photon})$$

where the usable values of R ($R = \sqrt{\Delta\eta^2 + \Delta\phi^2}$) and E_T^{cut} are related to the detector design, especially the noise level in the isolation cone. This simple analysis, with suppression of channels less than three times noise, has been studied with PYTHIA 5.5 [6] for the two systems, yielding backgrounds of 69 pb for the BaF_2 scintillator and 89 pb for the liquid argon systems. The irreducible $\gamma\gamma$ background is about 32 pb. This background can be further reduced by a number of design optimizations, which require more study. In the liquid argon calorimeter, for example, the ability to reject fake gammas depends on the choice of angular and longitudinal segmentation. Furthermore, a choice can be made to segment the calorimeter transversely just in the first few longitudinal depths, keeping the overall channel count constant. To further complement the shower shape sensitivity, the installation of strip readout near shower maximum is being studied. This may be done with 1 mm pitch strips for the electrode using a novel multiplexing scheme. A preradiator is also under study. A preradiator situated in front of the calorimeter employing one millimeter silicon strips has been shown to be capable of π^0 rejection of better than 80% with nearly full efficiency (>95%) for γ's up to 100 GeV [7] This results from the very narrow (< 0.5 mm wide) showers in this section. EGS Monte Carlo studies have shown an acceptable energy correction is possible. Finally, a powerful preradiator consisting of of 3-4 radiation lengths of scintillation and ionization sampling liquid krypton has been studied but is not part of the GEM baseline.

2.4.2.1.4 Photon and Electron Trigger

A possible design of a Level 1 trigger for isolated photons and electrons would require matching each electromagnetic calorimeter cell with the hadron calorimeter cells behind it. GEM is able to achieve a 35 kHz trigger with 85% efficiency for $H \rightarrow \gamma\gamma$ and $H^0 \rightarrow ZZ^* \rightarrow 4\,e$ [8]

2.4.2.2 *Hadronic Calorimeter*

2.4.2.2.1 *Jets*

The measurement of jets is essential for any general-purpose SSC detector such as GEM. For dijets from, say $W \rightarrow jj$, the mass resolution is determined both by the calorimeter energy and angle resolution and also by intrinsic limitations in the definition of a jet. Studies suggest that the latter dominates when the calorimeter energy resolution is

$$\frac{\Delta E}{E} \lesssim \frac{50\%}{\sqrt{E}} \oplus 2\%.$$

Angle resolution is important for studying the shapes of jets and for measuring single jet and multiple jet invariant masses, e.g. for high p_T $W \rightarrow jj$. For jets from QCD scattering processes the cross section for energy flow into a given solid angle is calculable; that is, uncertainties due to clustering algorithms are not an issue, the search being limited only by intrinsic calorimeter resolution. Thus the constant term in the calorimeter resolution should be minimized for such physics.

2.4.2.2.2 *Missing Transverse Energy $\not{E}_T$*

Both new, weakly-interacting particles and neutrinos give missing transverse energy $\not{E}_T$. The most demanding requirement on $\not{E}_T$ resolution is probably set by supersymmetry: since the Tevatron could detect gluinos and squarks up to about 200 GeV, one would like to detect $\not{E}_T \gtrsim 100$ GeV. The irreducible background is set by neutrinos from Standard Model sources, mainly heavy quarks and $W^{\pm}$ and Z^0 bosons at high p_T. The detector backgrounds should be smaller than this.

Missing energy is mainly measured by calorimetry, and the resolution on $\not{E}_T$ is primarily determined by intrinsic hadronic energy resolution in the central region, non-Gaussian tails from cracks in the central region, energy resolution in the forward calorimeter, and angular coverage and resolution in the forward calorimeter. The Gaussian term in the energy resolution of the central or forward calorimeter is not critical. Angular resolution in the forward calorimeter gives $\Delta p_T / p_T \ll 10\%$, which again has been shown to be sufficient, at least for the total $\not{E}_T$ cross section. Non-Gaussian tails in the central region will be limited by careful engineering to minimize dead material. Hence, it appears that the angular coverage is the crucial factor in determining the $\not{E}_T$ resolution.

For an idealized calorimeter which measures energies with Gaussian resolution and has no transverse shower spreading, it is known that covering $|\eta| < \eta_{max} = 5\text{–}5.5$ is sufficient to reject physics backgrounds [9]. For realistic showers adequate resolution can be obtained with a forward calorimeter at $z \approx 7$ m.

Production of new particles such as a Higgs or a technicolor resonance via WW fusion will lead to forward jets, since each of the W's is produced by $q \rightarrow W\, q$. Estimates of the effectiveness of such tags have varied widely. They may prove to be important and should be considered in the design of the forward calorimeter, but they are probably less important than the measurement of $\not{E}_T$.

2.4.3 Liquid Argon Calorimetry Option

There are many attributes of liquid Argon calorimeters which lead to its consideration for an SSC detector [10]. These include radiation resistance, uniformity of response, unit gain leading to the ability to calibrate to < 0.5%, the ability to segment longitudinally and transversely with a relatively modest increase in cost, experience in many large systems, and good energy resolution.

Recently a new concept for a liquid Argon EM calorimeter, called the accordion, has been developed. Beam tests have yielded impressive results [1]. The advantages of the accordion include excellent hermeticity, the elimination of numerous longitudinal connections by use of an electrode structure that follows the accordion-folds, and lower capacitance and inductance allowing short shaping times. The device tested at CERN has an electron energy resolution of $(10.1 \pm 0.4\%)/\sqrt{E} \oplus (0.2 \pm 0.2\%)$, and linearity from 30 GeV to 200 GeV of < 1% with a shaping time of 20 ns. Because the charge is naturally shared between two adjacent readout channels, the position resolution is $4.4\ \text{mm}/\sqrt{E}$. The module tested was divided in half longitudinally. By comparing the position in the front with that in the back an angular resolution $\Delta\theta = 6.1$ mrad was obtained at 120 GeV. This would be extremely helpful in determining whether the showers for $H \rightarrow \gamma\gamma$ candidates have a common vertex.

Since the energy resolution achieved so far in beam tests has not reached the level set by GEM, two methods of improving the accordion energy resolution are being developed. By replacing the Argon with Krypton, using the standard 2 mm thick absorber plates, the energy resolution calculated by GEANT is below $7.5\%/\sqrt{E}$. The same resolution can be reached, according to GEANT, by using 1 mm thick absorber plates together with a thin electrode structure attached to both sides of each plate. The unit cell designs for these two schemes are shown in figures 2.4-1a and 2.4-1b respectively. Both approaches are planned to be tested in a beam at BNL in the Spring of 1992. The mechanics of a parallel plate EM calorimeter using innovative striplines passing through slots in the absorber plates is also being explored.

The current conceptual design for the GEM liquid Argon calorimeter is shown in figure 2.4-2. The overall dimensions are set by the requirement of the minimum number of λ needed versus η. Once those dimensions are set, the EM calorimeter is designed for maximum hermeticity and for the minimum dead material in front of the active EM calorimeter. The maximum hermeticity for the EM is accomplished by ending the barrel section along a line of constant η and then have the cryostat walls closely follow that angle. The EM calorimeter in the endcaps is set back and overlapping so as to continue the coverage with a minimum angular loss. The vessels are made of aluminum so that there is 0.7 X_0 at 90°. The maximum dead material in front of the EM calorimeter is due to the vacuum and cold vessel walls just at the end of the barrel. Energy lost in the vessel walls will be corrected by using either a preradiator inside the cryostat or in a massless gap added to the first longitudinal section. Plans are to

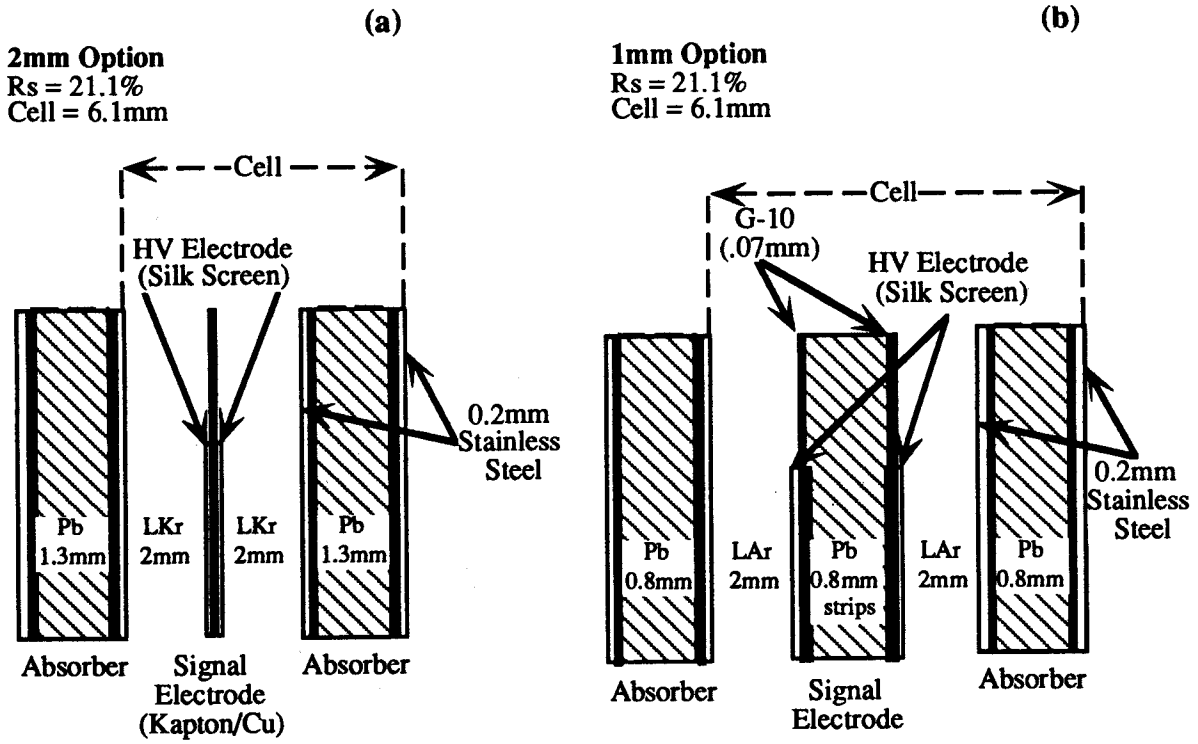

Figure 2.4-1 Liquid Argon Calorimeter Unit Cells

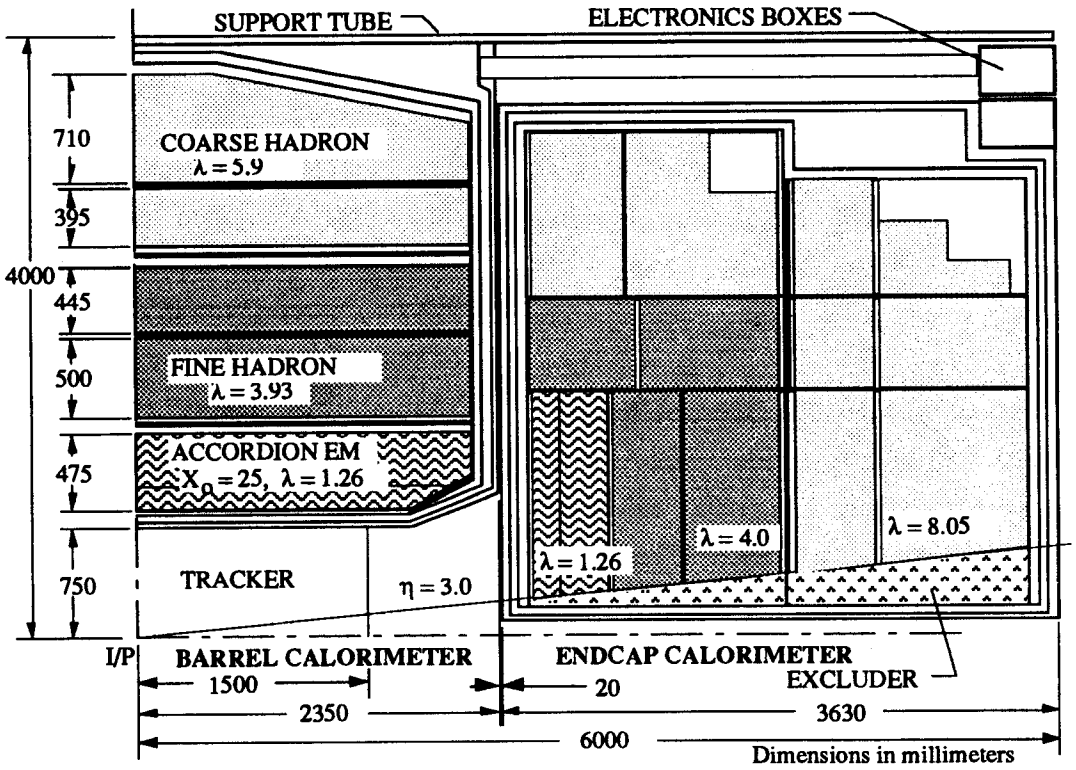

Figure 2.4-2 GEM Liquid Argon Calorimeter Conceptual Design

use 40 ns shaping time which leads to a total noise for nine (3×3) 0.04 towers of ~ 100 MeV.

The hadron calorimeter uses the "electrostatic transformer (EST)" concept to match the large capacitance of towers to the preamps [11]. This is shown schematically in figure 2.4-3. The hadron calorimeter is split into four sections longitudinally: two fine sampling sections and two coarse sampling sections. The goals of the fine sampling section are to have a sampling fraction of ~ 10% so that the signal to noise is sufficient for lepton and photon isolation as well as good hadronic energy resolution. The coarse section is used to measure the leakage of jets and so does not need such fine segmentation, but a sample must be taken every $\leq 4\ X_0$ in order to sample the electromagnetic component of hadron showers and catastrophic energy loss of muons. Iron (stainless steel) is the baseline absorber material since it minimizes the multiple scattering for muons, reduces the weight and is easy to handle. Lead might also be considered to improve the e/π response, or depleted uranium to allow more λ in a fixed radius, but both would have other disadvantages.

A detailed study of the coarse hadronic section will be done in order to specify it completely for the Technical Proposal. The design goal of the coarse section is to maximize the number of λ before the muon chambers which leads to a low (2%) sampling fraction. With the shaping time used in the fine hadronic section (100 ns) this would lead to a large thermal noise (1 GeV/ 0.08×0.08 cell).

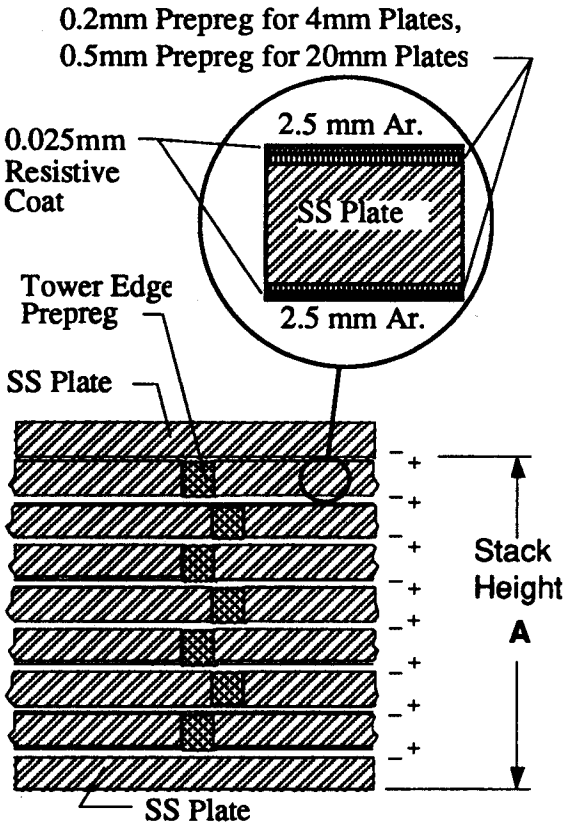

Figure 2.4-3 GEM Liquid Argon Hadron Calorimeter EST Concept

The intent is to use a longer shaping time to reduce this noise. A detailed study needs to be done with GEANT to determine whether this is feasible. If this fails, a reduction in the number of active λ will be considered either by using only fine sampling and adding passive absorber at the back or deploying a scintillating fiber calorimeter after the fine sampling liquid argon.

The parameters of the GEM liquid Argon calorimeter are presented in table 2.4-2.

2.4.4 BaF_2 Electromagnetic and Scintillating Fiber Hadron Option

A precision BaF_2 EM calorimeter backed up by a scintillating fiber HCAL has the advantages of very high resolution for electrons and photons, speed, uniform coverage and hermeticity, good resolution for hadron jets, and a deeper calorimeter to filter out hadrons within a given radius. Figure 2.4-4 shows a side elevation view of the BAF + HCAL system.

Table 2.4-2 Liquid Argon Calorimeter Parameters

Rapidity Coverage	$\|\eta\| \leq 3.$
Segmentation	
EM	$\Delta\eta = \Delta\phi = 0.04$
Hadronic	$\Delta\eta = \Delta\phi = 0.08$
Depth Segmentation	
EM	3 (1 may be preradiator)
Hadronic	4
Total Depth	
$\eta = 0$	12 λ
$\eta = 3$	14 λ
Total Weight (t)	2100
Number of Channels	80,000

Although the BaF_2 EM section is non-compensating, a GEANT simulation predicts good jet resolution with a small constant term can be obtained by using an HCAL section with an average e /π response $\approx$ 1.0. This is illustrated in figure 2.4-5, a GEANT simulation (which correctly predicts the $< e/\pi >$ ratio), where the optimal weighting of the energy deposited in the BaF_2 and in the HCAL is used to reconstruct the total jet energy.

The resulting GEANT prediction of jet response is linear, with Gaussian resolution functions and no resolution tails, and the fitted constant term is 1.4 $\pm$ 0.2%. The dependence of the resolution on the e/π of the HCAL behind the BaF_2 is shown in figure 2.4-6 for jets between 100 and 1000 GeV.

2.4.4.1 High Precision BaF_2 Electromagnetic Calorimeter

2.4.4.1.1 BaF_2 Detector Features.

The high sensitivity of the BaF_2 detector to new physics is the result of the following features: high speed (gating the signal in 16 ns), very high energy resolution, $\sigma_E/E = (2.0/\sqrt{E} \oplus 0.5\%)$, good position resolution (Δx and $\Delta y \approx$ 1 mm for EM showers), excellent e/π, γ/jet, and e/jet separation ($\sim 10^{-4}$), and good potential radiation resistance ($\geq 10^7$ rads demonstrated in small crystals).

2.4.4.1.2 BaF_2 Detector Concept.

The conceptual design of the BaF_2 calorimeter shown in figure 2.4-7 illustrates a central barrel calorimeter with an inner radius of 75 cm and an outer radius of 140 cm, covering a rapidity rangeof $|\eta| \leq 1.32$ ($30° \leq \theta \leq 150°$); and two endcaps, located at $z = \pm$ 164 cm, covering a rapidity range of $1.32 \leq |\eta| \leq 2.5$ ($9.4° \leq \theta \leq 30°$ and $150° \leq \theta \leq 170.6°$).

The BaF_2 calorimeter follows the proven uniform and extremely light structural design used in the BGO calorimeter, which has allowed L3 to achieve the very high resolution. Each crystal is housed in a precisely dimensioned, thin-walled (300 μm) carbon fiber-epoxy composite cavity, and is

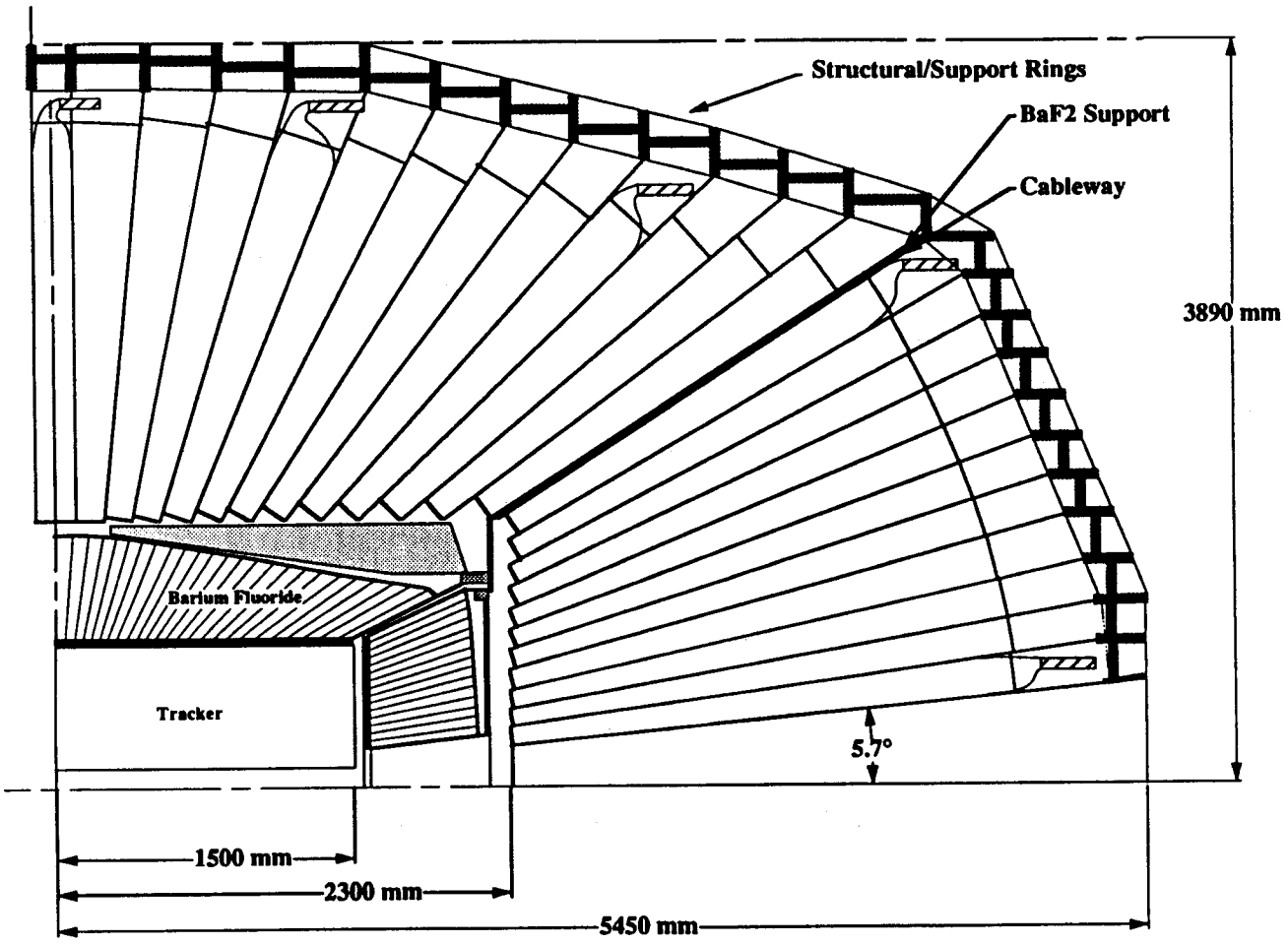

Figure 2.4-4 Side view of the GEM BaF_2 and Scintillating Fiber Hadron Calorimeter System

compressed by small fixtures mounted in each cavity against an inner core consisting of carbon fiber skins surrounding acrylic foam. A complete finite element analysis at ORNL has shown that in spite of its thinness, the structure is stable against the tensile and torsional loads provided by crystal weight and compression, with a large safety factor.

Table 2.4-3 shows the basic parameters of the GEM BaF_2 calorimeter.

Table 2.4-3 Features of the BaF_2 Calorimeter

Detector	Barrel	Two Endcaps
Rapidity Coverage	$\|\eta\| \leq 1.32$	$1.32 \leq \|\eta\| \leq 2.5$
Crystal Front/ Rear Face (cm^2)	3.1×3.1 / 5.1×5.1	2.3×2.3 / 3.1×3.1
Crystal Length (cm)	50	50
Crystal Number	10,880	4144
Crystal Volume (m^3)	8.4	2.2
Crystal Weight (t)	41.1	10.7

2.4.4.1.3 BAF Calorimeter Performance.

The performance of the BaF_2 calorimeter was computed with a GEANT simulation, including the effects of the carbon fiber walls, shower leakage due to summing (3 × 3) crystals, and 0.30 X_0 dead material representing the beam pipe, tracker, and mechanical support. The results are summarized in table 2.4-4. The intercalibration precision of 0.4% assumed in the table has been demonstrated with the RFQ calibration system developed by Caltech.

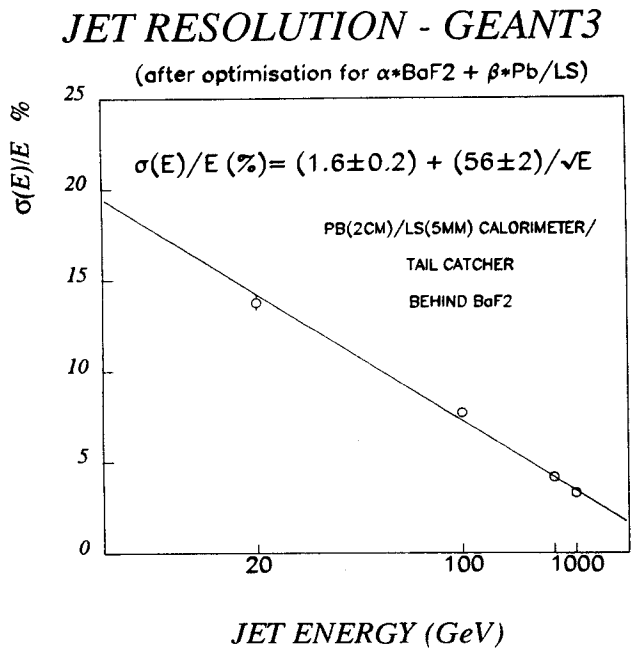

Figure 2.4-5 Jet Energy Resolution for the GEM BaF_2 and Scintillating Fiber Hadron Calorimeter System (20-1000 GeV)

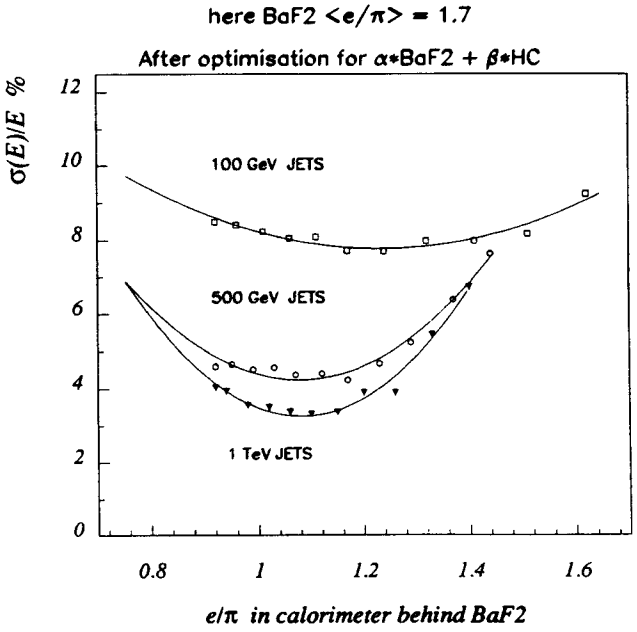

Figure 2.4-6 Dependence of the Energy Resolution on the <e/π> Ratio in the Scintillator Hadron Calorimeter Behind the BaF_2 EM Section

Table 2.4-4 Energy Resolution (%)

E(GeV)	5	10	100	500
Electrical Noise	0.4	0.2	0.02	0.004
Photoelectrons	0.2	0.14	0.045	0.02
GEANT	0.67	0.56	0.42	0.36
Intercalibration	0.40	0.40	0.40	0.40
Total	0.90	0.73	0.58	0.54

As shown in 2.4-8b, the resolution can be parametrized as $2\%/\sqrt{E} \oplus 0.5\%$. For comparison, figure 2.4-8a shows the energy resolution measured with 4000 L3 BGO crystals in a CERN test beam [12]. It can also be parametrized as $2\% \sqrt{E} \oplus 0.5\%$.

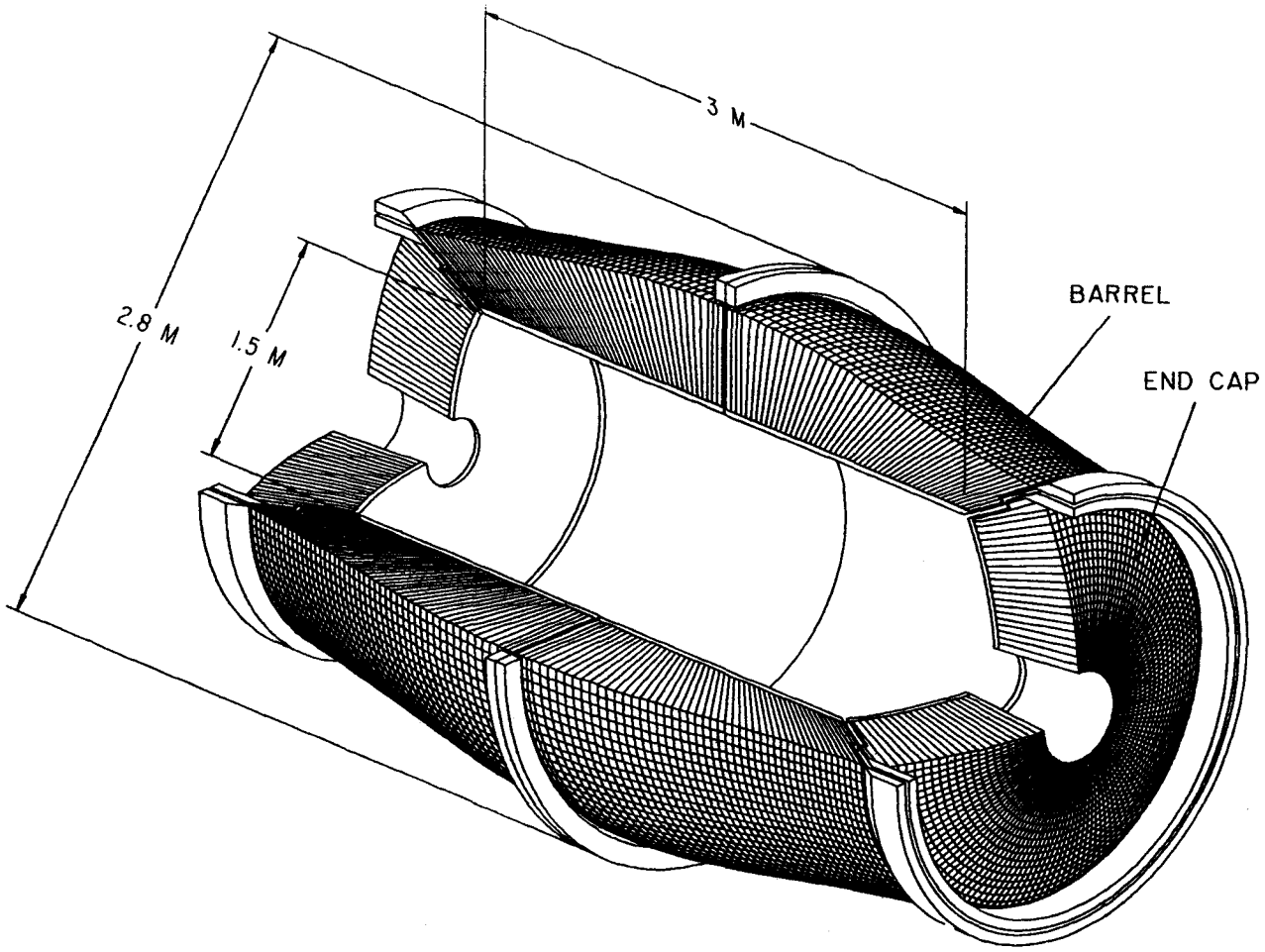

Figure 2.4-7 Conceptual View of the Barium Fluoride Calorimeter

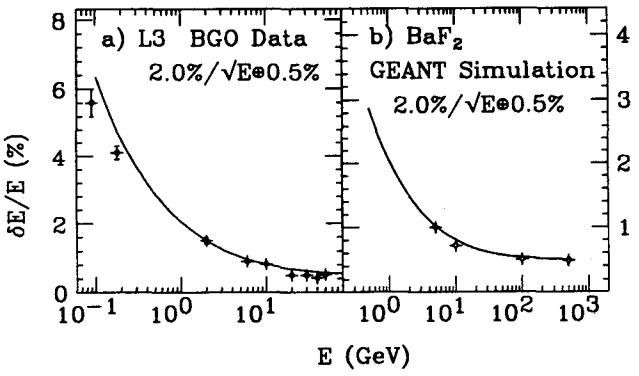

Figure 2.4-8 Energy Resolution of (a) L3 4000 crystal BGO calorimeter, measured at CERN, and (b) BaF2 calorimeter, calculated with GEANT simulation. The solid curves show 2% / $\sqrt{E}$ ⊕ 0.5%

2.4.4.1.4 R &D Progress in 1991 [13]

During 1991, SIC (Shanghai) and BGRI (Beijing) have established a production facility for large BaF_2 crystals, with major Chinese funding. The capacity is currently 140 twenty-five cm crystal pieces (tower-halves) per month (18% of full GEM rate requirements.) The first 98 crystal pieces and spares were delivered to Caltech by May, 1991. A Memorandum of Understanding was signed with SIC and BGRI management for production of rad-hard crystals at $2.5/cc.

The 49 crystal (50 cm long) prototype matrix was constructed by Caltech and UCSD, and is now in a test beam at Fermilab (T-849). The matrix is instrumented by Hamamatsu UV-selective K-Cs-Te R4406 phototriodes, which suppress the slow component and operate in 1T fields. (Thin UV-selective proximity focused photodiodes and UV-selective solid state devices with sharp cutoffs are under development.) Full suppression of the slow component is completed by fast preamp and shaping circuits developed by ORNL. A high transmittance, rad-hard RTV (KE-103) bonds the two crystal pieces of each calorimeter element. Light collection uniformity is $\sim \pm 7\%$, with typically 50 p.e./MeV. The tests of the crystal matrix with muons, electrons and pions will yield results on the resolution, e/π response, e/π separation algorithms and calibration with minimum ionizing particles by December, 1991.

A systematic series of radiation damage studies (up to 20 mrads of Co^{60} γ's, 10^{14} neutrons/cm^2 in some tests) have shown in small samples that: (a) the damage saturates at 10 - 100 krads, with no further damage to beyond 10 mrads; (b) there is no spontaneous annealing at room temperature; and (c) there is no permanent damage from γ or neutron radiation; complete recovery can be achieved by annealing at 500°C, or by a UV lamp. The radiation damage appears impurity or defect related and large crystals have not shown the same characteristics as small crystals. A systematic program to identify and eliminate the key impurities is underway, in collaboration with Optovac and the ORNL Solid State Division in the U.S., as well as with SIC and BGRI in China.

A GaAs preamp with risetime ~1 ns has been developed by Princeton, and tested with a vacuum phototriode on a large BaF_2 crystal using electrons up to 50 GeV. A gated integrator and 60 MHz digital readout pipeline is being developed at Princeton. Los Alamos is developing a GaAs amplifier based on MESFET transistor arrays with rad hardness to 10^{15} neutrons/cm^2 and 10^8 rads.

A structural analysis of the full GEM calorimeter has been completed at ORNL. The engineering and detailed design of the second prototype array including a carbon fiber structure which matches the full detector near $\eta = 0$ has been completed, and is ready for manufacture.

A UV laser and quartz fiber light monitoring system is under development at CMU. The L3 RFQ system completed at AccSys Inc. has been tested with a neutral beam on target and has been shipped to CERN. This will provide information on the calibration precision obtainable *in situ* in L3 during the 1992 LEP run.

2.4.4.1.5 R&D Program for 1992.

The most critical issue for the BaF_2 calorimeter is production of radiation hard, full size crystals. An expert panel has been commissioned to evaluate the risk of proceeding with an R&D program aimed at beginning mass production of radiation hard crystals by 1993. After reviewing current understanding of radiation damage in BaF_2, the panel will assess the prospects for this program. If sufficient promise appears, the extensive R&D program [13] being carried out at 13 institutions in the U.S., China and India will proceed for 1992 to

complete the development and engineering design of the BaF_2 calorimeter in 1992. If completed, this R&D program will culminate in the construction of the first production-quality BaF_2 crystal matrix composed of 81 full-sized crystal elements, integrated with a carbon fiber structure, and full speed front end electronics (gated integrator or fast shaper). The R&D program includes: BaF_2 crystal mass production, radiation damage tests, engineering design of the final prototype and full scale calorimeter, electronics readout development and testing, UV performance monitoring development, rad hard electronics readout development, beam and cosmic ray tests, BaF_2 crystal matrix assembly, and RFQ calibration facility funded under a DOE SBIR grant.

2.4.4.2 Scintillating Fiber Hadron Calorimeter

2.4.4.2.1 Baseline Design.

A scintillating fiber hadron calorimeter has been selected to complement the precision BaF_2 EM calorimeter option. A scintillating fiber hadron calorimeter combines high speed, compensation, compactness, and radiation resistance with a high degree of uniformity and hermeticity in a projective geometry. It also provides design flexibility in the choice of fiber diameter, fiber filling fraction, and lateral readout segmentation, thus allowing for optimal cost/performance trade-offs. Some longitudinal segmentation is possible through the separate readout of fibers terminating at different depths within the calorimeter, at a modest increase in readout channel count and cost.

The SPACAL collaboration has demonstrated the performance achievable with a scintillating fiber calorimeter in resolution, compensation, particle identification, speed, and radiation hardness [14]. The SSCintCAL collaboration has complemented this effort by developing cost-effective methods for calorimeter construction and engineering on the scale required for GEM [15]. Separate optimization of EM and hadronic calorimetry leads to different design decisions for such parameters as fiber diameter and filling fraction.

Figure 2.4-9 illustrates the baseline design of a scintillating fiber hadron calorimeter module for GEM. This design is based on 3 mm diameter fibers cast within an absorber matrix of lead and lead/bismuth alloy. The feasibility of casting 1-ton projective towers has been demonstrated by the SSCintCAL group, which has constructed several 1-ton prototypes prepared for a FNAL beam test. The absorber consists of a 60% / 40% mixture of fine lead shot and eutectic lead/bismuth alloy, where low melting-point alloy is percolated through a previously assembled fiber matrix/lead shot mixture within a mold. The resultant casting has higher density and lower cost than is achievable by casting fibers within eutectic alloy alone, while providing comparable structural integrity and dimensional control. Stress/strain measurements have shown that the resultant towers will be self-supporting under forces indicated by a finite-element analysis of a GEM scintillating fiber hadron calorimeter.

While efficient construction may argue for simultaneous casting of 4 physics towers as a modular "supertower", a single physics tower has been shown in figure 2.4-9 for simplicity. The lateral segmentation into physics towers is matched

with that of the EM calorimeter to .08 (η) × .08 (ϕ), with the option remaining for a future upgrade

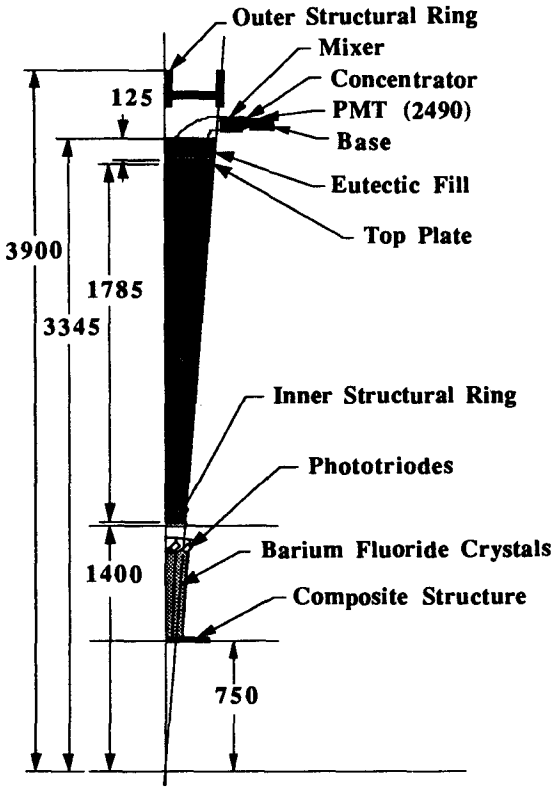

Figure 2.4-9 GEM Scintillating Fiber Hadron Calorimeter

increasing the transverse segmentation. The active depth of the hadron calorimeter alone is 9 λ at η = 0, increasing to 12 λ at η = 3, and it should be noted that the BaF_2 EM calorimeter provides an additional 1.7 λ of material upstream. Readout is accomplished through a mass-fiber splice between 3 mm fibers within the calorimeter module and 1 mm clear readout fibers, providing a flexible and compact method for aligning mesh dynode photomultipliers with the magnetic field.

2.4.4.2.2 Beam Test of the BaF_2+ Scintillator HCAL System in 1992

The primary objective of the FY92 R & D effort will be to construct a fully hadronic shower-containing set of scintillating fiber prototype towers embodying GEM's baseline design. The prototypes will be characterized in beam tests to measure detector performance and subsequently to assess alternative manufacturing techniques, to establish the mechanical integrity of the calorimeter system design, and to refine cost projections. The primary objective of the FY92 engineering effort will be to extrapolate from experience with prototype modules to the full GEM calorimeter, in particular addressing issues of mechanical tolerances, assembly and access, support structures, readout systems and cables, and optimized production techniques.

Prior experience with the infrastructure that developed in producing the first generation of cast fiber supertowers has raised confidence that a large fully containing prototype can be produced in a timely and efficient manner. The prototype will be tested and calibrated using high energy electron, pion and muon beams at CERN, together with the BaF_2 EM calorimeter prototype. The test will focus on resolution and effective compensation, e/π separation, and MIP calibration.

2.4.5 Forward Calorimetry

Physics with a forward calorimeter covers a range of topics and imposes a number of requirements. Foremost among these is the measurement of the p_T of particles close to the beam pipe in order to make the best estimate of global event p_T and therefore missing p_T due to neutrinos and other weakly interacting particles. Thus the forward calorimeter is an important ingredient in the construction of a hermetic detector. Missing p_T signatures that will be sought at the SSC will be of order 100 to 200 GeV/c or greater. A modest

measurement of the p_T of jets in the forward direction will be sufficient to ensure that the background due to mismeasurement will be small. The most critical parameter seems to be the range of coverage, i.e., how high in η can adequate p_T resolution be maintained.

Further study of forward calorimetry is needed. One option for the forward calorimeter is provided by a compromise between the best coverage and cost. This is a small forward calorimeter as close to the interaction region as possible. For the baseline design, the front face of the forward calorimeter is 6.5 m from the interaction region. Using Tungsten with a small sampling fraction gives the densest calorimeter possible and therefore the optimal transverse containment of hadronic showers. Depth segmentation would allow accurate position determination in the first segment with adequate energy determination in the sum over segments. A premium would be placed on extending the sensitive volume of the calorimeter as close to the beam pipe as possible, perhaps as close as 2 cm from the beam centerline.

Several technologies are under consideration for the forward calorimeter. Work on liquid Argon / Tungsten plate geometry, liquid scintillating spaghetti and high pressure gas tubes is proceeding in parallel. All three technologies are believed to perform adequately even in the very high radiation fields predicted at this close distance and at the higher luminosities projected for later years of running. A rough estimate of neutron albedo in the central tracking region suggests that the forward calorimeters contribute about the same amount as the rest of the detector.

Table 2.4-5 lists some parameters of the close-in forward calorimeter. Further study is underway to evaluate this configuration.

Table 2.4-5 Forward Calorimeter Parameters

Hadronic coverage (full resolution)	$3.0 < \eta < 5.0$
Hadronic resolution	$\Delta p_T / p_T \approx 10\%$
Distance (front face to IP)	6.5m
Depth	1.06 m
Mean radius	80 cm
Weight	40 t (each)
Electronic channels	1070 (each)

2.4.6 Calorimetry R&D Summary

The R&D program for the GEM calorimeter will advance the two systems selected to achieve the GEM goal of the best possible electromagnetic calorimetry: the liquid argon with accordion EM and BaF_2 with a scintillating fiber hadron calorimeter. The objective of the R&D plan is to prepare for a comparison of the two systems during FY92, so that a choice is made and further engineered for the Technical Proposal in November, 1992.

R&D on the liquid argon approach will emphasize the accordion concept, developing improved electromagnetic resolution with thinner radiator plates (1 mm) and testing liquid krypton in place of liquid argon with 2 mm plates. R&D on liquid argon hadron calorimetry (plates) will be limited.

R&D on BaF_2 will emphasize developing the fabrication process for large radiation hard crystals. An expert panel will review the prospects

for this achievement before FY92 R&D proceeds. In addition the first production-prototype system consisting of 81 full-sized crystals will be prepared with full speed electronics.

The R&D for the scintillating fiber hadron calorimeter will advance the technique of eutectic alloy/fine lead shot module fabrication and will include construction of a fully hadronic shower containing set of GEM towers for beam test in FY92. This test will combine the BaF_2 production-prototype with the scintillating fiber hadron calorimeter for evaluation as the GEM calorimeter system.

R&D on the forward calorimetry will proceed on liquid argon, liquid scintillator and high pressure gas tubes. A silicon strip preradiator prototype will be tested.

---

[1] B. Aubert *et al.*, "Performance of a Liquid Argon Electromagnetic Calorimeter with an "Accordion" Geometry," CERN-PPE-91 - 73, 1991 (Submitted on Nucl. Instr. and Meth.)

[2] H. Burkhardt *et al.*, Nucl. Instr. and Meth. A 268, 116 (1988).

[3] GEM Collaboration, SSC-EOI-0020, An Expression of Interst to Construct a Major SSC Detector, July 1991.

[4] CERN Green Book, "ECFA Workshop on LEP 200", Aachen, September, 1986.

[5] R. Y. Zhu, GEM Internal Note.

[6] H. Benson and T. Sjostrand, "A Manual to the Lund Monte Carlo for Hadronic Processes", PYTHIA version 5.5, June, 1991.

[7] J. Brau *et al.*, "GEM Preradiator", GEM -TN-91-18.

[8] R. Y. Zhu, Proceedings of ECFA LHC Workshop, Aachen, October 1990, Vol. III, 411.

[9] F.E. Paige and E. M. Wang, Proceedings of the Workshop on Calorimetry for the Supercollider, Mar. 13-17, 1989, U. of Alabama, Tuscaloosa, Alabama, World Scientific, p. 99.

[10] See for example, H.A. Gordon, Symposium on Detector Research and Development for the SSC, Oct. 15-18, 1990, World Scientific, p. 100.

[11] J. Colas, Proceedings of the Workshop on Calorimetry for the Supercollider, Mar. 13-17, 1989, U. of Alabama, Tuscaloosa, Alabama, World Scientific, p. 553

[12] B. Adeva *et al.*, Nucl. Instr. and Methods, A289 (1990), 35-102; J. Bakken *et al.*, Nucl. Instr. and Methods A275 (1989) 81.

[13] BaF_2 Collaboration, "A Precision BaF_2 Crystal Calorimetewr for the SSC," R&D Proposal and Progress Report Submitted to the SSCL, Sep., 1991.

[14] D. Acosta *et al.*, NIM A 305, 55 (1991); D. Acosta *et al.*, NIM A 302, 36 (1991); D. Acosta *et al.*, NIM A 294, 193 (1990); R. DeSalvo *et al.*, NIM A 279, 467 (1989); D. Acosta *et al.*, NIM A 308, 481 (1991); D. Acosta *et al.*, NIM A 309, 143 (1991); D. Acosta *et al.*, CERN-PPE/91-45 to be pub NIM B; D. Acosta *et al.*, CERN-PPE/91-195 to be pub NIM A.

[15] D. Brown *et al.*, IEEE Trans. Nucl. Sci. (1991); W. Worstell *et al.*, IEEE Trans. Nucl. Sci. (1990).

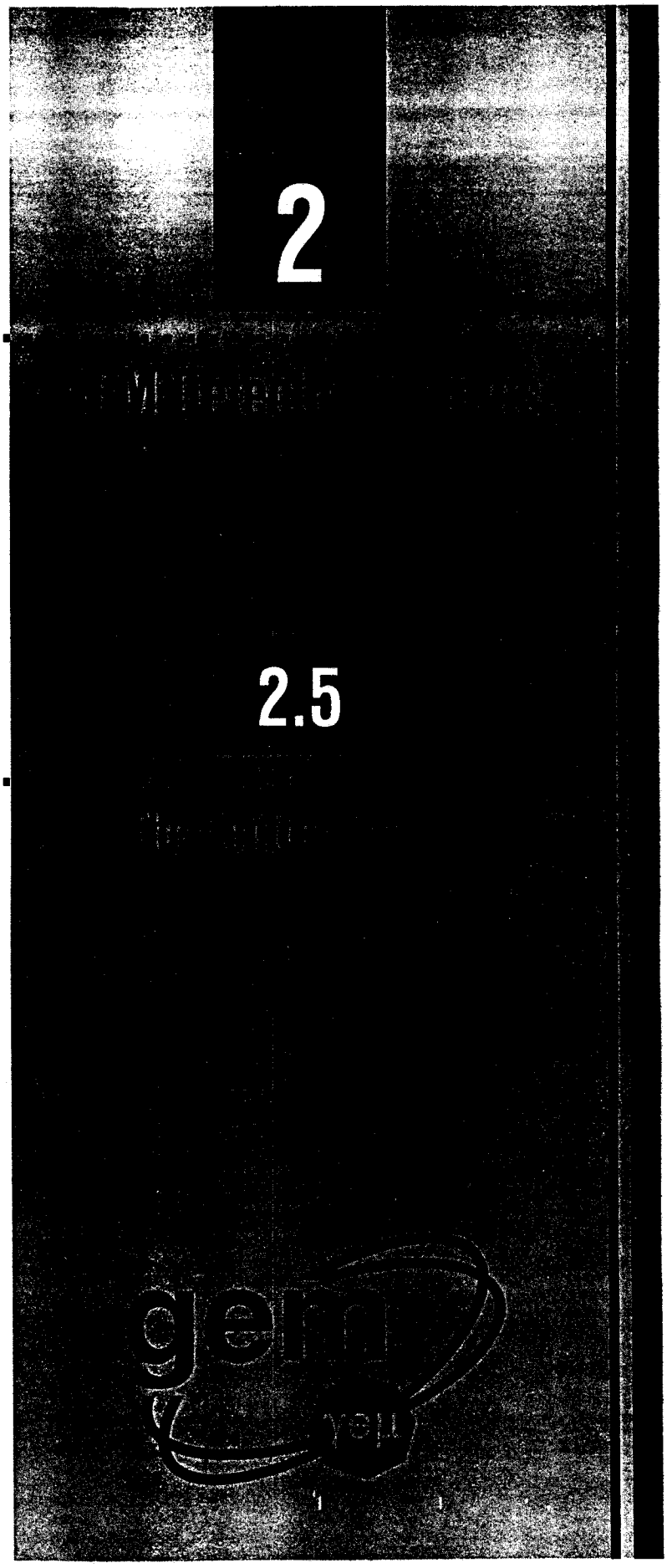
2
2.5

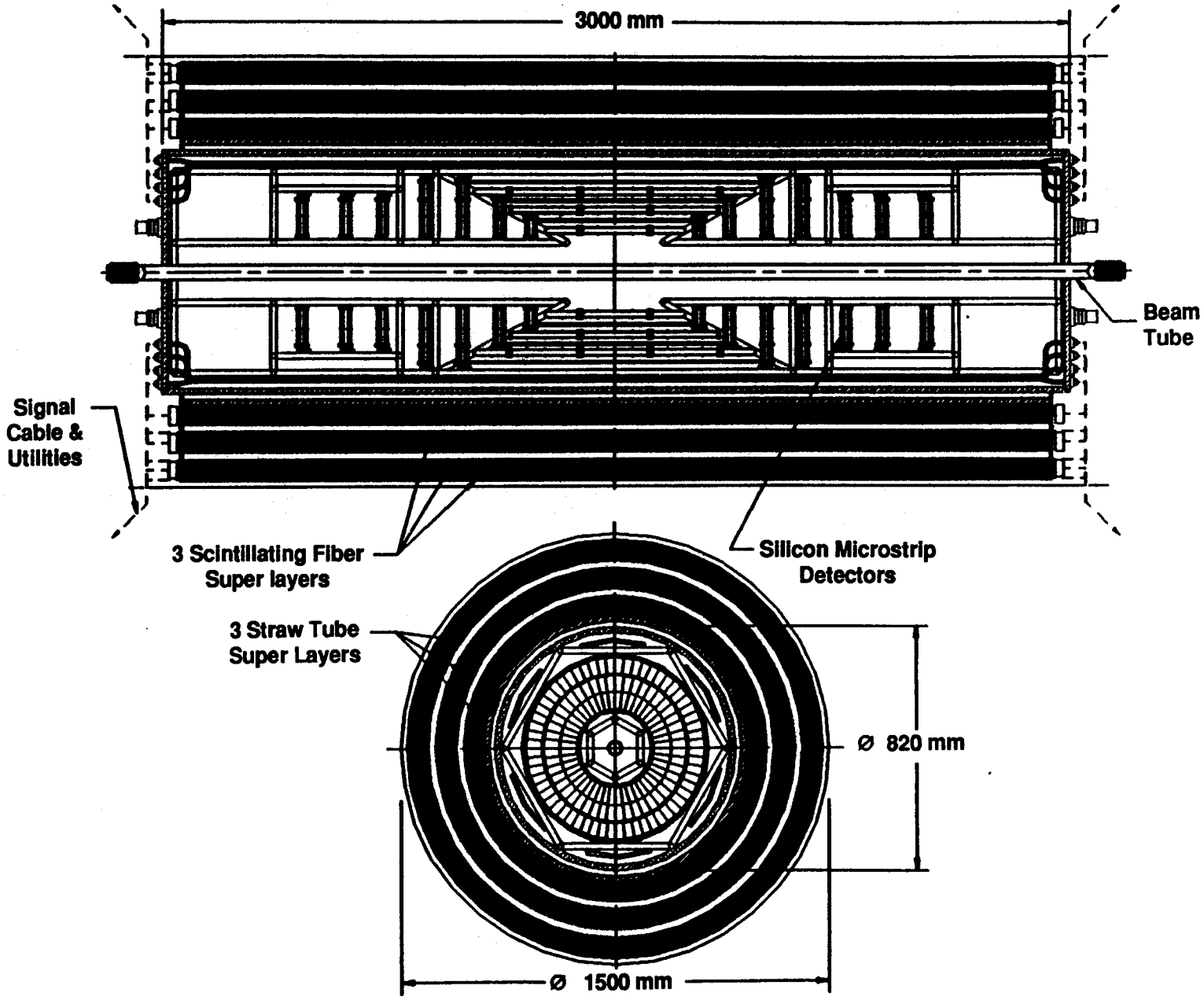

BASELINE CENTRAL TRACKER

2.5 The Central Tracker

The Central Tracker in the GEM detector will operate in the 0.8 T magnetic field of the large GEM superconducting solenoid. The tracker is compact, with a 75 cm outer radius and a total length of 300 cm. It covers a pseudorapidity of ± 2.5. At present there are two options under consideration for the design of this device. The first uses a silicon microstrip inner tracker surrounded by an outer tracker of straw tubes and scintillating fibers arranged in layers. This design was presented in the Expression of Interest [1] and the cost estimates in this Letter of Intent are based on this design. An alternate design, employing a somewhat smaller silicon microstrip inner detector surrounded by Interpolating Cathode Pad Chambers is being considered because its lower occupancy would enable the detector to operate well at luminosities of $10^{34}\,cm^{-2}s^{-1}$. One of the criteria for this alternate design is to keep its cost at or below the cost estimate presented for the EOI design.

2.5.1 Physics Goals and Design Parameters

The physics goals for the central tracking in GEM can be divided into two categories. The first are those features that are required to support the primary objectives of GEM, namely the detection of gammas, electrons and muons at high p_T. Some examples of these are:

- Identify the primary vertex of an event of interest, so that it can be separated from other pileup events in the memory time of the detector.
- Separate electrons and gammas using the presence or absence of a charged track pointing to an electromagnetic shower in the calorimeter.
- Provide track information for e, μ or γ isolation cuts, and to help with rejection of conversions and Dalitz pairs.
- Help with electron-hadron separation by providing a momentum measurement that can be compared with the energy deposition in the calorimeter.
- Help with rejection of background by matching the muon momentum measured in the central tracker with the momentum measured in the muon chambers.
- Determine the electron sign up to 400 GeV/c.

The tracker should be able to fulfill these goals well at the design luminosity of $10^{33}\,cm^{-2}s^{-1}$. These capabilities should also survive to luminosities up to $10^{34}\,cm^{-2}s^{-1}$. These minimum goals do not require full pattern recognition, but can be met by looking for hits in the tracker in a specific road extrapolated from the calorimeter or the muon system.

The second category of physics goals are more ambitious:

- Full reconstruction of the charged tracks in the event.
- Secondary vertex finding.
- Tracking at low momenta.

These features would enhance GEM's ability to address issues such as b and Top physics. They

are more demanding in that they require pattern, recognition capabilities and very good vertex resolution. It is expected that these more ambitious goals can be met at luminosities up to $10^{33}\,cm^{-2}s^{-1}$, but probably not much higher. This, however, seems satisfactory since the physics topics requiring these more ambitious features have relatively large crossections and can thus be studied at luminosities of $10^{33}cm^{-2}s^{-1}$ or below.

The parameters for the central tracker that will satisfy the goals outlined above are summarized in table 2.5-1.

Table 2.5-1 Design Parameters for GEM Central Tracking

Outer Radius	70 cm
Length	±150 cm
Rapidity Coverage	$\|\eta\| \leq 2.5$
Magnetic Field	0.8T
Occupancy	
at $\mathcal{L} = 10^{33}cm^{-2}s^{-1}$	$\leq 1\%$
at $\mathcal{L} = 10^{34}cm^{-2}s^{-1}$	~ 3%
2σ charge separation	$p \lesssim 400$ GeV/c
Momentum Resolution at 90°	
at high momenta (measurement limited)	$\Delta p/p^2 \sim$ (1 to 3) × 10^{-3} $(GeV/c)^{-1}$
at low momenta (multiple scattering limited)	$\Delta p/p \sim 2$ to 4%
Vertex Resolution	
along beam direction	$\delta z \sim 1$ mm
impact parameter	$\delta b \sim 20\ \mu$m above 10 GeV/c

2.5.2 Silicon Microstrip, Straw Tube and Scintillating Fiber Option

The baseline tracker design, shown on the section divider has evolved from the GEM EOI design [1]. The tracker is designed with two distinct systems: the inner silicon tracker and the outer straw tube drift chambers with scintillating fibers. The inner silicon tracker provides a precise vertex measurement and a fine grain track measurement. The outer tracker provides the outer measurement for the momentum determination. It also provides many layers for good pattern recognition and track finding.

2.5.2.1 Baseline Silicon Inner Tracker

The silicon tracker (ST) has undergone minor revisions since the GEM EOI. The dominant change affects the placement of the silicon ladders to provide full coverage everywhere in the pseudorapidity range ± 2.5.

The ST consists of six layers of silicon strip ladders. Each ladder is composed of two back-to-back single sided silicon sensors with a 5 mrad stereo angle between the two sensors. Each sensor is 300 μm thick with a strip pitch of 50 μm. Each pair of sensors provides a space point with a resolution of 10 μm in the r-ϕ plane and 3 mm in the r-z projection. The six layers of ladders are organized into three superlayers, each of which provides a track stub to a track finding algorithm. In the forward region the silicon sensors are mounted into disks with the strips projecting radially inward toward the beam axis. The ST is ~2.5 m long and extends to a radius of 40 cm.

2.5.2.2 *Straw/Fiber Outer Tracker*

The outer tracker is little changed from the EOI design [1]. It consists of three superlayers of straw drift tubes and scintillating fibers. Each superlayer is composed of 16 layers of 4 mm straw tubes along the z direction and four layers of 1 mm fibers placed in a ZZUV arrangement with a $\pm 10^{o}$ stereo angle for the UV layers. Each superlayer will provide a track stub measurement with a 25 μm r-ϕ accuracy and a 300 μm r-z accuracy.

2.5.3 Silicon Microstrip and Interpolating Pad Chamber Option

Some of the reasons for considering an alternate design to the "Baseline Design" described in the previous section are as follows:

- The calculated occupancy in the straw tubes of the Baseline Design is well in excess of 10% at the luminosity of $10^{33}\,cm^{-2}s^{-1}$. Since backgrounds in real life are likely to be worse than calculated, this technology is marginal at $10^{33}\,cm^{-2}s^{-1}$ and not useful at $10^{34}\,cm^{-2}s^{-1}$. With the Interpolating Pad Chambers (IPC's), considerably lower occupancy is possible, even at $10^{34}\,cm^{-2}s^{-1}$.
- Both the straw tubes and the scintillating fibers of the Baseline Design are stereo devices, i.e. all of the tracks in the tracker are projected onto a plane at the end of the device. In the high multiplicity and high luminosity environment of the SSC, tracking and pattern recognition would be much easier and more robust with a "3-D" device.
- The Baseline Design consists of three different technologies (silicon, straws, and fibers). It would be an advantage to reduce the tracker to two technologies.

The above considerations seem sufficiently weighty to cause serious consideration of an alternate design consisting of silicon microstrips and Interpolating Pad Chambers. A general schematic drawing of this design is shown in figure 2.5-1.

2.5.3.1 *The Silicon Inner Tracker*

The details of this silicon inner tracker are similar to those described in the Baseline Design of the previous section. However, the outer radius is reduced to 35 cm, and the overall length to 200 cm.

2.5.3.2 *The Interpolating Pad Chamber Outer Tracker*

The outer tracker consists of 9 layers of pad chambers both in the barrel region at radii between 35 and 70 cm, and in the forward region which extends from 20 to 70 cm in radius. The 9 layers are arranged in 3 superlayers with 3 layers each. Each barrel layer will consist of 16 chambers, each covering 24° in azimuth, with the largest chamber being 32 cm wide × 200 cm long. The forward layers will be divided into trapezoidal chambers about 50 cm × 50 cm each. The IPC's in this system will be very similar in concept and performance to chambers with chevron shaped cathode pads which have been constructed and are now taking data in experiment E-814 at Brookhaven AGS [2]. These chambers have various sizes up to 50 cm × 200 cm and have obtained a resolution of ~50 μm, or ~1% of the pad size.

Each of the chambers will be tilted in azimuth by the Lorentz angle of the gas (~6 to 9°) so that the $E \times B$ effect in the 0.8 T field does not degrade the resolution. This tilt also allows the chambers to be overlapped, eliminating dead regions due to electronics and structural elements (figure 2.5-1b).

The direction of good resolution in these chevron pad chambers is along the anode wire. Thus the wires in the barrel chambers will run across the chambers, in the "ϕ direction", keeping the wire length between 15 and 32 cm. In the forward chambers the wires will also run in the "ϕ direction," with wire length between 10 and 40 cm.

In the present design pad sizes are a uniform $\Delta\eta \times \Delta\phi = 0.001$ in all parts of the tracker. This results in a total of just under 300,000 pads for the entire device.

The anode wires will be spaced at about 2.5 mm intervals. To obtain precision better than the pad size in the "θ direction", readout of the anode wires is expected in at least one layer in each superlayer. A digital readout would provide a precision of ~700 μm in this direction. This precision in each of the superlayers will provide the required $\delta z \sim 1$ mm to separate event vertices at a luminosity of $10^{34}\,cm^{-2}s^{-1}$, when the silicon tracker is expected to be out of operation. This would require about 60,000 wires to be readout, which will be multiplexed at a level that satisfies the occupancy requirements.

The IPC readout electronics for each pad include a fast front end amplifier and shaper feeding into an analog pipeline which is multiplexed at the output by a factor of 256, giving a total of 1200 channels. The present design calls for the multiplexed analog outputs to be input to Mach-Zehnder electro-optic modulators, each of which is connected by a fiber optic cable to a remote 9 bit flash ADC system. The readout of the IPC wires can be accomplished with a simple comparator on each of the instrumented wires, followed by a multiplexed digital pipeline.

2.5.3.3 Engineering Design

The main concern of the engineering design of the central tracker is to:

- Guarantee sufficient rigidity and temporal stability so that systematic alignment errors can be kept below 10 μm within the silicon tracker and below 25 μm in the IPC system, in the relevant dimensions.
- Keep the entire system extremely light to achieve an acceptably small fraction of a radiation length (between 10 and 20%) in order to keep both multiple scattering and secondary interactions at a tolerable level.

Due in part to the work done in the Silicon Subsystem R&D effort [3], the engineering design of the silicon tracker is well advanced. The design of the IPC's is just beginning. The present thinking is to build each superlayer of 3 pad planes as a single mechanical unit, as shown in figure 2.5-2.

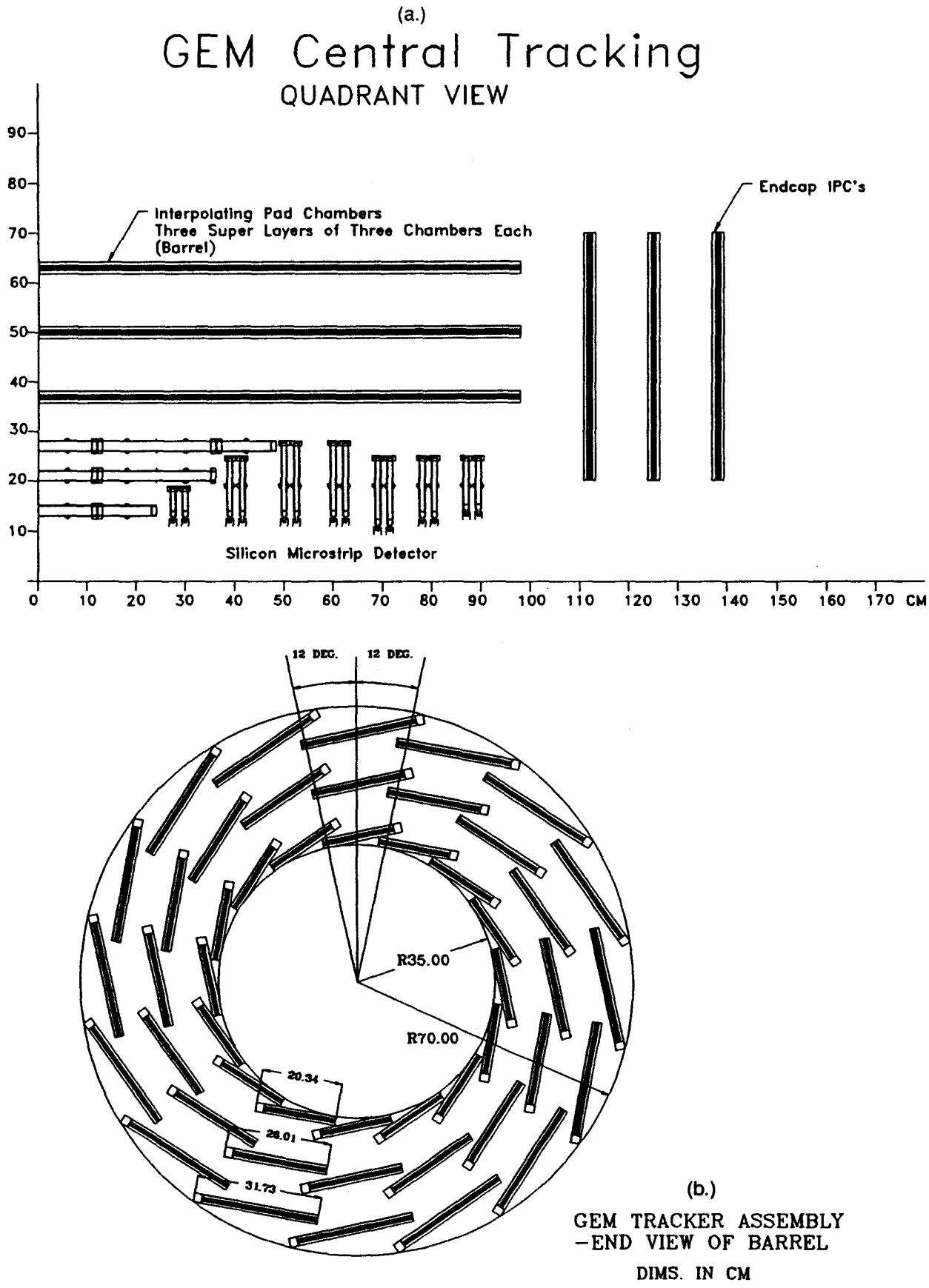

Figure 2.5-1 GEM Silicon Microstrip and Interpolating Pad Chamber Option

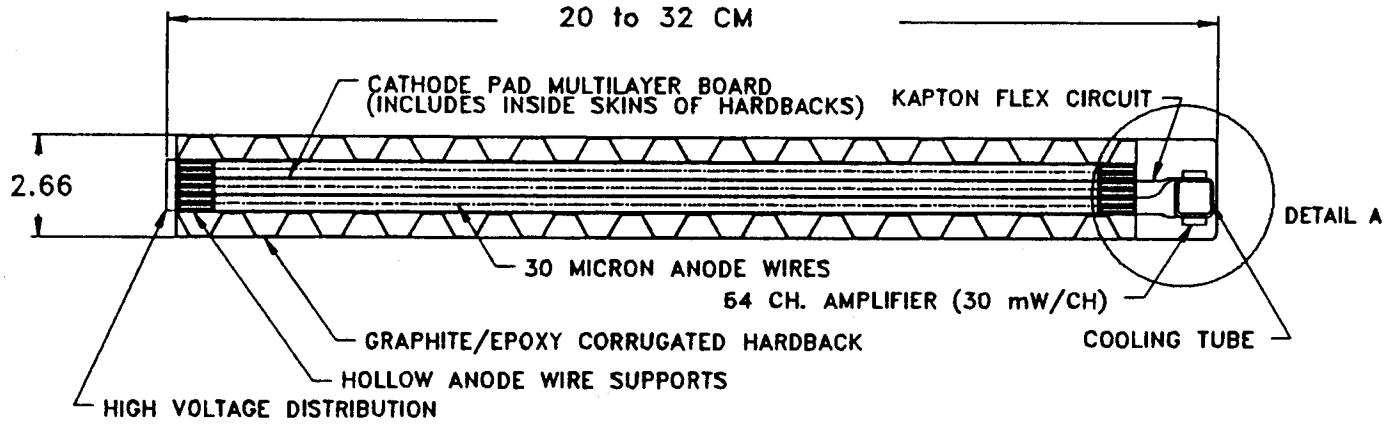

SECTIONAL OF TYPICAL BARREL MODULE

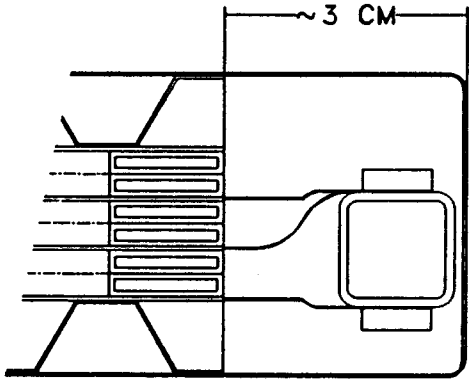

DETAIL A: SECTIONAL OF ELECTRONICS/COOLING LOCATION

Figure 2.5-2 GEM IPC Detail of Superlayer Module with Cathode Pad Amplifiers

2.5.3.4 Detector Performance

Initial calculations indicate that the silicon microstrip plus IPC tracker can meet all of the design criteria summarized in table 2.5-1. Detailed computer simulations of the momentum resolution of the tracker at high momenta (neglecting multiple scattering, which is negligible above 50 GeV/c) have been carried out. The resolution as a function rapidity is shown in figure 2.5-3. Sign selection can be obtained at the two sigma level up to 400 GeV/c. A detailed simulation code based on GEANT in which the geometry and the amount of material in the tracker are faithfully described is in progress. This program will be used to carry out the optimization of the tracker design.

2.5.4 Central Tracker R&D Plan

Of the four technologies being considered for GEM central tracking, only two, silicon and IPC's, are supported in the R&D program. While there are still many unanswered questions about straw tubes and scintillating fibers, the SDC tracking group is leading extensive R&D studies in both these areas, and members of the GEM tracking team are participating in some of this work. The limited resources available for R&D must be

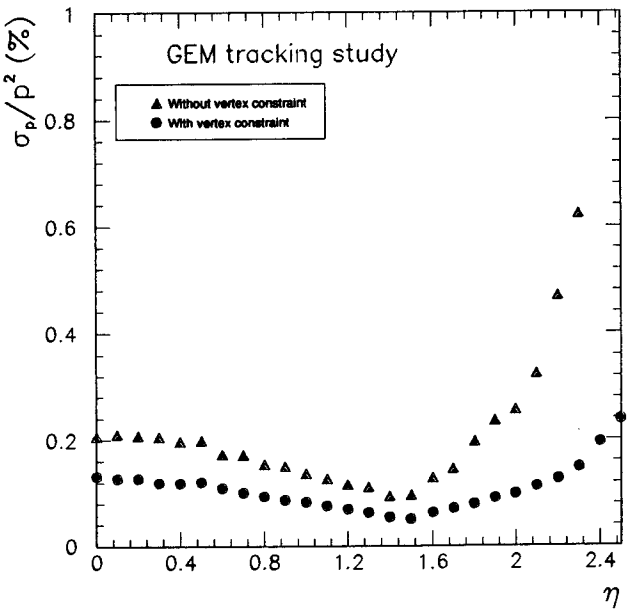

Figure 2.5-3 Tracker resolution in the momentum regime where multiple scattering may be neglected

devoted to providing answers to questions that are crucial to the program and that are unaddressed at present.

The R&D program for the GEM Central Tracker in FY92 has three major objectives with the overall goal of determining a final central tracker configuration by mid 1992, and producing a preliminary engineering design by the last quarter of 1992. The objectives of the R&D program are:

- Fully evaluate the capabilities of interpolating pad chambers for use as the outer detector in the central tracker.
- Construct Proof of Principle readout and trigger electronics for both silicon and IPC's.
- Resolve critical mechanical design issues.

What follows is an outline of the critical issues which will be addressed for silicon and IPC's in order to achieve the objectives in FY92.

2.5.4.1 Silicon Microstrip Inner Tracker

For the silicon inner tracker the primary R&D effort will be on the front end electronics design. Mechanical engineering must also continue on the support and cooling systems and on assembly and alignment. The major issues to be addressed in the electronics R&D will be the radiation resistance of rad hard bipolar electronics, their power levels and speed, design of a digital pipe line and multiplexer, 1st and 2nd level channel readout, and cabling and power distribution requirements. The mechanical engineering and R&D study will include the design and analysis of an electronics cooling system, design of the silicon ladder bridge, developing specifications for a double sided wafer and developing an in-situ alignment technique.

2.5.4.2 Interpolating Pad Chambers

A vigorous R&D program is required during the next year to demonstrate the viability of IPC's in the GEM central tracker environment. A key issue is the design and cost of rad-hard front end electronics. The radiation resistance of the IPC's at the gas gains needed to obtain 1% position resolution accuracy must be demonstrated using a gas with both the required drift speed and low Lorentz angle. It must also be demonstrated that the chambers can operate at the required speed without degrading the resolution. A mechanical design which minimizes the material thickness of the chambers must be developed in conjunction with engineering work on the support system,

cathode design and fabrication, electronics cooling, and gas and power distribution and alignment.

2.5.4.3 Other Technologies

The benefits of devices which provide "3-D" readout are also attractive to consider for the inner tracker. Both Silicon Pixels and Silicon Drift carry this potential and have been considered for use in GEM. At present, however, both suffer from a low level of technological maturity and the development of either for use in this detector requires greater resources than are available. Interest in these technologies remains very high, and any advances which might put these devices within range would be welcome.

---

[1] GEM Collaboration, "An Expression of Interest to Construct a Major SSC Detector", SSC-EOI0020, July 8, 1991.

[2] B. Yu *et al.*, "Investigation of Chevron Cathode Pads for Position Encoding in Very High Rate, Gas Proportional Chambers", BNL 44748, October 1990.

[3] W. O. Miller *et al.*, "Superconducting Super Collider Silicon Tracking Subsystem Research and Development", LA-12029, December 1990.

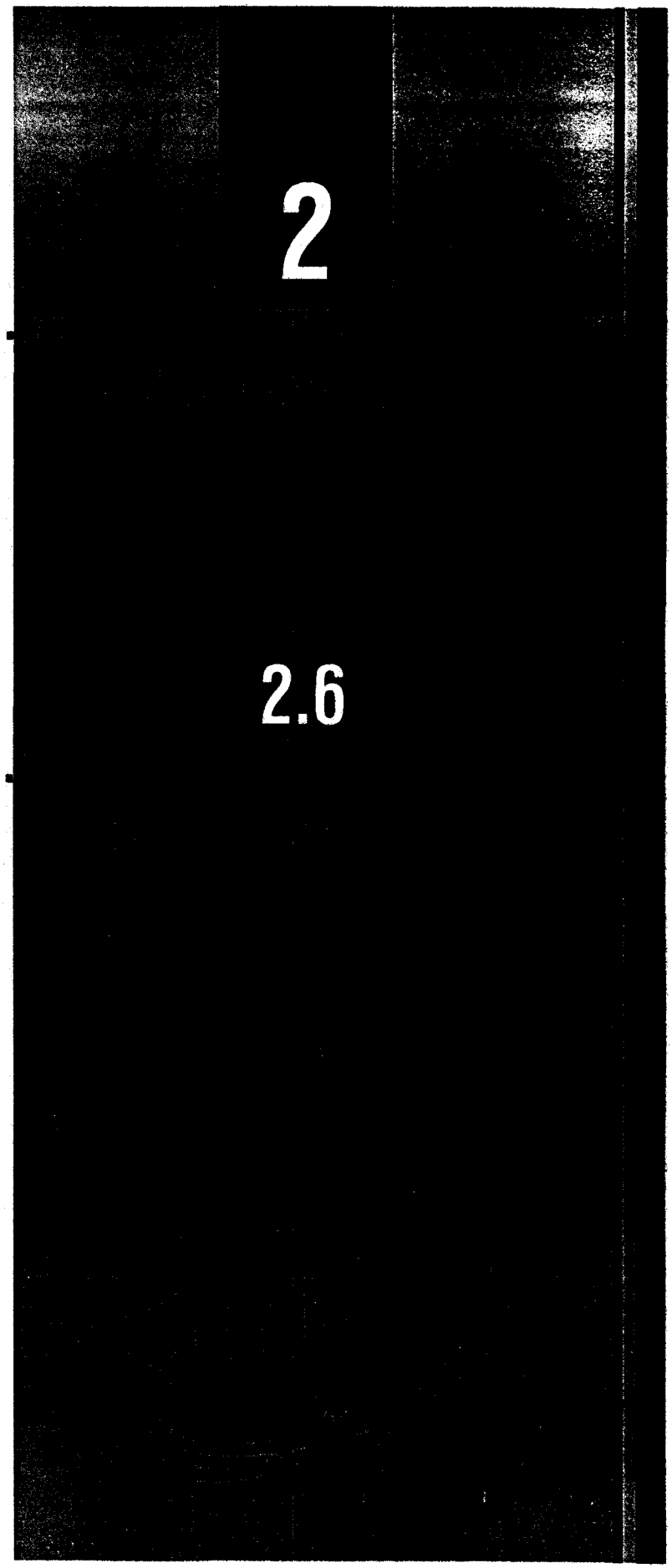
2
2.6

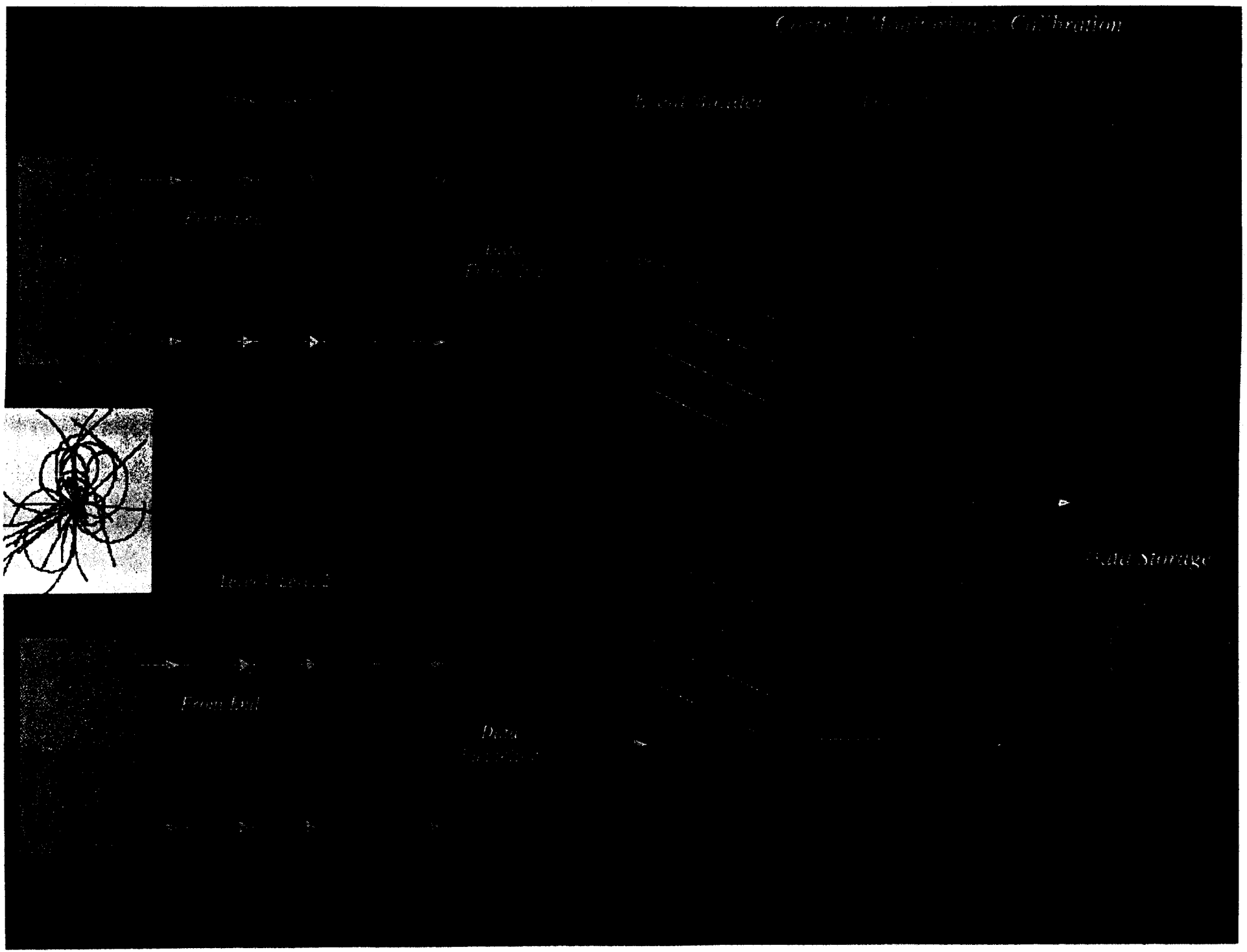

2.6 Trigger and Data Acquisition

The first two parts of this section describe general features of the trigger and data acquisition (DAQ), while the third presents specific trigger strategies along with sample rate estimates.

2.6.1 Trigger System

The trigger/DAQ system, shown in figure 2.6-1, will follow a conventional three-level approach: Level 1 is synchronous and pipelined; Level 2 is asynchronous, but monotonic; and Level 3 is a processor ranch. Event rates and latency times are summarized in table 2.6-1. The second column in table 2.6-1 specifies the maximum *average* input rate that can be sustained at each Level. To avoid overlapping events it may also be necessary to "throttle" the Level 1 accepts—i.e. it may be necessary to suppress Level 1 accepts spaced by less than ~ 1 μs. The rate handling capability of each level will be ten times greater than the design goal for the output rate of the preceding level. Although this presents a challenge, such an approach is essential to ensure reliable operation at $\mathcal{L} = 10^{33}\,\mathrm{cm}^{-2}\mathrm{s}^{-1}$ and to leave room for running at $\mathcal{L} = 10^{34}\,\mathrm{cm}^{-2}\mathrm{s}^{-1}$.

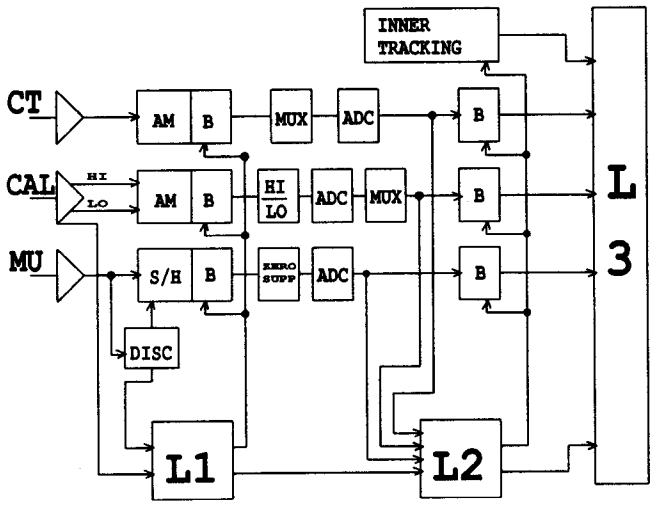

Figure 2.6-1 Block diagram of GEM trigger/DAQ system.

Table 2.6-1 Design goals for the GEM Trigger/DAQ System. Output rates are for operation at $\mathcal{L} = 10^{33}\,\mathrm{cm}^{-2}\mathrm{s}^{-1}$

GEM Trigger/DAQ Design Goals				
Lvl.	Max Av. Rate In	Rate Out	Latency	Comments
1	62 MHz	10 kHz	3 μs	Synchronous, Pipelined
2	100 kHz	300 Hz	100 μs	Asynchronous, Monotonic
3	3 kHz	10 Hz	—	CPU Ranch

2.6.1.1 Level 1

The Level 1 trigger decision will be based on a reduced set of calorimeter and muon system signals, encoded to a minimum number of bits, here called primitives. Specifically, trigger towers will be formed from electromagnetic (EMC) and hadronic (HCAL) calorimeter regions of size $\Delta\eta \times \Delta\phi = 0.2 \times 0.2$. Analog sums of the calorimeter elements comprising each tower will be flash encoded and compared to preset digital thresholds. Photon and electron triggers will be defined as energy depositions in EMC-towers accompanied by corresponding HCAL-tower depositions satisfying $E_{HCAL}/E_{EMC} < 1/10$. Jet triggers will be formed from local sums. Digitally formed global sums of trigger towers will allow for total transverse (and missing transverse) energy triggers.

Muon trigger primitives will be generated using hit patterns produced through discrimination of the

muon chamber signals, which will be projected onto look-up tables to define high-p_T candidates.

A Level 1 trigger decision will be formed for each bunch crossing from the *global* pattern of trigger primitives. It will be possible to trigger on single high-p_T electrons, photons, muons, or jets; on pairs of lower p_T leptons; or on any other combination of interest. Definition of a suitable set of Level 1 primitives is under study.

To simplify the system design and to avoid sampling more bunch crossings than necessary, the trigger signals from the Level 1 subsystems will tag the bunch crossing of the event. This imposes constraints on the design of the calorimeter trigger pickoffs and the design of the muon system.

2.6.1.2 Level 2

The Level 2 trigger is a distributed, pipelined digital-processor system designed around general data-driven principles. It will use digitized data from the calorimeter, muon, and central-tracking systems to refine trigger candidates identified by Level 1.

Calorimeter data with high precision and full granularity will be used to apply shower-shape and isolation cuts to electron and photon candidates. Electron candidates will be further refined by requiring stiff (p_T > 10 GeV/c) spatially-matched tracks in the central tracker. Investigation is currently underway to determine whether this is best done in the inner silicon tracker or in the outer tracker. Finally, digitized muon information will allow a precise determination of muon momenta.

2.6.1.3 Level 3

Level 3 will be a "ranch" of processors having access to information from the entire detector. See section 2.7.

2.6.2 Data Acquisition

The data acquisition system must provide deadtimeless operation at rates up to 100 kHz while taking into account the Level 1 trigger latency time of 3 μs. The architectures for the different components are described below and shown schematically in figure 2.6-1.

2.6.2.1 Calorimeter

After preamplifiers, shapers, and fast trigger pick-offs, the calorimeter signals will be sampled every bunch crossing with the samples stored in analog memories (AM). (A digital pipeline approach is also being investigated.) Seventeen bits of dynamic range will be achieved by splitting the input into high-gain and low-gain channels.

Upon receipt of a Level 1 trigger, up to 5 samples per signal will be transferred to a Level 2 derandomizing buffer. The buffered samples will be digitized with fast (≥ 1 MHz) 12-bit ADC's. The data will then be sent bit-serially to Level 2 after an approximate 10:1 multiplexing to reduce the cable count.

The ADC will be a custom device, or a commercial product, if one with reasonable cost and power consumption can be found.

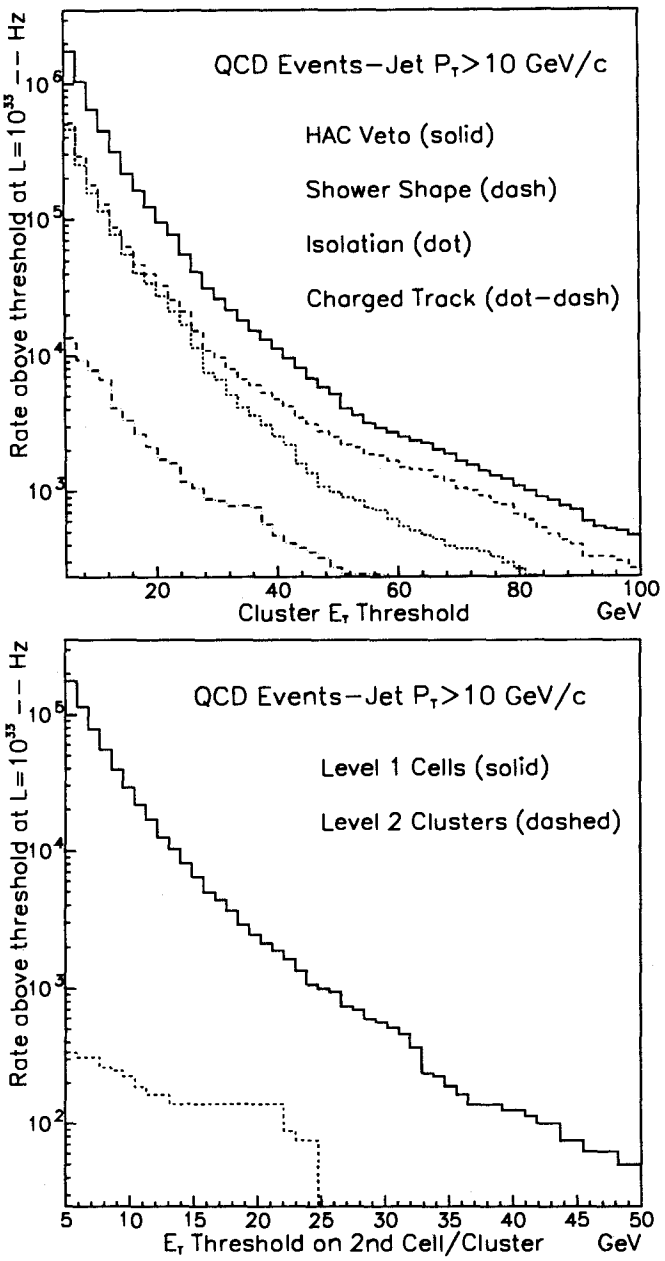

Figure 2.6-2 (a) Rates for single γ/e⁺ triggers, (b) rates as a function of the second highest energy γ/e⁺ cluster or cell in the event

2.6.2.2 Muon Pads

Low occupancy will allow the pipeline delay principal to be replaced by a simpler discriminator (DISC) driven sample-and-hold circuit (S/H), plus an analog derandomizing buffer. Upon receipt of a Level 1 trigger, the stored samples will be routed through an analog multiplexer to a 9-bit FADC. Although many (256 or more) channels will be serviced by a single MUX/FADC combination, the readout time will be greatly reduced by using the delayed discriminator bits to perform a selective scan of only the channels of interest. Digitized charge and address data will be sent bit-serially to Level 2.

2.6.2.3 Muon Drift-Wires

Circuits providing time-stamped leading-edge information with 1 ns resolution and multi-hit capability are already commercially available. With straightforward changes in readout architecture these circuits will be suitable for use in GEM.

2.6.2.4 Silicon Tracker

The front end of the silicon strip readout is composed of a bipolar amplifier/discriminator chip and a hardened CMOS pipeline chip. The pipeline is split into a Level 1 section, which operates at the bunch crossing frequency (62.5 MHz) and a Level 2 section, which operates at speeds up to 100 kHz. Upon receipt of a Level 2 accept, data will be read out via a serialized transmission of 640-channel - wide chip-level data registers. This data will be further multiplexed outside the main calorimetry and transmitted optically to the counting house, where DSP's will be used to zero suppress the incoming data. After suppression the expected event size is (assuming 5 M channels and 2 k hits/event) of order 50 kbits.

The trigger data from the silicon strip detector consists of a logical OR of 16 neighboring strips. This data is transmitted off-detector, on receipt of

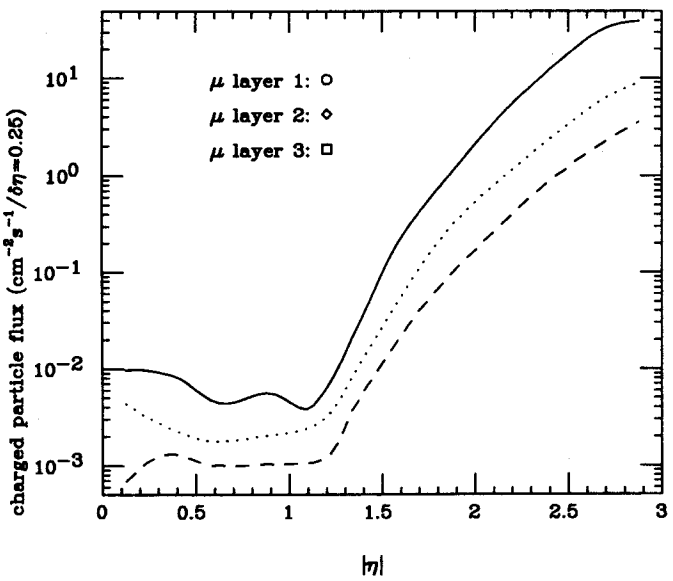

Figure 2.6-3 Charged particle rates versus |η| in the muon system

the Level 1 accept signal, via serial links operating at bit rates of 4MHz. Trigger processors located outside the calorimetry take the data and form coincidences between the layers, which provide a 14 GeV p_T cut-off (by assuming a 500 μm error on the beam position). Sectors with candidate tracks are then further processed to reconstruct the r - z direction of the candidate.

2.6.2.5 Central Tracker Pads

The Level 1 delay for the pad chambers will be achieved using SCA's in a manner similar to the calorimeter readout. In the case of pads, a single scale with nine bits of dynamic range will suffice. However, the pad electronics will be chamber-mounted and will need to be radiation tolerant. Analog outputs from the SCA will be combined on-chamber via analog multiplexers so as to reduce the bulk of cables needed to transmit the information from the tracker volume. One possibility for high-bandwidth analog links is fibers driven by electro-optic modulators [2].

Information for the Level 2 trigger can be extracted quickly by a selective scan of pads along roads defined by the calorimeter-defined electron candidate(s).

2.6.2.6 Dataflow and Event Building

Subsequent to a Level 2 trigger decision, data must be moved from buffers near the detector to the Level 3 ranch and be assembled into events in the process. Preliminary estimates of event sizes yield 300–400 kbytes, but in view of the uncertainties in these estimates a size of of 1 Mbyte/event is assumed, for a total data rate of 3 Gbyte/s.

These data will likely be carried over fiber links, since such links are compact, less prone to ground-loop problems, and capable of high transmission rates (systems operating at 125 Mbyte/s are now in use). In principle only a few dozen parallel links will be needed, but practical considerations, such as uneven loading induced by the natural divisions between detector subsystems, may require additional links.

The event builder accepts sub-event data from the parallel data paths, assembles the sub-events into full events, and then directs the full events to one of the processors in the Level 3 ranch. Event builders of varying levels of complexity are currently the subject of R&D [3]. Within GEM, those options will be investigated along with approaches such as using dual-port memory with interconnections to both the Level 2 data collection paths and the Level 3 ranch.

2.6.3 Trigger Strategies and Rates

From studies of two-jet backgrounds, strategies for calorimeter and muon triggers have been developed. Estimated rates for each trigger were determined using ISAJET and PYTHIA event generators combined with a GEANT model of the detector.

2.6.3.1 Electron and Photon Triggers

Detection of $H^0 \rightarrow \gamma\gamma$ is an important consideration in the design of all three levels of the GEM trigger. The comparatively indistinct signature of a low-mass state decaying to two photons requires a Level 1 trigger capable of identifying pairs of low-E_T photons, a Level 2 capable of detailed analysis with full calorimeter granularity and good energy resolution, and a DAQ/Level 3 system capable of digesting complete events at rates of 1 kHz or more.

Monte Carlo studies indicate that for $M_H = 80$ GeV, a Level 1 trigger efficiency of 95±3% can be obtained by requiring at least one EMC trigger cell with $E_T' > 50$ GeV or least two cells with $E_T' > 16$ GeV (the prime denotes EMC depositions with $E^T_{EMC}/E^T_{HLAC} > 0.9$). At Level 2, a shower-shape analysis requiring $E(3\times3) / E(5\times5) > 0.9$ where $E(3\times3)$ and $E(5\times5)$ refer to sums of the central nine and twenty-five EMC elements of the candidate photon shower. In addition, an isolation cut requiring

$$\sum_{R=0.3} E_T - E_T\,(5\times5) < 10\ \text{GeV}$$

is applied to each photon.

If two photons, each having $E_T > 15$ GeV, are required, the Level 2 efficiency is 92 ± 3%. Experience based on test-beam data shows that similar algorithms, implemented using massively parallel arrays of digital signal processors can be executed in 15μs [4] —which is already close to the goal of 10 μs/event. Selection of electrons proceeds along the same lines, but with an additional Level 2 requirement of a matching charged track with $p_T > 10$ GeV/c.

Rate estimates for the single and double $e^{\pm} / \gamma$ triggers are shown in figures 2.6-2a and 2.6-2b. The rates with the combined Level 1 and Level 2 requirements for $H^0 \rightarrow \gamma\gamma$ are about 10 kHz and 100-200 Hz, respectively. These triggers also provide acceptance for channels with $Z^0 \rightarrow e^+ e^-$ final states. The charged track rate estimates of figure 2.6-2a are optimistic in that they do not take into account false positives and inefficiencies due to pattern recognition failures.

2.6.3.2 Muon Trigger

Figure 2.6-3 shows the raw charged-particle rates for each superlayer in the muon system. Charged particle punchthrough was calculated using a GEANT-based parameterization and includes K and $\pi^{\pm}$ decays as well as prompt muons. The rates are quite low at all but the largest η and are well within the rate handling characteristics of the muon trigger counters — i.e., resistive plate chambers (RPC's) in the barrel and cathode pads in the endcaps. This situation bodes well for the formation of a robust muon trigger.

The Level 1 muon trigger is formed by identifying stiff tracks in the outer and middle muon chambers that appear to point back to the intersection point (IP) when viewed in the r–ϕ projection, as shown in figure 2.6-4a. Muon rates for the various triggers, along with the intrinsic rates for high-p_T muons are shown in figure 2.6-4b. With position segmentation of 5 cm in the barrel region, p_T thresholds up to 50 GeV can be imposed. The requisite resolution can be obtained from either the RPC's or the muon drift tubes, the former offering the advantages of short delay and simple tagging of the bunch crossing. In the end caps, segmentations ranging from 5 cm down to 3 mm are needed. Discriminator pickoffs from the muon pad chambers will be used for this purpose. Pad chamber timing resolution good enough to tag the bunch crossing will be obtained by OR'ing layers with staggered anode wires.

At Level 2, a p_T measurement is needed to further reduce the rate. Position measurements accurate to ~500 μm will be used to determine the angular deflection (bend angle) of candidate trajectories between the middle and outer superlayers, as shown in figure 2.6-4a.

---

[1] S. Kleinfelder, M. Levi, and O. Milgrome, Nucl. Phys. B (Proc. Suppl.) 23A (1991) 382.

[2] M. Lowry *et al.* Proc. of Symposium on Detector R&D for the SSC, Ft. Worth TX, p. 542, 1990. V. Radeka *et al.*, ibid, p 491

[3] E. Barsotti, A. Booth, and M. Bowden, Fermilab-Conf-90/61.

[4] S. Buono and D. Crosetto, "Test results of real-time algorithms executed on FDPP with SPACAL data", CERN/ECP 90-6 (1990).

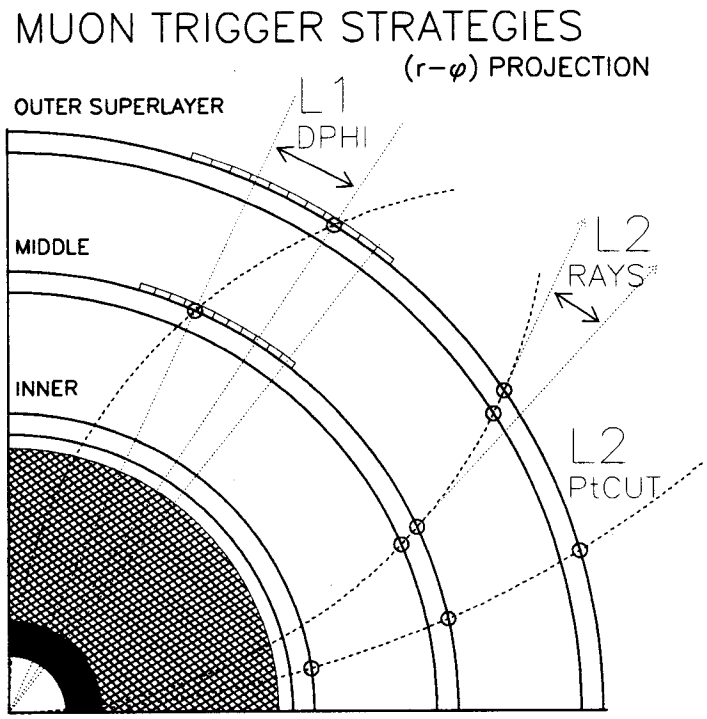

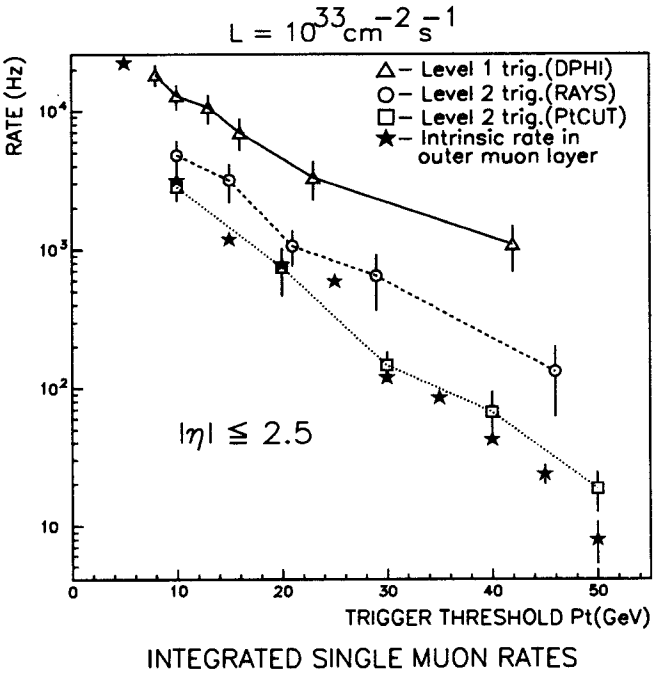

Figure 2.6-4 (a) Schematic depiction of the various muon triggers. (b) Level 1, Level 2, and intrinsic muon rates

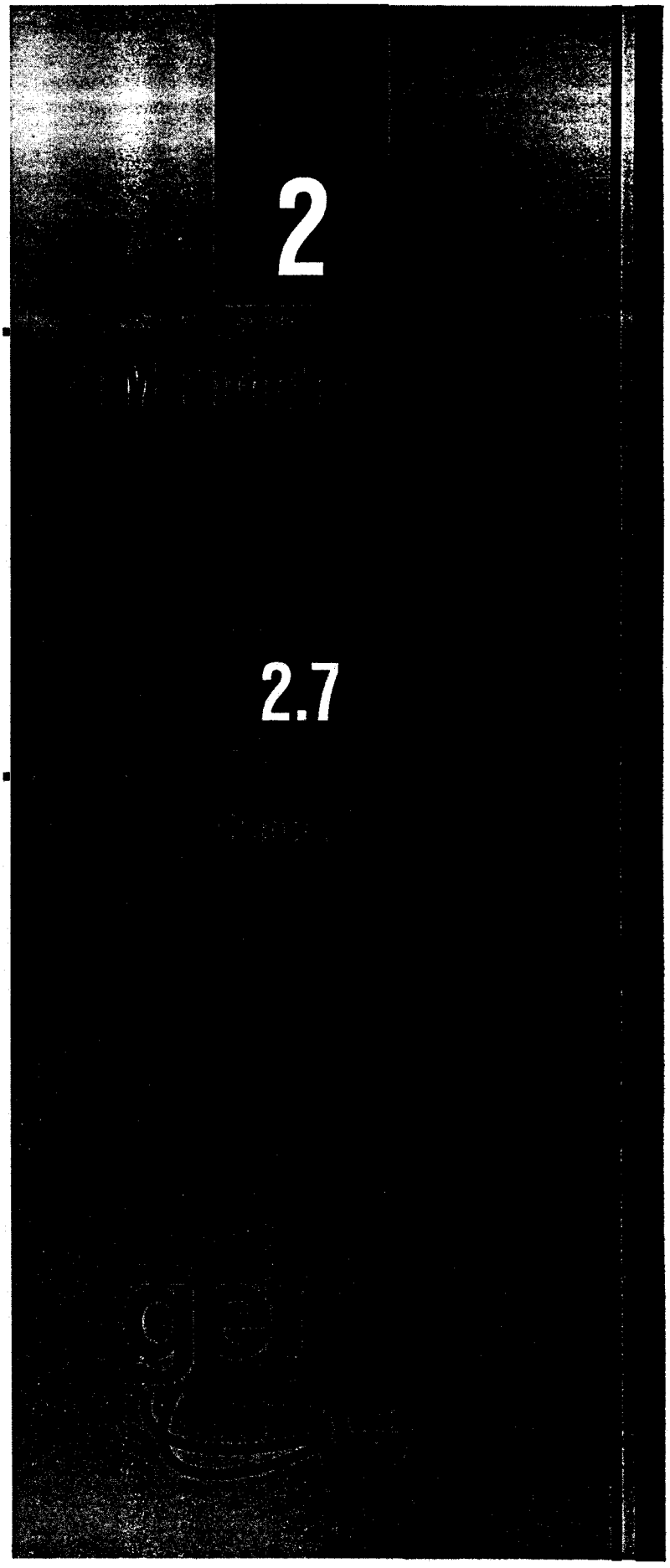
2
2.7

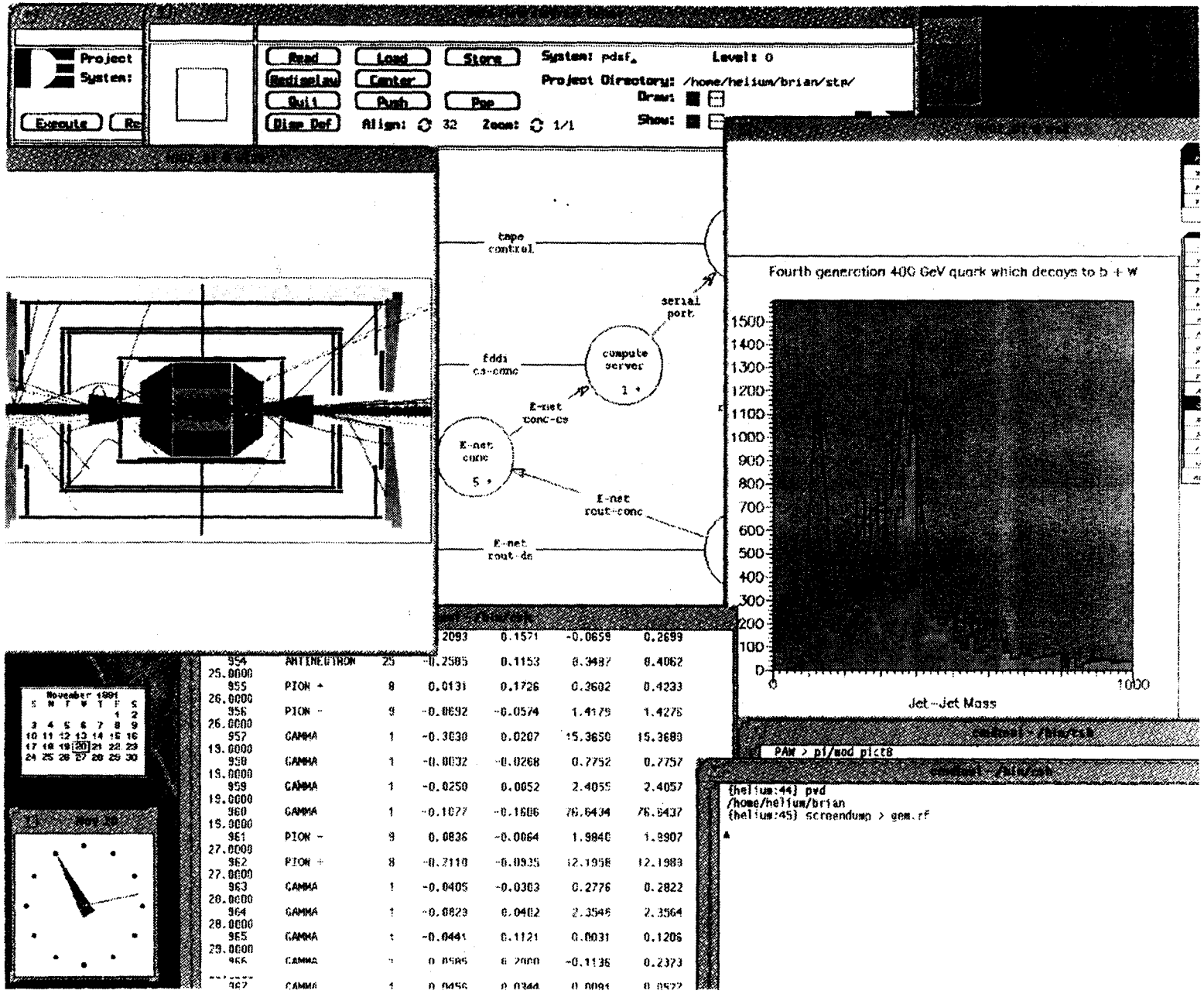
Project System:
Execute
Read
Load
Store
Redisplay
Center
Quit
Push
Pop
Disp Def
System: pdsf
Level: 0
Project Directory: /home/helium/brian/stp/
Draw:
Show:
Align: 32
Zoom: 1/1
tape control
serial port
fddi cs-conc
compute server 1
E-net conc-cs
E-net conc 5
E-net rout-conc
E-net rout-cs
Fourth generation 400 GeV quark which decays to b + W
1500
1400
1300
1200
1100
1000
900
800
700
600
500
400
300
200
100
0
0
1000
Jet-Jet Mass
PAW > pi/mod pict8
{helium:44} pwd
/home/helium/brian
{helium:45} screendump > gem.rf
November 1991
S M T W T F S
1 2
3 4 5 6 7 8 9
10 11 12 13 14 15 16
17 18 19 20 21 22 23
24 25 26 27 28 29 30
954 ANTINEUTRON 25 -0.2585 0.1153 0.3487 0.4062
25.0000
955 PION + 8 0.0131 0.1726 0.3602 0.4233
26.0000
956 PION - 9 -0.0692 -0.0574 1.4179 1.4276
26.0000
957 GAMMA 1 -0.3030 0.0207 15.3650 15.3680
13.0000
958 GAMMA 1 -0.0032 -0.0268 0.7752 0.7757
19.0000
959 GAMMA 1 -0.0250 0.0052 2.4055 2.4057
19.0000
960 GAMMA 1 -0.1077 -0.1606 76.6434 76.6437
19.0000
961 PION - 9 0.0836 -0.0064 1.9840 1.9907
27.0000
962 PION + 8 -0.2110 -0.0935 12.1958 12.1988
27.0000
963 GAMMA 1 -0.0405 -0.0303 0.2776 0.2822
20.0000
964 GAMMA 1 -0.0823 0.0402 2.3548 2.3564
28.0000
965 GAMMA 1 -0.0441 0.1121 0.0031 0.1206
29.0000
966 GAMMA 1 0.0585 6.2000 -0.1136 0.2373
967 GAMMA 1 0.0456 0.0344 0.0091 0.0522

2.7 Computing

This section describes the GEM approach to on-line computing including "Slow Control" and the "Level 3" filter, data storage, off-line computing (processing and analysis), and communications and networking.

Widely-adopted standards, open systems and commercial products will be used where those are available and of adequate performance. This approach will enhance portability, reduce costs, and assure professional support.

The Slow Control functions will be fully computerized, and will allow shifts of physicists to operate the detector safely and obtain data of assured high quality.

The Level 3 filter will take data from the detector at rates up to 3 kHz and ideally reduce the rate to 10 Hz before sending it to off-line processing and the main mass store.

In keeping with the goals expressed in section 2.6.1, the off-line processing will be designed to keep up with data coming from the detector corresponding to an event rate of up to 100 Hz, and to do substantial additional work.

The expectation is that volume-produced components with high speed links to distribute the load across the resulting "ranches" will be used. By using similar equipment, it is anticipated that the on-line computers will be available for off-line use when the Collider is not running. The intent is to purchase the bulk of the hardware in the 1997-1998 time frame to maximize capability at turn-on.

The bulk of the reconstruction (PASS1) will be done at SSCL. For the analysis, emphasis will be on distributed participation with the master versions of the data stored at SSCL, and the largest concentration of computing power also at the SSCL. This will give more freedom in choice of system architecture and help in treating data consistently. Consequently, there will be a need for wide-band networks reaching all participants, including those outside the U.S. If the bandwidth is inadequate, data summaries will be transferred to analysis centers accessible to those participants.

A sketch of the GEM computing model is shown in figure 2.7-1, and has two main features: the data are recorded directly in the final store (there is no intermediate moving of tapes from detector to computer center), and the off-line initial reconstruction pass will keep up with the data from the detector.

2.7.1 Organization

The computing effort will be supported by a central group at SSCL which will build a full GEANT simulation of the detector in cooperation with the detector subgroups and maintain this model through a process of versions and updates. This effort will be carried out through a coordinator from each subsystem. The group will have other functions including maintaining central code libraries and data bases, developing solutions for managing distributed systems, developing user interfaces, coordinating installation of hardware and software for the on-line system, and working

with the SSCL support groups. To support this, there will be coordinators for various activities besides simulation: on-line, slow control, reconstruction and analysis, networks, non-U.S. efforts, etc. One important function will be to work with vendors to pursue development of network and computer interconnect technology, both the hardware and the software, to be sure that the GEM systems will function as envisaged. The size of this group should increase over the course of the project to 10-15 physicists (some of them long-term visitors) and 20-30 programmers.

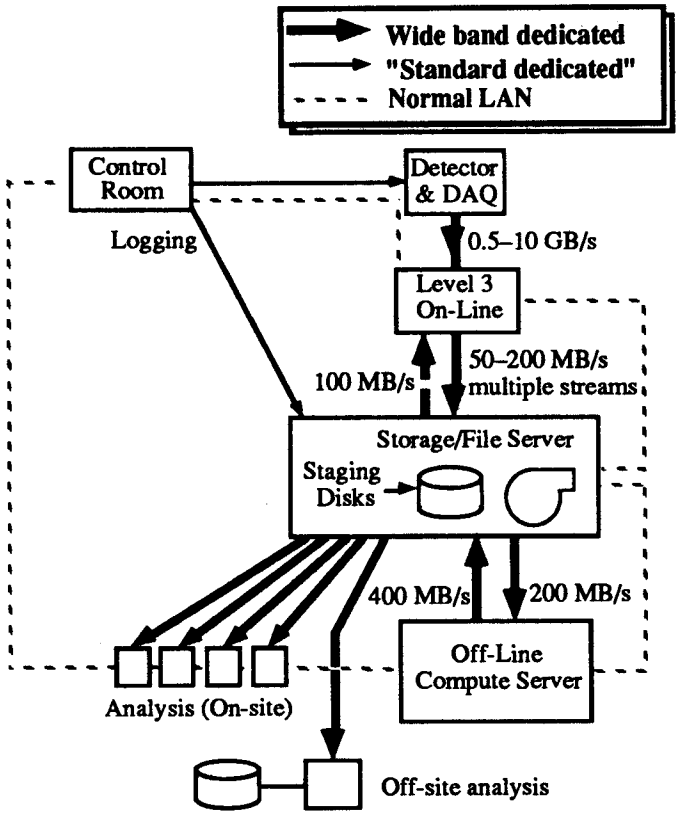

Figure 2.7-1 Computing Model and Data Flow

2.7.2 On-line Computing

This includes the control systems for the detector and its subsystems and data bases for Level 1 and Level 2 triggers, the event builder, and the Level 3 processors.

2.7.2.1 Slow control systems

The slow control system will permit the safe operation of the detector by shifts of physicists, and have built-in checks to assure that the data being collected is of the necessary quality. Requirements include starting and stopping runs, with a "cold" start in 30 minutes and a "warm" start or stop in one minute (not including magnet changes). Appropriate alarm systems will be included. The control system will send a stream of calibration and status data to the main store.

Detector subsystems will be monitored and controlled by a system of workstations using common software. The "slow" data acquisition and control hardware for this purpose will be part of the detector subsystem.

2.7.2.2 On-Line (Level 3)

Based on trigger simulations, the event builder and Level 3 system is to process up to 3 kHz of events, and reduce that to no more than 100 Hz. Event size estimates range from 350 kilobytes (kB) to more than 1 MB; 1 MB is assumed as a working value. With an estimate of 50 SSCUP-seconds of processing for each event, 150,000 SSCUPs will be required for Level 3 (The SSCUP is

approximately a VUP for HEP code). This estimate is uncertain and there are plans to improve it.

The resulting stream of data at 100 MB s^{-1} will be sent over a dedicated wide-band network to the off-line system and to high-capacity recorders in the main store. The event stream may be separated into a number (10-20) of output streams of related events (e.g., by trigger with some overlap between streams), both to ease processing and to match the capability of the recorders.

2.7.3 Data Storage

The data from the experiment will be immediately recorded in the single main storage system used for all work. Thus all data output from Level 3, from the first event to the most recent, will be available for study. Storage expectations and requirements are based on the need for 3 PB/yr of data plus reconstructed events in a near-line status, where any event can be accessed automatically in a few minutes. Data summaries will likely be needed to facilitate analysis. The main store will thus consist of a mix of mass storage devices (e.g., tape robots) and fast-access devices (e.g., disk arrays). Research into the hardware and software architecture of this system is necessary.

One issue under consideration is whether SSC data should be simultaneously recorded in an independent system located elsewhere (without the requirement of five-year near-line availability) to protect against a fire or other disaster destroying five years of data.

2.7.4 Off-line Computing

The main tasks for the next several years include: simulating the interaction of the physics processes with the detector, helping refine the design of the detector, modifying the simulation in the light of test beam experience, testing Level 1, Level 2 and Level 3 filter tactics, and developing and testing analysis programs on simulated data. This will require increasing computing capacity, and the current PDSF (Physics and Detector Simulation Facility) at SSCL is expected to grow to carry much of this effort. Plans should be made to study networking inside and outside the laboratory, to make fully interactive graphics available off-site.

The basic requirement for off-line reconstruction is based on the CDF estimate (S. Geer, private communication) of 2,100 VUP-seconds/MB of data for PASS1, assuming that CPU time is proportional to event size. For 1 MB events this therefore translates to a need for 210,000 SSCUPs of power for GEM's PASS1, to keep up with the incoming data during a run. At least one more PASS1 (e.g., because of re-calibrations) will be active, along with a variety of other tasks (DST creation, simulation on the basis of experience, analysis). Thus there is a total requirement of 600,000 SSCUPs, larger than the estimate for the on-line system. The two requirements are related: the data rate into storage may be reduced by more complex (and time-consuming) algorithms in Level 3, while Level 1 and Level 2 trigger settings can reduce the overall flow, allowing less processing in Level 3, but keeping the off-line load the same.

2.7.4.1 Analysis

It is planned to make large data sets available to users, by using high-rate (100 MB s^{-1}) connections to powerful workstations. Typically, a 1 nb sub-sample may occupy 1 TB, and 50-100 such sub-samples should be available. The access methods will be a subject for a research effort in cooperation with SDC. The analysis activity will also make use of the off-line computer facility, as noted above.

The desire to make all the event data, the calibration data, and any sub-samples part of one database clearly favors one central system. However, in practice it may be convenient to transfer sub-samples to institutions which do not have adequate access over a network but which can arrange to have appropriate computing facilities.

2.7.5 Communications and Networking

Our strategy depends on the availability of wide-band networking, in the several Gbit per second range, for both LAN and WAN applications. Closely coupled systems (e.g., HPPI) for this already exist, while high-rate optical fibers will become cost-effective. As noted, such networks are needed for a variety of purposes: command and control, moving data between the on-line and off-line systems and the storage system, and making large samples of data accessible from off-site. This latter item will require new network capacity, all the way to the end user.

There is also a need for teleconferencing capability to communicate between various sites, including sites within the SSCL.

2.7.6 Magnetic Fields

It is felt that the stray field from the base-line magnet can be dealt with: the major part of the computing facilities can be in fields less than 10 G, and other items can be shielded. Tests will be done to ensure that components operate (shielded if appropriate) in the expected fields.

2.7.7 Research and Development

Computer R&D plans are directed toward preparation of the Technical Proposal. They include cooperation with SSC and SDC on database access methods, software methodology studies, and system architecture studies.

3

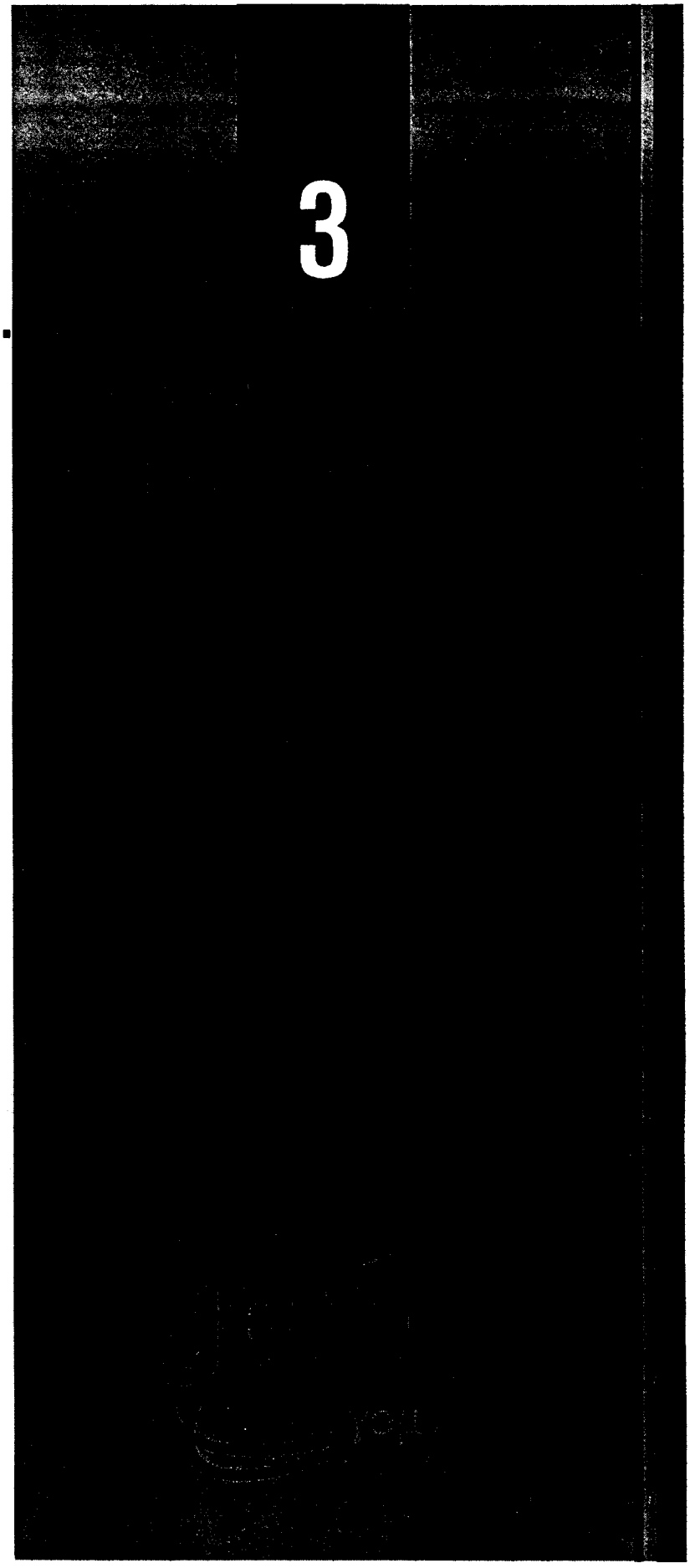

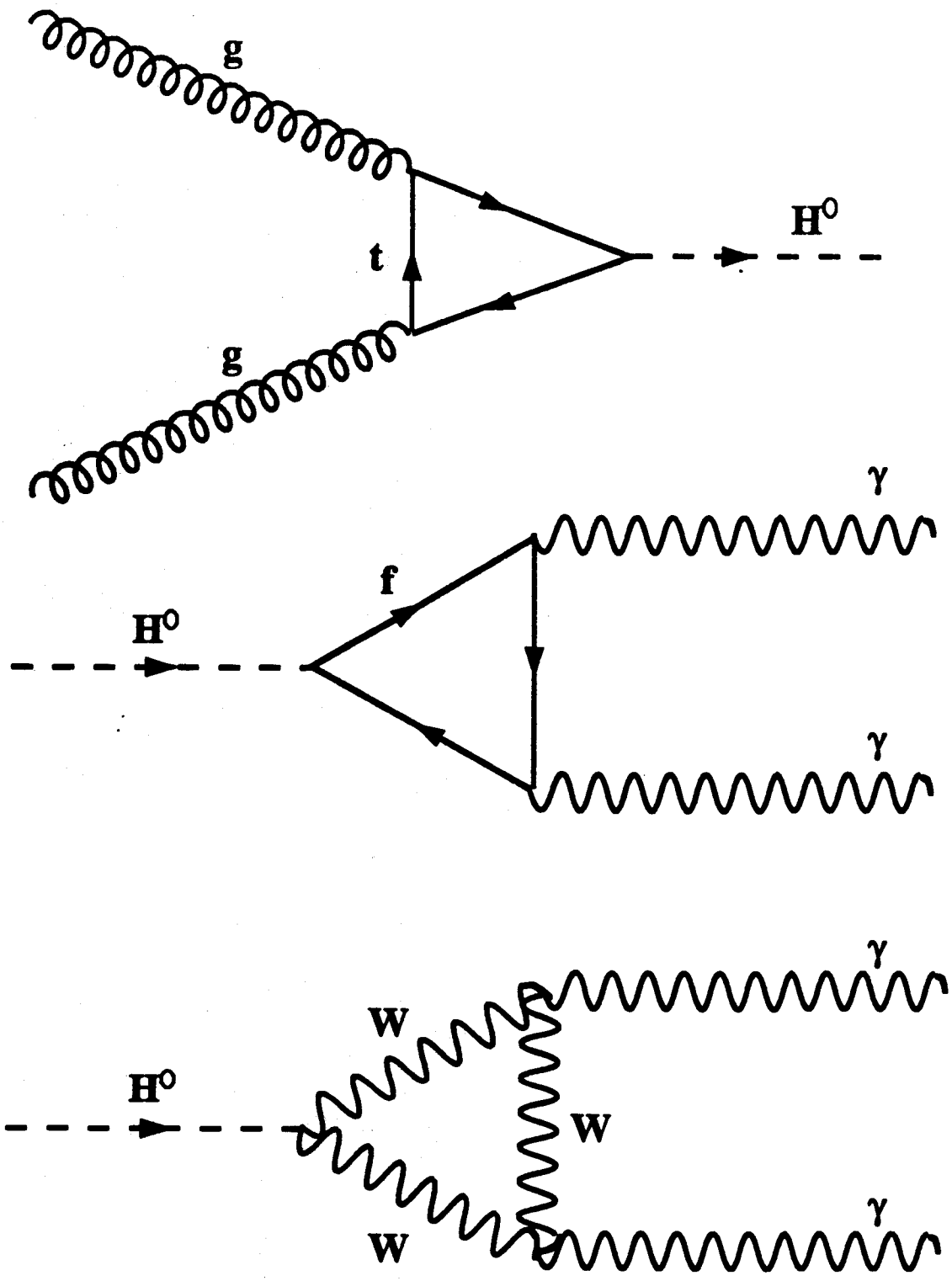
g
t
H⁰
g
γ
f
H⁰
γ
γ
W
H⁰
W
γ
W
γ

3.0 PHYSICS PERFORMANCE OF THE GEM DETECTOR

3.1 Introduction

The GEM detector is designed to discover and study in detail the physics of electroweak symmetry breaking and to search for the origin of the meaning of flavor and other new physics by high-precision measurement of photons, electrons and muons [1]. This will be achieved by using the best attainable electromagnetic calorimetry, and by measuring muon momenta outside the calorimeter in a large open magnetic volume. Hadronic energy will also be measured with good accuracy. These systems cover the central region, $|\eta| \leq 2.5$–3.0, where new, high-p_T physics will occur. They will be able to operate at the ultrahigh luminosities, $\mathcal{L} \gtrsim 10^{34}\ \mathrm{cm}^{-2}\mathrm{s}^{-1}$ that may be necessary to study the physics of the 1 TeV energy region. The central-region systems will be augmented by tracking and by forward calorimetry to provide missing transverse energy ($\not{E}_T$) and limited forward jet measurements.

These physics and design considerations are illustrated through the responses made in this chapter to the PAC's five questions regarding GEM's discovery potential, and to the sixth question, regarding evolution of the experiment beyond initial operation. In brief:

1. GEM will be able to discover the standard Higgs boson, H^0, if it exists anywhere in the mass range 80 to 800 GeV. For the most part, this will be done in one year at $\mathcal{L} = 10^{33}\ \mathrm{cm}^{-2}\mathrm{s}^{-1}$ using the electromagnetic (EM) and muon systems. The QCD backgrounds to $H^0 \rightarrow \gamma\gamma$ are larger than realized previously. More than ever, defeating these backgrounds requires the precision of the EM calorimeter. At the high-mass end, the $H^0 \rightarrow Z^0 Z^0 \rightarrow \ell^+\ell^-$ $\ell^+\ell^-$ search mode will be augmented by modes in which one Z^0 decays into a pair of jets or neutrinos.
2. GEM will be able to find a 250 GeV top quark decaying to W^+b and/or H^+b and measure its mass to a few GeV. The H^+ mass could also be measured to a few GeV provided that $B(t \rightarrow H^+b) \cdot B(H^+ \rightarrow q\bar{q}') \gtrsim 1\%$. In addition to tagging $t\bar{t}$ production by isolated leptons, or by jets containing muons [1], a new method will be used which forces the p_T of the top quark to be large, with a consequent improvement of the signal-to-background ratio.
3. GEM can discover quickly a 400 GeV $t' \rightarrow W^+b$, with very little background from t-production. The t' mass can be measured to a few GeV with hadronic calorimetry covering $|\eta| < 3$. A 300 GeV gluino can be discovered in one year via its $\not{E}_T$ signature by employing forward calorimetry over $3 < |\eta| < 5$. It is also possible to discover pair-produced gluinos using a like-sign dilepton signature that does not require forward calorimetry.
4. The dijet mass resolution of the GEM hadronic calorimeter, using any of the options, is 5 GeV for a Z^0 resulting from the decay of an 800 GeV H^0 and subsequently decaying to a pair of jets. This is crucial to the search for a heavy Higgs in the $\ell^+\ell^-$ jet jet mode. The mass resolution for a 1 TeV $Z^{0\prime}$ decaying to a pair of jets is 3.5%.
5. GEM's precise electromagnetic and robust muon systems give it a unique reach for new

physics. This is exemplified by: the ability to search for H^0 in photon and electron modes; reliable access to flavor physics by tagging *b*-quarks — hence *t*-quarks — by measuring inclusive muons outside the calorimeter; and by the survivability of these systems to $\mathcal{L} = 10^{34}\text{cm}^{-2}\,\text{s}^{-1}$. The increased power given by GEM's ultrahigh luminosity capabilities is illustrated by incisive studies that can be carried out in just one year on a 4 TeV Z^0 decaying to $\ell^+\ell^-$, and on a world in which quarks and leptons are found to have substructure at 25 TeV.

In the studies to answer the PAC questions, the GEM detector has generally been parameterized using the baseline design that incorporates:

1. BaF_2 or LAr EM calorimetry, with $\Delta E / E = (1.5\text{–}7.5)\% / \sqrt{E} \oplus 0.5\%$ up to $|\eta| = 2.5$ and with segmentation $\Delta\eta \times \Delta\phi = 0.04 \times 0.04$
2. Hadron calorimetry with $\Delta E / E = (50 - 60)\% / \sqrt{E} \oplus 2\%$ and segmentation $\Delta\eta \times \Delta\phi = 0.08 \times 0.08$ for $|\eta| < 3$, and forward calorimetry covering $3 < |\eta| \lesssim 5$
3. Muon measurement for $|\eta| < 2.5$ in an external solenoidal field, B = 0.8 T, with $\Delta p_T / p_T^2 \simeq 10\%$ / TeV for $|\eta| \leq 1.5$. The muon system is operable at $\mathcal{L} = 10^{34}\text{cm}^{-2}\,\text{s}^{-1}$ and higher with the single-muon trigger threshold raised to about 50 GeV.
4. Central tracking giving unambiguous space points out to $|\eta| = 2.5$, rather than projected points.

Signal and background events for the physics processes studied were generated with PYTHIA 5.5 [2] and ISAJET 6.36 – 6.43 [3] and analyzed with model detectors incorporating the above design parameters. Where it was important — such as in the response of the BaF_2 calorimeter to isolated-photon candidates from multiple π^0's and to hadronic energy, muon energy losses in the calorimeter, and issues related to forward coverage and $\not{E}_T$ — full GEANT simulations have been used to deduce the parameterizations.

3.2 Search for the Standard-Model Higgs Boson

Question 1: How would you observe a Higgs boson in the following mass regions: 80 < M_H < 180 GeV, M_H = 200 GeV, 400 GeV, 800 GeV? Please address the signals, backgrounds, and triggering strategies in each case.

The standard model has been verified to about the 0.1% level. If it is correct, there remains to be found only the top quark and the standard Higgs boson. Theoretical analyses indicate that the top quark lies below 200 GeV, within reach of the Tevatron collider. The assumption that m_t = 140 GeV was used in the analyses for the H^0.

Experiments at LEP II should discover H^0 if it is lighter than 80 GeV. Theoretical arguments indicate that new physics must occur near 1 TeV if $M_H \gtrsim 650$ GeV. Therefore, SSC experiments must cover thoroughly the range M_H = 80–800 GeV to test—or exclude—the Standard Model. If the H^0 is heavier than 800 GeV, it will be so broad that it will not be recognizable as a resonance; special techniques and extended running at ultrahigh luminosity, $\mathcal{L} \gtrsim 10^{34}\text{cm}^{-2}\,\text{s}^{-1}$, will be required to find it.

All signals for the Higgs boson at the SSC involve photons, electrons and muons, each of which must be very well identified and measured if the backgrounds are to be overcome. The GEM detector's design ensures that H^0 can be found in one to two years — if it exists below 800 GeV.

3.2.1 Higgs Search: 80 GeV < M_H < 180 GeV

In this mass range the principal decay modes of the Higgs are $H^0 \to b\bar{b}$, $c\bar{c}$, and $\tau^+\tau^-$. Since these are hopelessly swamped by backgrounds, it is necessary to rely on the rare decays $H^0 \to \gamma\gamma$ and $H^0 \to ZZ^* \to \ell\bar{\ell}\,\ell'\bar{\ell}'$, where $\ell = e, \mu$. The $\gamma\gamma$ mode is useful for 80 GeV < $M_H \lesssim$ 160 GeV and the ZZ^* mode for 140 GeV < M_H < 180 GeV. The $\gamma\gamma$ mode was studied using PYTHIA 5.5 and JETSET 7.3 [2]; the ZZ^* modes were studied using ISAJET 6.36 [3]. In both cases, GEANT-based parameterizations of the detector response were used.

3.2.1.1 $H^0 \to \gamma\gamma$ [4]

The $H^0 \to \gamma\gamma$ cross section at the SSC varies from 50 to 200 fb for 80 < M_H < 160 GeV. There are two very large backgrounds. The irreducible background from $q\bar{q} \to \gamma\gamma$ and $GG \to \gamma\gamma$ has σ = 275 pb for $\hat{p}_T^{\gamma} >$ 20 GeV [5]. The second background is from misidentified jets alone or with single photons. The total rate for jets with $\hat{p}_T >$ 20 GeV is 2 mb, while the total γ - jet rate is 235 nb.

Since the Higgs is very narrow, the signal will be observable provided that the $\gamma\gamma$ mass resolution is $\Delta M_{\gamma\gamma} / M_{\gamma\gamma} \lesssim$ 1%. This requires precision measurement of the photon energies and spatial resolutions of $\lesssim$ 1 mm on the photon vertex and the shower positions. Sufficient energy and shower centroid resolution can be achieved with GEM's proposed BaF_2 or LAr calorimeter. A vertex resolution of 0.5 mm is achievable by using the central tracker to determine charged tracks associated with the $H^0 \to \gamma\gamma$ event.

The real $\gamma\gamma$ background can be reduced by requiring $|\eta_\gamma| < 2.5$, $E_T^{\gamma} > 20$ GeV, $|\cos\theta_\gamma^*| < 0.9$, and $|\eta_{\gamma\gamma}| < 3.0$. After these cuts, the $\gamma\gamma$ cross section was reduced to 42 pb for $M_{\gamma\gamma} > 70$ GeV, while the Higgs signal acceptance was at least 55%.

Backgrounds from QCD jets and γ-jet production were reduced first by isolation cuts. To simulate these cuts, dijet and γ-jet events were generated, and the EM energy and a part of the hadronic energy (determined by GEANT) were deposited in the EM calorimeter cells with parameterized shower spreading. A photon candidate with transverse energy E_T^{photon} was found by summing a 3×3 cluster of cells surrounding the one hit by the photon. Charged particles were tracked through the magnetic field, and any photon cluster hit by a charged particle was rejected. The photon candidate was rejected if it did not pass the calorimetric isolation cut

$$\sum_R E_T - E_T^{photon} \leq E_T^{cut} + 0.1\, E_T^{photon}$$

where the sum is over the E_T of the cells in a cone of size $R = \sqrt{(\Delta\eta)^2 + (\Delta\phi)^2}$ about the photon cell. Based on the expected noise and pileup performance of the BaF_2-plus-scintillator option

and the LAr calorimeter, the following isolation parameters were chosen:

$$R = 0.75 \qquad E_T^{cut} = 5\ \text{GeV} \qquad (BaF_2)$$

$$R = 0.60 \qquad E_T^{cut} = 10\ \text{GeV} \qquad (\text{LAr}).$$

Many of the isolated photon candidates consist of several photons from multiple π^0's. A shower shape analysis was used to reduce these. The mean opening angle, $\bar{\theta} = \sum \theta_i E_i / \sum E_i$ was calculated for each candidate from the energies E_i and angles θ_i of the individual photons. A GEANT simulation showed that isolated-photon candidates from multiple π^0's can be rejected by their shower shape if $\bar{\theta} > 5$ mrad [6]. For LAr, a more restrictive cut at the equivalent of $\bar{\theta} = 1$ mrad was made, as would be appropriate with a preradiator. Alternatively, a calorimetric isolation cut using clustering to reduce the effect of noise in LAr could be implemented, allowing a background rejection similar to that for BaF_2 [4]. These cuts reduced the QCD backgrounds over the range 75 – 165 GeV to:

$$\sigma_{jj} = 20\ \text{pb} \qquad \sigma_{\gamma j} = 21\ \text{pb} \qquad (BaF_2)$$

$$\sigma_{jj} = 20\ \text{pb} \qquad \sigma_{\gamma j} = 24\ \text{pb} \qquad (\text{LAr}).$$

Figure 3.2-1 shows the $M_{\gamma\gamma}$ distribution for M_H = 80, 100, 120 and 150 GeV, after these selections. The significance of the signals is 3.0, 5.5, 9.7 and 9.4 (2.3, 4.3, 7.3 and 7.7) standard deviations for BaF_2 (LAr) in one SSC year.

3.2.1.2 $H^0 \rightarrow Z Z^* \rightarrow \ell^+\ell^- \ell^+\ell^-$ [7]

This process has the best signal-to-background ratio for the mass range M_H = 140–180 GeV. The

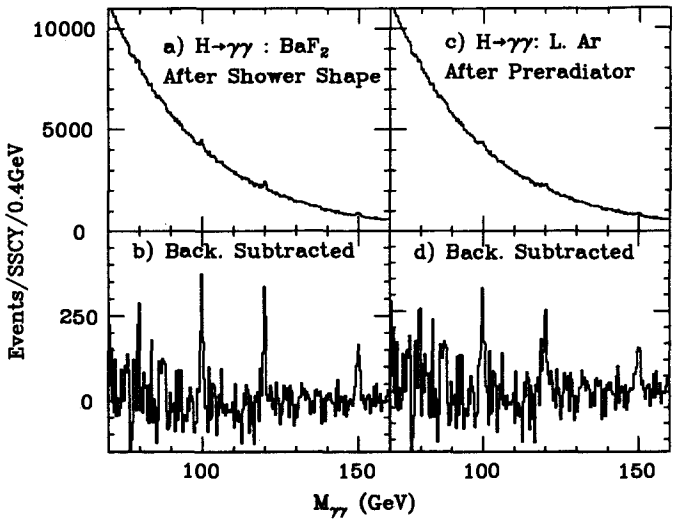

Figure 3.2-1 H → γγ mass distributions and background-subtracted mass distributions for various Higgs masses. Left: BaF_2 calorimeter. Right: LAr calorimeter

principal backgrounds come from QCD jets, $Z\gamma^*$ and $ZQ\bar{Q}$, where $Q = b, t$. Events were required to have four leptons with $p_T > 5$ GeV and $|\eta| < 2.5$, at least two leptons with $p_T > 10$ GeV, and

$$\sum_{R=0.3} E_T - E_T^{\ell} < 5\ \text{GeV} + 0.1\ E_T^{\ell}$$

$$86\ \text{GeV} < M_{\ell_1^+\ell_1^-} < 96\ \text{GeV},$$

$$10\ \text{GeV} < M_{\ell_2^+\ell_2^-} < 90\ \text{GeV}.$$

The acceptance for the Higgs signal is 42%. The QCD backgrounds were rejected by the isolation cut and the $M_{\ell^+\ell^-} > 10$ GeV cut. The remaining backgrounds involving a real Z^0 were rejected mainly by the second mass cut.

The electron simulations were done for the BaF_2 and LAr options. The uncertainties on the event vertex and shower position were assumed to be σ_z = 1 mm. Calorimeter cracks were not taken into account [8]. To show the advantage of GEM's precision EM calorimeter, simulations for a "sampling" calorimeter with resolution $\Delta E / E = 15\% / \sqrt{E} \oplus 1\%$ were also performed.

The muon simulations used the GEM baseline muon system; muon energy losses in the calorimeter were taken into account. It is assumed that the central tracker can determine the event vertex with σ_z = 1 mm and the track angle to within a few mrad. If the angular information from the central tracker is lost at $\mathcal{L} = 10^{34}$ cm^{-2} s^{-1} and only the muon chambers can be used, the mass resolution for $H^0 \rightarrow ZZ^* \rightarrow \mu^+\mu^-\mu^+\mu^-$ becomes only 5–7% worse.

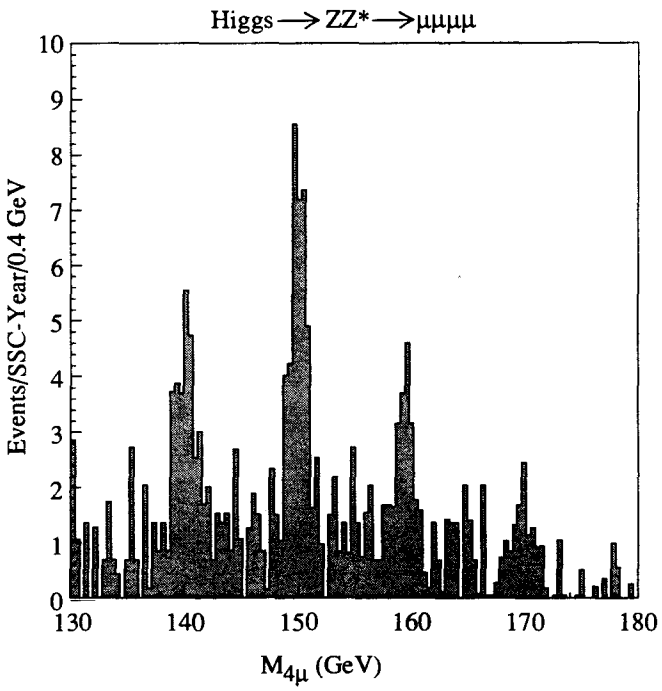

Figure 3.2-2 Mass distribution for H → ZZ* → $\mu^+\mu^-\mu^+\mu^-$ (M_H = 140, 150, 160, 170 GeV)

The signals and backgrounds in the four-muon mode are shown in figure 3.2-2, for M_H = 140, 150, 160 and 170 GeV for a standard SSC year. The four-electron channel is shown in figure 3.2-3 for the BaF_2 option, the LAr option, and the "sampling" calorimeter. The $e^+e^-\mu^+\mu^-$ resolution is also excellent. For $M_H \approx$ 170 GeV it is important to be able to search in all the four-lepton channels; discovery in any one channel alone would require several year's running at nominal luminosity.

3.2.2 Higgs Search: 200 GeV < M_H < 600 GeV

In this mass range, the "gold-plated" signals $H^0 \rightarrow Z^0Z^0 \rightarrow \ell_1^+\ell_1^-\ell_2^+\ell_2^-$, where ℓ = e and μ, can be used. The backgrounds come from hadronic jets, heavy quark decays, and $W^\pm$ and Z^0 production. These were reduced to below the $q\bar{q} \rightarrow Z^0Z^0$ background by the same cuts as for the ZZ^* mode plus the requirement $|M_{\ell\ell} - M_Z| < 5$ GeV. GEM's resolutions permit such a stringent cut. At M_H = 200 GeV, the EM calorimeter resolution has little effect on the 4 ℓ mass distribution if the Z^0 mass constraint is used. At 400 GeV and higher masses, the Higgs boson's natural width makes the two EM resolutions indistinguishable. The mass distributions for the sum of the lepton channels are shown in figure 3.2-4 for M_H = 200, 400 and 600 GeV for the BaF_2 EM calorimeter [1].

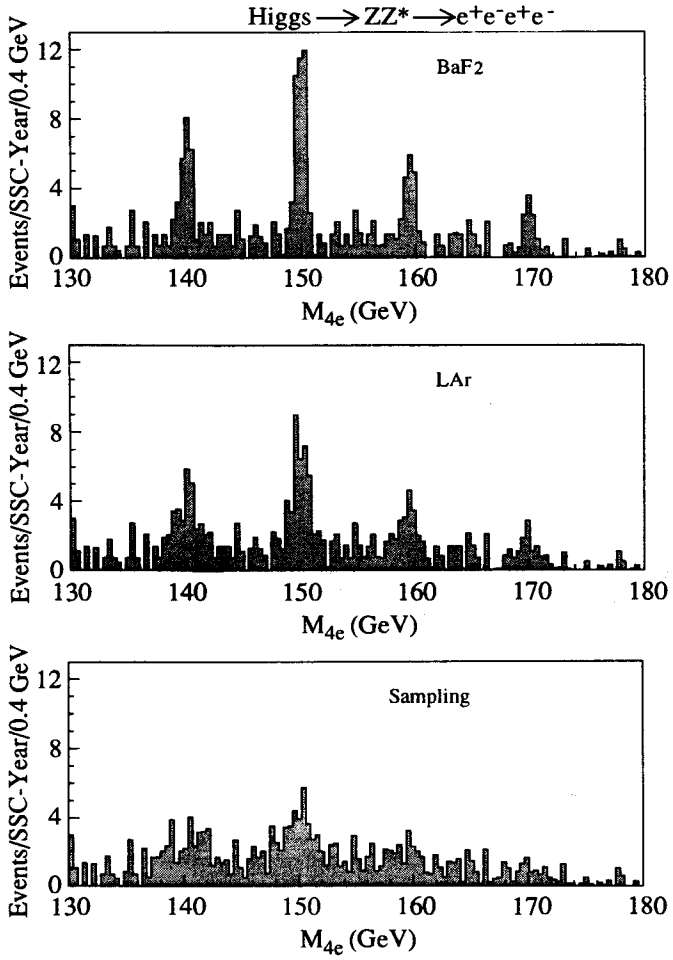

Figure 3.2-3 Mass distributions for $H \rightarrow ZZ^* \rightarrow e^+e^-e^+e^-$.(a) BaF_2; (b) Liquid Argon; (c) "Sampling" calorimetry (M_H = 140, 150, 160, 170 GeV)

3.2.3 Higgs Search: $M_H = 800$ GeV

At M_H = 800 GeV, the Higgs width is 260 GeV. The cleanest signal is still $H^0 \rightarrow Z^0Z^0 \rightarrow \ell_1^+\ell_1^- \ell_2^+\ell_2^-$ but the rate is quite low. With the same event selections as for lower masses, 40 signal events over a background of 13 were obtained in the range 600 GeV < $M_{4\ell}$ < 1000 GeV (see figure 3.2-4d) [1]. While this might be adequate for discovery, confirmation in other modes clearly is desirable. Therefore, the modes $H^0 \rightarrow Z^0Z^0 \rightarrow \ell^+\ell^- jet\ jet$ and $\ell^+\ell^-\nu\bar{\nu}$, which have larger signals, were also considered.

3.2.3.1 $H^0 \rightarrow \ell^+\ell^- jj$ [9]

By far the largest background to this process comes from Z^0-production with associated jets. Because the jets have high p_T and low invariant mass, it is a good approximation to simulate this background by the Z^0 + jet process. This was done using ISAJET 6.43. Events were selected by requiring:

- Two isolated leptons (each with $E_T^{cut} = 5$ GeV within a cone of R = 0.3) with $|\eta| < 2.5$ and $p_T > 50$ GeV, satisfying $|M_{\ell\ell} - M_Z| < 5$ GeV and $p_T^{\ell\ell} > 200$ GeV.
- At least two jets defined with narrow cones, R = 0.2, each with $|\eta| < 3.0$ and $p_T > 50$ GeV, satisfying $|M_{jj} - M_Z| < 10$ GeV and $p_T^{jj} > 250$ GeV.
- $M_{\ell\ell jj} = 800 \pm 150$ GeV.

The details of the $Z^0 \rightarrow$ jet-jet reconstruction are discussed in section 3.5. The Higgs signal and background for one SSC year are shown in figure 3.2-5. There are 235 signal events over a background of 780. The background may be determined by studying the sidebands, 71 GeV < M_{jj} < 81 GeV and 101 GeV < M_{jj} < 111 GeV. The statistical error on the mass determination is about 7 GeV. The mean of the background-subtracted distribution, however, is at 850 GeV, due to systematic variation of the acceptance. It would be necessary to understand this shift to 10% to make the systematic error smaller than the statistical one.A more realistic goal of 20–50% would result in a systematic error of 10–25 GeV.

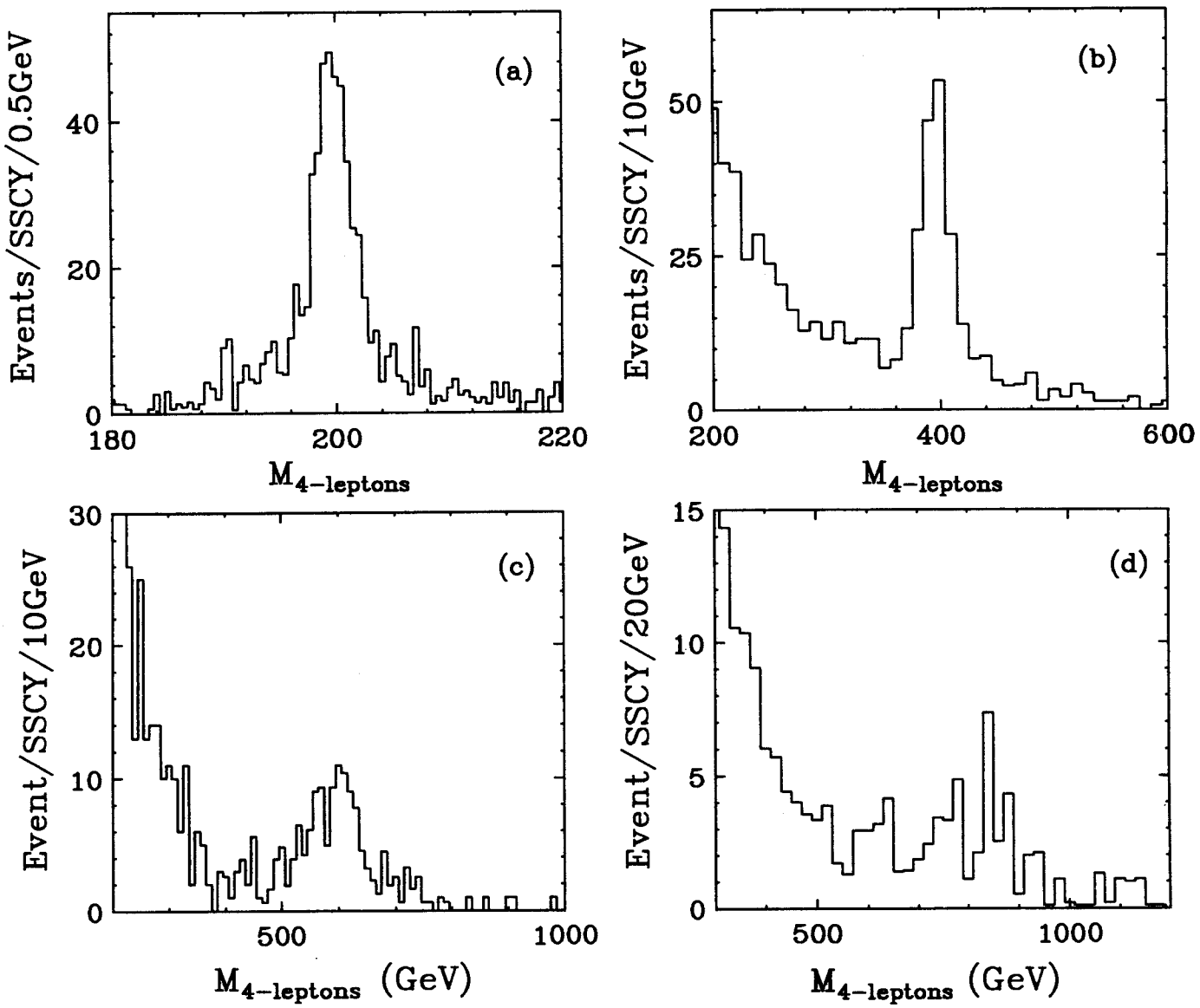

Figure 3.2-4 Mass distributions for H $\rightarrow$ $\ell\ell^-\ell'\ell'^-$ and background summed over $\ell = e$ and μ for (a) M_H = 200, (b) 400, (c) 600, and (d) 800 GeV.

3.2.3.2 $H^0 \rightarrow \ell\ell^-\nu\bar{\nu}$ [10]

The most important background for $H^0 \rightarrow \ell\ell^-\nu\bar{\nu}$ comes from Z^0 + jets. ISAJET was used to generate 600 k background events in six p_T ranges, from 50 to 3600 GeV. The detector response to these events was simulated incorporating the following effects:

- η_{max} for hadron calorimetry coverage was varied over the range 3.0–5.5.
- The effect of the transition between the end cap and forward calorimeters at $|\eta| = 3$ was studied using a GEANT shower library for the forward region, $2.5 < |\eta| < 5.0$, with the forward calorimeter 6 m from the interaction point [11].

- The effect of the e/h response of the calorimeter was studied using a parameterization for LAr (with $e/h = 1$) and for BaF_2 plus spaghetti (with $1 \leq e/h \leq 2$) [12].

In addition to lepton cuts similar to those used for other channels, events were required to have no jet (defined by R = 0.7) with $p_T > 50$ GeV in the ϕ-cone 180° ± 45° opposite the reconstructed Z^0. This removes events in which E_T is carried away by neutrinos.

The background for various rapidity coverages is shown in figure 3.2-6 for one SSC year. The background is insensitive to $\eta_{max} \geq 4.0$ for $M_H \geq 600$ GeV. The effect of the calorimeter response is insignificant for $1.0 \leq e/h \leq 2.0$. Figure 3.2-7 shows the signal and background for $M_H = 800$ GeV and $\eta_{max} = 5.0$. There are 50 signal events over a background of 34 with 250 GeV < $\not{E}_T$ < 500 GeV.

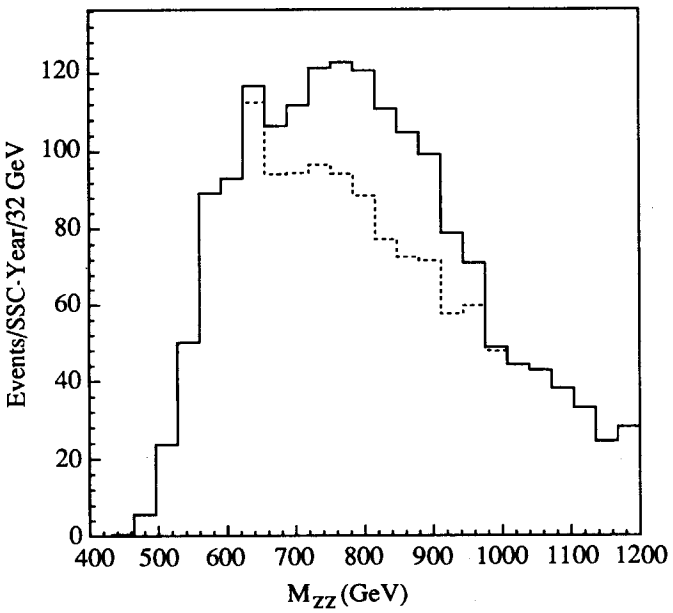

Figure 3.2-5 Signal and background for $H \rightarrow \ell^+\ell^- jj$ with $M_H = 800$ GeV

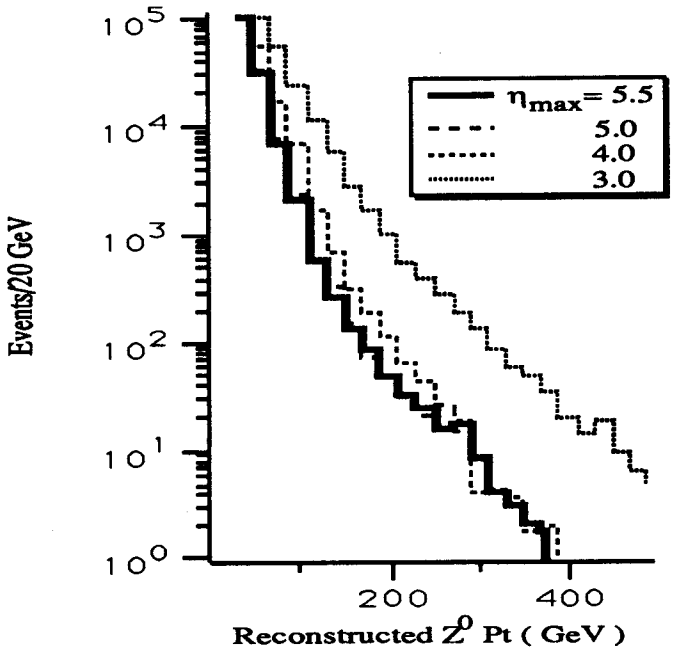

Figure 3.2-6 Background from unbalanced Z^0 for $H \rightarrow \ell^+\ell^- \nu\bar{\nu}$, for various values of η_{max}, for one SSC year

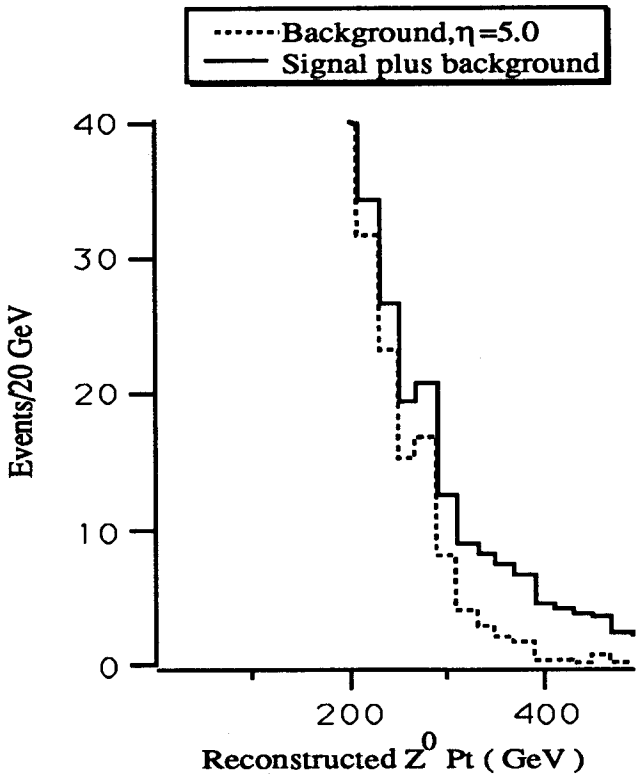

Figure 3.2-7 Signal and background for $H \rightarrow \ell^+\ell^- \nu\bar{\nu}$ with $M_H = 800$ GeV and $\eta_{max} = 5.0$, for one SSC year

3.2.4 Higgs Search Trigger Strategies

The details of the GEM trigger strategies are presented in section 2.6. Here, the strategies most crucial for the Higgs search modes involving photons, electrons and muons are briefly outlined. Recall that the E_T and p_T cuts used for the various Higgs searches were:

$H^0 \rightarrow \gamma\gamma$	$E_T > 20$ GeV
$H^0 \rightarrow ZZ^*$	≥ 4 leptons with $p_T^l > 5$ GeV ≥ 2 leptons with $p_T > 10$ GeV
H^0 (800 GeV)	$p_T^l > 50$ GeV $p_T^{\mu} > 200$ GeV

3.2.4.1 Photons and Electrons

The Level 1 (L1) trigger for $H^0 \rightarrow \gamma\gamma$ and $H^0 \rightarrow e^+e^-e^+e^-$ requires at least one EM cell with $E_T >$ 50 GeV or at least two cells with $E_T > 16$ GeV. The strategy for reducing the L1 trigger rate while maintaining high efficiency for the signals is to use matching electromagnetic and hadron calorimetry (ECAL and HCAL) groups. Typically, an ECAL group covers $\Delta\eta \times \Delta\phi = 0.2 \times 0.2$, i.e., 5×5 ECAL cells. Each ECAL group is matched with an overlapping HCAL tower behind it. An HCAL veto, requiring that E_T(HCAL tower) < $0.1 \cdot E_T$(ECAL group), is used to reject the QCD background. This L1 trigger reduces the QCD background to 10–20 kHz, while its efficiency for the Higgs signals is better than 85%.

The L2 trigger uses calorimeter information to require that each cluster satisfy:

1. The ratio of the sums $E(3 \times 3) / E(5 \times 5) > 0.9$, where $E(n \times n)$ is a sum over the highest-energy EM cell and the n^2-1 cells surrounding it.
2. An isolation cut which sums up the excess E_T within $R < 0.3$ and requires that it be less than 10 GeV.

This reduces the L2 rate to a few hundred hertz.

3.2.4.2 Muons

GEM's measurement of muons outside the calorimeter where particle rates are low means that it can trigger efficiently on both relatively low-p_T muons at $\mathcal{L} = 10^{33}\text{cm}^{-2}\text{s}^{-1}$ and moderately high-p_T muons from TeV -scale sources at $\mathcal{L} = 10^{34}\text{cm}^{-2}\text{s}^{-1}$. The raw muon rates for $|\eta| <$ 2.5 at $\mathcal{L} = 10^{33}\text{cm}^{-2}\text{s}^{-1}$ have been computed from minimum bias events, QCD dijets, $t\bar{t}$ production, $W^{\pm}$ + X, Z^0 + X and Drell-Yan production of $\mu^+\mu^-$; they are shown in table 3.2-1 for several values of p_T.

Table 3.2-1 Muon Production Rates at $\mathcal{L} = 10^{33}\text{cm}^{-2}\text{s}^{-1}$

p_T^{μ} (GeV)	N_{μ} (Hz)	$N_{\mu\mu}$ (Hz)
5	9.1k	88
10	1.9k	17
20	280	5.0

The L1 trigger will be designed to require one muon with $p_T > 20$ GeV or two muons with $p_T >$ 10 GeV. The hits in the barrel muon chamber drift tubes or the forward chamber pads can be combined to form a crude p_T cut for the L1 trigger which ranges down from about 50 GeV. At $\mathcal{L} = 10^{33}\text{cm}^{-2}\text{s}^{-1}$ and for $|\eta| < 2.5$, an L1 rate of about 3 kHz (1kHz) for a p_T cut of 20 GeV (50

GeV) is expected. An actual p_T measurement is made by the L2 trigger. The L2 rates are about 1 kHz and 100 Hz for p_T cuts of 20 GeV and 50 GeV. At Level 3, a close-to-final measurement of p_T^{μ} is made and a rate of only a few hertz is expected for $M_{\mu\mu} = M_Z \pm 5$ GeV.

3.3 Top-Quark Physics

Question 2: Assume a top quark with a mass of 250 GeV. How is it discovered in your detector? How accurately could the mass be measured? Can its decay properties be determined? For example, if the top decays to a charged Higgs with a mass of 150 GeV, at what branching ratio level can this process be detected?

The top quark will be important at the SSC for its own sake and as a background and signal for new physics. Therefore, it is important to study top production in detail, a task for which GEM is very well suited.

GEM can exploit the large $t\bar{t}$ cross section and then rely on its muon and calorimeter systems to discover and weigh the top by several methods. The simplest analysis relies on finding isolated $e^{\pm}\mu^{\mp}$ events from W^+ and W^- decays, with events tagged by inclusive muons from b-quarks [1]. If the theoretical error on the cross section is 50%, as seems plausible, then the rate for these events determines m_t to about 10%. Various distributions, such as $M_{e\mu}$, may be used to determine m_t. A more refined mass determination involves tagging both an isolated lepton and an inclusive muon from one t-decay and then reconstructing the recoiling trijet system from $t \rightarrow W^+b$ [1].

3.3.1 Top-Quark Discovery and Mass Determination

Because the $t\bar{t}$ rate is so large for $m_t = 250$ GeV, a new method that gives a very good signal-to-background ratio by cutting harder on the events is described here. The only significant background in this method is $W^{\pm}$ + jets production. $t\bar{t}$ events and background were generated using ISAJET 6.43. The detector response was simulated incorporating the GEM segmentation and resolution. Events were selected having an isolated electron or muon with $p_T > 30$ GeV and at least four jets with $p_T > 50$ GeV found using a narrow cone, R = 0.2. Only the four highest-p_T jets found were used in the analysis. The jet cones were then expanded to R = 0.7 to determine the jet energies. The reason for using this two-step process is to distinguish three jets from a top quark even when they are somewhat overlapping. The lepton plus the nearest jet were required to be within R = 2.0, and to have $|\vec{p}_T^{\,l} + \vec{p}_T^{\,jet}| > 250$ GeV, thus forcing the top to be produced at high p_T.

After one jet had been associated with the lepton, the three remaining jets were identified with the recoil t or $\bar{t}$, provided that they were within R = 1. They were required to have a combined $p_T > 350$ GeV, and to satisfy $E_T(R = 1.0) / E_T(R = 1.3) > 0.95$, consistent with the expected noise and pileup for either calorimeter option.

After these cuts, the masses of all pairs of jets in the recoil system and the mass of the whole recoil system (R < 1.0) were calculated. The pair mass, figure 3.3-1, shows a narrow peak slightly higher than the W mass. The full mass, figure 3.3-2,

shows a peak close to the assumed top quark mass with Δm = 13 GeV and very little background. The background is dominated by combinatorial effects of the $t\bar{t}$ events themselves, although the $W^{\pm}$ + jets background also contributes.

These selection criteria are quite restrictive, but since the $t\bar{t}$ cross section is large, the accepted cross section after all cuts is still 1 pb. The signal-to-background ratio is substantially better than the SDC analysis [13] using a vertex detector tag and is comparable to the L* analysis using a double muon tag of a b jet [14]. The statistical error on the top mass is negligible. The error will be limited by how well systematic effects are understood. The calorimeter resolution and jet reconstruction can be checked by looking at the $W^{\pm} \rightarrow q\bar{q}'$ mass, and the effects of higher-order QCD processes and the underlying event can be studied by making a similar selection for $e^{\pm}\mu^{\mp}$ decays. Given all these handles and the small mass shifts found in this simulation, it appears that m_t can be determined to a few GeV.

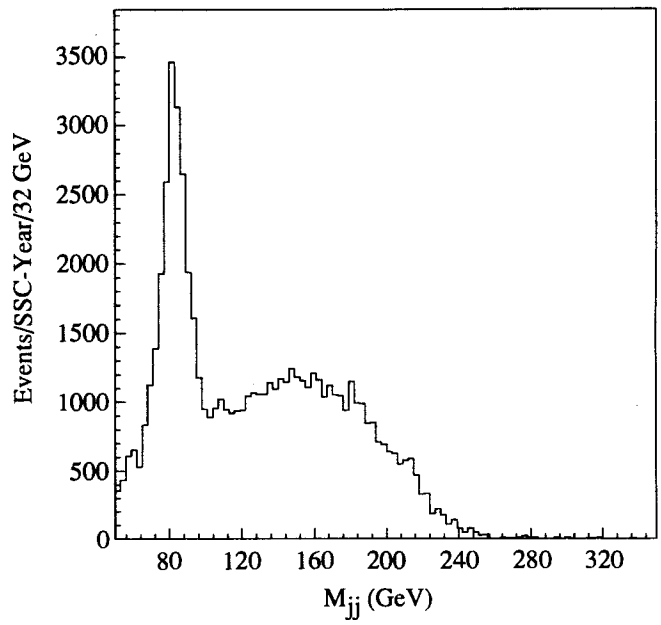

Figure 3.3-1 Reconstructed $W^{\pm} \rightarrow jj$ mass distribution and background with high-p_T top selection

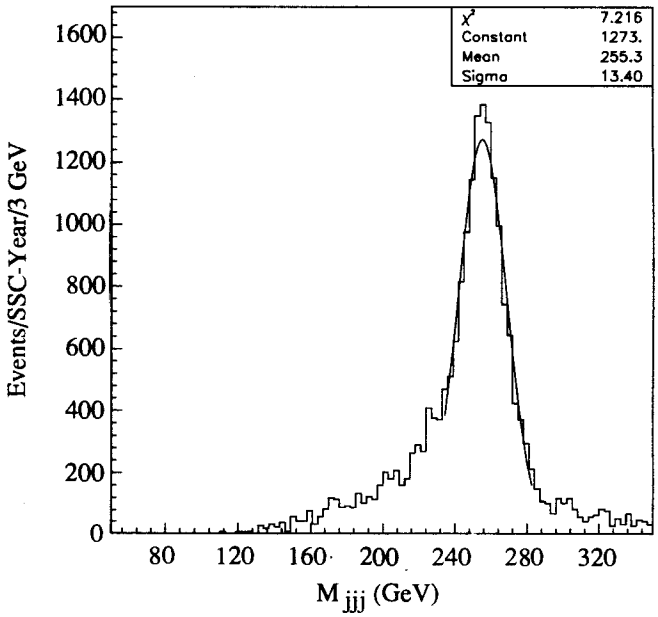

Figure 3.3-2 Reconstructed $t \rightarrow jjj$ mass distribution and background with high-p_T top selection

3.3.2 Top Decays: $t \rightarrow H^+ b$

If there is a charged Higgs boson lighter than the top quark, then the standard decay $t \rightarrow W^+ b$ and the nonstandard decay $t \rightarrow H^+ b$ are expected to be comparable. The H^+ is expected to decay either into $c\bar{s}$ or $\tau^+\nu$.

The method for detecting and reconstructing $t \rightarrow H^+ b$, with $H^+ \rightarrow c\bar{s}$, is similar to that just discussed for $t \rightarrow W^+ b$. Top events with one standard semileptonic decay and one charged Higgs decay were generated assuming m_t = 250 GeV and M_H = 150 GeV. Events were

selected as described above. In addition, the event is vetoed if any dijet mass satisfied 60 GeV < M_{jj} < 100 GeV. This removed events in which both top quarks decayed to W*b*. The reconstructed dijet mass distribution is shown in figure 3.3-3, assuming branching ratio $B(t \rightarrow H^+ b) \cdot B(H^+ \rightarrow c\bar{s}) = 1\%$. This is to be compared with the dijet mass distribution for standard model decays, after the M_{jj} cut, also shown in figure 3.3-3. A 1% branching ratio gives a 9.5σ (statistical) effect with 510 events on a background of 2860 in 128 GeV < M_{jj} < 172 GeV.

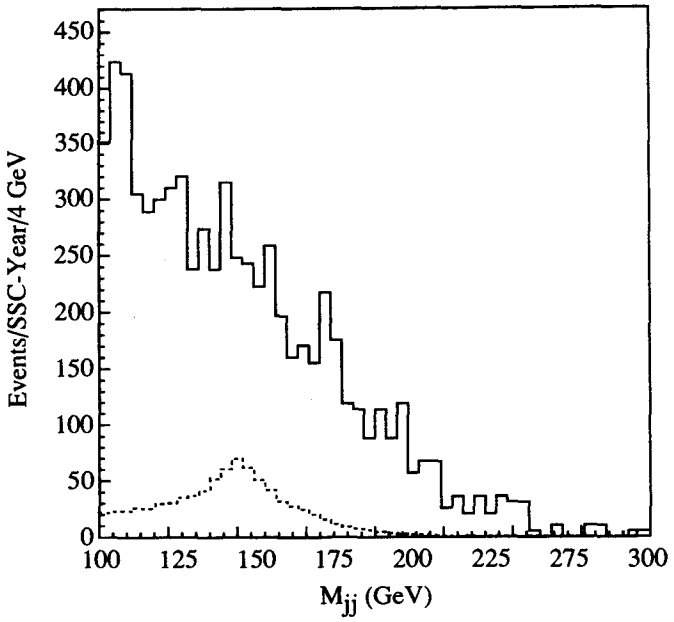

Figure 3.3-3 Reconstructed dijet mass distributions from *t*-decays with $M_{jj} = M_W \pm 20$ GeV veto. Dotted: $t \rightarrow H^+ b$ with a 1% combined branching ratio. Solid: $t \rightarrow W^+ b$ (with limited Monte Carlo statistics)

If $H^+ \rightarrow \tau^+ \nu$ is the charged Higgs' dominant decay mode, one must trigger on one semileptonic top decay and look for violations of $e-\mu-\tau$ universality in the other decay. The $\tau \rightarrow \pi\nu$ decay should be well identified in GEM using the vertex detector to see a displaced vertex and requiring a match between the hadronic energy in the calorimeter and the momentum of the single track. About 2% of the $\tau \rightarrow \pi\nu$ decays are found to give a pion with $p_T > 50$ GeV. Therefore, a 2% combined branching ratio $B(t \rightarrow H^+ b) \cdot B(H^+ \rightarrow \tau^+ \nu)$ would give a statistically significant signal of 400 events on a background of 2000.

3.4 Missing Energy Signals

Question 3: To demonstrate the missing E_T capability of your experiment, show the discovery capability for: (a) A 400 GeV quark which decays to b+W; (b) A 300 GeV gluino. For purposes of background calculations assume a top mass of 150 GeV. Include the effects of initial state gluon radiation, missing muons and neutrinos, pileup, and clustering uncertainties.

Detector-induced backgrounds for missing transverse energy ($\not{E}_T$) have been studied using a combination of idealized calorimeter simulations and full GEANT shower simulations. The idealized calorimeter, with uniform segmentation $\Delta\eta = \Delta\phi = 0.1$ for $\eta < 6$ and perfect energy resolution, was used to study $\not{E}_T$ distributions for 20000 jet events generated with ISAJET 6.43 for 50 GeV < p_T^{jet} < 800 GeV. A UA1-type jet algorithm with a cone R = 0.7 was used to find clusters with $E_T > 10$ GeV. Figure 3.4.1 shows the $\not{E}_T$ distributions calculated using the whole calorimeter and using the sums of clusters in various η intervals. Evidently, for $\not{E}_T \gtrsim 100$ GeV, it is sufficient to sum clusters, implying that pileup of soft events is not very important. Also, covering $\eta \lesssim 5$ avoids dominance of the cross section for $\not{E}_T \gtrsim 100$ GeV by backgrounds from detector effects. Less η coverage is sufficient for

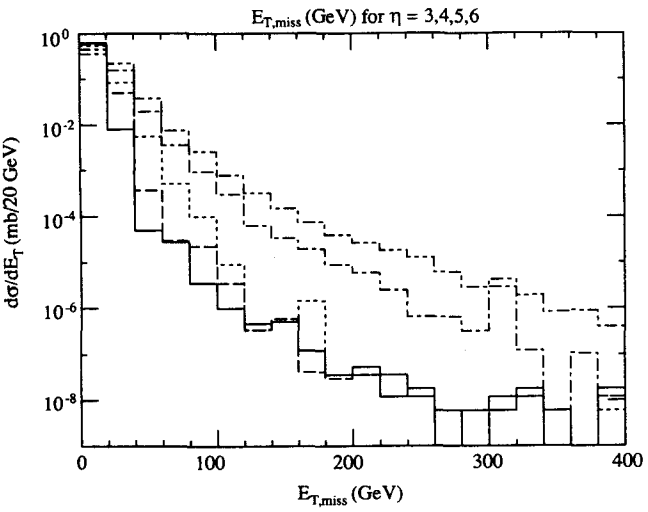

Figure 3.4-1 $\not\!\!E_T$ distributions for an idealized calorimeter. Solid curve: sum of calorimeter, essentially the sum of the neutrinos. Broken curves: sums of clusters with E_T > 10GeV and η < 6, 5, 4, and 3 in order as curves are higher

larger $\not\!\!E_T$ or to measure $\not\!\!E_T$ in selected events, as illustrated in the t' analysis.

Full GEANT shower simulations have been carried out to study the contribution of the edge at $\eta \approx 3.0$ between the endcap and forward calorimeters [11]. This effect, which was included in the gluino study does not give a dominant contribution to the $\not\!\!E_T$ distribution. Full simulations have also been carried out to determine the p_T resolution of the forward calorimeter, with the result that $\Delta p_T / p_T < 10\%$ for particles whose showers are contained [10]. This resolution was added to the idealized calorimeter for clusters with $\eta > 3$. It was found to increase the $\not\!\!E_T$ cross section by less than a factor of two for $\not\!\!E_T \gtrsim 50$ GeV, decreasing at larger $\not\!\!E_T$ [15]. It is expected that more complex signatures which rely mainly on $\not\!\!E_T$ to reject the background will require similar η coverage.

3.4.1 Search for $t' \rightarrow Wb$, $m_{t'} = 400$ GeV [16]

If a 400 GeV heavy quark decays dominantly into $W^+ b$, then its signatures are similar to the t, which is the dominant background. ISAJET was used to generate $t'\bar{t}'$ and $t\bar{t}$ events with 50 GeV < p_T < 800 GeV; the cross sections are 200 pb and 10 nb respectively. The detector response was simulated using the GEM calorimeter resolution and segmentation, with coverage extending either to $\eta_{max} = 3$ or to $\eta_{max} = 5$. Events were selected containing one isolated lepton with $p_T^{\ell} > 150$ GeV and $|\eta| < 2.5$, $\not\!\!E_T > 100$ GeV, and four jets with $p_T > 50$ GeV in R = 0.7 and $|\eta| < 2.5$. Then the t' mass was determined either by combining the $W^{\pm} \rightarrow \ell^{\pm}\nu$ momentum with that of a jet or by reconstructing the jets from the other t'.

The $W^{\pm} \rightarrow \ell^{\pm}\nu$ can be reconstructed using the two components of $\not\!\!E_T$ plus the constraint of the $W^{\pm}$ mass to calculate $\vec{p}_\nu$. The $W^{\pm}$ was required to have $p_T^W > 200$ GeV and $|\eta_W| < 1.5$; both solutions of the quadratic equation were used. It was then combined with any of the four jets satisfying $\cos(\phi_W - \phi_j) > -0.8$ to form the mass. Even calorimeter coverage for $|\eta| < 3$ gives sufficient resolution to produce a peak at about 388 GeV with a full width of 46 GeV, as shown in figure 3.4.2. The background under the peak is dominated by combinatorial background from the $t'\bar{t}'$ events rather than by $t\bar{t}$ or $W^{\pm}$+ n-jet events. If the calorimeter extends to $|\eta| = 5$, then the width is reduced to 34 GeV.

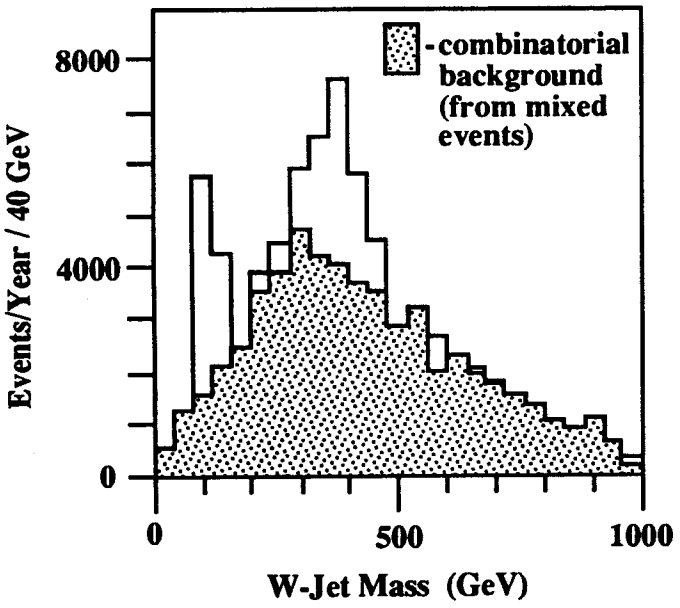

Figure 3.4-2 Reconstructed combined mass of $W^{\pm} \rightarrow \ell^{\pm} \nu$ plus a jet from t' decay and background

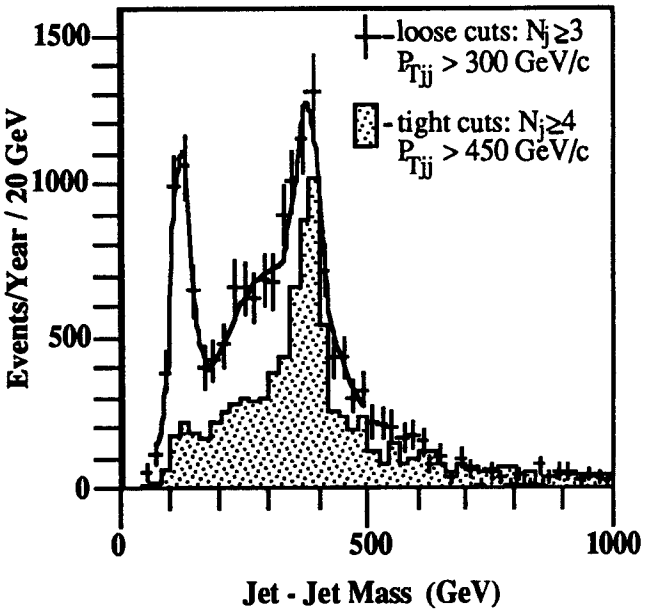

Figure 3.4-3 Two jet mass distribution from $t' \rightarrow Wj$ with $W \rightarrow jj$ reconstructed as one jet

The more direct approach is to select as before a leptonic decay, missing energy, and at least three jets, and to reconstruct the mass of the recoiling jets. The $W \rightarrow jj$ is found as a single jet with R = 0.7 and combined with the other highest p_T jet. The combined system is required to have $p_T > 450$ GeV to reduce the combinatorial background. These cuts left 0.2 pb of the t' signal. The resulting mass distribution (figure 3.4-3), shows a clean peak at 378 GeV with a width $\sigma_M \approx 25$ GeV. As for the t, the error on the t' mass will be limited by systematics at the few GeV level. Comparing the rates and distributions for the two analyses could provide a first hint of nonstandard t' decays.

3.4.2 Search for Gluinos, $m_{\tilde{g}} = 300$ GeV [17]

For this analysis, the minimal supersymmetric extension of the standard model [18], with two Higgs doublets and superpartners for all the normal particles, was assumed. Since there is a conserved R-parity, the gluinos cascade down to the lightest supersymmetric particle, $\tilde{\chi}_1^0$, which is stable and escapes the detector, giving the characteristic $\not{E}_T$ signature of supersymmetry. It was assumed that squarks are heavier than the gluino. Then all gluino decays are calculable in terms of three parameters, the gluino mass $m_{\tilde{g}}$, a supersymmetric Higgs mass μ, and $\tan \beta = v_2 / v_1$. For this analysis, $m_{\tilde{g}} = 300$ GeV, $\mu = -300$ GeV, and $\tan \beta = 2$ were chosen.

The physics backgrounds to the $\not{E}_T$ signature are heavy quark production and $W^{\pm}$ and Z^0 production at high p_T. Signal and background events were generated with ISAJET 6.43 and put through a calorimeter simulation incorporating the GEM segmentation and covering $|\eta| < 5$. The energy resolution was calculated taking into account dead material from a detailed design of the EMPACT/TEXAS liquid argon calorimeter, including the cracks at $|\eta| \approx 1.5$ between the

barrel and endcaps. The resolution for the GEM liquid argon calorimeter is expected to be similar. The effect of the transition at $|\eta| = 3$ between the endcap and forward calorimeters was also included, based on a parameterization of a full GEANT shower simulation of single particles in this region. Shower spreading was not explicitly included elsewhere, but a separate GEANT simulation showed that shower spreading in the forward calorimeter gives $\Delta p_T / p_T \lesssim 10\%$; this does not dominate the overall observed $\not{E}_T$ distribution [10,15]. Hence, the backgrounds found by this analysis are believed to be realistic.

Jets were found using the UA1 cluster algorithm with R = 0.7. Events were selected having at least 5 jets with $E_T > 75$ GeV and $|\eta| < 3$, a transverse sphericity $S_T > 0.2$, and no muons or isolated electrons with $p_T > 20$ GeV and $|\eta| < 2.5$. While it is important to study leptonic decays of gluinos, the lepton veto improves the signal/background ratio, presumably by removing $t\bar{t}$ events. The $\not{E}_T$ cross sections for the signal and the backgrounds after these cuts are shown in figure 3.4.4. This signal should be quite convincing after careful study of the heavy quark and $W^{\pm}$ and Z^0 backgrounds.

Since the gluino is a Majorana fermion, gluino pairs give substantial cross sections for isolated like-sign dileptons, 110 pb for the case considered. The standard model physics backgrounds, including $t\bar{t}$ and $W^{\pm}W^{\pm}$ events, have been shown to be small [19]. Thus, only detector-induced backgrounds were considered here. The momenta of the muons are easily measured. For

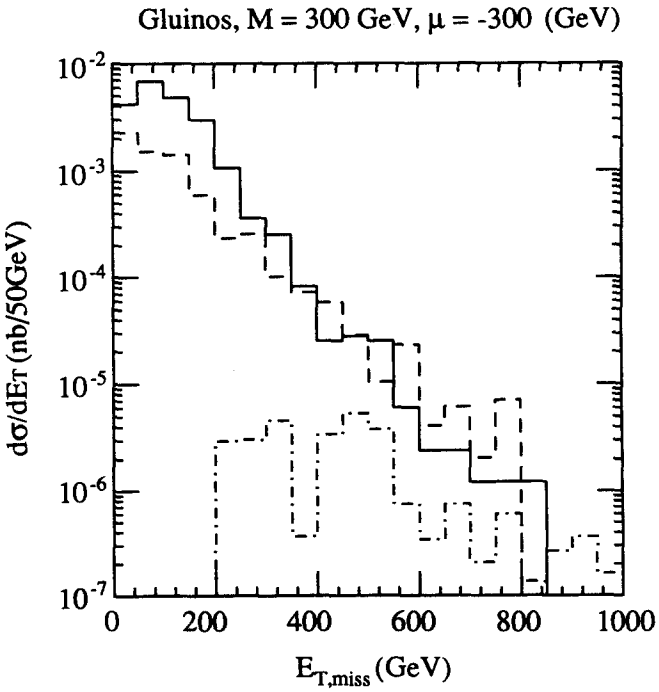

Figure 3.4-4 $\not{E}_T$ signal after cuts for 300 GeV gluino and backgrounds. Solid: gluinos. Dashed: heavy quarks. Dotted: $Z^0 \rightarrow \nu\bar{\nu}$

the electrons, the central tracker resolution is taken to be Gaussian in $1 / p_T$ with

$$\frac{\Delta(1/p_T)}{(1/p_T)} = \varepsilon p_T \qquad \eta < \eta_0$$

$$\frac{\Delta(1/p_T)}{(1/p_T)} = \varepsilon p_T \left(\frac{\sin\theta_0}{\sin\theta}\right)^2 \qquad \eta > \eta_0$$

where $\varepsilon = 2 \times 10^{-3}\,\mathrm{GeV}^{-1}$ and $\eta_0 = -\ln\tan(\theta_0/2) = 1.5$. The significance of the sign determination, $S = (1/p_T) / \Delta(1/p_T)$, is plotted in figure 3.4.5 for electrons from gluino events. The signs of about 90% of the highest-p_T electrons and almost all of the next-highest ones are determined to 3σ or better. Even if the gluino mass were $\mathcal{O}$(1 TeV), the GEM central tracker would still be useful.

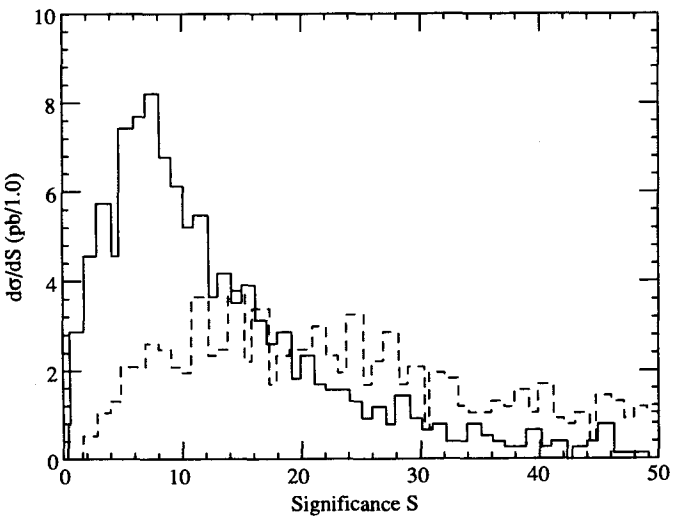

Figure 3.4-5 Significance of sign determination for like-sign electrons from 300 GeV gluinos. Solid: highest-p_T electrons. Dashed: next highest-p_T electrons

3.5 Jet Energy Resolution

Question 4: Demonstrate the jet energy measurement of your proposed detector by studying the decays (a) $Z^0 \rightarrow$ jet + jet (specify the Z^0 production model used); (b) $Z^{0\prime} \rightarrow$ jet + jet ($M_{Z'} = 1$ TeV; assume standard couplings).

The effect of the GEM calorimeter's energy resolution and segmentation on dijet mass resolution was studied for the processes $Z^0 \rightarrow$ jet + jet and $Z^{0\prime} \rightarrow$ jet + jet where the Z^0 came from the decay of a heavy Higgs particle and a $Z^{0\prime}$ mass of 1 TeV was assumed. It was found that a major contribution to the jet-jet mass resolution is "intrinsic" to the measurement of jets in a calorimeter and that the proposed calorimeter options do not seriously degrade the resolution that could be achieved with a perfect calorimeter.

Both GEM electromagnetic calorimeter options have good energy resolution for photons and electrons. For single hadrons, GEANT studies of the proposed systems have shown that a resolution of $50\% / \sqrt{E} \oplus 2\%$ can be achieved. This is consistent with test beam results obtained for spaghetti and liquid argon calorimeters. The GEM calorimeter is designed to have a transverse segmentation, both in η and in ϕ, of 0.04 in the electromagnetic section and 0.08 in the hadronic section. It has been shown that this segmentation has little effect on mass resolution once account is taken of transverse shower spreading in the calorimeter [20].

The calorimeters proposed by GEM are not perfectly compensating. This is particularly true in the nonsampling electromagnetic section (BaF_2). Recent GEANT studies have yielded a 2% constant term for jets as long as the backup hadronic calorimeter is nearly compensating. While this result must be verified in future test beam studies, it seems that the effect of a noncompensating electromagnetic section may not be very severe. We will include this additional 2% constant term below to give our best estimate of the effect of a noncompensating calorimeter.

3.5.1 Mass Resolution in $Z^0 \rightarrow$ jet + jet [9]

The study of $Z^0 \rightarrow$ jet + jet used Z^0's from the decay of 800 GeV Higgs particles, $H^0 \rightarrow l\bar{l}q\ \bar{q}$. This gives energy and p_T distributions for the Z^0's which are relevant to SSC physics processes. Events were produced using ISAJET 6.43. (The Z^0 line width is not included in this generator.) The

selection of the $H^0 \rightarrow \ell^+\ell^- q\bar{q}$ events was described in Sec. 3.2.4. Recall that in addition to the $Z^0 \rightarrow \ell^+\ell^-$ selections, two jets with $p_T > 50$ GeV in narrow cones, R = 0.2, were required. The cones were then expanded to R = 0.7, and the sum of the two jets was required to have $p_T > 250$ GeV. The dijet mass was calculated by summing the four-momenta in a cone R = 0.7 around the sum of the jet pair, treating calorimeter hits as massless particles. Events were vetoed if the extra energy between R = 0.7 and R = 1.0 around this axis was greater than 5% of the total.

With the above mass reconstruction method, three important effects, "intrinsic" to the measurement of jets with a calorimeter, contribute to the resolution:

1. Energy carried away by undetectable neutrinos;
2. Hadrons from the fragmentation of a quark falling outside the cone which defines a reconstructed jet;
3. Particles from the underlying event falling within the jet defining cone.

The mass resolution achieved by the above method with a perfect calorimeter is 2.6 GeV. Effects 2 and 3, which arise from the difficulty of jet definition after fragmentation, are larger than the effect of missing neutrinos. The cumulative effect of segmentation and energy resolution of the calorimeter is shown in table 3.5-1. All resolutions quoted are standard deviations of gaussian fits to the peaks of the distribution (see figure 3.5-1). Note that the segmentation effect will be present in any calorimeter due to transverse shower spreading.

Table 3.5-1 $Z^0 \rightarrow$ jet + jet Mass Resolution

Condition (cumulative)	Resolution (GeV)
Perfect detector	2.6
0.08 by 0.08 segmentation	3.9
$50\%/\sqrt{E} \oplus 2\%$ resolution	4.8
Additional 2% constant term for jets	5.1

Figure 3.5-1 shows the reconstructed mass distribution including all effects except the additional 2% constant term due to non-compensation. The high and low energy tails are almost entirely due to the effects present in a perfect detector. Other studies, too detailed to be reported here, have also been made. For example, by vetoing events with charged leptons, one can slightly improve the resolution because events with missing neutrinos are eliminated. The resolution can also be improved, at the expense of a reduction of the acceptance, by making a restrictive isolation cut.

3.5.2 Mass Resolution in $Z^{0\prime} \rightarrow q\bar{q}$ [21]

The process $Z^{0\prime} \rightarrow q\bar{q}$, with $M_{Z'} = 1$ TeV, was generated with PYTHIA version 5.4. An E_6 model with a very narrow width ($\sin\theta_6 = -1$, $\Gamma_{Z'} = 6$ GeV) was used in order to understand better the effects of clustering, segmentation, and energy resolution on the dijet mass resolution.

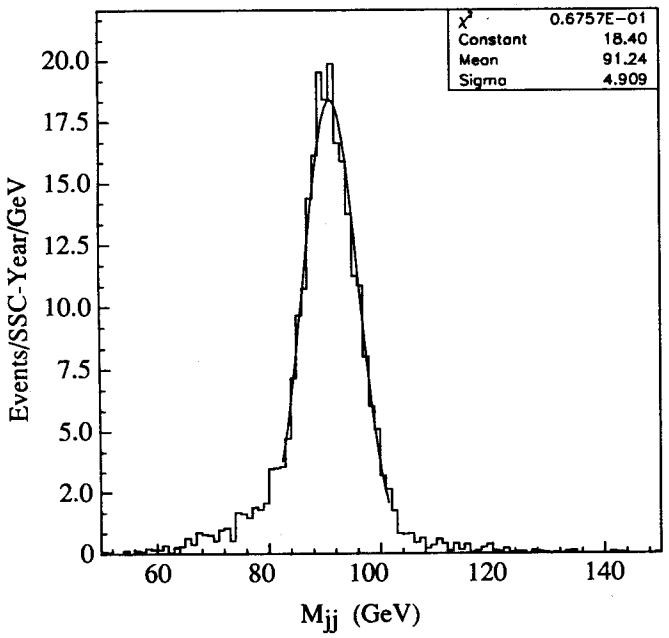

Figure 3.5-1 Reconstructed $Z^0 \rightarrow jj$ mass distribution including all effects except the additional 2% constant term

In the detector simulation, particles were assigned to calorimeter cells. The improved granularity of the portion of hadronic energy deposited in the electromagnetic section was ignored; it is assumed to be a small effect. Hadrons optionally were given a finite lateral shower size based on a simple analytic ansatz. Energy resolution for individual particles was applied assuming the form $\Delta E / E = a / \sqrt{E} \oplus b$, where a and b will be specified below.

A UA1-type cluster algorithm was performed on the calorimeter cells using R = 0.7. The invariant mass of jet pairs were then formed, and the pair yielding a mass nearest $M_{Z'}$ was retained, provided the rapidity of both jets was less than 2.5. The resulting mass distributions, shown below for two cases, were then fit to a gaussian distribution near $M_{Z'}$ plus a polynomial background. The resolution is defined as $\Delta M / M$, where ΔM and M are the standard deviation and mean of the fitted gaussian, respectively. The mass resolution was determined for four cases:

1. Perfect energy resolution was assumed. The intention here was to determine the "intrinsic" resolution for jet systems. To a lesser extent the contribution from the finite transverse tower granularity is included, but this is relatively small. The fitted mass distribution is shown in figure 3.5-2.
2. Energy resolution was included for individual particles with parameters a = 0.075 (0.50) and b = 0.005 (0.02) for the electromagnetic (hadronic) components of the showers. There was no degradation of the dijet mass resolution in this case.
3. Same as 2, except that finite shower widths were included as mentioned above.
4. Same as 3, except an additional 2% constant term is added to the jet resolution to account for the lack of compensation. Figure 3.5-3 shows the mass distribution for this case.

The results are summarized in table 3.5-2 below. The dijet resolution is dominated by "intrinsic" effects. While the calorimeter has some effect, it does not worsen the resolution due to clustering very much. Small departures from the parameters used here result in minor differences from these results.

Table 3.5-2 $Z^{0\prime}$ (1 TeV) → jet + jet Mass Resolution

Condition (cumulative)	Resolution (%)
Perfect detector with GEM segmentation	2.8
50% / $\sqrt{E} \oplus$ 2% resolution	2.8
Transverse shower width included	2.9
Additional 2% constant term for jets	3.5

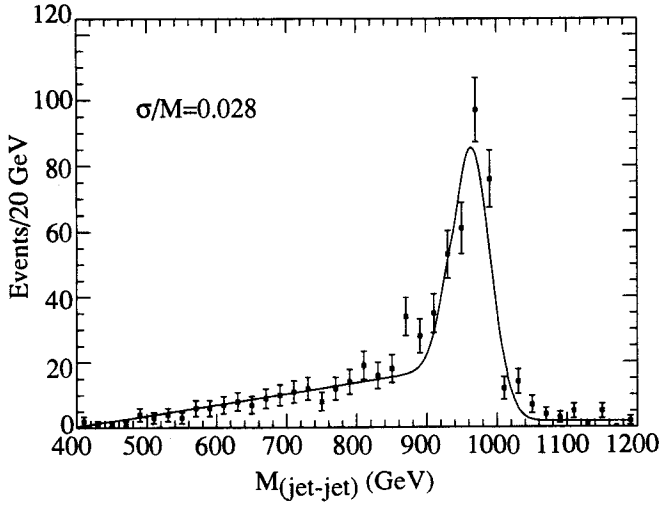

Figure 3.5-2 Reconstructed $Z^{0\prime}$ (1 TeV) → *jj* mass distribution for a detector with segmentation as in GEM and perfect energy resolution

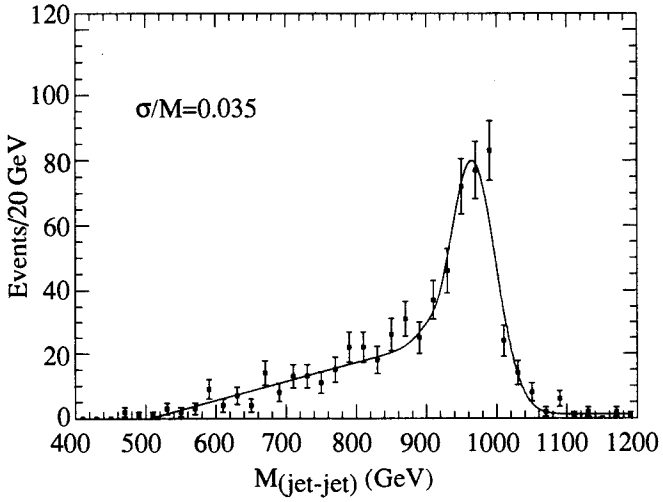

Figure 3.5-3 Reconstructed $Z^{0\prime} \rightarrow jj$ mass distribution for a detector with segmentation and energy resolution as in GEM with the transverse shower width included.

3.6 Complementarity of GEM to SDC

Question 5: Demonstrate the complementarity of the proposed detector and physics goals to the SDC.

There will be new physics in the TeV energy region, *but the nature of that physics is not yet known.* The SSC experimental program must cover the full range of existing ideas, with the flexibility to go beyond them as theory and experience dictate. All proposed new physics signatures involve photons, electrons, muons, jets, heavy flavors and/or missing energy. The complement of SSC detectors must measure *all* these signatures with precision and good background rejection. Thus, GEM will be complementary to the SDC detector if:

- It is *significantly better* than SDC in certain areas, allowing a broader range of discoveries.
- It has *significant overlap* with SDC in other areas, providing independent cross-checks.

To discuss quantitatively GEM's complementarity to SDC, it is necessary to know what SDC is. As this is being written, the SDC design is still evolving from that presented in its LOI [13]. Presumably it will continue to emphasize precise tracking in a large volume with the solenoid in front of the calorimeter. Up to $|\eta| = 3$, it will have electromagnetic and hadronic calorimetry with EM resolution in the $15\%/\sqrt{E} \oplus 1\%$ range; coarse hadronic calorimetry will cover $|\eta| = 3$ to ~ 5. The muon measurement will cover up to $|\eta| = 3$, with $\Delta p_T / p_T^2 \approx 13\%$ / TeV up to $|\eta| =$ 1.5, achieved using the central tracker.

The GEM design philosophy emphasizes precise photon, electron and muon measurements which are robust at high luminosity. The design parameters were summarized in section 3.1. The precision and robustness of GEM's calorimetry and muon systems give it the capability to discover new physics processes. A partial list of physics topics for which it offers unique strengths includes:

1. Search for the Higgs in the channel $H^0 \rightarrow \gamma\gamma$, for 80 GeV $\leq M_H \lesssim$ 160 GeV. (See section 3.2.2.)
2. Search in the $\gamma\gamma$ channel for other light scalar bosons (h^0, π_T^0) occurring in nonminimal and supersymmetric extensions of the standard model and in technicolor models of electroweak symmetry breaking [22].
3. The best mass resolution for $H^0 \rightarrow ZZ^* \rightarrow e^+e^-$ e^+e^- for 140 GeV $\lesssim M_H \lesssim$ 180 GeV. (section 3.2.2.)
4. Measurement of the spin of a Higgs (or similar particle) in the mass range 140 GeV $\lesssim M_H \lesssim$ 400 GeV using the angular distribution of the muons in $H^0 \rightarrow \ell^+\ell^-\ell^+\ell^-$ at ultrahigh luminosity, $\mathcal{L} \gtrsim 10^{34}\,cm^{-2}\,s^{-1}$.
5. Search for a very heavy Higgs ($M_H \gtrsim$ 800 GeV) in the four-lepton channel at ultrahigh luminosity.
6. Assured access to a wide range of flavor physics through tagging b quarks, and hence t quarks, by precise measurement of inclusive muons without using the central tracker to detect displaced vertices. Examples include heavy t, b' or t' (sections 3.2.3, 3.2.4); a charged Higgs or technipion in decays such as $t \rightarrow H^+b$ (section 3.2.3); and technipions carrying ordinary color, such as $\eta_T \rightarrow t\bar{t}$, $\pi_{Q\bar{Q}} \rightarrow t\bar{t}$, $t\bar{b}$, and $\pi_{Q\bar{L}} \rightarrow b\,\tau^+, t\,\tau^+$ and, especially, the rarer modes $b\mu^+$, $t\mu^+$ [22].
7. Search for the charged technirho in $\rho_T \rightarrow Z^0 W^\pm \rightarrow \ell^+\ell\ell^\pm\nu_\ell$ in the likely mass range M_{ρ_T} = 1.5–2.0 TeV [22]. The rate is very small and requires $\mathcal{L} = 10^{34}\,cm^{-2}\,s^{-1}$, but the only important background is the $W^\pm Z^0$ continuum.
8. High-precision measurements of the mass, width and couplings of a $Z^{0\prime}$ with $M_{Z'} \approx 4$ TeV by high-statistics studies of its $e^+e^-$and $\mu^+\mu^-$ decays at $\mathcal{L} = 10^{34}\,cm^{-2}\,s^{-1}$. (section 3.6.1 below.) With somewhat less precision this can be done for heavy W′ bosons as well.
9. Search for quark/lepton substructure in the Drell-Yan process, $\bar{q}q \rightarrow \ell\ell^-$, up to a scale $\Lambda \simeq$ 40 TeV in one year at $\mathcal{L} = 10^{34}\,cm^{-2}\,s^{-1}$. The Lorentz structure of the effective contact interaction can be well-studied in one year for $\Lambda \lesssim$ 25 TeV. (section 3.6.2, below.)

3.6.1 Physics at Ultrahigh Luminosity [23]

To illustrate the enhanced physics reach offered by GEM's robust systems discussions here focus on one-year studies at $\mathcal{L} = 10^{34}\,cm^{-2}\,s^{-1}$ of a 4 TeV $Z^{0\prime}$ boson and of a potential quark/lepton substructure scale at 25 TeV. If either of these phenomena exist, it is certain that they will involve identical couplings to electrons and muons, regardless of the underlying theory. Flavor-asymmetric couplings would violate the very stringent limits on flavor-changing neutral currents. For these analyses, a simplified version of the GEM detector with appropriate resolutions has been simulated. The most important

simplifications were to neglect multiple-scattering and calorimetric energy losses of the muons and to ignore hadronic energy deposition in the EM calorimeter. It is believed that these approximations do not affect the results significantly.

3.6.1.1 $Z^{0\prime} \rightarrow \ell^+\ell^-$ at $M_{Z'} = 4$ TeV

To test GEM's ability to distinguish, *in one year*, different extended gauge models through the width and forward-backward asymmetry (A_{FB}) of the $Z^{0\prime}$, two cases were considered:

1. The LR model, in which $SU(2)_L \otimes SU(2)_R \otimes U(1)$ breaks down to $SU(2)_L \otimes U(1)$. The $SU(2)_R$ coupling was taken to be the same as the $SU(2)_L$ one. The extra Z-boson of this model is called Z_1.
2. A model in which the grand-unification group SO(10) breaks down to $SU(5) \otimes U(1)$, then to $SU(2)_L \otimes U(1)$. Such a model may have an extra $Z^{0\prime} \equiv Z_2$ well below the unification scale.

The left- and right-handed couplings to quarks and leptons in the two models are given by

$g_L^u = \beta + \gamma$; $g_R^u = \beta$; $g_L^d = \beta - \gamma$; $g_R^d = \beta$; $g_L^\ell = -3\beta - \gamma$, and $g_R^\ell = -3\beta$.

Here, $\beta_1 = 0.117$, $\gamma_1 = -2.838$ and $\beta_2 = 0.408$, $\gamma_2 = -0.817$. For both models, the $Z^{0\prime}$ was assumed to decay only to known fermions (with m_t = 140 GeV).

PYTHIA 5.5 was used to generate 1000 Drell-Yan e^+e^- and $\mu^+\mu^-$ events with $M_{\ell^+\ell^-} > 3.6$ TeV for $M_{Z'}$ = 4 TeV; no cut was put on p_T^ℓ. Pileup events corresponding to $\mathcal{L} = 10^{34}\text{cm}^{-2}\,\text{s}^{-1}$ were included. Pileup was found never to be an important factor with the cuts described below. The total cross section was 6.3 fb for the Z_1 model and 4.9 fb for the Z_2 model. Thus, the SSC would produce a thousand 4-TeV $Z^{0\prime} \rightarrow \ell^+\ell^-$ events, in each mode, in 1.5–2 years at $\mathcal{L} = 10^{34}\text{cm}^{-2}\,\text{s}^{-1}$.

Events were selected to have two isolated leptons, each with $|\eta| \leq 2.5$ and a measured mass $M_{\ell^+\ell^-} \geq$ 3 TeV. The isolation criterion was

$$\sum_{R=0.5} E_T - E_T^\ell \leq 25\ \text{GeV} + 0.02\, E_T^\ell.$$

In addition, muons are required to have $\Delta p_T / p_T \leq$ 0.4 for good charge determination and $|\cos\theta^*| \leq$ 0.9, where θ^* is the angle between the outgoing μ^- and the incoming quark (taken to be the direction of $y_{boost} = y_{Z'} = (\eta_{\ell^+} + \eta_{\ell^-}) / 2$. The acceptances were 96% for $Z_{1,2} \rightarrow e^+e^-$ and 70% for $Z_{1,2} \rightarrow \mu^+\mu^-$.

The process $Z^{0\prime} \rightarrow \mu^+\mu^-$ has a potentially significant background from $t\bar{t} \rightarrow \mu^+\mu^- + X$. 400 k $t\bar{t} \rightarrow \mu^+\mu^- + X$ events with $m_{tT} > 2.5$ TeV and $\hat{p}_T^t > 125$ GeV were simulated, corresponding to five months of SSC running at $10^{34}\,\text{cm}^{-2}\,\text{s}^{-1}$. This background was completely insignificant after the above cuts.

The $Z_1 \rightarrow e^+e^-$ mass distribution is shown in figure 3.6.1 for one SSC year at $\mathcal{L} = 10^{34}\text{cm}^{-2}\,\text{s}^{-1}$. It was assumed that angular measurements could be made with the central tracker; the $M_{e^+e^-}$ distribution is not significantly different without tracking. The fitted mass is $M_1 = 4001.5$ GeV. The measured Z_1 width is 113.5 GeV, compared to a perfectly measured value of 110.6 GeV. For the

Z_2 model, M_2 = 3990.1 GeV was found. This downward shift is due to γ / Z / Z′ interference. The width was fitted to be 76.6 GeV with the tracker and 80.7 GeV without it, compared to a perfectly measured value of 71.0 GeV. Including systematic errors in the mass scale, the Z′ mass should be measured to 0.5%. The Z′ width can be determined in one year to 5–15%, depending on the performance of the tracker at ultrahigh luminosity.

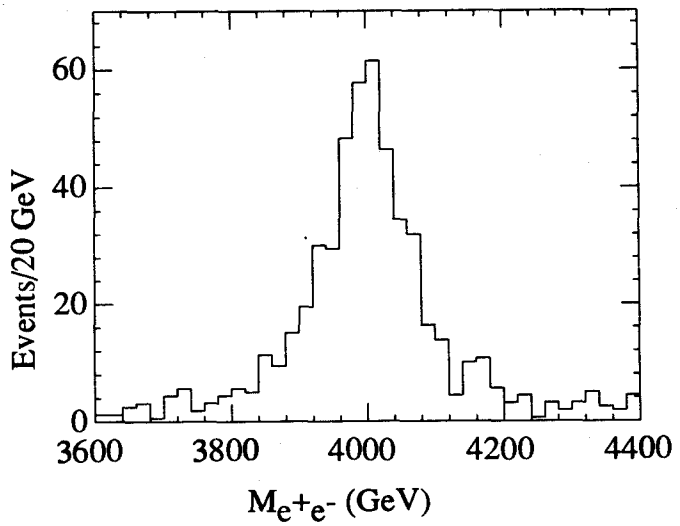

Figure 3.6-1 $Z^{0\prime} \rightarrow e^+e^-$ **for** $M_{Z'}$ **= 4 TeV, including GEM resolutions, for** $\int \mathcal{L}\,dt = 10^{41}\,cm^{-2}$

The dimuon mass distribution for the Z_1 model is shown in figure 3.6.2 including the effect of the muon resolution. Since backgrounds are insignificant, a ~1% mass determination could be made. The muon system also measures the forward-backward asymmetry, $A_{FB} = (n_+ - n_-) / (n_+ + n_-)$, where $n_+(n_-)$ is the number of muons with $\cos\theta^* > 0$ (< 0). Based on one year's running (or 1.5–2 years for 1000 produced events) the following would be obtained:

$$A_{FB} = 0.086 \pm 0.048\ (0.038) \qquad (Z_1 \text{ model})$$

$$A_{FB} = -0.064 \pm 0.053\ (0.037) \qquad (Z_2 \text{ model})$$

The theoretical expectations are 0.10 and – 0.09, respectively.

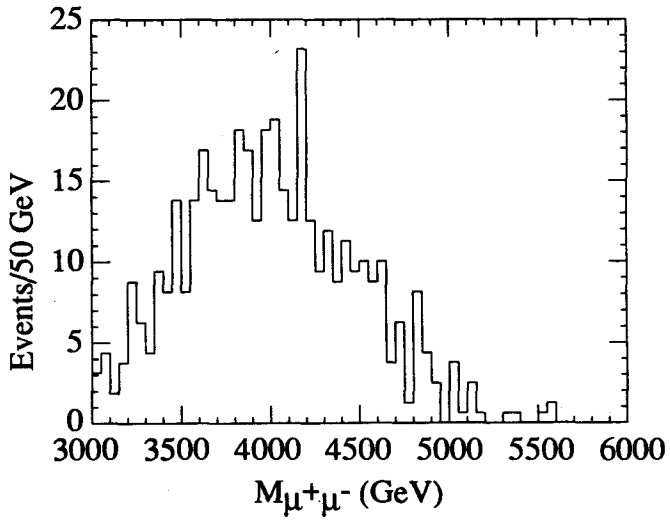

Figure 3.6-2 $Z^{0\prime} \rightarrow \mu^+\mu^-$ **for** $M_{Z'}$ **= 4 TeV, including GEM resolutions for** $\int \mathcal{L}\,dt = 10^{41}\,cm^{-2}$

Finally, in one year at $\mathcal{L} = 10^{34}\,cm^{-2}\,s^{-1}$, a $Z^{0\prime}$ boson could be discovered with mass in excess of 10 TeV if its couplings to quarks and leptons are comparable for those of the standard Z^0 [23].

3.6.1.2 Quark / lepton substructure at Λ = 25 TeV

If quarks and leptons are composite at the scale Λ, this will be manifested at energies $\sqrt{\hat{s}} = M_{l^+l^-} << \Lambda$ by the appearance of effective four-fermion contact interactions, $\mathcal{L}_\Lambda$, producing an excess of events at

high $M_{\ell^+\ell^-}$. The $\cos\theta^*$ distribution of the outgoing μ^- will be altered from the Drell-Yan expectation of $a + b\cos^2\theta^*$ by the Lorentz structure of $\mathcal{L}_\Lambda$.

According to [22], a "perfect" SSC experiment could just detect substructure at the scale Λ = 20–25 TeV in a standard SSC year. To demonstrate GEM's power to probe and study high scales by running for one year at $10^{34}\text{cm}^{-2}\text{s}^{-1}$ two different models for the contact interaction $\mathcal{L}_\Lambda$ were considered:

1. The "left-left isoscalar" (ISO) model, with contact interaction

$$\mathcal{L}_{\text{ISO}} = -\frac{4\pi}{\Lambda^2}\bar{Q}_{La}\gamma^\mu Q_{La}\ \bar{L}_{Lb}\gamma_\mu L_{Lb},$$

   where $Q_{La} = (u_a, d_a)_L$ and $L_{La} = (\nu_a, \ell_a)_L$ are left-handed quark and lepton fields and a,b = 1,2,3 label generations. This interaction alone has a $(1 + \cos\theta^*)^2$ angular distribution.

2. The "helicity-nonconserving" (HNC) model, with contact interaction

$$\mathcal{L}_{\text{HNC}} = \frac{4\pi}{\Lambda^2}\,\varepsilon_{ij}\,\bar{Q}_{Lia}u_{Ra}\,\bar{L}_{Ljb}\ell_{Rb} + \text{hermitian conjugate},$$

   where i, j = 1,2 label indices in an electroweak doublet and $\varepsilon_{12} = -\varepsilon_{21} = 1$. This interaction is theoretically unlikely, but was studied here because it generates an isotropic angular distribution.

PYTHIA 5.5 was used to generate 1000 standard Drell-Yan events $\bar{q}q \to \mu^+\mu^-$ with 2 TeV < $M_{\mu^+\mu^-}$ < 10 TeV and p_T^μ > 160 GeV, and 1500 events each for the ISO and HNC models with Λ = 25 TeV. Pileup at $\mathcal{L} = 10^{34}\text{cm}^{-2}\text{s}^{-1}$ was included. The cross sections were 3.5 fb, 10.8 fb and 11.5 fb, respectively. To eliminate the $t\bar{t}$ background and obtain well-measured muons, events were selected as for $Z^{0\prime} \to \mu^+\mu^-$, but with $M_{\mu^+\mu^-}$ > 2.5 TeV and $|\cos\theta^*| < 0.85$.

The measured $M_{\mu^+\mu^-}$ distributions of the two highest-p_T muons surviving these cuts are shown in figure 3.6.3 for standard Drell-Yan and the ISO and HNC models. The numbers of events with $M_{\mu\mu}$ > 2.5 TeV for the three models are 85 (DY), 455 (ISO) and 560 (HNC), corresponding to acceptances of 25%, 42%, and 49% respectively. One year's $t\bar{t}$ events yield 5000 muon pairs with $M_{\mu^+\mu^-} \geq 2$ TeV, but only 5 survive these cuts.

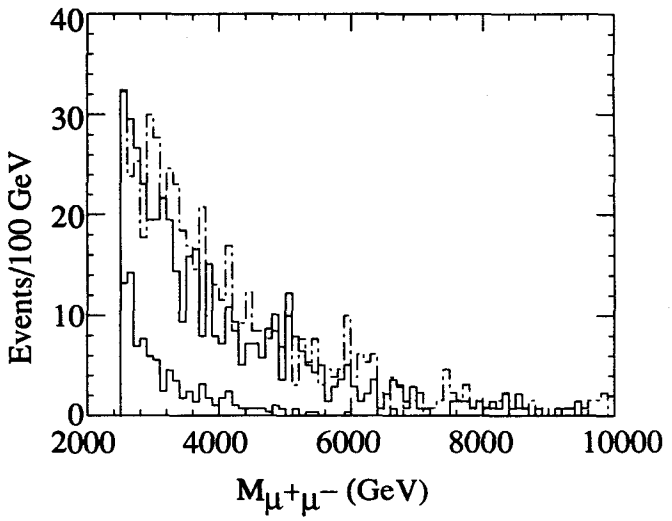

Figure 3.6-3 $\mu^+\mu^-$ mass distributions including compositeness interactions with Λ = 25 TeV for $\int \mathcal{L}\,dt = 10^{41}\text{cm}^{-2}$. Upper solid: ISO model, dot-dashed: HNC model, lower solid: standard model

The $\cos\theta^*$ distributions are shown in figure 3.6.4. The tendencies to a $(1 + \cos\theta^*)^2$ distribution in the ISO model and a flat one in the HNC model clearly distinguish the two cases and show that the method for determining $\cos\theta^*$ works quite well at high invariant masses. The forward-backward asymmetries are:

$A_{FB} = 0.344 \pm 0.100$ (Drell-Yan)

$A_{FB} = 0.269 \pm 0.045$ (ISO)

$A_{FB} = 0.005 \pm 0.042$ (HNC)

Finally, the quark/lepton substructure scale $\Lambda \simeq 40$ TeV can be accessed in either electron or muon channels in one year at $10^{34}\,cm^{-2}\,s^{-1}$. Substructure at this scale would generate an excess of ~ 70 events over the standard Drell-Yan expectation, fourteen times greater than the expected $t\bar{t}$ background with the cuts used here [23].

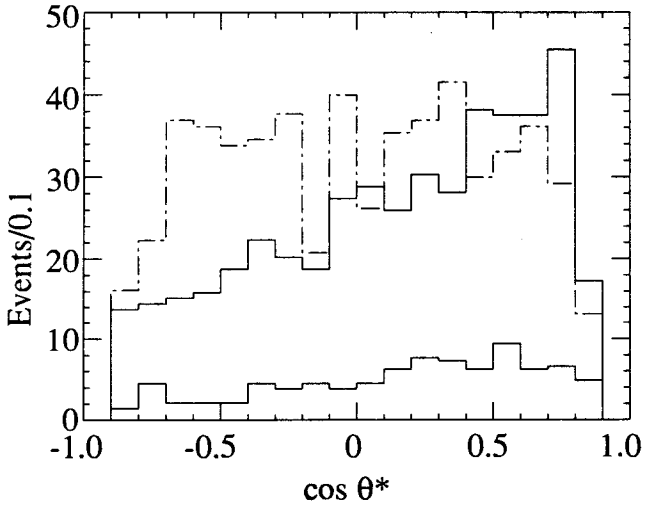

Figure 3.6-4 $\mu^+\mu^-$ angular distributions including compositeness interactions with Λ = 25 TeV for $\int \mathcal{L}\,dt = 10^{41}cm^{-2}$. Upper solid: ISO model. dot-dashed: HNC model, lower solid: standard model

3.7 Future Enhancements to GEM

Question 6: Outline options for the evolution of your experiment beyond initial operation at the SSC.

The GEM detector was conceived during 1991 and presented in the EOI, where the general concept and possible technological implementations were discussed, and in this LOI, where a detector is presented which is much better defined. During 1992, final technology choices will be made and presented in the technical design report. In this process, a rigorous design to cost approach for GEM is being followed and the cost is fully expected to stay within the 500 M$ guideline.

At present, as described in section 4.0, target costs and guidelines for subsystems appear to be consistent. Nevertheless, as the procedure and design evolve, it may be that, either due to funding or cost considerations, choices will have to be made. The choice is likely to be between reduced performance of certain subsystems (e.g., reduced granularity) or deferring some features of the proposed detector. Since reduced performance has lasting consequences, it is the general philosophy, where possible, to maintain the performance as stated in this LOI, even if this results in deferring some features past initial running.

The presently conceived GEM detector has a number of features that might become *planned enhancements* out of necessity, even though all of these represent features already justified by known SSC physics considerations. Examples include a calorimeter preradiator (giving improved calorimeter performance and background rejection), field shaping in the forward direction

(giving improved momentum resolution (see figure 2.3-4b), and forward calorimeters giving improved η coverage. The choice of what if anything might be deferred will depend on the physics importance of each for early running, on whether access or other considerations permit later installation, and on the cost implications.

A second class of future enhancements consists of those that will be motivated by technological developments or new physics considerations. Technical advances between now and SSC running will almost certainly make it desirable to replace (at some point) certain elements of the detector with new versions better suited to explore the full physics potential of the SSC. An example could be improved techniques for tracking which would enable full performance up to $\mathcal{L} \sim 10^{34}\,\mathrm{cm}^{-2}\,\mathrm{s}^{-1}$. Both a design where units are accessible and replaceable and continuing R&D on promising techniques are essential elements in allowing such upgrades. New physics considerations might also motivate various upgrades. For example, if new theoretical ideas and the initial SSC results themselves point to the need for improved muon resolution, we would implement additional muon chambers outside the single coil magnet. As is shown in figure 2.3-4a this can lead to a significant improvement in performance and result in a strong physics advantage to the single coil magnet design.

A very important feature of GEM is its ability to expand its physics scope by using higher luminosity, by changing essentially only the trigger. Section 3.6.1 presented a detailed discussion of new physics accessible to GEM at ultrahigh luminosity.

Overall, good access to the detector elements, allowing both replacement and improvements, will be the key to making GEM a detector that can evolve and improve, as needed. We fully recognize that the long time until the realization of our SSC detector, and the long lifetime needed to exploit the physics, will require that special attention be paid to flexibility and enhancements in the design.

3.8 Conclusion

We have demonstrated the discovery potential of the GEM detector throughout this chapter. Most of this potential derives from GEM's precision calorimetry and muon systems and their ability—if new, high-mass physics requires it—to operate at ultrahigh luminosity. We have emphasized particularly the complementarity of both the design goals and physics capabilities of the GEM and SDC detectors. Together, these two large detectors promise the broadest and most incisive studies of the TeV energy scale at the SSC. We conclude with the following statement from the GEM EOI which, we are convinced, still holds:

> *Two complementary detectors have additional advantages over one very large one. Two collaborations promote a variety of styles and approaches to technical problems. Two detectors have different systematic errors. Two collaborations provide a healthy spirit of competitiveness that will help obtain the physics in a timely fashion. Finally as illustrated in this document, it is entirely feasible to build a detector with the desired complementarity to SDC and correspondingly increased physics coverage that is within the guidelines established by the Laboratory and the PAC.*

[1] GEM Collaboration, "An Expression of Interest to Construct a Major SSC Detector", (SSC EOI-0020), July 8, 1991.

[2] H.-U. Bengtsson and T. Sjostrand, A Manual to the Lund Monte Carlo for Hadronic Processes; T. Sjostrand, The Lund Monte Carlo for Jet Fragmentation and e^+e^- Physics.

[3] F. E. Paige and S. D. Protopopescu, BNL-38774 (1986).

[4] R. Y. Zhu, Signal and Background of $H \rightarrow \gamma\gamma$ with the Proposed GEM Calorimeter, GEM Internal Note GEM-TN-91-32.

[5] $\hat{p}_T$ is the transverse momentum of either particle in a $2 \rightarrow 2$ process in their center of mass frame. It is not the measured p_T because of initial and/or final state radiation.

[6] H. Yamamoto, Shower Shape and Preradiator Study for $H \rightarrow \gamma\gamma$ Background, GEM Internal Note GEM-TN-91-33.

[7] B. Zhou, GEM Internal Note.

[8] For the BaF_2 option, the exit crack for the central tracker cable is about 2.7%.

[9] H. Ma, GEM Internal Note.

[10] G. E. Forden, "Calorimetry Geometry and Response Effects on SSC Physics" to appear in Proceedings of the Workshop on Detector and Event Simulation in High Energy Physics, Amsterdam, The Netherlands, 8–12 April, 1991.

[11] G. E. Forden, Forward Calorimeter Transition, z Position and Segmentation, to appear in the Proceedings of Particles and Fields '91, Vancouver, British Columbia, August 18-22, 1991.

[12] G. E. Forden, Calorimeter e/h Effects on Reconstructing High p_TW/Z to Hadrons, to appear in the proceedings of Particles and Fields '91, Vancouver British Columbia, August 18-22, 1991.

[13] SDC Collaboration, "Letter of Intent", SSC–LOI0001 (1990).

[14] L* Collaboration, "Letter of Intent" , SSC-LOI0002 (1990).

[15] F. E. Paige, GEM Internal Note.

[16] A. Vaniachine, GEM Internal Note.

[17] S. A. Kahn, *et al.*, GEM Internal Note.

[18] H. Haber and G. Kane, Phys. Rept. **117,** 75 (1985) and references therein.

[19] H. Baer, X. Tata, and J. Woodside, FSU-HEP-910731 (1991).

[20] A. Bay, *et al.*, *Snowmass 1988 Proceedings*, p. 882.

[21] R. Frey, GEM Internal Note.

[22] E. Eichten, I. Hinchliffe, K. Lane, and C. Quigg, Rev. Mod. Phys. **56,** 579 (1984). These and other processes will be simulated for GEM over the next year. We are reasonably confident that their backgrounds are managable.

[23] E. Carlson, M. Golden, K. Lane, L. Randall and E. Simmons, in preparation. We are indebted to T. Sjostrand for embedding the compositeness cross sections in PYTHIA and helping us to iron out the wrinkles.

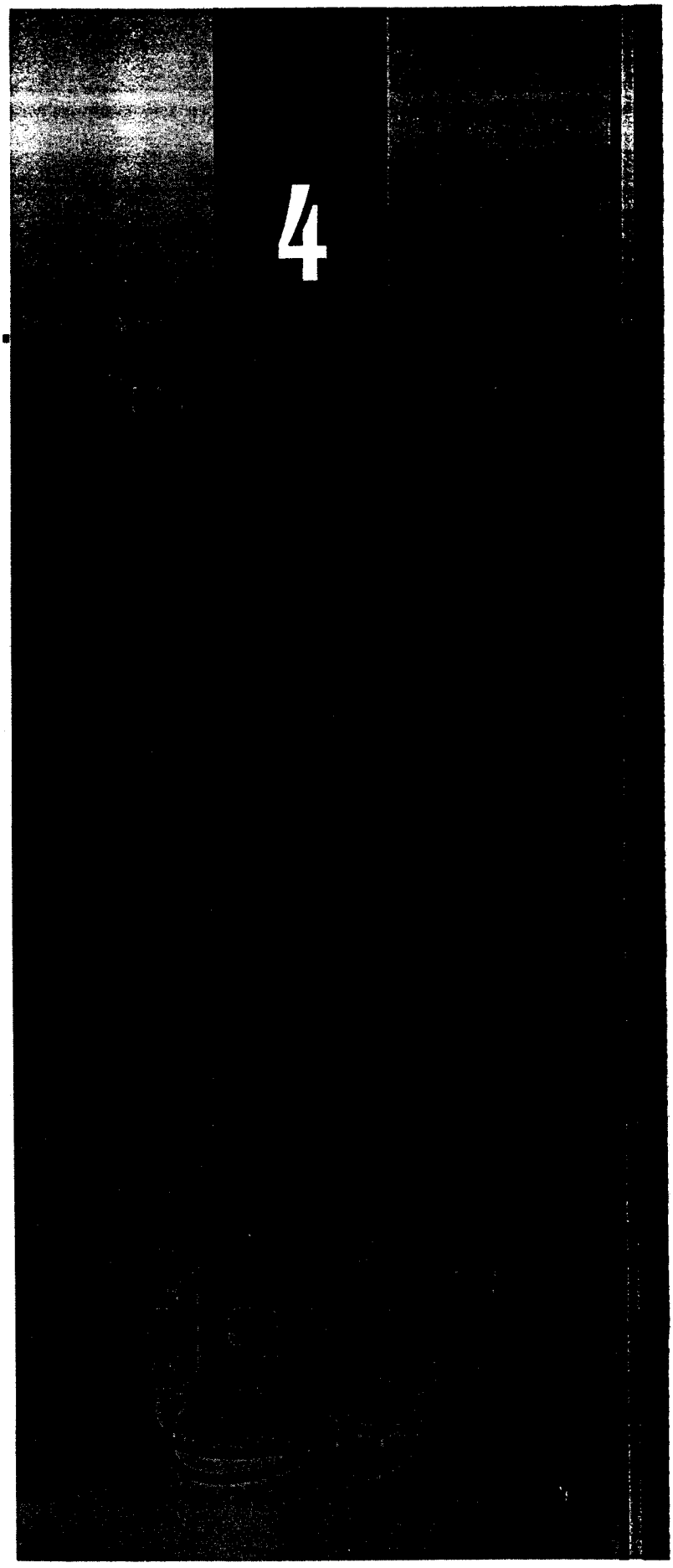
4

Initial Cost Targets ($Millions)

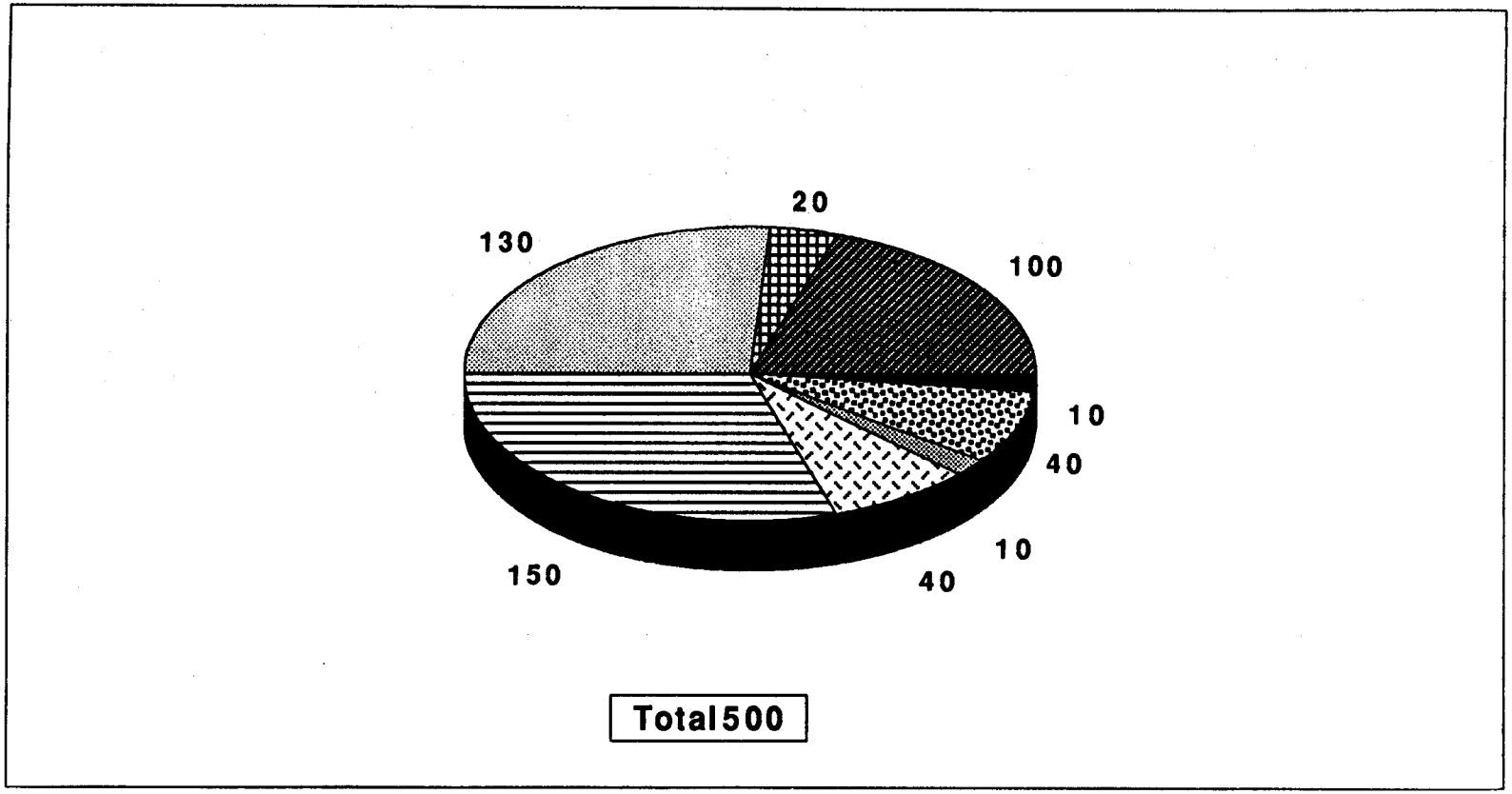

4.0 COST AND SCHEDULES

The GEM collaboration is committed to a "design to cost and schedule" approach. As stated in the EOI, the required physics performance sought by this collaboration appears to be achievable within the cost targets that have been adopted. The SSC Laboratory, with the advice of the Program Advisory Committee, has recommended a maximum total cost of 500 M$ as guidance for the design of a major detector. The SSC Laboratory has further stated that the collaboration should assume an initial budget of DOE funds of 225 M$ for each major detector, with a 100 M$ sum available to address the combined needs, as they emerge, of the planned two major detectors. The Laboratory has urged that early and firm identification be made of nonfederal funding sources to supply the shortfall.

This guidance has been followed, by taking several major actions. With the support of the SSC Laboratory, an initial engineering team was organized which includes the experienced estimators active in the EMPACT/TEXAS and L* collaborations. An initial set of cost targets for each GEM subsystem was defined [1]. Table 4.0-1 shows these targets. The targets were based upon the knowledge gained in the EMPACT/TEXAS and L* cost estimates, the reports of the L* and SDC cost reviews chaired by Dennis Theriot, and the ongoing design studies. The targets are in FY1991 dollars and include all EDI&A and contingency, and assume that all electronics costs which can be associated with a subsystem are included in the subsystem target. Thus, the Trigger and Computing targets apply only to items that stand outside of all subsystems. The Structures category applies to the large central membrane and support tube, and other large structures which involve large costs and highly engineered elements. Elsewhere in the Letter of Intent, the structures costs are reported with the magnet system.

This set of targets defines the initial cost discipline to be included in all GEM system designs. At periodic points in the design, the individual targets may be adjusted, preserving the total, as part of a comprehensive review of the design status, physics priorities and cost information.

Table 4.0-1 Initial GEM Subsystem Cost Targets

Subsystem	Cost Target (M$)
Magnet	100
Structures	20
Muon system	130
Calorimeters (all)	150
Tracker	40
Trigger	10
Computing	10
R&D	40
Total GEM Detector	500

Another major part of the design-to-cost approach has been the inclusion of subdetector cost estimates in the basis of each of the technology choices that the collaboration has made since the GEM EOI. The calorimeter selection process, for example, used detailed cost estimates for all major options; reference [22] is an example of the estimate used in the hadron calorimeter selection. As the system definitions advance, these estimates will play an increasingly important role in guiding

the design. However, as several major choices of technology have been made only recently, and the technologies for preradiators, forward calorimetry, and outer tracker are undergoing study, the subsystem cost targets have not yet been updated or refined.

To make the use of the estimates effective and reliable, a detailed uniform cost estimating methodology has been developed to be applied by all GEM designers [3]. This plan includes detailed guidance on estimating, and reporting standards designed to incorporate the lessons learned in previous SSC reviews. This will yield an estimate with the most reliable basis possible and aid in future reviews by accommodating the analytical tests used in the review process in a natural way. For example, all labor rates have been defined; engineering, design, inspection and administration estimates have been separately identified; the basis of contingency estimates have been documented; and standards for estimate backup reports have been set. A hierarchy of estimate bases has been defined; at each level the goal is that the cost of a high percentage of elements be estimated on the basis of vendor responses to GEM design drawings.

For several GEM subdetectors with the most developed designs, the estimates are within, or close to, our targets. For example, the combined magnet and structures, budgeted for 120 M$ plus a portion of the R&D funds, is now estimated at 105 M$. This includes the structures and the R&D.

As the cost estimates are developed to reliable levels, any excess over the 500 M$ target for the entire detector will be addressed by refining designs to reduce costs, or identifying subsystem staging options. We will present a report on the GEM cost estimate at the presentation of this LOI before the Program Advisory Committee.

The GEM detector schedule has been studied in the context of the single-shaft underground hall and with the guidance of the GEM Magnet Technical Panel. The critical path in the GEM schedule is the magnet design and fabrication, which must be completed prior to installation of the detector elements in the underground hall. This portion of the critical path extends to early 1996. The final portion of the critical path is the underground installation of the subdetectors. Figure 4.0-1 shows the schedule under these assumptions.

However, additional slack in this schedule is being sought with the multiple-shaft option, with design studies which are attempting to redefine the order of the subdetector installation and integration, and with continuing studies of magnet fabrication options.

Availability of the magnet fabrication hall in 1993 and beneficial occupancy of the underground hall in early 1996 are the two most critical milestones in this schedule.

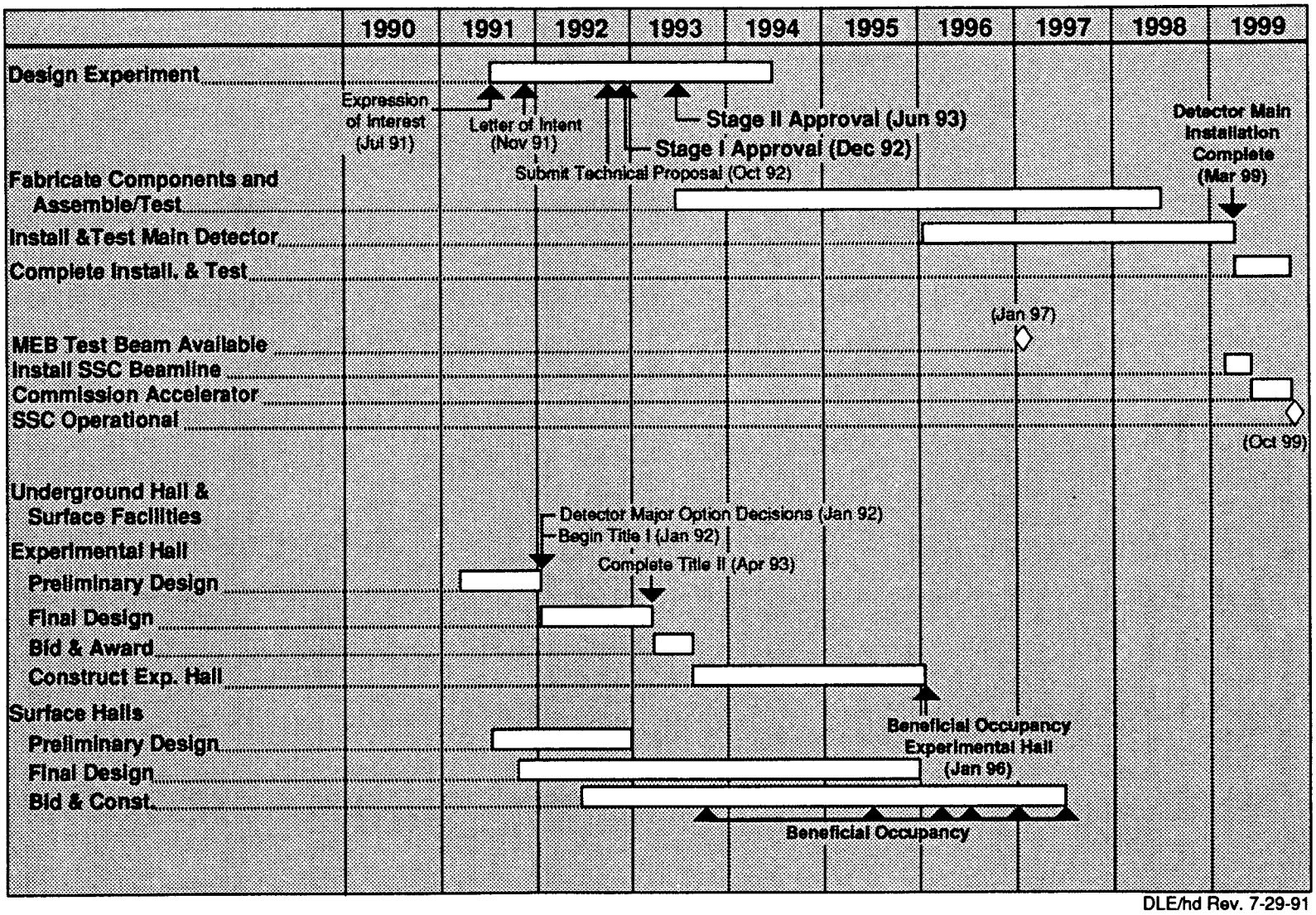

Figure 4.0-1 Preliminlary GEM Schedule

[1] GEM Engineering Meeting, July 29, 1991.

[2] M.J. Rennich, C.L. Claffey, M.K. Singhal. C.C. Eberle, Oak Ridge National Laboratory, "GEM Detector Cost and Design Study for Scintillating Hadron Calorimeters", GEM TN-91-20, September 22, 1991

[3] Richard Sawicki, Lawrence Livermore National Laboratory, "GEM Cost Estimating Plan", GEM TN-91-17, September 30, 1991.

5

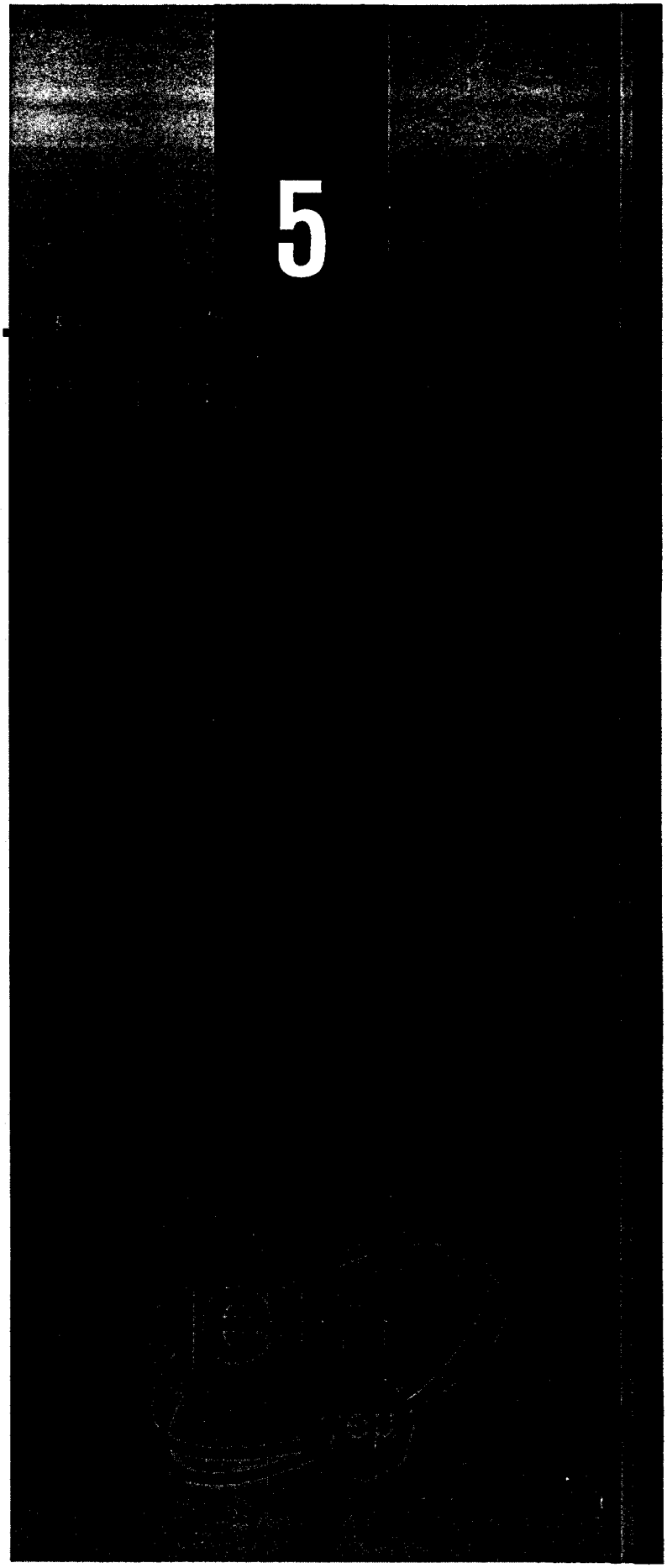

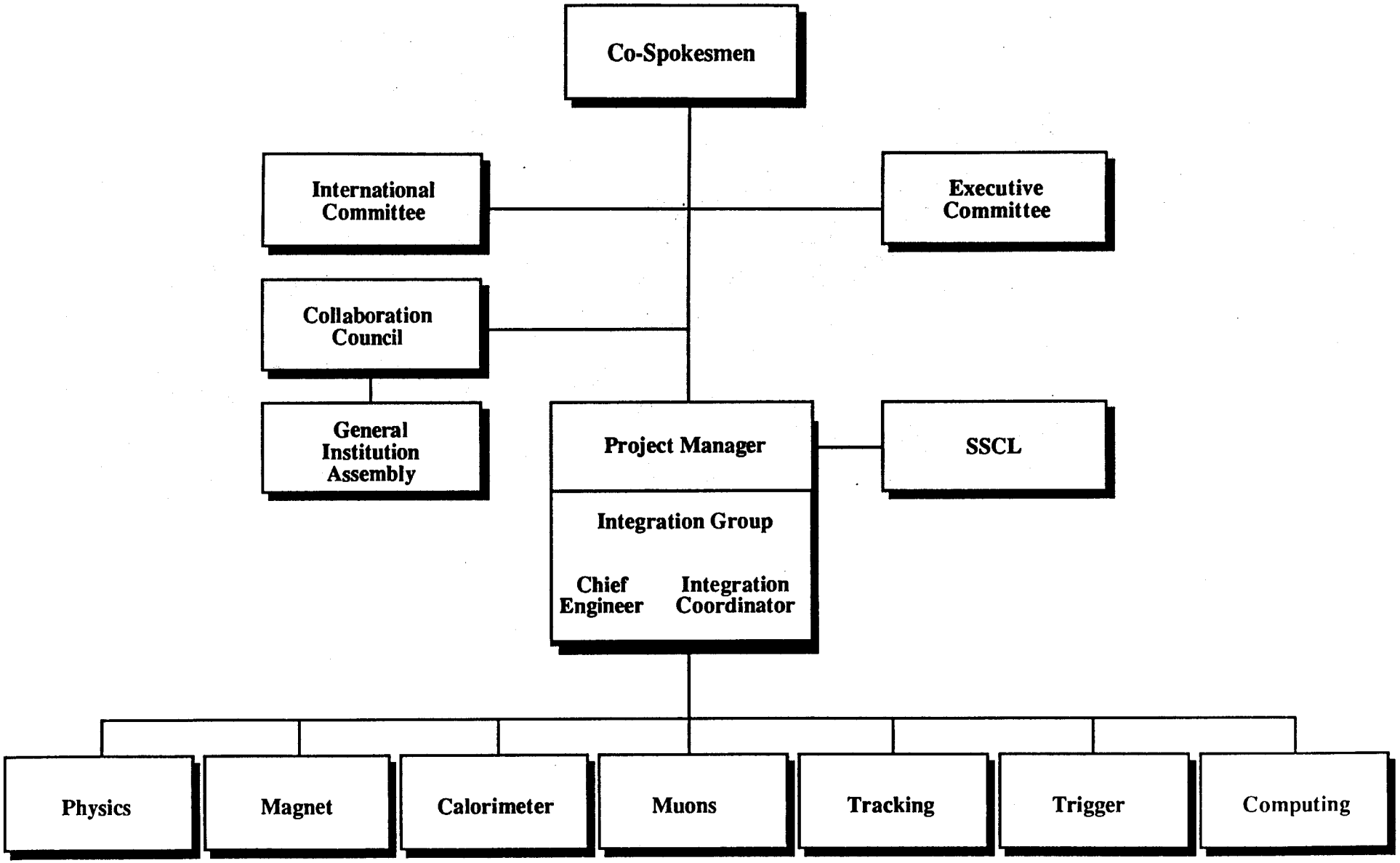
Co-Spokesmen
International Committee
Executive Committee
Collaboration Council
General Institution Assembly
Project Manager
SSCL
Integration Group
Chief Engineer
Integration Coordinator
Physics
Magnet
Calorimeter
Muons
Tracking
Trigger
Computing

5.0 COLLABORATION ORGANIZATION

An organization for preparing the Expression of Interest (EOI) and Letters of Intent (LOI) for designing, building and utilizing a major detector at the SSC has been established by the GEM Collaboration. The co-chairs (Barish and Willis) are responsible for organizing and implementing the EOI and LOI for such a detector. In addition, several sub-groups were established, reporting to the co-chairs. These are the Collaboration Council consisting of one person from each participating institution; the sub-systems unit consisting of the individuals leading the efforts of defining the major sub-systems: calorimeter, muons, magnet, tracking, trigger, and computing; and the LOI Task Force established for coordinating the efforts in preparing the above documents consisting of Physics, Detector Parameters, Cost and Schedules, R&D Engineering Tests, and the LOI document itself; and an Executive Committee whose main task is to validate the technical and budgetary decisions. A general assembly of all the members of the GEM Collaboration is also included. This organization is displayed in figure 5.0-1 and has been functioning for the past six months.

In order to proceed further, the collaboration has agreed that a modified interim organization has to be established (See the color figure preceeding this section.). As such it was proposed and agreed that Barish and Willis continue as co-spokesmen. It is expected that the former will take a leading role more in the management area and the latter more in the technical domain. The Collaboration Council, as noted earlier consisting of one person from each participating institution, is retained. This is the body which has the ultimate authority since it is the representative group of the GEM collaboration. The General Institutes Assembly which consists of all individuals from all institutions of the collaboration is also retained. The Executive Committee whose essential function is to validate all technical decisions and assure program management and accountability is retained, reshaped and enlarged. This change is forced by the necessity to make critical technical decisions on the GEM detector components as well as management organization.

In this interim organization the members of the Executive Committee will be selected by the co-spokesmen in consultation with the Coordination Council. It is now time to formalize the existence of an International Committee since an important component of the GEM collaboration will be the participation of individuals from non-American institutions. The existence of such a body will facilitate and ease the participation of foreign nationals in GEM.

The most important change in the proposed organization is the inclusion of the post of Project Manager. The time has come where day-by-day supervision and tight control has to be exercised over the numerous subsystems that are being designed. This requires a full-time person devoted to getting things done in an expeditious manner; this is the Project Manager. This individual should be stationed for the most part at the SSCL and be the main link between GEM and the SSCL. The various critical sub-systems, physics, management, calorimeter, muons, tracking, trigger systems and computing will have their individual leaders and report to the Project Manager who in turn reports to the co-spokesmen. Finally, an Integration Group, which is a staff function to the Project Manager, is to be formed. Their main task will be to assure the proper meshing of components and communication between the systems.

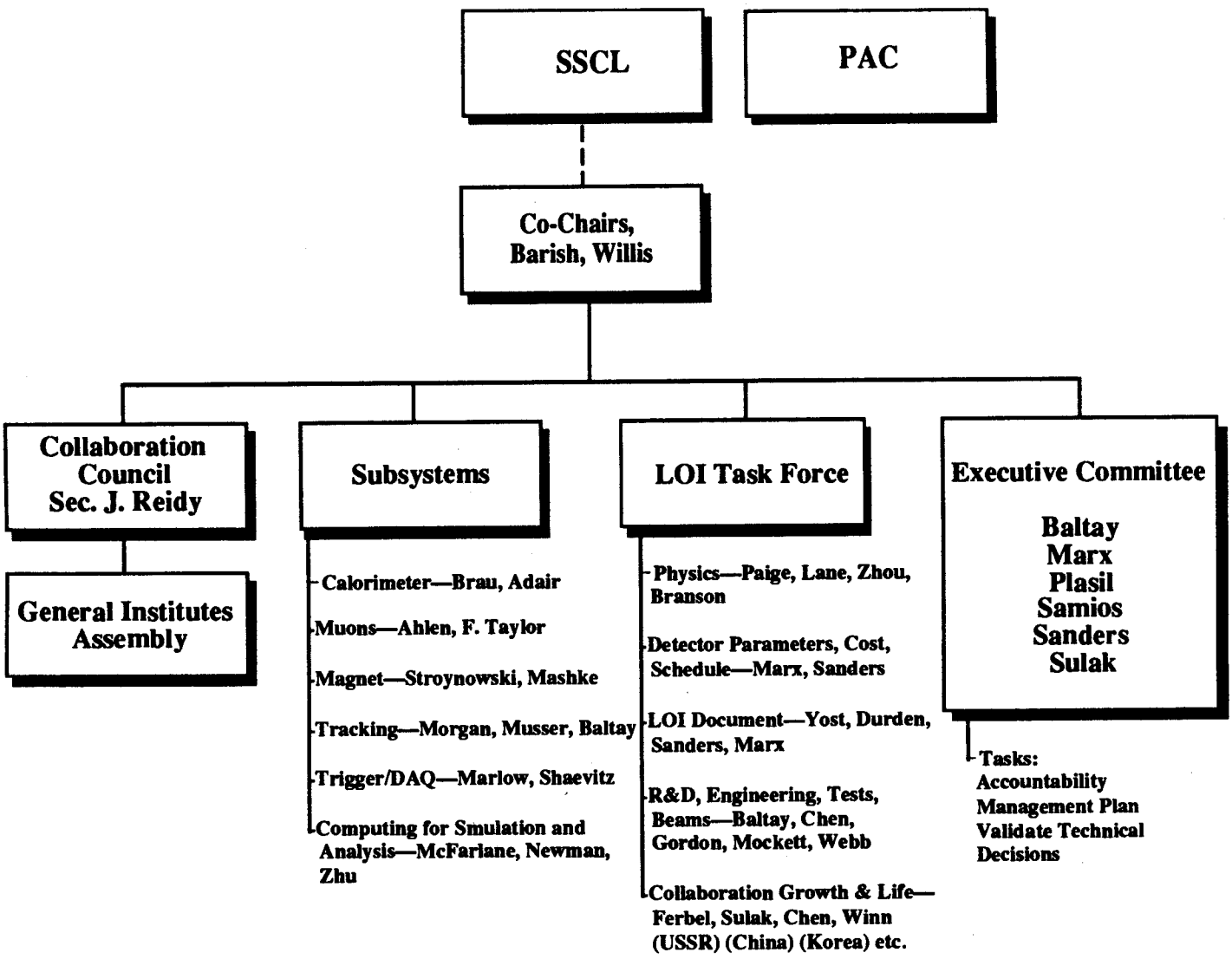

Figure 5.0-1 GEM Collaboration Organization

One further iteration of the GEM organization is expected when the actual construction of this detector is begun. This is forecast to be sometime in late 1992 or early 1993. In this final organization, an orderly system for making all appointments including that of the spokesperson will be set up. In addition, the normal tenure of all appointed positions will be determined.

6

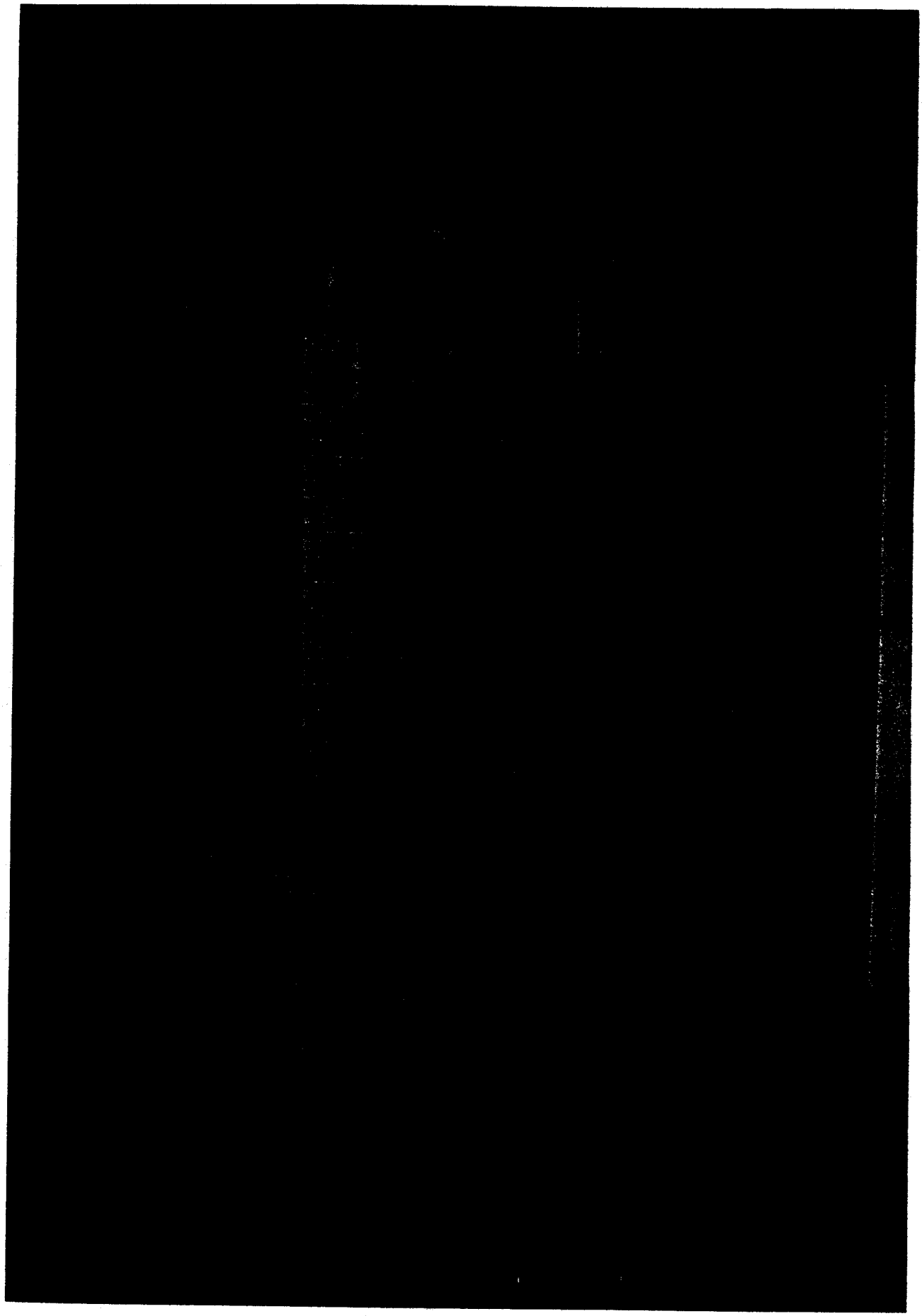

6.0 R&D PLAN AND FUNDS REQUESTED FOR FY92

The GEM collaboration is working towards the preparation of a detailed Engineering Design Report/Technical Proposal for the detector by late fall 1992. In preparation for this a vigorous R&D program and engineering design effort has to take place during the coming year. There is enthusiasm, energy, and ability within the collaboration to pursue a very broad program of studies. However, to be able to achieve this program with the very limited R&D and engineering funds that are expected to be available in FY92, a concerted effort had to be made to focus the program to the minimum set of topics that are absolutely required to allow the necessary design decisions to be made in a timely fashion. The narrowing of the range of technologies considered for various detector subsystems is described in section 2 of this Letter of Intent. The options still under consideration define the R&D program that is planned for the following year. The components of this R&D program are described in the discussion of the various subsystems elsewhere in this LOI. There is only a very brief summary in this section.

6.1 System Integration

A strong engineering effort will be required to provide the planning for the overall detector architecture and support structure and the integration of the various subsystems into this overall structure. It is anticipated that the funding for this effort will not come from the R&D funds but from Project Management funds at the SSC, which is not explicitly covered in this LOI.

6.2 Magnet

The large superconducting magnet represents a critical path item for GEM. Rapid progress mandated by the very tight construction schedule requires a large amount of engineering effort in this coming year on the calculation of the magnet forces, design of the support structure, cryogenic and electrical system, etc. A vigorous R&D program is required this year to arrive at an acceptable design of the critical path elements of the magnet, i.e. the choice of the superconducting coil conductor and its stabilizer, the coil winding procedures and the necessary tooling. This has to be of the highest priority in the GEM R&D program for this coming year.

6.3 Calorimetry

The choice of the technologies for the GEM Central Calorimeter has been narrowed down to two options: a lead liquid argon or krypton electromagnetic and a liquid argon hadronic section, or a barium fluoride electromagnetic calorimeter followed by a lead scintillating fiber hadronic part. Thus the main thrust of the R&D effort will concentrate on pursuing these three technologies. Considering the size and mass of these devices, there is a need to start a substantial effort in this coming year on the overall engineering design of the central calorimeter. There will also have to be a more modest R&D program on the forward calorimeter and a small effort on the choice of a pre radiator.

6.4 The Muon System

The R&D program on the muon system is needed to develop the technologies for muon momentum measurement, beam crossing tagging, and the muon trigger. The program will concentrate on Pressurized Drift Tubes or Limited Streamer Drift Tubes for muon tracking in the barrel region, Cathode Strip Chambers for the end cap regions, and Resistive Plate Chambers for the beam crossing tag and the Level 1 muon trigger for the barrel region. There will also be a need to get started on the engineering designs for the support structure, alinement system, and overall muon system integration. There will also be an effort to construct a full scale Prototype Tester at the SSC lab.

6.5 Central Tracking

The central tracker R&D effort will concentrate on Interpolating Pad Chambers for the outer tracker and on Silicon Microstrip Detectors for the inner tracker. While there are still many unanswered questions about the other technologies under consideration, i.e. straw tubes and scintillating fibers, the SDC tracking group is leading extensive R&D studies in both of these areas, and members of the GEM tracking group are participating in some of this work. These very limited resources must be focused on questions that are particular to the GEM design and are not pursued by the other detector. The benefits of "3D" devices such as Silicon Drift or Silicon Pixel detectors are also attractive to consider. It is felt, however, that both of these are at a less mature state of development and require greater resources to purse than are currently available. Their future development by others will be followed with great interest.

6.6 Trigger and Data Aquisition

The R&D program in this area will concentrate on three crucial topics: Analog Pipeline and ADC development, Digital Pipeline and Level 1 Trigger, and the development of electro-optical modulators to transmit analog signals on optical fibers.

6.7 Computing

A very modest effort on Computing for GEM will concentrate on refining the technical proposal for computing, support the necessary subsystem and integrated detector simulation work, and on laying the groundwork for the final GEM Computing System.

The funding required in Fiscal Year 1992 for the GEM R&D program is summarized in table 6.0-1.

Table 6.0-1 GEM Engineering and R&D Funding Requests for FY92 in FY92 K$

1.	System Integration		0*
2.	Magnet		5,000
	Engineering design	2,600	
	R&D on conductor etc.	2,400	
3.	Calorimetry		4,622
	Liquid Argon Krypton	1,170	
	Barium Fluoride	1,209	
	Scintillating Fiber	610	
	Forward Calorimeters	75	
	Preradiators	140	
	System Engineering	1,418	
4.	Muon System		2,700
	Pressurized Drift Tubes	400	
	Limited Steamer Drift Tubes	480	
	Cathode Strip Chambers	500	
	Resistive Plate Chambers	300	
	System Engineering	700	
	TTR Facility	240	
	SCARF Test Facilities	80	
5.	Central Tracking		935
	Interpolating Pad Chambers	335	
	Silicon Microstrip Detectors	600	
6.	Trigger and Data Aquisition		965
	Calorimetry	375	
	Central Tracker	465	
	Trigger and DAQ	125	
7.	Computing		100
	Software development tools	40	
	Simulation Integration	15	
	System Architecture Studies	45	
8.	GEM R&D Reserve		678
	GEM total for FY92		15,000

* Funded by Project Management Funds at the SSC, which are not a part of this request.

The initial requests from the various subsystems were considerably larger than these numbers, which are the results of extensive discussion within the collaboration reducing costs and prioritizing projects to fit into the available R&D budget of 15 M$. The GEM R&D plan and funding requests are described in much more detail in a document "The GEM Engineering and R&D Proposal" submitted to the SSC Laboratory on Nov. 27, 1991.

Acknowledgements

We gratefully acknowledge the support staff of the SSCL who worked tirelessly to put this document together. We wish to especially acknowledge Tom Coyne, Holly Durden, Linda Fowler, Bryan Lakey, Teresa McMillan, Wanda Rice, Cindy Thomas, and Lynn Webb. These people successfully weathered cantankerous physicists and horrendous hours to make this possible.

gem

November 30, 1991

SSCL-SR-1184
GEM TN-92-49

GEM Letter of Intent

November 30, 1991

Contact Persons

Barry Barish
Caltech
HEP 256-48
Pasadena, CA 91125
818/356-6684
Barish@Cithex.Bitnet

William Willis
Nevis Laboratory
Columbia University
P.O. Box 137
Irvington, NY 10533
914/591-8100, ext. 208
Willis@Nevis.Bitnet

Prepared in collaboration with the Superconducting Super Collider Laboratory, operated by the Universities Research Association Inc, for the Department of Energy under Contract No. DE-AC35-89ER40486.

GEM Collaborators

Adelphi University: R. Steiner

Universidad de los Andes: J. P. Negret

University of Arizona: G. E. Forden, J. P. Rutherfoord, L. Shaver, M. A. Shupe

Beijing Glass Research Institute: G. Chen, Z.Z. Dai, X.Y. Dong, Y.C. Gao, T.Z. Li, G.T. Liu, Z.Q. Liu, S.Q. Man, S.X. Ren, Z.L. Su, Y.T. Wang, O. Wen, H. Xiao, H.Z. Yang, F.C. Zhang, F.Y. Zhang, J. Zhang, J.Q. Zhang, Y.N. Zheng

Beijing University, China: D. Jiang, C. Lai, H. Liu, S. Xia, Y. Ye

Institute of High Energy Physics, Beijing: W. Gu, Y. Gu, Y. Guo, Y. Huang, J. Li, C. Mao, H. Sheng, R. Xu, D. Zhang, B. Zhuang

Boston University: S. P. Ahlen, E. Booth, R. Carey, S. Dye, M. Golden, T. Hazen, D. Higby, T. Johnson, K. D. Lane, A. Marin, J. P. Miller, D. Osborne, B. L. Roberts, J. Shank, J. L. Stone, L. R. Sulak, D. Warner, J. S. Whitaker, R. J. Wilson, W. A. Worstell, B. Zhou

Brookhaven National Laboratory: M. S. Atiya, I-H. Chiang, B. Gibbard, H. Gordon, J. S. Haggerty, S. Kahn, H. W. Kraner, P. Kroon, D. Lissauer, L. S. Littenberg, H. Ma, D. Makowiecki, M. J. Murtagh, P. O'Connor, L. Paffrath, F. E. Paige, V. A. Polychronakos, S. Protopopescu, V. Radeka, D. C. Rahm, S. Rankowitz, P. Rehak, S. Rescia, L. Rogers, N. P. Samios, D. Stephani, I. Stumer, H. Takai, M. J. Tannenbaum, C. L. Woody, S. P. Yamin

Brown University: M. Widgoff

Bucharest University: C. Besliu

Institute of Atomic Physics, Bucharest: A. Aculai, C. Blaj, H. Bozdog, L. Butacu, M. Ciobanu, A. Dorobantu, D. Ighicianu, G. Pascovici, V. Popa, G. Radulescu, D. Spanu, C. Stan-Sion, V. Valeanu, K. Zimmer

University of California - San Diego: J. G. Branson, W. Brower, H. E. G. Kobrak, R. Masek, H.P. Paar, R. A. Swanson, M. Sivertz

California Institute of Technology: B. C. Barish, G. Gratta, M. Gruenewald, D. Kirkby, W. Lu, R. Mount, H. B. Newman, S. Shevchenko, X. Shi, Z. Y. Wei, H. Yamamoto, R.Y. Zhu

Carnegie-Mellon University: M. J. Clemen, R. Edelstein, A. Engler, T. Ferguson, R. W. Kraemer, J. S. Russ, R. B. Sutton, H. Vogel

Changwon National College, Korea: C.H. Hahn

Chonnam National University, Korea: H.I. Jang, J.Y. Kim, T.I. Kim, I.T. Lim, M.Y. Pac

CINVESTAV, Mexico: H. Castilla-Valdez, G. Herrera-Corral

Columbia University: Y. Au, E. Aprile, A. Bolotnikov, T. Bolton, D. Chen, M. Leltchouk, M. Moulsen, R. Mukherjee, J. Parsons, P. C. Rowson, M. Seman, M. Shaevitz, W. Sippach, W. Willis

University of Delhi South Campus: V. Kapoor, R. K. Shivpuri

Draper Laboratory: F. Ayer, C. Elder, T. Hamilton, M. Hansberry, F. Nimblett, D. Sullivan, E. Womble

Drexel University: C. Lane

Joint Institute for Nuclear Research, Dubna: G.D. Alekseev, A.V. Bannikov, L.S. Barabash, S.A. Baranov, D.A. Belosludtsev, Yu. E. Bonyushkin, V. N. Bychkov, G.A. Chelkov, Yu. V. Ershov, V. Frolov, I.A. Golutvin, N.V. Gorbunov, Yu. A. Gornushkin, V.A. Kalinnikov, M.N. Kapishin, A.G. Karev, V.Yu. Karzhavin, M. Yu. Kazarinov, V. D. Kekelidze, S. V. Khabarov, V.S. Khabarov, B.A. Khomenko, N. N. Khovansky, Yu.T. Kiryushin, O. Klimov, A.V. Korytov, V.M. Kotov, Z.V. Krumstein, P.A. Kulinich, G.A. Kvirikashvili, V.N. Lysiakov, A.L. Lyubin, A.V. Makhankov, V.L. Malyshev, Yu.P. Merekov, S.A. Movchan, A.A. Nozdrin, A.K. Odishvili, A.G. Olshevski, V.D. Peshekhonov, Yu.P. Petukhov, A.A. Popov, D. Pose, T. Predo, T.G. Progulova, V.A. Sashin, Yu.V. Sedykh, S.Yu. Selyunin, D.A. Smolin, V.N. Spaskov, G.T. Tatishvili, L.G. Tkatchev, V.V. Tokmenin, L.S. Vertogradov, A.V. Vishnevsky, V.S. Yamburenko, A. I. Zinchenko

Fairfield University: D. R. Winn

Universidad de Guanajuato, Mexico: A. Gonzalez, A. Morelos, G. Moreno, L. Villasenor

Gunsan National University, Korea: J.Y. Ryu

Gyeongsang National University, Korea: K.S. Chung, S. H. Chung, I. G. Park, J. S. Song, C.S. Yoon

Universität Hamburg: E. Fretwurst, G. Lindstroem, V. Riech

Harvard University: E. Carlson, E. H. Simmons

University of Science and Technology of China, Hefei: Z. H. Bian, M. F. Cai, Y. M. Fang, R. D. Han, L. Y. Hao, X. S. Lin, B. A. Liu, W. Mei, Q. C. Shi, H. M. Wang, Z. M. Wang, S. L. Wu, S. L. Xing, J. H. Xu, X. L. Xu, K. Z. Xu, B. X. Yang, B. J. Ye, X. Q. Yu, J. Zhang, Y. Z. Zhou

University of Houston: K. Lau, B. W. Mayes, L. Pinsky, J. Pyrlik, R. Weinstein

University of Iowa: N. Akchurin, D. Kadrmas, K. Langland, E. R. McCliment, Y. Meurice, F. Olchowski, Y. Onel, M. Reno, V. Rodgers

Indiana University: E. D. Alyea, C. Bower, M. Gephard, R. M. Heinz, S. Mufson, J. Musser, S. Nutter, J. Pitts

Korea University: S. D. Chang, B.G. Cheon, J. H. Cho, C. O. Kim, T.Y. Kim, S. B. Lee, S.W. Nam

Kurchatov Institute of Atomic Energy: M. A. Vasiliev

Lawrence Livermore National Laboratory: E. Ables, R. Bionta, J. M. Bowers, H. C. Britt, M. H. Capell, A. K. Chargin, G. A. Deis, O. D. Fackler, J. Heim, C. Johnson, M. Lowry, C. F. McConaghy, M. Mugge, K. M. Skulina, K. VanBibber, T. J. Wenaus, S. Wineman, C. R. Wuest

Lebedev Physical Institute: V. Tikhomirov

Los Alamos National Laboratory: R. Barber, J. G. Boissevain, M. Brooks, D. Brown, T. Coan, R. M. Farber, S. F. Hahn, J. Kapustinsky, W. W. Kinnison, K. S. Lackner, A. S. Lapedes, D. M. Lee, W. B. Maier, G. B. Mills, G. H. Sanders, D. Sharp, B. Smith, W. F. Sommer, W. E. Sondheim

Louisiana State University: R. McNeil

Marshall Space Flight Center: K.H. Moom

Martin Marietta Astronautics: J. Coulson, N. J. DiGiacomo, B. Easom, K. Killian, L. Mason

Massachusetts Institute of Technology: P. Burrows, W. Busza, Y-H. Chang, M. Chen, H. Ding, J. I. Friedman, M. P.J. Gaudreau, E. D. Hafen, P. Haridas, J. Kelsey, H. Kendall, V. Lebedenko, D.B. Montgomery, L. S. Osborne, I. A. Pless, L. Randall, L. Rosenson, R. Shuvalov, J. D. Sullivan, S. Sumorok, F. E. Taylor, R. Verdier, B. Wadsworth, X. J. Yan, X. Zhang

University of Michigan: D. Levin, S. McKee, G. Tarlé, A. Tomasch

Michigan State University: M. A. Abolins, C. Bromberg, R. J. Miller

University of Mississippi: L. M. Cremaldi, B. Moore, J. J. Reidy

Institute for Theoretical and Experimental Physics, Moscow: V. Balagura, A. Bolozdynya, Y. Efremenko, A. Golutvin, P. Gorichev, L. Gusev, Yu. Kamyshkov, I. Korolko, A. Koutchenkov, A. Kovalenko, L. Laptin, V. Lebedenko, P. Murat, V. Nagovitsin, A. Nepejpivo, A. Ostapchuk, F. Ratnikov, A. Savin, S. Shevchenko, K.Shmakov, I. Tikhomirov, V. Tchernyshev, V. Tchistilin, V.A. Vinogradov

Institute of Nuclear Physics, Novosibirsk: L. Barkov, D. Grigoriev, B. Khazin, S. Klimenko, E. Kuraev, M. Leltchouk, V. Malyshev, A. Maslennikov, S. Redin, Yu. Shatunov, E. Solodov, A. Onuchin, V. Panin, S. Peleganchuk, V. Sidorov, Yu. Tikhonov

Institute of Nuclear Problems, Minsk: M. Baturitsky, A. Degtiarev, A. Kubasov, V. Mikhailov, V. Shuljak, N. Shumeiko

Moscow Engineering Physics Institute: V. Grigoriev, P. Nevski, M. Potekhin, A. Sumarokov, V. Tcherniatin, A. Vanyashin

Moscow State University: A. A. Arodzero, G. Bashindzhagyan, P. F. Ermolov, Yu. V. Fisyak, A. N. Larichev, M. M. Merkin, V. S. Murzin, N. A. Sotnikova, A. G. Voronin, S. A. Zotkin, V. Yu. Zhukov

National Teacher's University, Korea: S. N. Kim

Northwestern University: D. Buchholz, B. Gobbi, H. Schellman

Oak Ridge National Laboratory: M. L. Bauer, S. Chae, H. O. Cohn, C. Eberle, Yu. Kamyshkov, J. Moore, F. Plasil, K. Read, M. Rennich, R. A. Todd, K. Young

University of Oregon: J. E. Brau, R. Frey, K. Furuno, D. M. Strom, C.J. Zeitlin

University of Pittsburgh: W. Cleland, E. Stern

Princeton University: P. Denes, M. Ito, D. Marlow

Riken Institute: M. Suzuki, T. Takahashi

University of Rochester: T. Ferbel, G. Fanourakis, M. Zielinski

Rutgers University: P. Jacques, M. Kalelkar, R. J. Plano, P. Stamer, G. B. Word

St. Petersburg Nuclear Physics Institute: V.T. Gratchev, A.G. Krivshich, O.E. Prokofiev, V.M. Samsonov, V.V. Sarantsev, N. K. Terentyev

Saitama University: K. Masuda, E. Shibamura

Universidade de São Paulo: O. P. Eboli, C. O. Escobar, P. Gouffon, M. Luksys, S. F. Novaes

Shanghai Institute of Ceramics: X.L. Fang, P.X. Gu, J.K. Guo, G.Q. Hu, S.K. Hua, Z. D. Ji, P.J. Li, D.Z. Shen, G.S. Shen, E.W. Shi, W.T. Su, Z.Y. Wei, Y.Y. Xie, L. Xu, Z.L. Xue, D.S. Yan, Z.W. Yin, X.L. Yuan, G. M. Zhao, Y.L. Zhao, W.Z. Zhong, R.M. Zhou

Shanghai Institute of Nuclear Research: J. Bao, D. Cao, S. Chen, D. Jiang, X. P. Li, S. Lin, H. Liu, T. Rong, L.R. Shen, K. Sheng, H. Wan, F. H. Yu, W. H. Zheng, D. Zhu, F. Zhu

Sookmyeong Women's University: J.N. Park

University of South Carolina: C. Rosenfeld, J. R. Wilson

Southern Methodist University: F. Olness, R. Stroynowski, V. Teplitz

SSC Laboratory: L. R. Cormell, P. Dingus, M. Harris, J. Kuzminski, A. W. Maschke, W. K. McFarlane, N. Mehta, R. Meinke, G. Mitselmakher, K. Morgan, B. Parker, L.A. Roberts, B. Scipioni, R. Soundranayagam, F. Stocker, J. Thomas, A. Vaniachine, L. Villasenor, G. P. Yost

State University of New York at Albany: M. S. Alam, I.J. Kim, Z.C. Ling, B. Nemati, J.O'Neill, H. Severini, C.R. Sun

State University of New York at Stony Brook: R. Engelmann, C.K. Jung, M. D. Marx, R. L. McCarthy, M. Mohammadi, M. Rijssenbeek, C. Yanagisawa

Syracuse University: G. C. Fox, W. Furmanski, T. Haupt

Technion - Israel Institute of Technology: J. Goldberg

Tbilisi State University: N. S. Amaglobeli, W. P. Dzhordzhadze, A. J. Mchedlishvili, D. A. Mzavia, R. G. Shanidze, F. G. Tkebuchava

Tel Aviv University: G. Alexander, A. Beck, G. Bella, O. Benary, I. Cohen, E. Etzion, R. Heifetz, Y. Oren, N. Paz

University of Tennessee: S. Berridge, W. M. Bugg, Y.C. Du, R. Kroeger, I. Tsveybak, A. Weidemann

Temple University: S. H. Kettell, W. K. McFarlane

University of Texas at Austin: C. C. Allen, G. W. Hoffmann, K. Lang, M. R. Marcin, J. L. Ritchie

Texas A&M University: C. Gagliardi, G. Glass, R. Tribble, R. C. Webb

Tongji University, China: L. Y. Chen, J. Du, M. Gu, J. Wang, L. M. Wang, X. Wu, K. H. Xiang

Tsinghua University, China: J. An, K. Kang, Y. Lin, G. Liu, D. Mai, W. Ni, R. Shang, J. Wang, S. Xu, Z. Xu, J. Zhang

Vanderbilt University: R. S. Panvini, J. P. Venuti

Vassar College: C. Schwarz

Waseda University: T. Doke, A. Hitachi, N. Ishida, T. Kashiwagi, J. Kikuchi

University of Washington: V. Cook, J. Eisenberg, D. Forbush, P.M. Mockett, S. Sutlief, F. Toeus

Washington University: J. Beatty, W. Binns, D. Crary, D. Ficenec, J. Klarmann

Wonkwang University: S.Y. Bahk

Yale University: R. K. Adair, C. Baltay, R. Ben-David, W. Emmett, H. Kasha, S. L. Manly, S. Sen, J. Turk

TABLE OF CONTENTS

1

Introduction

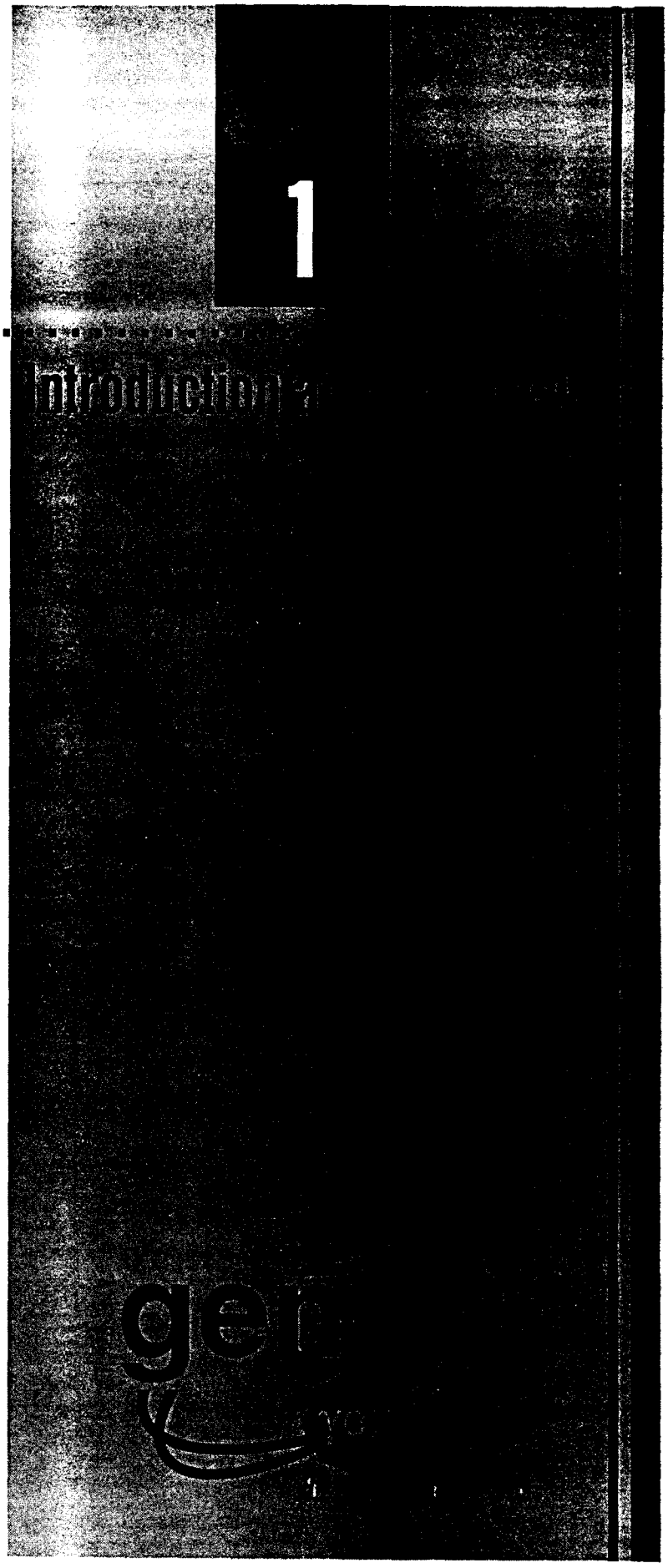

GEM

DETECTOR ISO SECTION (LAr OPTION)

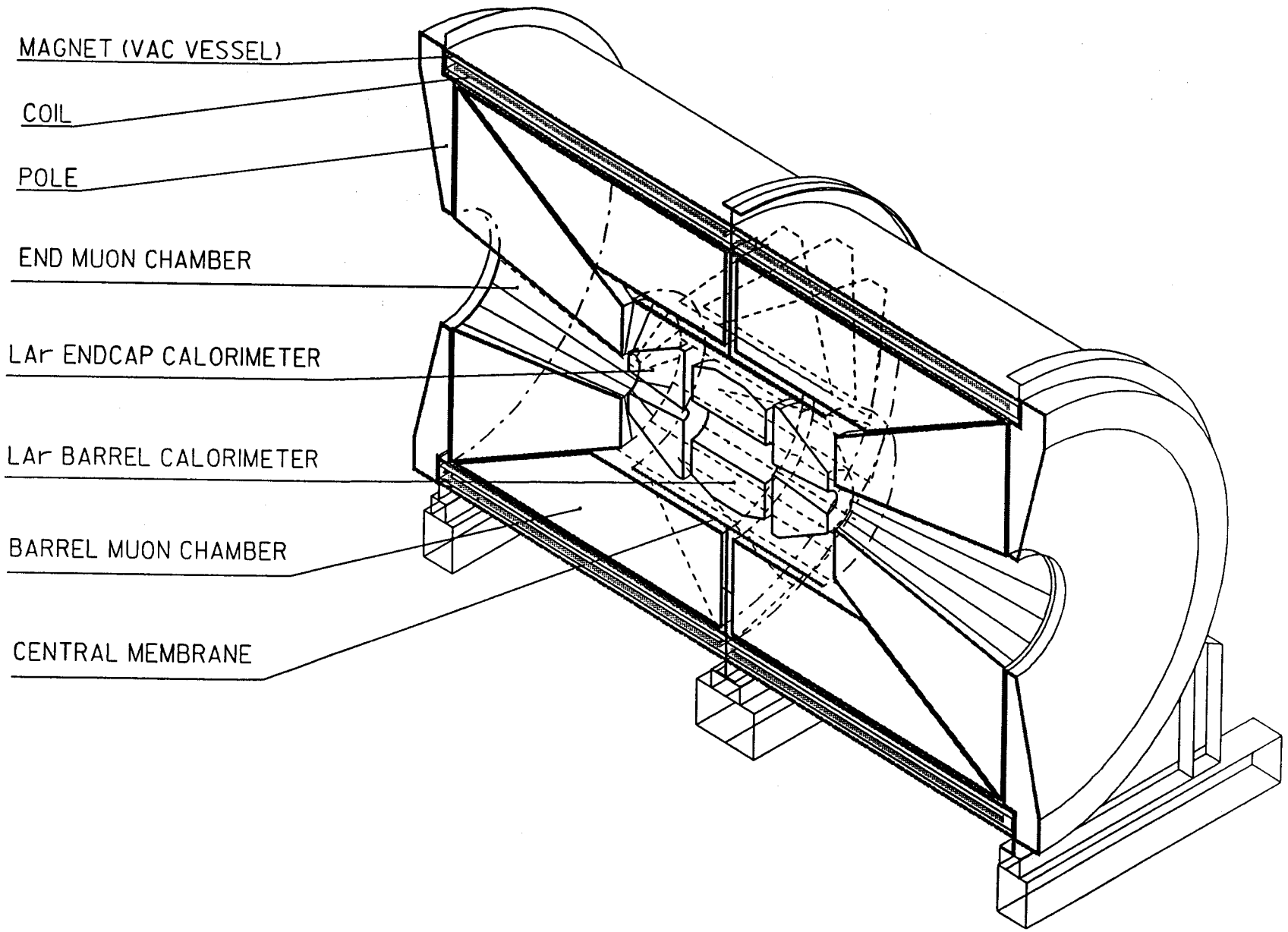

1.0 INTRODUCTION AND OVERVIEW

The construction of the Superconducting Super Collider offers an unprecedented increase in the energy available to reveal new aspects of the structure of matter. It has long been known that collisions with a small distance between two constituents in the incident protons are associated with the production of particles with large momenta transverse to the incoming protons, and that the characterisics of such collsions are controlled by the fundamental strong and electroweak interactions. This fact underlies the discovery of the $W^{\pm}$and Z^0 bosons at the SPS Collider at CERN and the continuing search for the top quark at the Tevatron Collider at Fermilab. With its much greater energy and luminosity the SSC will greatly extend such measurements. There are strong theoretical reasons to believe that this will lead to an understanding of the origin of the $W^{\pm}$and Z^0 masses, perhaps through the discovery of the predicted Higgs particle. It may also lead to an explanation of the quark and lepton masses, to the discovery of new and striking symmetries, such as the existence of supersymmetric particles—a whole world of particles mirroring the familiar particles but with different spin and higher masses, or to the discovery of completely new interactions.

In the realm of such short-distance collisions the particles of interest are not the mesons and nucleons but rather the particles which directly participate in the fundamental interactions. These are charged leptons — electrons, muons and taus; uncharged neutrinos; photons; $W^{\pm}$ and Z^0 bosons, which are detected by their decays into leptons; and quarks and gluons, which are not detected directly but reveal themselves as "jets" of many mesons and nucleons in a narrow cone. To study short-distance collisions at the SSC it is advantageous to design a detector which measures charged leptons, photons and jets, but largely ignores individual mesons and nucleons. This allows more freedom to concentrate on the most accurate possible measurement of the fundamental particles, and to adopt detection strategies which enable operation at a very high rate of collisions, as high as the billion per second which the SSC should reach after some development.

This document describes an experiment which has been designed on these principles. GEM stands for Gammas (photons), Electrons and Muons. Precise measurement of these will be the main emphasis of the detector, though jets will be measured as well. By finding how much transverse energy is missing in the collision, it will be possible to deduce the presence of energetic neutrinos.

Photons and electrons will both be accurately measured by the same device—an electromagnetic calorimeter. The intention is to measure the energy of high energy electrons and photons to an accuracy of better than one percent, while determining their position to about one millimeter. This opens up the possibility of discovery of the Higgs particles in the low mass region, around 80 to 140 Gev, where the decay into two photons is the only mode with a reasonably favorable signal-to-background ratio. GEM will excel at this difficult task. The precise energy measurement of electrons plays a vital role as well in the discovery of more-massive Higgs by the decay first into two Z particles, which yield four charged leptons. The background is more favorable in this case, but the rate is low and the discovery must be made with a small number of events. Such precision might

also be useful in the search for many other hypothetical particles.

To obtain this performance in the electromagnetic calorimeter, there is an ongoing program of research and development exploring the most promising techniques for giving the highest resolution in this range of energy. A relatively small tracking volume has been accepted in order to minimize the overall size of the calorimeter, which thereby gives greater freedom in choosing detector technologies and mechanical structures. A study of the many possible technologies has yielded two strong candidates which will give the best and most cost effective performance. These two technologies are noble-liquid ionization detectors and barium fluoride crystal scintillators. The goal is to make this important choice within one year.

Hadronic calorimetry is given less emphasis in GEM but is still important. It is needed to help identify photons, to search for possible substructure of quarks by looking for deviations from the predicted rates for jets, to contribute to the search for Higgs by detecting the decay of Z^0s to jets, and to detect neutrinos or other non-interacting particles by measurement of missing transverse energy. In the central region scintillating-fiber hadron calorimetry would be used with the barium fluoride electromagnetic calorimeter option or liquid ionization hadron calorimetry with the liquid ionization electromagnetic calorimetry option. The methods of extension of the calorimetry to the most forward angles is still under study.

The GEM design for muon measurement relies on tracking in a magnetic field outside the calorimeter, which is made sufficiently thick that the muon tracking is well-shielded from the high particle flux from the interaction point. Hence, it should work well even at the highest collision rates possible at the SSC. High precision on the muon momentum is attained by measuring the curvature in a magnetic volume. The track length will be about 5 m. Track detectors of high point accuracy and stable alignment which are relatively insensitive to the magnitude and direction of the magnetic field have been chosen. This gives more flexibility which is particularly important in the forward direction. Here, the choice of a detector relying on charge interpolation on cathode strips allows a convenient mechanical design. Such a design would adapt very well to the problems of rapidly varying density of background muons and required trigger granularity. An important consideration, particularly in the "barrel" region where most of the tracking detector area is found, is the choice of a detector which achieves approximately the desired tracking accuracy in a single measurement rather than by averaging many measurements.

The cost of the total system of magnet and tracking detectors within this strategy has been studied, with a performance goal for muon momentum measurement of 5% at 90° for muons of 500 GeV/c. A minimum has been found at fields near 0.8 T and the chosen magnet size. The cost of the magnet itself is dominated by conventional structures, since rather little superconductor is required. There are a number of advantages in a magnet with iron only in the poles which fill the

ends of the solenoid. The magnet is then relatively light compared to the many thousand tons which would be required for a return yoke, saving many months of installation time and a major cost as well. This also provides a useful region outside the coil in which, at some future time, additional tracking could be placed to yield a substantial improvement in accuracy at high muon momenta. The requirements for working in the fringe field of such a magnet have been studied, and will be summarized in section 2.2.

The measurement of particle momentum in a solenoidal field degrades rapidly at forward angles. The feasibility of improving the measurement for angles in the 10 to 30 degree range by adding iron cones to the poles is being studied, since potential improvements of more than a factor of two are possible.

The goals of tracking particles in the central volume inside the GEM detector have been carefully analyzed. The performance will inevitably be limited by the relatively small magnetic field and radius provided in the design, but there are compensating advantages for particle tracking itself. The number of tracks which curl up inside the tracking detectors is relatively small, reducing the load on pattern recognition. The small size of the detector structures gives a possibility of achieving a small amount of material and a low number of conversions of photons to electron pairs near the beam pipe. The current design of the tracker provides unambiguous three-dimensional space points. All of these things are important, given the aim of retaining tracking capability at very high collision rates. The details of the design are still evolving. Section 2.5 relates the present status of these studies.

The trigger system must cope with the succession of beam crossings every 16 ns with more than one event in each crossing. When a trigger is derived from one detector system, it is important that the data in other detector systems should be recorded in a way which allows the correlation to the same beam crossing. The trigger must be available quickly and the resulting strobe must be distributed back to the detector-mounted electronics in only a few microseconds so that the data buffers can be of the minimum length. Satisfactory solutions to these demands have been identified in a multilevel trigger system.

A great deal of engineering, and research and development must be accomplished in the year between the submission of the Letter of Intent and the Technical Proposal. The necessary work is briefly described here, and in greater detail in a series of proposals. The engineering is underway to give a preliminary cost estimate within less than two months, which will allow for design refinement to help maintain a total cost within the stated guideline of 500 M$.

The management of GEM has evolved since the collaboration was formed in June of 1991. The collaboration includes physicists who were working with L*, EMPACT, or TEXAS, and many who were new to the SSC program. An interim management scheme was adopted in the July meeting to carry through to the preparation of this Letter of Intent. A more formal plan is now being set up to allow GEM to proceed on to the next phase. An important goal of the collaboration is

the creation of a truly international framework for this experiment. Very extensive contacts have been established in many countries around the world and a large number of physicists from different countries have been invited to visit the SSC Laboratory. The leadership of the collaboration has already visited institutes in several countries and will continue to seek a very broad participation in GEM. Plans have also been made to include physicists from the international community in all levels of the management.

2

2.1

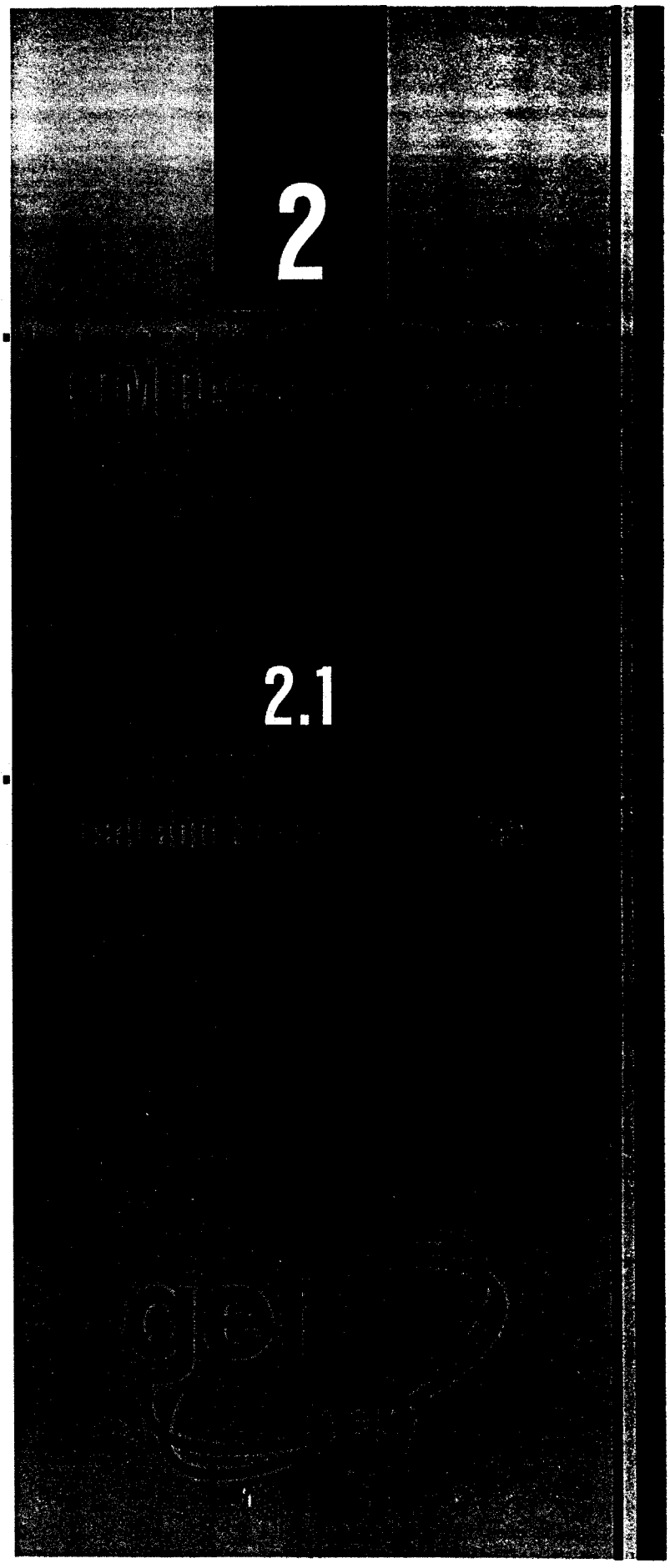

GEM'S EXPERIMENTAL HALL

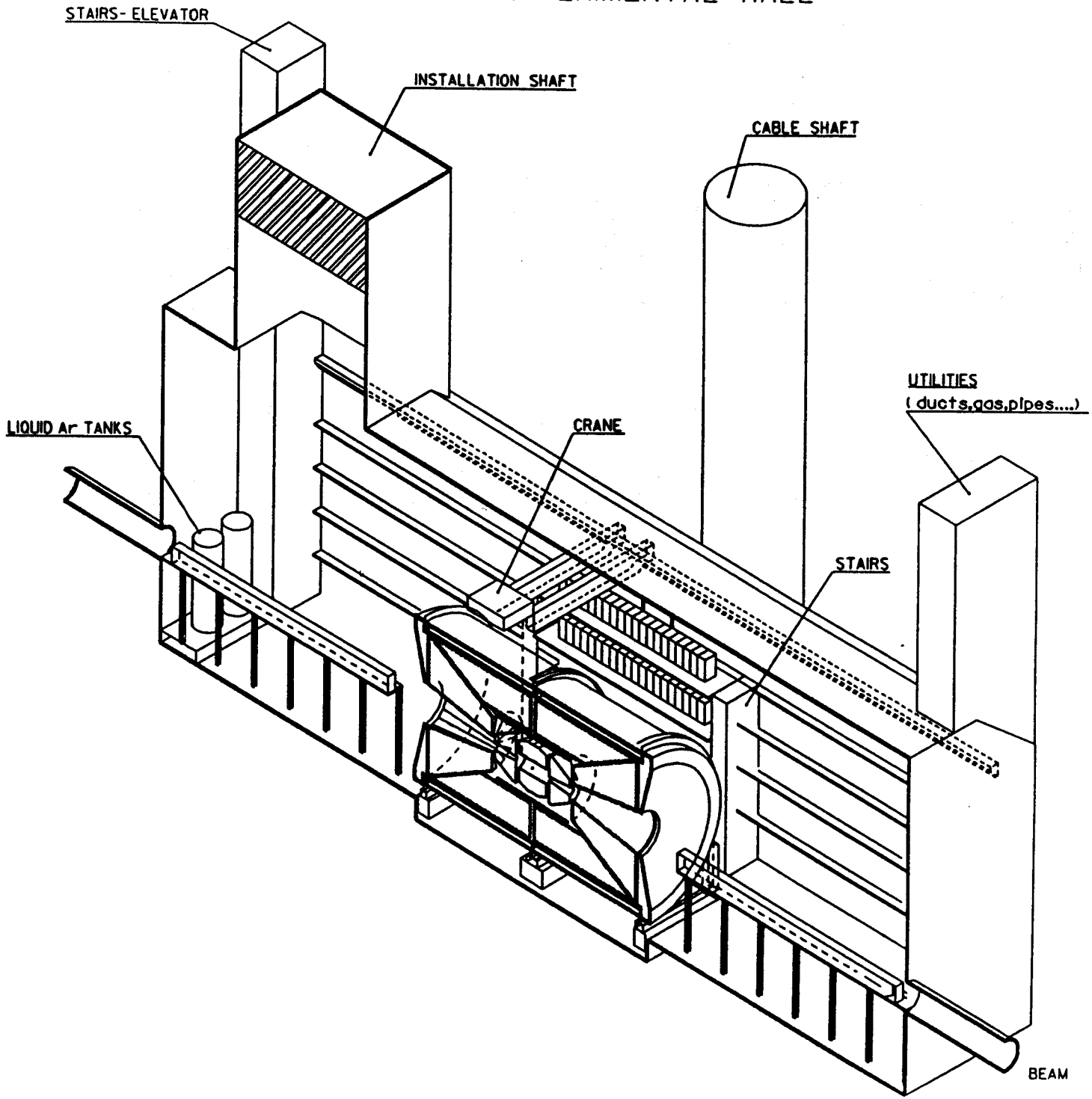

2.0 GEM DETECTORS

2.1 Detector Hall and Surface Facilities

Since the submission of the Expression of Interest (EOI), the conceptual design of the underground detector hall and surface facilities has undergone considerable study and revision. The design of a 26 m wide caverned hall at IR1, which had been the favored option by the architect/engineer firm PB/MK, has now been rejected based upon the results of geotechnical studies. A new design concept for a cut-and-cover hall at the East Campus site IR5 is under early study. A goal of this new study is the definition of the date upon which the underground hall will be available for detector component installation. Similarly, the definition of the required surface facilities is undergoing revision. The most significant issue related to the surface facilities is the need for the magnet coil fabrication hall early in 1993.

The original West Campus sites for GEM and SDC were located in Austin chalk, above a base of Eagleford shale. The stability of Austin chalk led to a recommendation that the smaller GEM detector be accommodated in a caverned hall with a maximum span of 26 m. This was the basis of the EOI design, and this concept placed no limitations on the detector and offered construction schedule advantages over the cut-and-cover construction method. A concern, at that time, was the poor stability of the underlying Eagleford shale.

Following additional geotechnical studies, PB/MK reported that the West Campus sites offered unacceptable foundation risks for the proposed major detectors, as the Eagleford shale reached maximum elevation in the detector site vicinities. The SSC Laboratory reviewed the recommendations and consulted with its own Physics Research and Conventional Construction Divisions, and with the SDC and GEM collaborations. This has resulted in a decision to relocate both major detectors on the East Campus where the Austin chalk offers superior foundation stability. The SSC Laboratory decision has been transmitted to the Department of Energy for approval of this project change. Pending this approval, both detector sites are now being planned at the conceptual level for the East Campus and mobilization for comprehensive geotechnical studies has begun. It is not known at this time whether the relocation will result in modified facility costs or delayed availability of the underground halls. These issues are being studied carefully by PB/MK.

The superior geologic characteristics at the East Campus promise several advantages for GEM. The hall can now be excavated by the cut-and-cover technique, which may permit greater hall width. This entails a small cost penalty which will not be accepted without offsetting technical advantages. The cut-and-cover technique permits additional installation shafts over the hall, within the excavation area, as these shafts require only emplacement of the shaft walls prior to the backfill, which would be reduced by the shaft volumes. Multiple shafts may offer significant installation and maintenance flexibility. This may reduce the required installation period. Hall width choices are permitted which may include the

volumes for forward electronics racks and underground cryogenic equipment for the magnet and cryogenic calorimeter options. These possibilities are under vigorous study by the SSC Laboratory, PB/MK, and GEM. The figure on the divider page shows a cutaway of the single-shaft cut-and-cover hall concept now being studied. It should be noted that prior to the decision to relocate the detector halls, the GEM collaboration, working with the SSC Laboratory, completed the version of the document specifying [1] the facility requirements. As these requirements are not site specific, they are guiding the East Campus design study.

Selection of the specific sites at the East Campus for GEM and SDC will depend upon the detailed geologic characteristics discovered during geotechnical studies. Each detector has distinct support concepts and floor stability requirements. The current concept for the SDC hall has a wider span. The difficulty of excavating the wider hall in the Taylor marl layers at IR5 has resulted in a preference for the SDC hall to be constructed at IR8. The slightly greater depth of the IR5 site provides the option of reduced return flux at the surface from the GEM solenoid. For these reasons, current planning assumes location of GEM at IR5, and SDC at IR8.

Figure 2.1-1 shows the current layout concept for surface facilities at the IR5 site. The halls are arranged so that transport of the large coil and calorimeter assemblies is over a very short distance to the headhouse area through which they will be lowered into the hall. The magnet fabrication schedule is very tight. A critical milestone is the availability of the surface hall for magnet coil fabrication. This hall is required in September 1993. Since this hall is located just outside the excavation region for the underground facility, no interference is expected in the two schedules.

However, it is a major current concern that the required change control procedures, which will ratify the decision to move the major detectors to the East Campus, will delay Title I design of the magnet fabrication hall. This could result in insufficient time to fabricate the magnet, install and test it, and complete the detector installation prior to the 1999 commencement of the physics program. The GEM collaboration is working closely with the SSC Laboratory, PB/MK, and the DOE area office, to facilitate rapid decisions on the critical issues identified in this chapter.

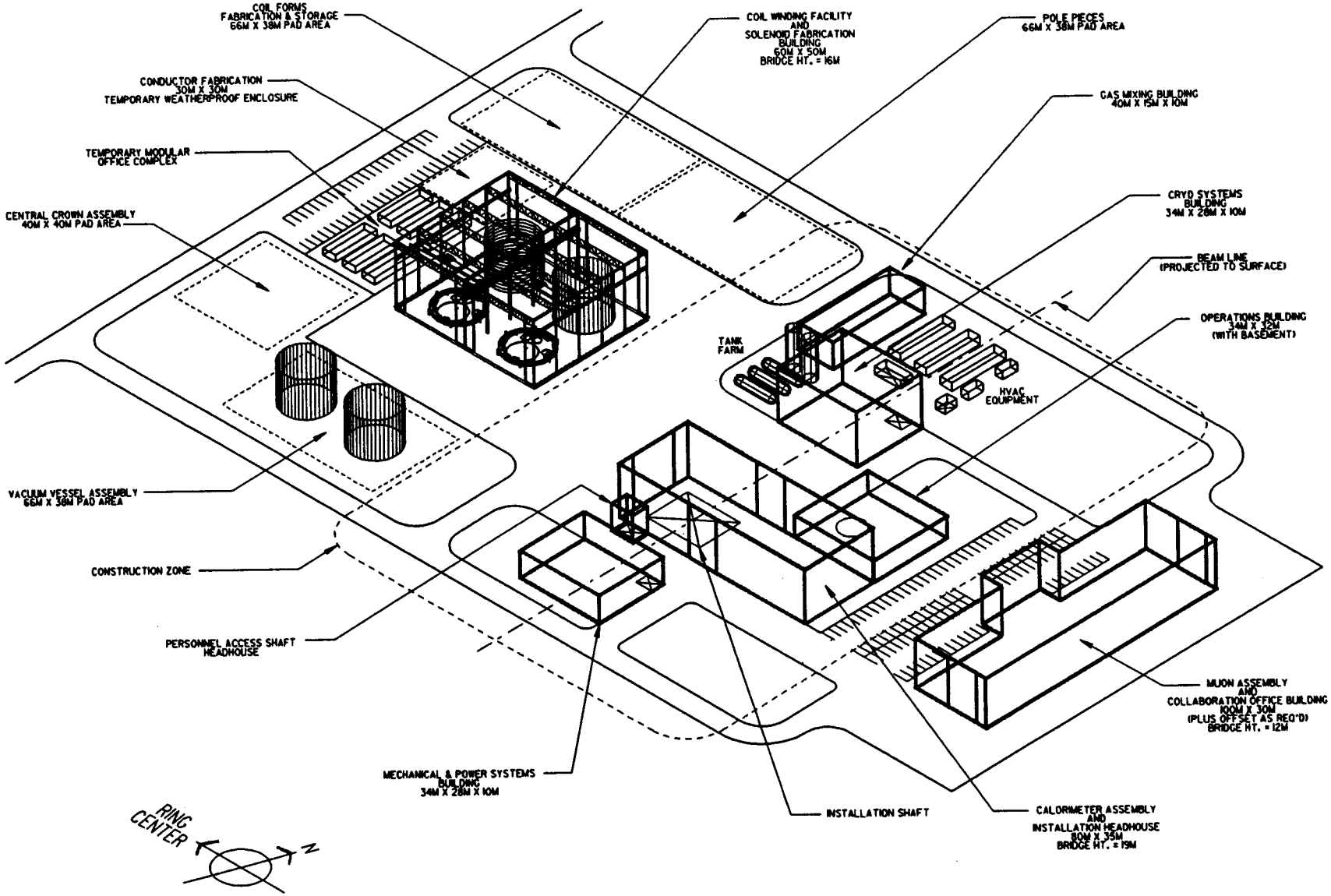

GEM SURFACE FACILITIES

Figure 2.1-1 GEM Surface Facilities Conceptual View

[1] Element specification for the Gamma, Electron, Muon Detector Collaboration (GEM) Experimental Facilities (User Requirements), GCT-000001, November 6, 1991.

2

2.2

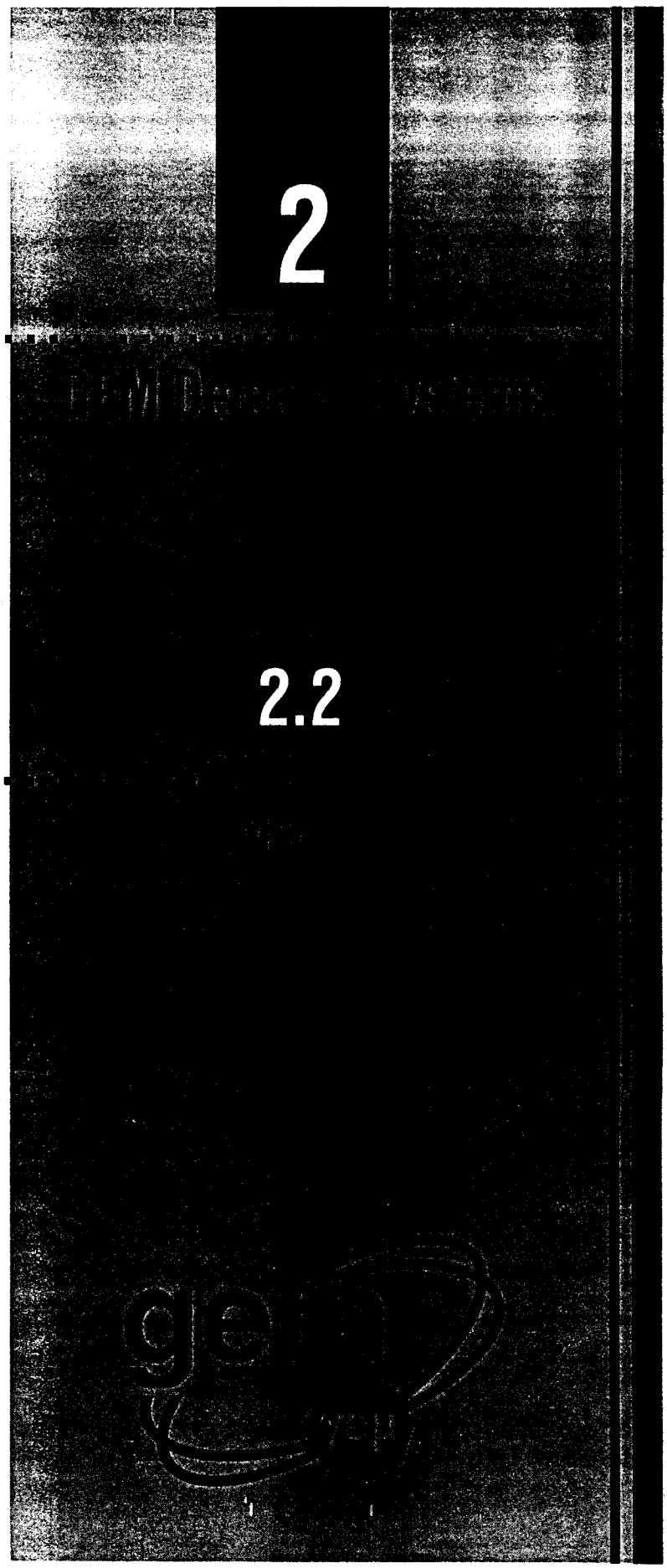

GEM MAGNET

WITH THICK POLE PIECES

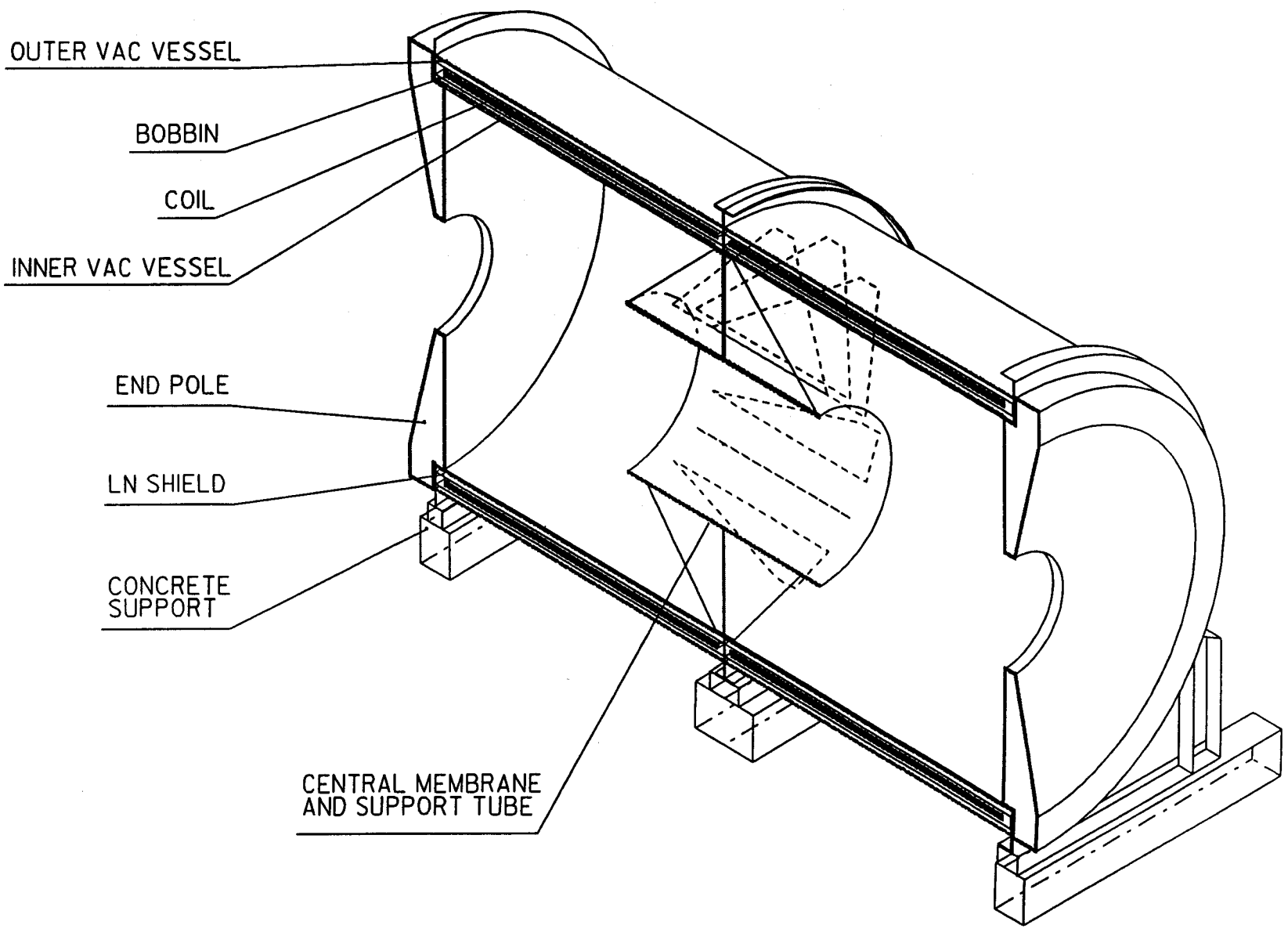

2.2 Magnet

The physics goals of the GEM experiment include, among others, high resolution measurements of the muons emitted at large transverse momentum in proton - proton collisions. The aim of the design concept is to have 5% momentum resolution for 500 GeV muons at 90 degrees assuming 100 micron measurement errors and no vertex constraint. Such resolution should be achieved over a broad central region of rapidity in order to provide sufficient acceptance for multimuon events. In addition, it is desirable to avoid placing material in front of the calorimeters which would reduce their performance. These requirements lead to the concept of a large aperture solenoidal magnet with muon tracking stations inside the uniform magnetic field.

The GEM Collaboration is proposing a large superconducting solenoid with field shaping iron end poles. Within this concept, the design has not yet been optimized either for the field or for the radius, but the proposed magnet could have a field of 0.8 T, an outside diameter of 20.4 m, an inner diameter available for tracking and calorimetry of 16.6 m, and a pole-to-pole inside length of 29 m. Other relevant parameters are: total stored energy of 2.04 GJ, operating current of 52.5 kA, discharge time of about 2 hours and an emergency discharge time of about 5 min. A list of parameters is given in table 2.2-1; the schematic drawing of the magnet is shown in figure 2.2-1. The corresponding resolution of the muon measurement expected for this baseline request and muon system performance described in the next section is shown in figure 2.2-2.

The design team comprises magnet designers and engineers from the MIT Plasma Fusion Center, Lawrence Livermore National Laboratory and National High Magnetic Field Laboratory (Florida). In addition all aspects of the design have been scrutinized by the GEM Magnet Technical Panel convened by the SSCL to study issues related to the feasibility of the technical concept, the cost estimate, the proposed schedule and operational issues. The membership of the panel included national and international magnet design experts as well as representatives of major industrial firms. The Panel found the concept of the GEM magnet to be feasible, the cost estimate to be credible and the construction schedule tight but possible. All recommendations of the panel are incorporated in the present design.

Table 2.2-1 Major Parameters List

1.	Central induction	0.80 T
2.	Mean radius of windings	8.9 m
3.	Outer radius of outer cryostat vessel	9.45 m
4.	Inner radius of inner cryostat vessel	8.40 m
5.	Coil length, end-to-end (per half)	14.44 m
6.	Cryostat vessel length	30.0 m
7.	Conductor length (total)	24 km
8.	Number of turns	408
9.	Total mass of coil windings (per half)	238 t
10.	Total mass of cryostat vessel (each half)	717 t
11.	Total mass of iron end pole (each)	2950 t
12.	Radial pressure on windings	255 kPa
13.	Inductance	1.47 H
14.	Number of ribs per coil assembly	3
15.	Central membrane maximum Z	0.025 m
16.	Winding minimum Z	0.25 m
17.	Axial force on poles	63.5×10^6 N
18.	Axial force on conductor	27.9×10^6 N
19.	Magnet axis height above hall floor	13.0 m

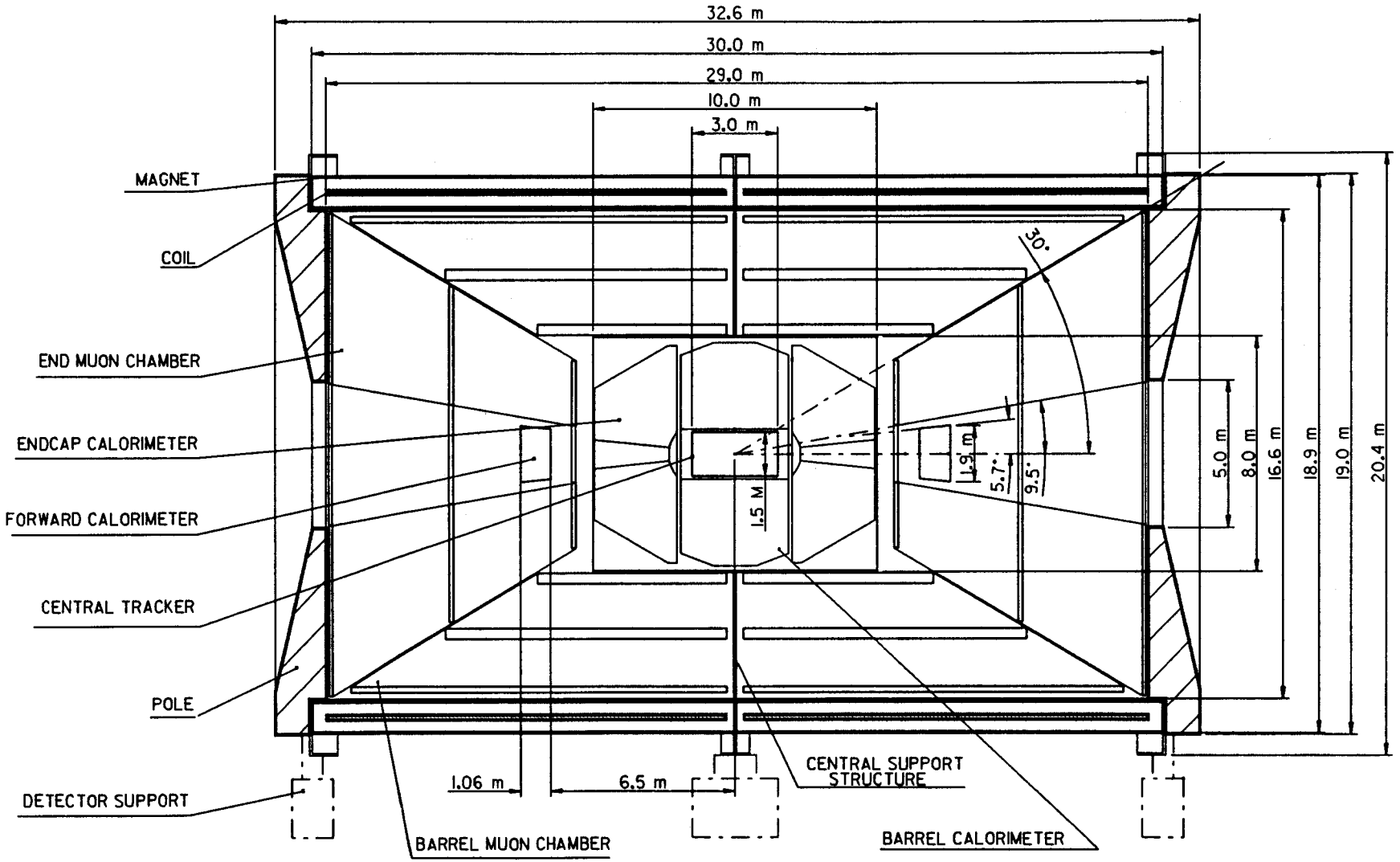

Figure 2.2-1 Schematic Drawing of the Magnet

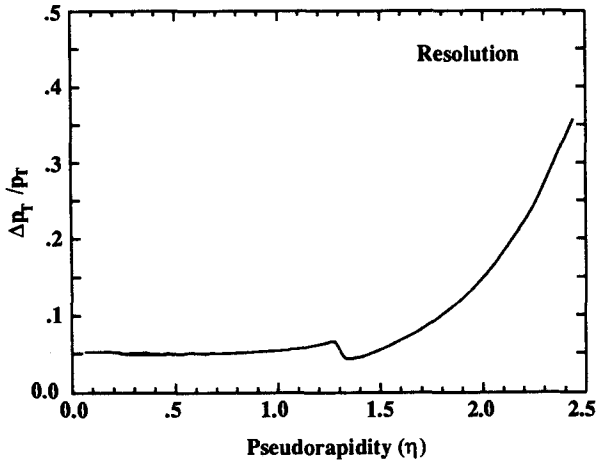

Figure 2.2-2 Momentum resolution of muons with p_T = 500 GeV as function of the pseudorapidity

The magnet will be constructed from two independent sets of single layer windings. The coil will be wound on the inner side of the 5 cm thick bobbin. The bobbin will be constructed in 24 separate cylindrical sections, 1.2 m long each. Each section will be wound separately. The winding will be surrounded by a liquid nitrogen radiation shield. Details of the assembly are shown in figure 2.2-3. The coil assemblies will be supported within the vacuum vessel by titanium rods connecting to both the 4 K coil assembly at one end and to the ambient temperature vacuum vessel at the other end. Support against gravity will be provided by a system of 16 titanium rods oriented roughly tangentially to the bobbin and connected to each end of the bobbin. This arrangement distributes the loads over 8 support points, and minimizes localized stress. Furthermore, the supports allow some axial and radial freedom to accommodate cooldown motion. Support against the axial Lorentz force on the coil will be provided by a set of 16 axially oriented rods providing a tensile preload and preventing any buckling problems.

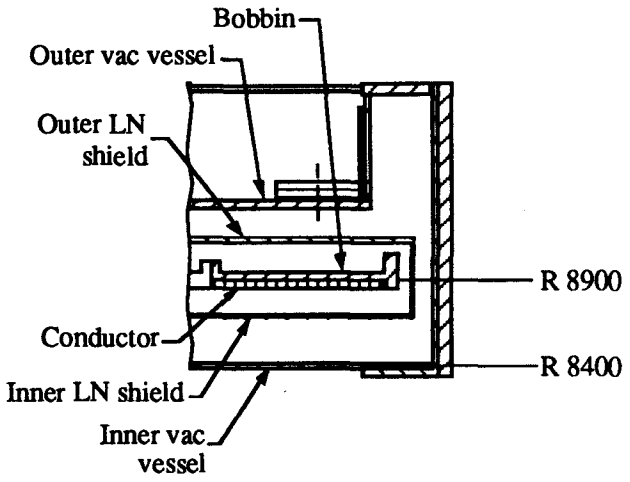

Figure 2.2-3 Details of the magnet coil assembly (dimensions in mm)

The mechanical structure will have a central support membrane sandwiched between the two halves. The membrane will provide structural support for the cryostat as well as a support for the muon chambers. The membrane will also support a tube containing calorimeters and the central tracker.

The cooling for the magnet coil will be obtained by the natural convection flow provided by the thermal syphon method. The tubing attached to the outside of the coil bobbin will be connected to headers on the top and bottom to promote free convection. The system can handle all heat loads including thermal radiation, cold mass support conduction and heating in the area of conductor joints. A separate low-flow loop will provide liquid helium to the conductor itself, but this helium will be used only for stabilization, not for cooling. The refrigeration system will be patterned on that of the accelerator.

There are several proposed conductor designs. All of them include standard niobium-titanium conductor with either copper or aluminium stabilizer. The designs differ in the liquid helium cooling arrangements ranging from a passive to a forced flow scheme. The choice of the conductor will be made based on its stability and the manufacturing scheme. A high priority R&D program of conductor development and tests will be initiated in the next few months. The design and costing is based at present on a high stability "cable-in-conduit" conductor with copper stabilizer.

The total cost of the magnet and its mechanical support system is estimated to be 104.7 M$ including contingency. The breakdown of the cost estimate for major subcomponents is given in table 2.2-2.

Table 2.2-2 Cost estimates for magnet subcomponents in k$

		Cost Estimate	Contingency
1.	Magnet R&D	4871	0
2.	Preliminary Design	4903	0
3.	Coil assemblies	36446	10255
4.	Poles and support	14874	3138
5.	Central detector support	4095	983
6.	Power/protection	832	136
7.	Cryogenics	8680	1418
8.	Vacuum	856	97
9.	Controls	285	51
10.	Installation	6925	1799
11.	Management	3552	568
Total		86319	18445
Grand total			104764

The iron magnet poles serve as field shaping components and not as a flux return. In the proposed design, there will be a fringe magnetic field in the experimental hall, access shafts and on the earth's surface immediately above the interaction region. The fringe field and the corresponding forces on ferromagnetic components has been calculated at all points in the hall, access shafts and on the surface using full two-dimensional, axisymmetric, finite element programs developed for plasma fusion confinement calculations. The field in the underground area will range from about 0.2 T close to the magnet poles to ~0.02 T at the end of the experimental hall. All the forces on the structural components of the hall, including crane rails and supporting structure appears to be small except in the immediate vicinity of the poles. The surface field will have a maximum of about 40 gauss immediately above the detector and the 5 gauss perimeter will extend over an oval area of about 200 by 180 m. This field will require local shielding of operation and control areas on the surface and institution of special operational procedures for the GEM experiment. These procedures, described in [1], will be based on experiences gained at other large magnet facilities with unconstrained fields (MRI hospital installations, plasma fusion facilities, FNAL 15' Bubble Chamber etc.). They will include restricting access to the detector when the magnet is on, securing ferromagnetic objects in the hall, etc. Local shielding of specialized equipment may be needed, although most of the problems associated with equipment working in a magnetic field can be minimized by the choice of less sensitive components and alignment with respect to the field lines. The surface area affected by the magnetic field will be inaccessible to the public. A proposal to shield the surface with a 15 cm thick iron plate appears to be a possible and cost

effective backup scheme. Complete discussion of fringe field related issues can be found in [1].

The magnet represents a critical path item in the GEM detector construction schedule. The experiment has to be completed at the beam turn-on time. The construction schedule derived with this constraint requires that the magnet should be manufactured, assembled and tested in the experimental hall before the end of September 1996. Rapid progress mandated by such an aggressive construction schedule requires timely completion of the engineering design studies and an early decision on the manufacturing scheme. In particular, intensive studies of the conductor and its stabilizer and of the winding scheme and the associated tooling are part of the FY92 R&D proposal. The engineering studies planned for the coming year include completion of preliminary design and specifications for mechanical supports, cryogenic, power supplies and power protection systems and for the magnet control and monitoring systems. The R&D program includes study leading to the choice of the conductor design, development and test, in conjunction with industrial partners, of a sample length of the conductor and development of a technique for making conductor joints. It includes also design and development of specialized tooling for conductor manufacturing and winding. Detailed engineering models [1] of the magnet and of the muon system will allow for optimization of the design with respect to the cost, size, and field value.

Because of its size, the proposed magnet will have to be constructed on site at the SSC Laboratory. A manufacturing plan calls for construction of two halves of the coil and the associated cryogenic systems in the surface building situated near the interaction region, and a complete assembly and test of the magnet in the underground hall. This plan requires the availability of the surface fabrication hall in 1993 and early definition and implementation of procurement strategy.

Additional design work on the improvement of the momentum resolution at larger values of rapidity has been initiated as well. The most promising option is to modify the shape of the iron pole to concentrate magnetic field flux at small angles. More detailed discussion of such options is given in the next section. All the options studied preserve the capability of the GEM detector for further improvements of muon momentum resolution by addition of muon chambers outside of the magnet coil.

---

[1] Considerations Leading to the Choice of Open Field Magnet, GEM Note No. GEM TN-91-30.

2

2.3

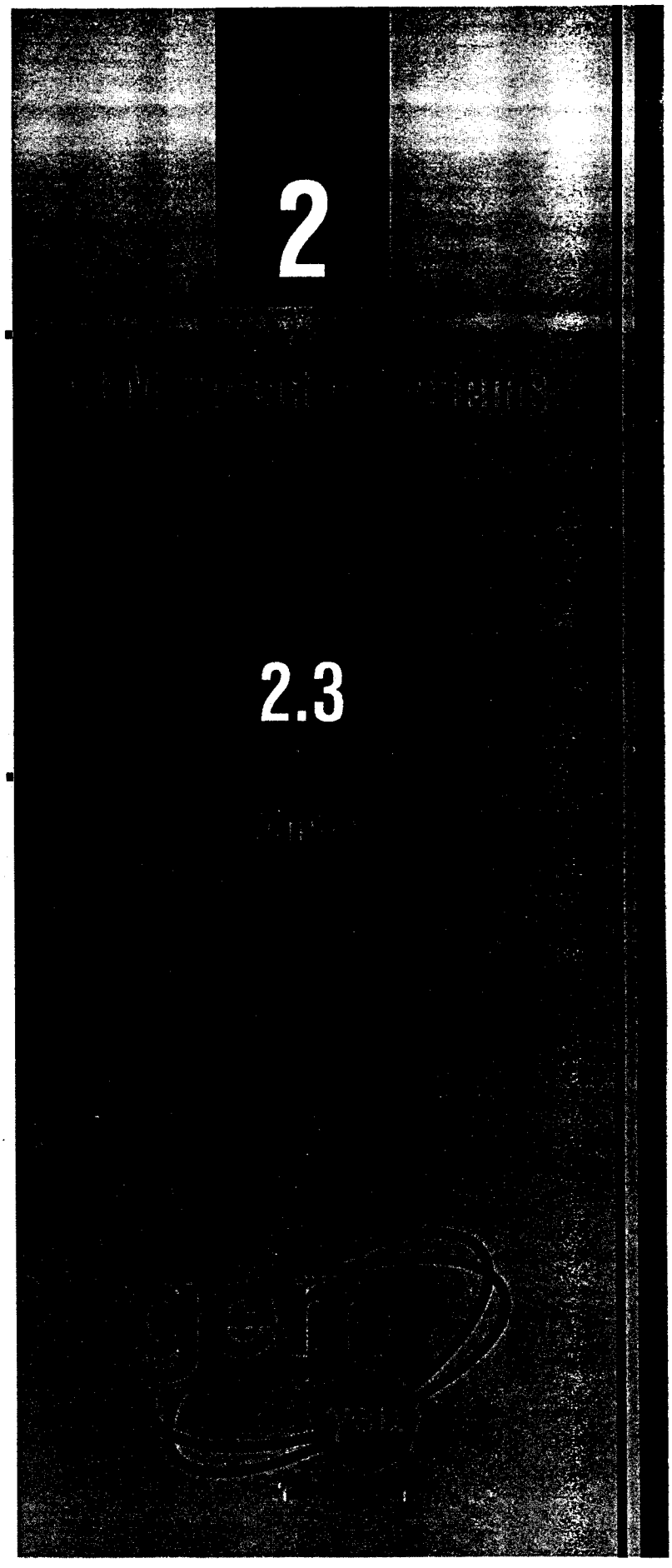

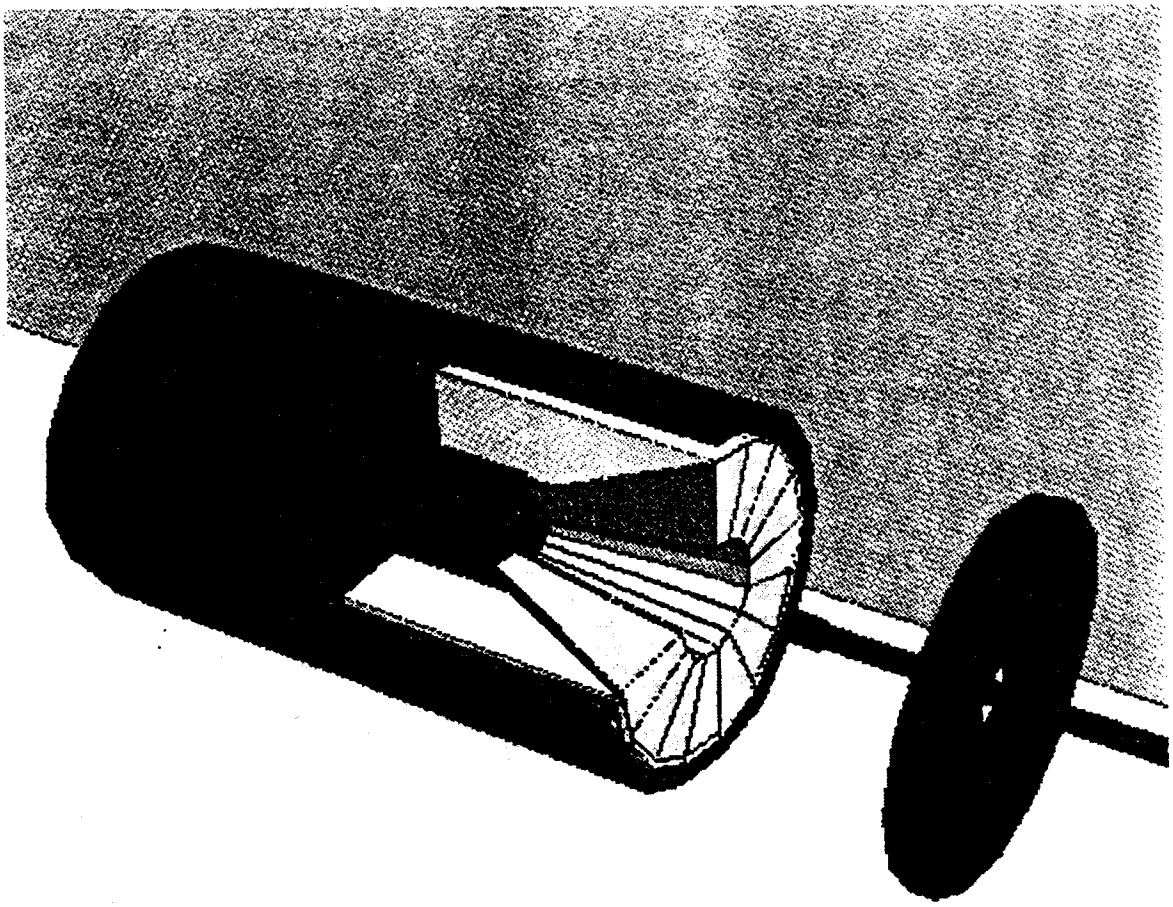

GEM Muon Subsystem

2.3 Muons

2.3.1 Introduction

The detection and momentum analysis of muons provide important access to rare and potentially important physics at the SSC. Reactions where the muon system is essential include: Higgs scalar production, production of new heavy Z bosons, gauge boson scattering, the high mass Drell-Yan process, technicolor, and supersymmetry. The expectation is that all of these processes, if real, will occur at a low rate.

To access this important physics, the GEM Muon System will furnish the following:

(1) muon identification,

(2) charge assignment,

(3) p_T trigger - both Levels 1 and 2,

(4) beam crossing time marker, and

(5) muon momentum determination from a few GeV/c to a few TeV/c.

Muons are unique in their great penetrating power, providing a distinct advantage in carrying out searches for new physics at the SSC. With sufficient material in the electromagnetic and hadron calorimeters, particle rates in the muon system are low enough to enable triggering and momentum measurements to be made reliably with luminosities at the $10^{34}\,cm^{-2}\,s^{-1}$ level. The GEM muon system will detect muons with 98% solid angle coverage and with high precision measurements of the momenta.

Our design goal of a muon system with large background rejection and good momentum resolution, which can be triggered selectively on large transverse momentum, requires that the detection elements be placed outside the hadron calorimeter. Figure 2.3-1 shows a schematic of the GEM muon system. Chambers are located in three superlayers between the calorimeter and the magnetic coil or endplate in both the central and

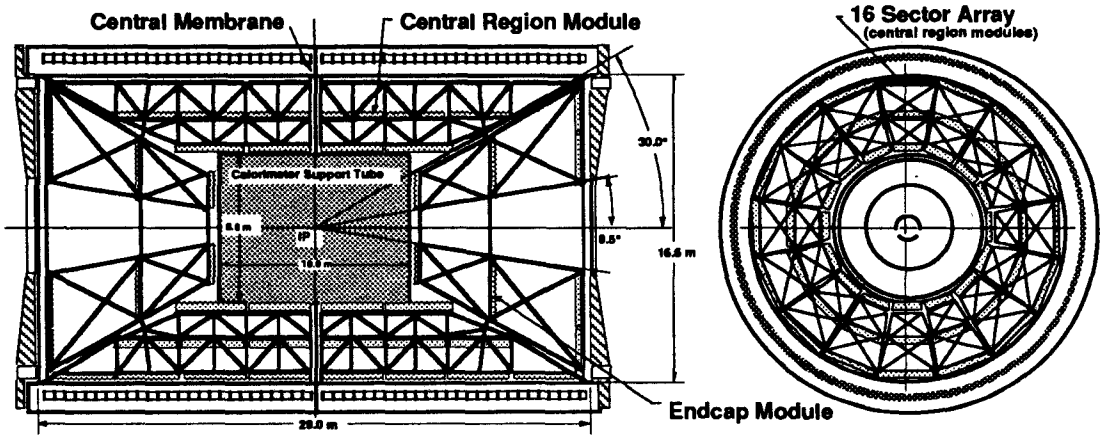

Figure 2.3-1 Overview of the GEM Muon System. The dimensions of the large solenoidal magnet are indicated. Shown are the placement of the muon chambers in both side and end view

endcap regions. The amount of material within the muon tracking system is kept to a minimum so that multiple scattering is small. A trigger based on transverse momentum of the muon is generated by trigger chambers located in each of the three superlayers.

The following table summarizes the baseline design of the GEM Muon System.

Table 2.3-1 Configuration of GEM Muon System

Dimensions of system:		
Length of magnet		29 m
Inside diameter of magnet		16.6 m
Uniform magnetic field		0.8 T
Calorimeter length		10 m
Calorimeter diameter		8 m
Calorimeter thickness at 90 degrees		12 λ
General characteristics of muon chambers:		
Intrinsic single layer resolution		100 μm
Layer-to-layer within a superlayer		25 μm
Superlayer-to-superlayer		50 μm
Global alignment systematics		200 μm
An 8 layer superlayer is <10% X_o		
Barrel region:		
Angle region: 30° to 90° ($1.32>\eta>0$)		
For momentum reconstruction and Level. 2 trigger:		
Three superlayers:	Bend plane	8-8-4 layers
	Nonbend plane	2-4-4 layers
Channel segmentation		3 cm
Channel count:	Bend plane	133 k
	Nonbend plane	25 k
For Level 1 trigger:		
Three superlayers:	Bend plane	2-2-2 layers
	Nonbend plane	2-2-2 layers
Channel count:	Bend plane	18 k
	Nonbend plane	21 k
Endcaps:		
Angle region: 10° to 30° ($2.44>\eta>1.32$)		
For momentum reconstruction and Level 1 & 2 trigger:		
Three superlayers:	Bend plane	4-4-3 layers
	Nonbend plane	2-2-2 layers
Channel segmentation		5 mm
Channel count:	Bend plane	231 k
	Nonbend plane	21 k

Momenta are reconstructed by measuring the sagitta S(m) given by $S = 0.3\ B\ L^2/8p$ for a trajectory at 90° to the beam, where L (m) is the length of magnetic field B (T) traversed, and p (GeV/c) is the momentum. In order to achieve good momentum resolution, the sagitta S (m) must be made as large as practically possible. Thus, $B \cdot L^2$ is the term to maximize and a large radius magnet of moderate field can provide a cost effective high resolution muon system.

2.3.2 Design Criteria

Various studies have been done to determine the technology independent specifications for the GEM muon system based on physics criteria.

(a) Momentum resolution. It is convenient to parameterize the muon momentum resolution, $dp/p = [(ap)^2 + b^2]^{1/2}$. The term b, dependent on multiple scattering in the middle module and pseudorapidity, limits the resolution at low momentum. The term a, which depends primarily on pseudorapidity, is determined by systematic alignment errors and module spatial resolution. This term limits high momentum measurements.

The low momentum specification for the measurement resolution comes from consideration of the intermediate mass Higgs search ($140 < M_H < 180$ GeV/c^2) through the process $H \rightarrow ZZ^* \rightarrow 4$ muons, which is expected to have a very small line width. To achieve clean detection of the Higgs and an estimate of its width, $b < 1\%$ is required. Thus the number of

radiation lengths in the middle superlayer must be < 10%. Figure 2.3-2 illustrates the point.

For large momentum, the most stringent constraint for resolution arises from the requirement of being able to assign charge to each of the two muons from the decay of a high mass Z′ so that accurate measurements of the forward/backward asymmetry can be made. As statistics limit Z′ searches even at the highest luminosity, only a small fraction of decay muons should be allowed to have charge misidentified, implying $dp/p < 30\%$ for about 3σ confidence level charge assignment. The heaviest Z′ accessible at the SSC has a mass of about 6 TeV/c^2, implying that $a = dp/p^2 = 1.0\times10^{-4}$ GeV^{-1}.

Several factors contribute to the momentum resolution in an actual system. There is the intrinsic muon chamber spatial resolution, the alignment errors, the multiple scattering smearing, and the precision of the B-field. Given the baseline design outlined in table 2.3-1, the momentum resolution as a function of angle and momentum for the baseline muon system is shown in figure 2.3-3. At 90° $dp/p = 4.5\%$ for $p =$ 500 GeV/c. With the parameters tabulated, it has been found that over most of the momentum range, the resolution is limited by the spatial resolution of the tracking chambers. Note that the muon charge can be determined to better than the 3 σ level for $p < 4$ TeV/c.

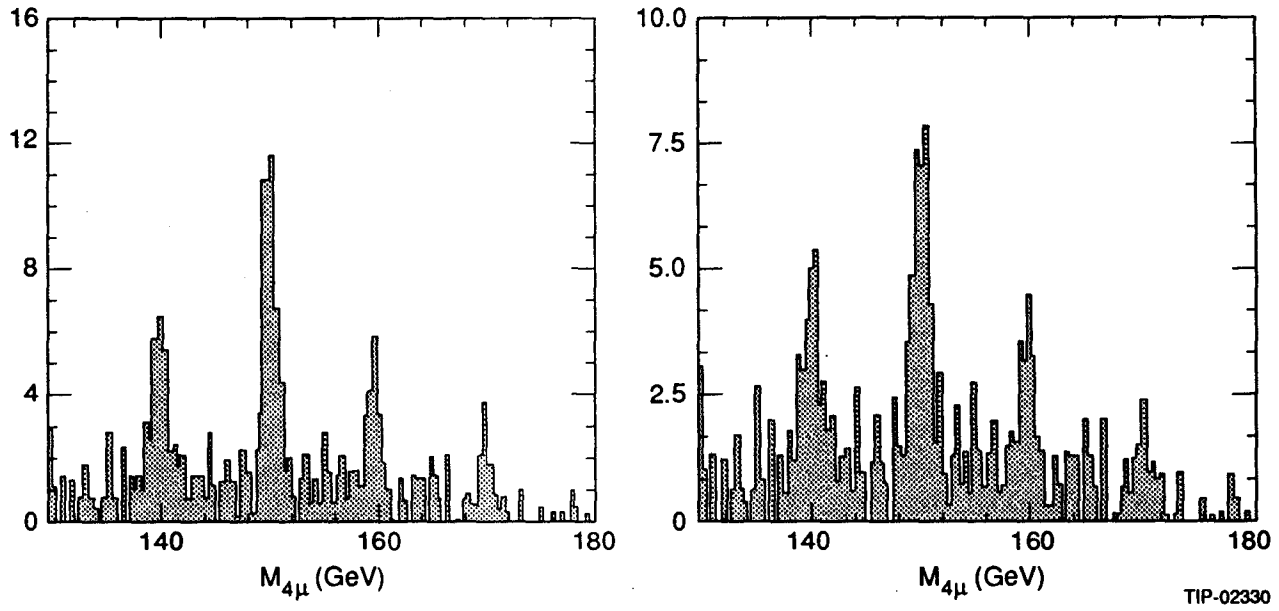

Figure 2.3-2 The reconstructed Higgs mass distribution for several values of mass is shown for two resolutions of the muon system, quantified by the number of radiation lengths in the middle superlayer. 1% on left, 10% right

Various improvements of the momentum resolution at high energies and in the forward direction can be effected at relatively low cost. Among the enhancements being considered are the addition of tracking chambers external to the magnet and B-field shaping in the forward direction. Furthermore, the reconstruction of the muon trajectory can be constrained to go through the primary interaction vertex leading to increased resolution. Figure 2.3-4a shows the enhanced performance if another superlayer consisting of three layers of chambers is placed 3 m outside the

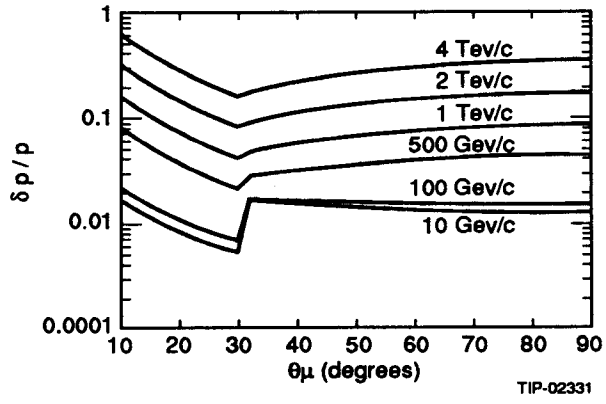

Figure 2.3-3 The muon momentum resolution of the baseline system is shown versus polar angle

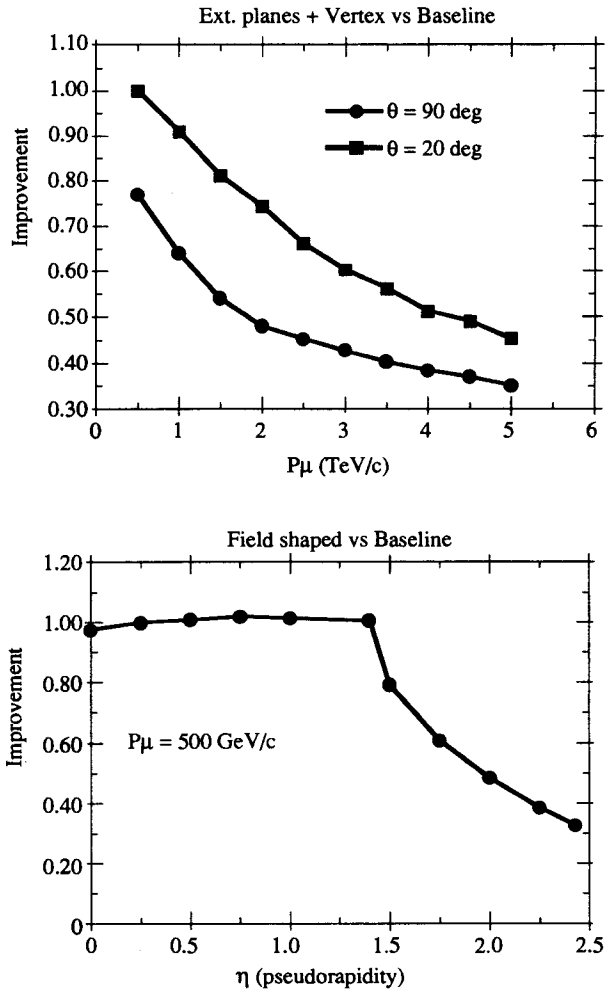

Figure 2.3-4 (a) The improvement of the momentum resolution by the addition of a vertex constraint and external muon planes is shown for two muon polar angles as a function of muon momentum. (b) For a 500 GeV/c muon the improvement of the momentum resolution by shaping the B-field in the forward direction is given as a function of pseudorapidity

magnet, and if the vertex is constrained transversely by 200 μm. The effect of shaping the B-field by increasing the radial component in the forward direction is shown in figure 2.3-4b. While it is believed that the baseline performance is quite good, evaluations are being done in terms of cost versus benefit.

(b) Rapidity coverage. To obtain good statistics for the Higgs to 4 muon channel (either through ZZ* or ZZ) a large solid angle (i.e., pseudorapidity) coverage for the muon chambers is required. For detection of the Higgs the goal is to maximize $N(\sigma) = N(\text{Signal})/\sqrt{N(\text{Background})}$. From the studies of Higgs production and detection, it has been found that $N(\sigma)$ is roughly

constant, having a value of about 6, for muons out to a rapidity of about 2.5. And a rapidity coverage of $-2.5 < \eta < 2.5$ provides about 90% acceptance for a 4 TeV/c^2 Z′ and even greater acceptance for a heavier Z′. (See figure 2.3-5.)

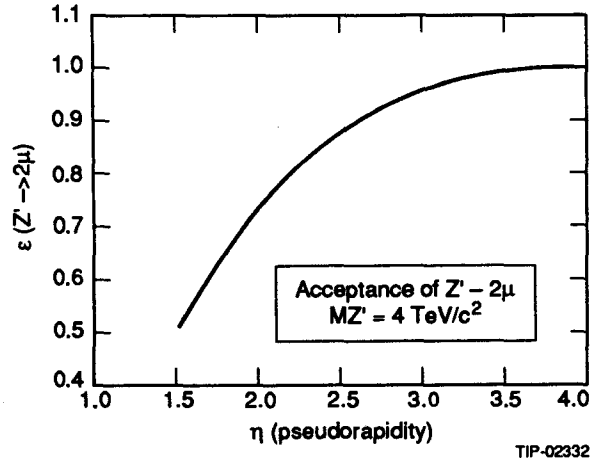

Figure 2.3-5 The acceptance of a 4 TeV/c^2 Z′ as a function of pseudorapidity

(c) Chamber Occupancy. The design goal limits the occupancy at $\mathcal{L} = 10^{34}$ cm^{-2} s^{-1} below a few percent in order to guarantee an unambiguous muon track-finding efficiency of nearly 100%. Figure 2.3-6 shows the muon rate as a function of pseudorapidity, η, for the inner, middle and outer modules, assuming 12 λ in the barrel calorimeter, and 14 λ in the endcap calorimeter. For a 4 m by 3 cm diameter drift tube, with a 3 μs Level 1 trigger delay time, the occupancy would be 1% in the barrel. In the endcap region, the rate increases to about 150 Hz/cm^2 in the inner modules at η = 2.5. For a 1 m long and 5 mm wide cathode strip chamber, and a Level 1 delay time of 3 μs, the occupancy would be less than 3%.

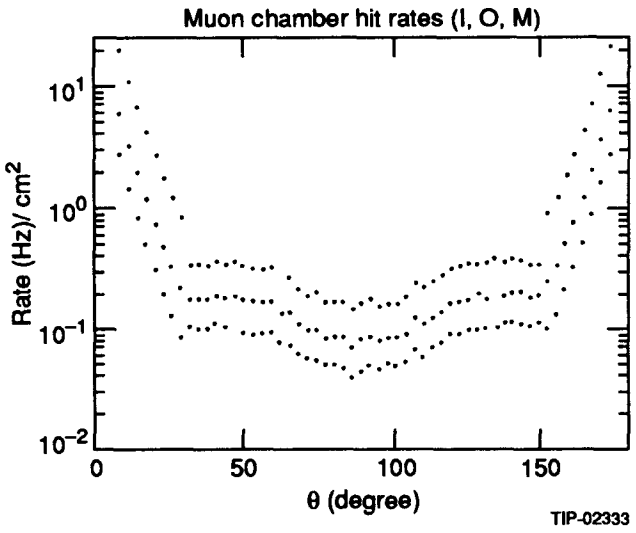

Figure 2.3-6 The muon rate/cm^2 at $\mathcal{L} = 10^{33}$cm^{-2}s^{-1} as a function of pseudorapidity for the three superlayers

Such occupancies are much lower than would be the case for tracking elements located inside of the calorimeter. Benefits of the relatively low rate outside the calorimeter extend to triggering as well. Figure 2.3-7 shows that the rate of muons above 5 GeV/c is a factor 100 lower than the total muon particle rate, implying that the p_T muon trigger is not seriously challenged.

(d) Energy Loss in the Calorimeter. Proper correction of muon energy loss in the calorimeter is very important for high energy muon measurements. As shown in figure 2.3-8, the energy loss spectrum has a significant high energy tail due to radiation processes. One requirement for the calorimeter is the ability to satisfactorily measure this energy loss to permit muon measurement accuracy at the level specified above. Another requirement is that it provide adequate shielding for the muon system. To

preserve a conservative safety margin regarding particle rates in the barrel even at the highest luminosities requires at least 12 λ for the barrel calorimeter.

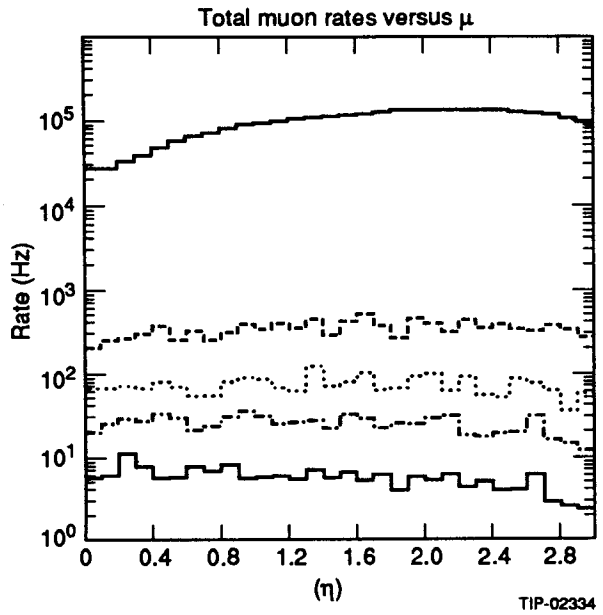

Figure 2.3-7 The total muon rate as a function of pseudorapidity for p_T cuts of 0, 5, 10, 15, 25 GeV/c

2.3.3 Description of Technologies

This section describes the technology options considered for the final design of the GEM muon system. For the barrel region, pressurized drift tubes (PDT) and limited streamer drift tubes (LSDT) are being investigated for the muon momentum reconstruction and Level 2 trigger. In the barrel region the Level 1 trigger and the beam cross tagging will be provided by resistive plate counters (RPC). For the endcaps cathode strip chambers (CSC) operated in the proportional mode seem to be the most attractive candidate technology. These chambers can be adapted to the radial geometry of that region, and will provide both the muon reconstruction as well as the beam tagging and Levels 1 and 2 trigger signals.

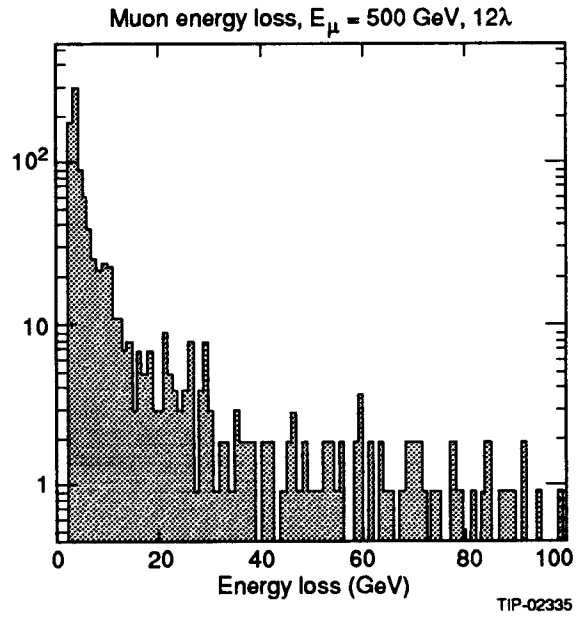

Figure 2.3-8 Energy loss distribution of a 500 GeV/c muon in the calorimeter

(a) Pressurized Drift Tubes. Precise tracking is possible with cylindrical tubes, operated with axes parallel to the magnetic field, due to the simple electric field configuration and the independence of the time-to-distance function on the angle of incidence. The cylindrical geometry of tubes enables improvement of resolution through pressurization as $1/\sqrt{\text{Pressure}}$ by the reduction of the diffusion coefficient, and improved statistics of cluster formation [1].

The GEM PDT's will be aluminum tubes with 300 μm wall thickness, and about 3 cm diameter. A possible configuration of the tubes is for the inner and middle modules each to consist of 8 layers of staggered tubes, and the outer to have 4 staggered layers. The number of radiation lengths in the

central modules would be 8.5% X_0, consistent with the technology independent specifications of the muon system.

The PDT alignment is based on accurate placement of wire ends relative to end plate fiducials. This can be achieved with precision machined reference end plates, and precision fabricated end plugs, pins and ferrules. It is believed that the required precision is achievable by calculating wire position from resonant frequency measurements. Such measurements can be made non-invasively with current-magnetic field excitation, and phase shift analysis. Wire holding through crimp and solder techniques will enable long term stability. Measurements have demonstrated that wire position can be predicted correctly within a few μm. (For 4 m wires tensioned at 80% of the yield strength, the sag will be about 230 μm.) At the sector level, alignment will be achieved with straight-line monitoring techniques such as those used successfully in L3.

(b) Limited Streamer Drift Tubes System. The chambers of this technology are envisaged to be rectangular boxes containing 4 layers of wires, each running through its own U-profiled cathode operated in the limited streamer mode. The positioning of the wires is achieved by supporting them on accurately machined insulating bridges running across the width of the chamber and through slots in the cathode at this support point. The bridge in turn is held against a reference point on the wall of the chamber which can be monitored or aligned from outside. The cathodes are to be made of thin aluminum, possibly coated to minimize secondary electron emission. The cathodes are held in place by a mechanical system separate from the bridges [2].

The chamber design has the flexibility of being made to any length with wire supports at any point of choice to minimize sag, and thus not rely on calculating a large correction. The wires can be laid down in multiples (as is done with Iarocci tubes), inspected, and tested for position and tension before being covered. All chamber parts can be manufactured by state of the art machine shops.

The wires will be operated in limited streamer mode. It has been demonstrated that the combination of large and fast pulses give good drift time measurements [2]. The use of aluminum cathodes makes the tube itself a good transmission line that preserves the rise time of the streamer pulse for drift time measurement and gives a coarse spatial measurement along the wire using instrumentation at both ends of the wire. Because the wires lie in cathodes which are open at the top, instrumented strips can be placed over this open side to obtain a measurement of position orthogonal to the drift time measurement and correlated with it by the common timing signal. In this way an x-y coordinate for each track can be obtained all in one chamber. The chambers have been tested using Laser beams, cosmic rays, and the 0.5 TeV/c beam at Fermilab.

(c) Resistive Plate Counters. Resistive Plate Counters (RPC) work at a uniform electric field of about 40 kV/cm between parallel electrode plates, 2 mm thick, with a resistivity about 10^{11} Ω cm [3]. The electrode plates can be made of plastic phenolic (bakelite) or resistive glass. The field

electrodes are formed by graphite varnish (~ 500 kΩ per square) painted on the outside surface of the 2 mm plates. The readout of the chambers is achieved by means of pick-up strips insulated from the field electrodes by a 0.3 mm thick polyethylene film. The voltage induced is about 0.5 V into 50 Ω with timing characteristics fast enough to tag the 16 ns beam crossings.

RPCs with dimensions up to 0.5 × 0.6 m^2 have been used in many experiments. It is planned that the GEM RPCs will have dimensions of up to 3.3 × 4.0 m^2.

The RPC system will be employed in all three superlayers of the barrel and will completely cover the precision muon measuring components as seen from the interaction point. (See figure 2.3-1.) RPCs will furnish three-dimensional space points for particles passing through the system. Short RPC strips running perpendicular to the magnetic field lines will give the x-coordinate, while long RPC strips running parallel to the magnetic field lines will give the y-coordinate.

The logic for the Level 1 trigger has four components: (1) three-fold coincidence timing in the non-bend plane, (2) straight-line space fit to three points in the non-bend plane, (3) three-fold timing in the bend plane, and (4) three-point sagitta measurement in the bend plane. The signal timing and space-point fitting placed in coincidence with the non-bend plane eliminates most punch-throughs, low energy tracks, and random pick-up noise. Putting the bend plane signals in coincidence with the non-bend plane further reduces the random pick-up noise problem. The sagitta measurement in the bend plane determines the transverse momentum (adjustable from 10 to 100 GeV/c) which activates the trigger.

(d) Cathode Strip Chambers. The high rate environment of the endcap region makes considerable demands on the triggering and tracking technology. Hence, cathode strip chambers (CSC) are being considered. These have a high flexibility in terms of channel segmentation, pattern recognition capability, and trigger speed [4].

The chambers will be deployed in 3 superlayers at z = 6, 10, and 14 m. Each superlayer features modular construction with trapezoidal modules, each of which spans 22.5° of azimuth, resulting in a structure with 16-fold symmetry. The superlayers have modules containing four chambers. In the outermost superlayer only three planes will be instrumented at startup.

Each chamber consists of two cathode planes (only one segmented) with an anode plane between them. The anode wires have a pitch of 2.5 mm and the distance between the cathodes is 5 mm. The precision azimuthal coordinate is obtained by charge interpolation between neighboring strips. Measurements made with this configuration indicate a resolution of order 50 μm per strip, insensitive to anode wire placement, gas gain, pressure, and temperature, and magnetic field nonuniformities.

For a maximum occupancy rate of 10 Hz the total number of channels is 252k. The superlayers closest to the absorber cover a relatively small area. If necessaryt, more planes could be added

for increased pattern recognition with a relatively modest increment in the total channel count.

The spatial resolution of these chambers in the azimuthal direction is limited by the dynamic range of the charge signal referenced to the rms noise, which is proportional to the capacitance of the cathode strip and inversely proportional to the square root of the integration time. In order to operate the chambers at a relatively low gain (~2–3×10^4) the intention is to use an integration time of about 1 μs. Using an analog multiplexer a single ADC can digitize a large number of channels. Monolithic circuits developed for reading out silicon detectors meet the requirements for such a readout system. A parallel branch feeds a discriminator and the resulting signal is used for the formation of the Level 1 trigger.

The logic for the Level 1 trigger in the endcap region roughly follows the scheme used in the barrel, with the following enhancement. The fine segmentation of the trigger elements (5 mm wide strips) permits measurements of local vectors along the muon trajectory. By correlating the local vectors from the second and third superlayers, it will be possible to determine the muon transverse momentum at the first level of the trigger. The radial coordinate (nonbend plane) and the bunch crossing assignment are provided by reading the anode wires.

2.3.4 Mechanical Engineering of the Muon System

The barrel region muon support system is arranged in 16 measurement modules per end as shown in figure 2.3-1. These modules utilize an aluminum truss structure to support the muon chambers. Each module is attached to the endplates of the magnet cryostat, with kinematic hardware.

The support structure design will employ bolted and pinned clevis joints. This design permits the layered assembly of the truss joints to be disassembled and reassembled with accuracy. The maximum deflection will be less than 2 mm in any orientation and the stresses less than 2 kpsi for a central module weight of 10 tons.

The structure of the endcap region will be similar in concept to the central region but will be constructed of lighter cross section tubing appropriate for the 1 ton per module weight expected for the trapezoidal-shaped CSC design. The same 16-fold symmetry of the central region will be translated to the endcap regions and the endcap modules will be attached kinematically to the respective barrel region module structure.

In both regions there will be interface structures between the chambers and the support structure which will direct the support load through the truss nodes. The connection between the chambers and these structures will be flexural elements which permit predictable translation of the chambers in a plane.

Alignment of the muon chambers within a module will be accomplished by means of multiple straight-line monitors, similar to those successfully used to monitor and maintain alignment of the L3 muon system, to an accuracy of 10 μm rms. Actuators will control this alignment either in an automated closed loop or manually. Initial

alignment will be accomplished with precision surveying techniques.

2.3.5 Muon System R&D Plan

In order to design and build the GEM muon system a number of R&D issues have to be resolved. During FY92 there will be a study of the technologies discussed above, with the following specific objectives:

- Design and construct large scale prototypes of each of the technologies discussed above during the winter and spring of '92.
- Compare performance of competing technologies, e.g. PDT and LSDT in the barrel, by the summer of '92. Choose the best technology and concentrate effort leading to a full engineering design. Check that technologies are compatible as an integrated muon system in terms of noise, timing signals, etc.
- Certify that the triggering devices (RPC in barrel and CSC in endcaps) will operate reliably in their respective environments.
- Develop and evaluate chamber alignment scheme.
- Design, construct, and critique a scaled prototype chamber support fixture.

To focus the effort on the final evaluation of the triggering and tracking technologies, as well as study their operation in an integrated muon system, a cosmic rays test rig is envisioned. This setup (named TTR for Texas Test Rig) will be established at the SSCL and will be the central facility of the GEM muon group during the R&D and engineering design phases.

The strategy is to maintain some degree of flexibility during the early stages of the R&D program, keeping in mind that backup solutions should be considered in the event that a particular technology does not work out. The parameters of the technologies described above are nominal, and serious R&D studies are needed to design a practical system. Coordination of the design of the muon system with the evolving GEM detector will be important.

2.3.6 Summary

The design of the GEM Muon System is based on a large solenoid with muon tracking chambers placed outside the hadron calorimeter and inside the magnet coil. In this way, high precision reconstruction of muon tracks is possible, even in the highest rates being envisioned for the SSC. The system will provide a trigger dependent on the transverse momentum of the muons. An active R&D program is envisioned to determine which tracking and triggering technologies will be used and to develop support structures which will satisfy the demanding alignment criteria.

[1] Z. Zhou *et al.*, NIM A287, 439, (1990). S. Ahlen, *et al.*, Part. World 1, 168, (1990), Bing Zhou, *et al.*, IEEE Trans. NS-37, 1564 (1990), A. Tomesch, *et al.*, NIM A241, 265 (1985)

[2] L. S. Osborne *et al.*, Toroidal Spectrometer Group Progress Report, SSC Prog. Rep. No. 218, September 15, 1991

[3] R. Cardarelli *et al.*, NIM A263, 20, (1988), M. Bertino et al., NIM A283, 654, (1989)

[4] R. Debbe *et al.*, BNL-45402, (presented at the Symp. on Det. Res. for SSC, Forth Worth, TX, 1990), B. Yu *et al.*, BNL-44748, (presented at 1990 IEEE Nucl. Sc. Symp. Arlington, VA (1990)

2

2.4

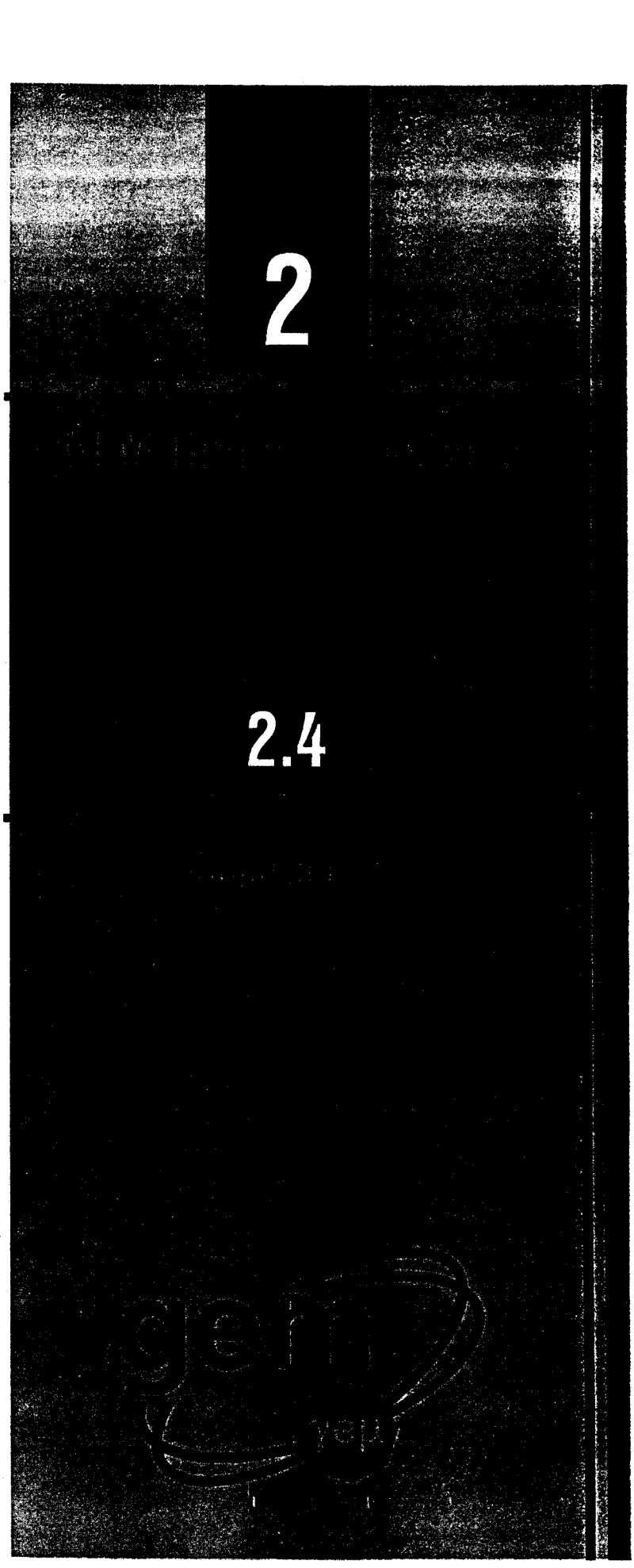

Liquid Argon Calorimeter

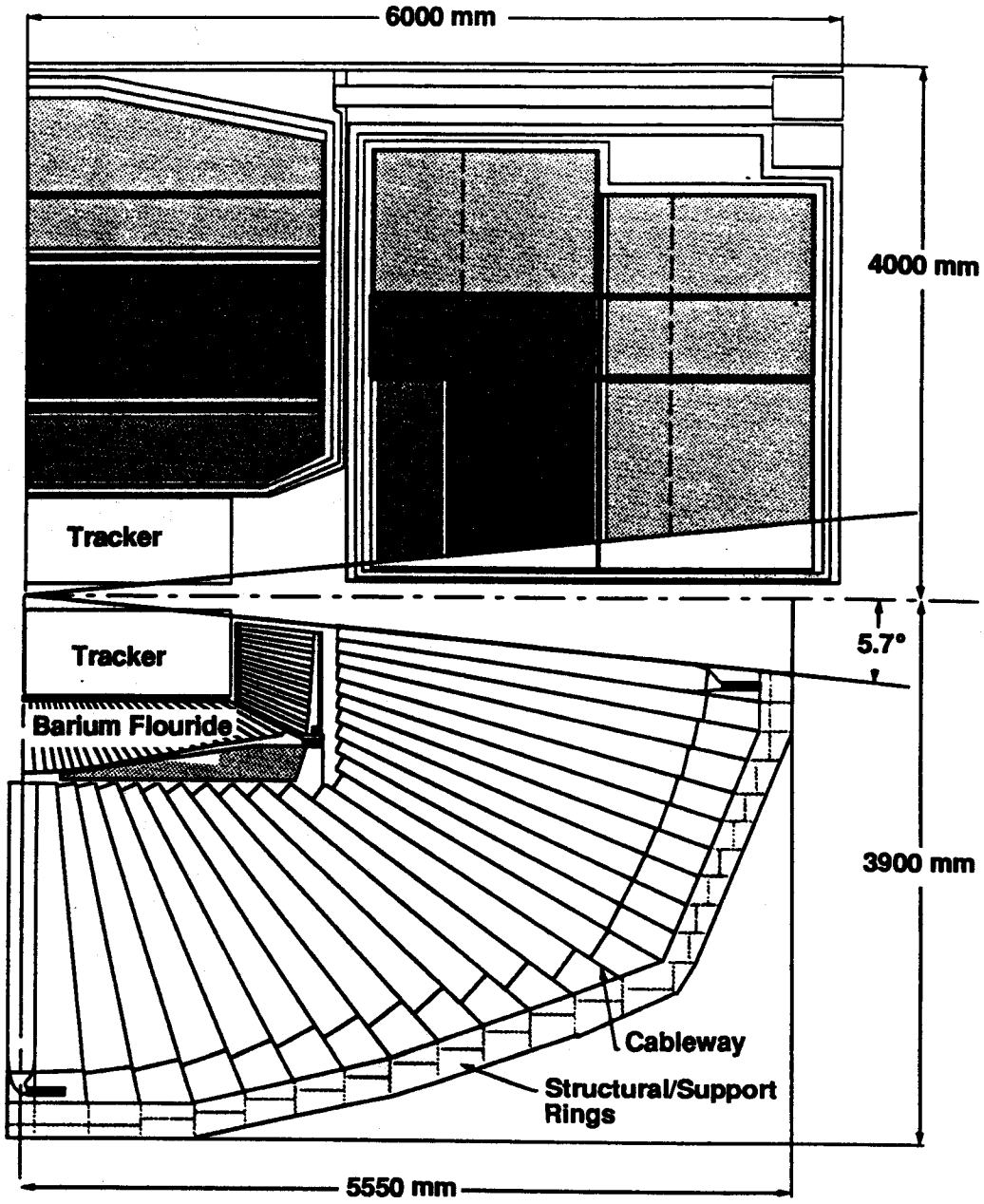

BaF2 with Scintillating Fiber Hadron Calorimeter

2.4 Calorimetry

2.4.1 Introduction

High precision electromagnetic (EM) calorimeters will have unique physics discovery potential at the SSC: in the search for Higgs particles in the mass range between 80 and 180 GeV, and in the search for new physics signatures involving electrons and photons beyond the Standard Model. GEM has thus been designed as a precision lepton and photon detector, where the calorimetry system is the centerpiece of the experiment. One of the principal goals of GEM's experimental design—and its R&D program—is to achieve the best feasible EM resolution, combined with good resolution for hadron jets and missing E_T.

2.4.1.1 BaF_2 with Scintillating Fiber Hadron Calorimeter, and Liquid Argon/Krypton Options

The high resolution, speed, and radiation resistance requirements, and the need to complete the R&D and engineering design of the optimal calorimetry system which fits within the budgetary constraints in 1992, have pointed the way towards two complementary systems:

- BaF_2 crystal high precision EM section, followed by a scintillating fiber hadron calorimeter.
- A Liquid Argon (LAr) calorimeter with a fine sampling accordion [1] EM section, where the EM resolution is improved by the use of Liquid Krypton (LKr) and/or thin plates in the accordion.

The complementary advantages of the two approaches are summarized below.

- BaF_2 Precision Crystal EM; with Scintillating Fiber HCAL
  - Higher intrinsic EM resolution: $\sigma_E/E = (2.0 / \sqrt{E} \oplus 0.5)\%$.
  - High uniformity for the EM section, based on the proven carbon fiber-epoxy composite mechanical support system design used by L3.
  - Higher EM and HCAL speed, resulting in a somewhat higher signal to noise ratio in an isolation cone, when searching for events containing isolated electrons or photons:
  - Effective compensation: the intrinsically non-compensating EM section (e/π response ratio ~ 1.7) can be compensated by adjusting the $e/\pi \approx 1$ in the hadron calorimeter behind the BaF_2. This leads to a small constant term (below 2%) in the resolution for jets.
- Liquid Argon with Accordion EM; Liquid Krypton Option
  - Intrinsic stability resulting from the use of ionization with unity gain and readout of the peak current, leading to ease of calibration.
  - Large systems involving plates have been tested [2], and have demonstrated the requisite resolution and small systematics (below the 0.5% level).
  - Intrinsically radiation resistant.

- Good uniformity and position resolution has been demonstrated in test beam modules.
- Ease of segmentation longitudinally allowing excellent angular resolution for photons.
- Experience in many large systems: SLD, D0, H1, NA34, etc.

2.4.1.2 *GEM Calorimetry: Rationale and Selection Procedure for the Two-Pronged Approach*

Despite the advances on the R&D, conceptual and engineering design, and simulation studies of a full GEM calorimeter made for both systems over the last year, each requires one more year of R&D before the final choice of the system which best meets GEM's physics goals can be made. Some of the principal issues for each system are summarized below.

The BaF_2 system, while providing a potentially large performance gain in energy resolution in the search for new physics, carries with it a higher risk. Production of large radiation hard crystals has not yet been achieved (the target date for a milestone demonstration of large rad-hard crystals is in the third quarter of 1992). In order to assess the risk, a panel of internationally recognized experts on radiation damage in materials in general, and on crystals in particular, is now reviewing the progress towards radiation hardness achieved up until now by SIC and BGRI in China. Following this review — if the level of risk is judged acceptable—the panel is expected to provide expert guidance on the research methods and the scope of the program required to achieve the required radiation hardness, with large scale production scheduled to start in 1993.

The Liquid Argon system has demonstrated stable performance in test beams—with EM resolution for an accordion module[1] at the level of $\sigma_E/E = 10\%/\sqrt{E}$ with a constant term consistent with zero. However, it has yet to demonstrate a resolution of $\sigma_E/E = (7.5/\sqrt{E} \oplus 0.5)\%$ or better, the performance goal set by optimizing sensitivity to the Higgs in the 80–140 GeV mass range at the SSC. In addition to test beam results with liquid krypton and/or a thin-plate accordion module, with the beam incident over a range of angles which is representative of the proposed GEM detector, the overall engineering design for this option will be developed rapidly and in detail over the next several months.

As the R&D proceeds during 1992, test beam results, other performance data, and the detailed engineering design, will be used to carry out a series of full detector simulations. The simulations for each calorimeter option will include a sufficiently detailed representation of the overall GEM detector geometry, its cracks and inactive regions, its readout characteristics, and the principal systematic effects, to objectively compare the two systems. The overall performance of each system in terms of its resolution, uniformity and hermeticity will be completed, and illustrated in terms of a series of physics examples — including Higgs, SUSY, and other new searches for new physics. This process will be finished, and the final GEM calorimetry system will be chosen in time for the submission of the Technical Proposal in the Fall of 1992.

2.4.2 Physics Requirements

2.4.2.1 Electromagnetic Calorimeter

An important potential discovery for the GEM electromagnetic calorimeter (EMC) is the Higgs boson in a mass range between 80 and 180 GeV through its $\gamma\gamma$ and $ZZ^* \rightarrow 4\ell$decay modes [3]. While the 4ℓdecay mode will allow GEM to detect a Higgs with a mass heavier than 140 GeV, the $\gamma\gamma$ decay mode will cover a gap between 140 GeV and the upper limit for Higgs detection at LEP Phase II (80 GeV) [4].

$H \rightarrow \gamma\gamma$ detection places stringent requirements on the overall detector design, especially on the design of the EMC. Because of the small production cross-section (50 to 200 fb) and the narrow decay width (5 to 10 MeV) of the Higgs boson in this mass range, and because of the huge irreducible $\gamma\gamma$ background and QCD jet background, the discovery potential is directly related to the reconstructed $\gamma\gamma$ mass resolution and the ability of the detector to reject background. Note that GEM requires the capability to distinguish photons from electrons with close to 100% efficiency (either from the central tracker or a pre-shower stub detector) so that the electron pair background, which has a rate of 2 Hz at the SSC, may be rejected effectively.

2.4.2.1.1 Energy Resolution

A simple parametrization of the energy resolution of a calorimeter can be expressed as:

$$\frac{\sigma_E}{E} = \frac{a\%}{\sqrt{E}} \oplus b\%$$

where **a** and **b** are two constants and E is the energy being measured. Table 2.4-1 lists the time factor in discovering the Higgs by using the $\gamma\gamma$ decay mode as a function of **a** and **b**, normalized to the BaF_2 resolution goal **a** = 2.0 and **b** = 0.5. A calorimeter with a resolution of **a** = 7.5 or better has a significant advantage over an experiment that does not emphasize EM resolution.

Table 2.4-1 Effect of Energy Resolution: a and b

	a = 2.0	5.0	7.5	10	15
b = .25	0.63	1.2	1.7	2.2	3.3
b = 0.5	1.0	1.4	1.8	2.3	3.4
b = .75	1.4	1.7	2.1	2.6	3.6
b = 1.0	1.8	2.1	2.4	2.9	3.7

2.4.2.1.2 Photon Direction Measurement

Since a photon does not leave a track in the central tracking detector, the photon angle information may be obtained by using: (1) longitudinal sampling in the EMC to measure the direction of the shower (the liquid ionization option easily provides this), and/or (2) correct event vertex tagging by the central tracker to determine the origin of the shower. When running at the SSC design luminosity of $10^{33}\,cm^{-2}s^{-1}$ GEM will find the correct event vertex by selecting the vertex with the largest multiplicity of stiff charged tracks in the angular region covered by the central tracker. Since the vertex *z* resolution (500μm) is better than the position resolution for many of the photons in the EMC, the angular

contribution to the mass resolution is dominated by the position resolution of the calorimeter, however the effect of the position resolution on the intermediate-mass Higgs discovery potential is negligible for a resolution of 2 mm. A good vertex z resolution of less than few mm is very important, if the EMC has no longitudinal segmentation. Without angular information from either of the above techniques, the discovery time for the Higgs would increase by as much as a factor of five.

2.4.2.1.3 Photon Identification and QCD Background Rejection

There are copious π^0's, and thus photons, produced at the SSC. The production cross section of QCD two jet events is 2 mb for $p_T > 20$ GeV and of γ-jet events is 237 nb. A narrow neutral jet with multiple photons would fake an isolated photon. Single photons may also be produced in the parton shower process, which will cause irreducible QCD background. To identify real photons and to reject QCD jet background, an isolation cut, shower shape analysis and a preradiator may be used [5].

One simple isolation analysis requires

$$\sum_{r<R} E_T - E_T^{photon} < (E_T^{cut} + 0.1\, E_T^{photon})$$

where the usable values of R ($R = \sqrt{\Delta\eta^2 + \Delta\phi^2}$) and E_T^{cut} are related to the detector design, especially the noise level in the isolation cone. This simple analysis, with suppression of channels less than three times noise, has been studied with PYTHIA 5.5 [6] for the two systems, yielding backgrounds of 69 pb for the BaF_2 scintillator and 89 pb for the liquid argon systems. The irreducible $\gamma\gamma$ background is about 32 pb. This background can be further reduced by a number of design optimizations, which require more study. In the liquid argon calorimeter, for example, the ability to reject fake gammas depends on the choice of angular and longitudinal segmentation. Furthermore, a choice can be made to segment the calorimeter transversely just in the first few longitudinal depths, keeping the overall channel count constant. To further complement the shower shape sensitivity, the installation of strip readout near shower maximum is being studied. This may be done with 1 mm pitch strips for the electrode using a novel multiplexing scheme. A preradiator is also under study. A preradiator situated in front of the calorimeter employing one millimeter silicon strips has been shown to be capable of π^0 rejection of better than 80% with nearly full efficiency (>95%) for γ's up to 100 GeV [7] This results from the very narrow (< 0.5 mm wide) showers in this section. EGS Monte Carlo studies have shown an acceptable energy correction is possible. Finally, a powerful preradiator consisting of of 3-4 radiation lengths of scintillation and ionization sampling liquid krypton has been studied but is not part of the GEM baseline.

2.4.2.1.4 Photon and Electron Trigger

A possible design of a Level 1 trigger for isolated photons and electrons would require matching each electromagnetic calorimeter cell with the hadron calorimeter cells behind it. GEM is able to achieve a 35 kHz trigger with 85% efficiency for $H \rightarrow \gamma\gamma$ and $H^0 \rightarrow ZZ^* \rightarrow 4\,e$ [8]

2.4.2.2 *Hadronic Calorimeter*

2.4.2.2.1 *Jets*

The measurement of jets is essential for any general-purpose SSC detector such as GEM. For dijets from, say $W \rightarrow jj$, the mass resolution is determined both by the calorimeter energy and angle resolution and also by intrinsic limitations in the definition of a jet. Studies suggest that the latter dominates when the calorimeter energy resolution is

$$\frac{\Delta E}{E} \lesssim \frac{50\%}{\sqrt{E}} \oplus 2\%.$$

Angle resolution is important for studying the shapes of jets and for measuring single jet and multiple jet invariant masses, e.g. for high p_T $W \rightarrow jj$. For jets from QCD scattering processes the cross section for energy flow into a given solid angle is calculable; that is, uncertainties due to clustering algorithms are not an issue, the search being limited only by intrinsic calorimeter resolution. Thus the constant term in the calorimeter resolution should be minimized for such physics.

2.4.2.2.2 *Missing Transverse Energy $\not{E}_T$*

Both new, weakly-interacting particles and neutrinos give missing transverse energy $\not{E}_T$. The most demanding requirement on $\not{E}_T$ resolution is probably set by supersymmetry: since the Tevatron could detect gluinos and squarks up to about 200 GeV, one would like to detect $\not{E}_T \gtrsim 100$ GeV. The irreducible background is set by neutrinos from Standard Model sources, mainly heavy quarks and $W^{\pm}$ and Z^0 bosons at high p_T. The detector backgrounds should be smaller than this.

Missing energy is mainly measured by calorimetry, and the resolution on $\not{E}_T$ is primarily determined by intrinsic hadronic energy resolution in the central region, non-Gaussian tails from cracks in the central region, energy resolution in the forward calorimeter, and angular coverage and resolution in the forward calorimeter. The Gaussian term in the energy resolution of the central or forward calorimeter is not critical. Angular resolution in the forward calorimeter gives $\Delta p_T / p_T \lesssim 10\%$, which again has been shown to be sufficient, at least for the total $\not{E}_T$ cross section. Non-Gaussian tails in the central region will be limited by careful engineering to minimize dead material. Hence, it appears that the angular coverage is the crucial factor in determining the $\not{E}_T$ resolution.

For an idealized calorimeter which measures energies with Gaussian resolution and has no transverse shower spreading, it is known that covering $|\eta| < \eta_{max} = 5\text{–}5.5$ is sufficient to reject physics backgrounds [9]. For realistic showers adequate resolution can be obtained with a forward calorimeter at $z \approx 7$ m.

Production of new particles such as a Higgs or a technicolor resonance via WW fusion will lead to forward jets, since each of the W's is produced by $q \rightarrow W\, q$. Estimates of the effectiveness of such tags have varied widely. They may prove to be important and should be considered in the design of the forward calorimeter, but they are probably less important than the measurement of $\not{E}_T$.

2.4.3 Liquid Argon Calorimetry Option

There are many attributes of liquid Argon calorimeters which lead to its consideration for an SSC detector [10]. These include radiation resistance, uniformity of response, unit gain leading to the ability to calibrate to < 0.5%, the ability to segment longitudinally and transversely with a relatively modest increase in cost, experience in many large systems, and good energy resolution.

Recently a new concept for a liquid Argon EM calorimeter, called the accordion, has been developed. Beam tests have yielded impressive results [1]. The advantages of the accordion include excellent hermeticity, the elimination of numerous longitudinal connections by use of an electrode structure that follows the accordion-folds, and lower capacitance and inductance allowing short shaping times. The device tested at CERN has an electron energy resolution of $(10.1 \pm 0.4\%)/\sqrt{E} \oplus (0.2 \pm 0.2\%)$, and linearity from 30 GeV to 200 GeV of < 1% with a shaping time of 20 ns. Because the charge is naturally shared between two adjacent readout channels, the position resolution is $4.4\ \text{mm}/\sqrt{E}$. The module tested was divided in half longitudinally. By comparing the position in the front with that in the back an angular resolution $\Delta\theta = 6.1$ mrad was obtained at 120 GeV. This would be extremely helpful in determining whether the showers for $H \rightarrow \gamma\gamma$ candidates have a common vertex.

Since the energy resolution achieved so far in beam tests has not reached the level set by GEM, two methods of improving the accordion energy resolution are being developed. By replacing the Argon with Krypton, using the standard 2 mm thick absorber plates, the energy resolution calculated by GEANT is below $7.5\%/\sqrt{E}$. The same resolution can be reached, according to GEANT, by using 1 mm thick absorber plates together with a thin electrode structure attached to both sides of each plate. The unit cell designs for these two schemes are shown in figures 2.4-1a and 2.4-1b respectively. Both approaches are planned to be tested in a beam at BNL in the Spring of 1992. The mechanics of a parallel plate EM calorimeter using innovative striplines passing through slots in the absorber plates is also being explored.

The current conceptual design for the GEM liquid Argon calorimeter is shown in figure 2.4-2. The overall dimensions are set by the requirement of the minimum number of λ needed versus η. Once those dimensions are set, the EM calorimeter is designed for maximum hermeticity and for the minimum dead material in front of the active EM calorimeter. The maximum hermeticity for the EM is accomplished by ending the barrel section along a line of constant η and then have the cryostat walls closely follow that angle. The EM calorimeter in the endcaps is set back and overlapping so as to continue the coverage with a minimum angular loss. The vessels are made of aluminum so that there is 0.7 X_0 at 90°. The maximum dead material in front of the EM calorimeter is due to the vacuum and cold vessel walls just at the end of the barrel. Energy lost in the vessel walls will be corrected by using either a preradiator inside the cryostat or in a massless gap added to the first longitudinal section. Plans are to

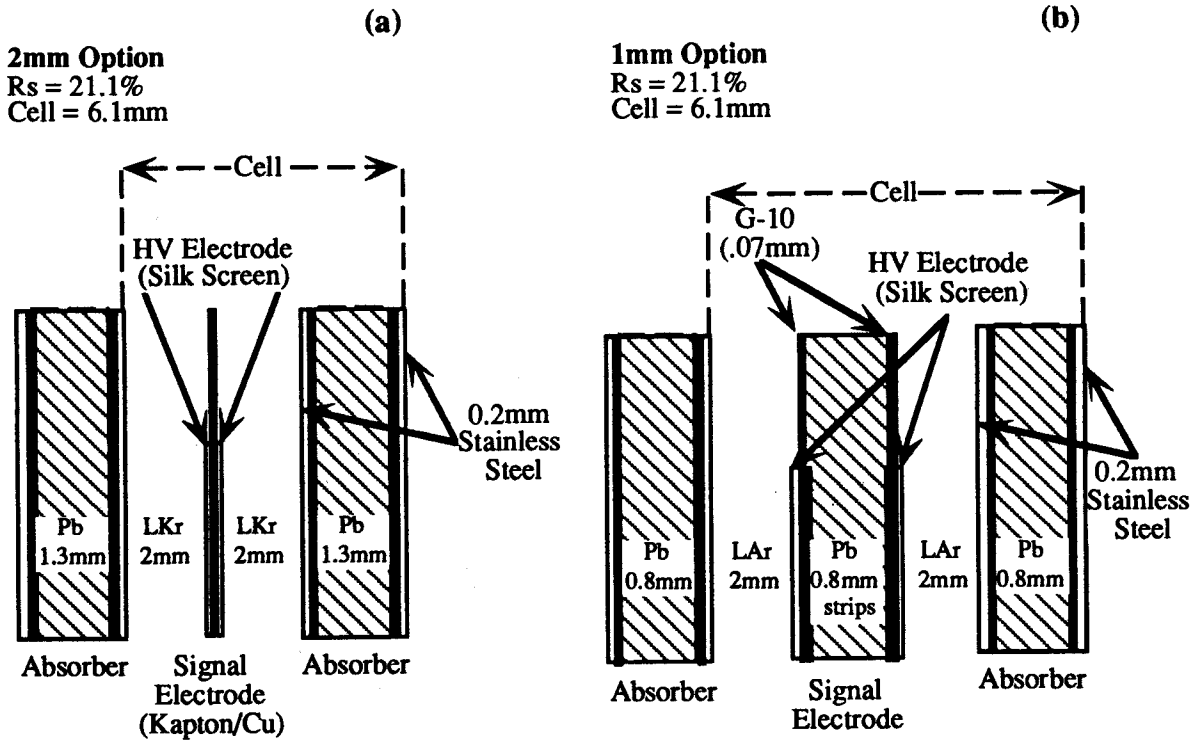

Figure 2.4-1 Liquid Argon Calorimeter Unit Cells

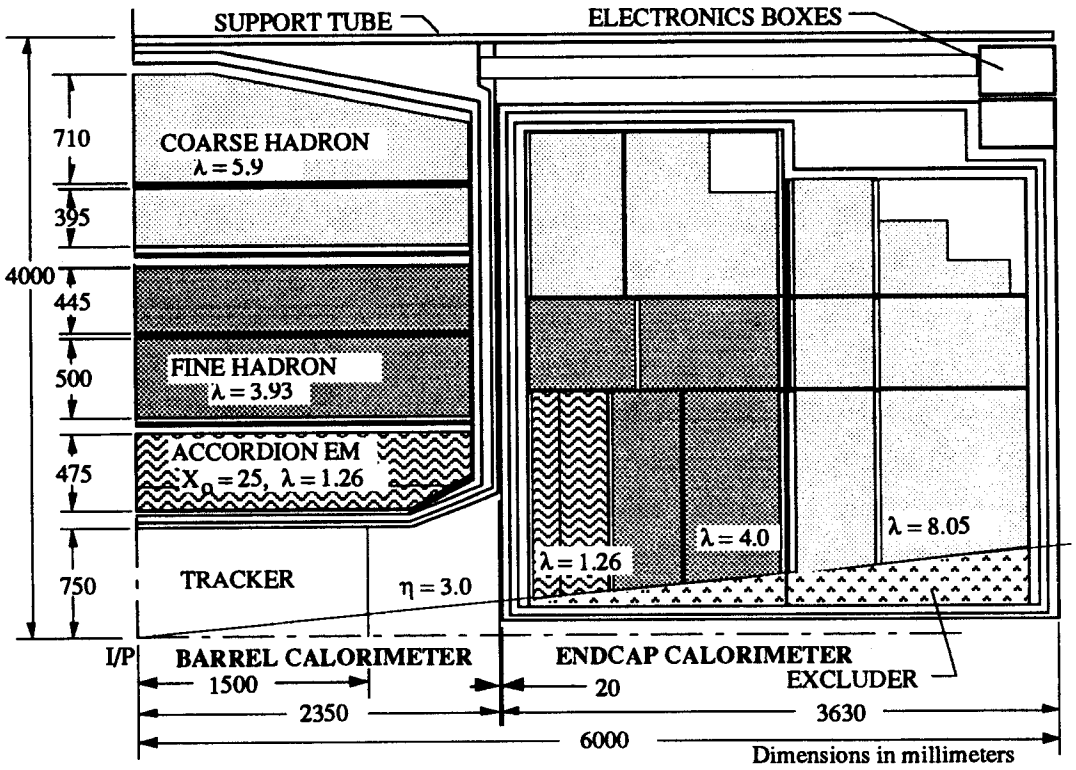

Figure 2.4-2 GEM Liquid Argon Calorimeter Conceptual Design

use 40 ns shaping time which leads to a total noise for nine (3×3) 0.04 towers of ~ 100 MeV.

The hadron calorimeter uses the "electrostatic transformer (EST)" concept to match the large capacitance of towers to the preamps [11]. This is shown schematically in figure 2.4-3. The hadron calorimeter is split into four sections longitudinally: two fine sampling sections and two coarse sampling sections. The goals of the fine sampling section are to have a sampling fraction of ~ 10% so that the signal to noise is sufficient for lepton and photon isolation as well as good hadronic energy resolution. The coarse section is used to measure the leakage of jets and so does not need such fine segmentation, but a sample must be taken every $\leq 4\ X_0$ in order to sample the electromagnetic component of hadron showers and catastrophic energy loss of muons. Iron (stainless steel) is the baseline absorber material since it minimizes the multiple scattering for muons, reduces the weight and is easy to handle. Lead might also be considered to improve the e/π response, or depleted uranium to allow more λ in a fixed radius, but both would have other disadvantages.

A detailed study of the coarse hadronic section will be done in order to specify it completely for the Technical Proposal. The design goal of the coarse section is to maximize the number of λ before the muon chambers which leads to a low (2%) sampling fraction. With the shaping time used in the fine hadronic section (100 ns) this would lead to a large thermal noise (1 GeV/ 0.08×0.08 cell).

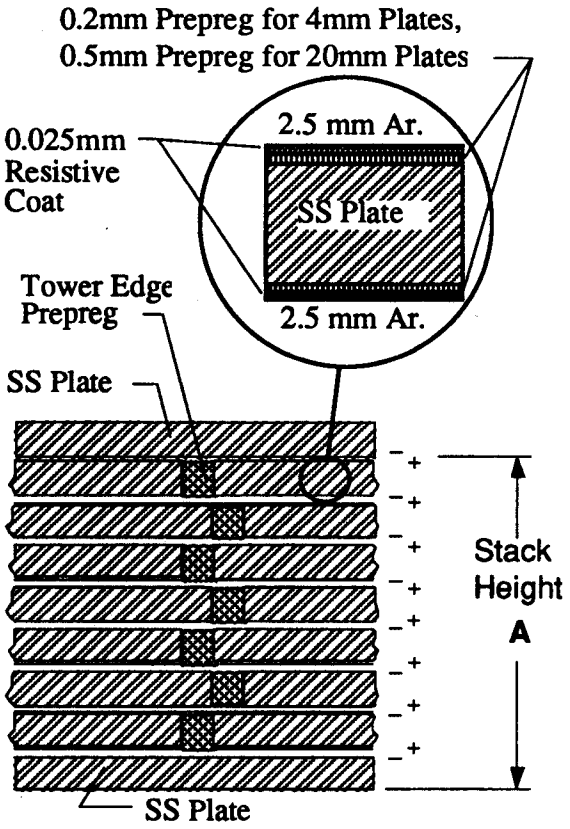

Figure 2.4-3 GEM Liquid Argon Hadron Calorimeter EST Concept

The intent is to use a longer shaping time to reduce this noise. A detailed study needs to be done with GEANT to determine whether this is feasible. If this fails, a reduction in the number of active λ will be considered either by using only fine sampling and adding passive absorber at the back or deploying a scintillating fiber calorimeter after the fine sampling liquid argon.

The parameters of the GEM liquid Argon calorimeter are presented in table 2.4-2.

2.4.4 BaF_2 Electromagnetic and Scintillating Fiber Hadron Option

A precision BaF_2 EM calorimeter backed up by a scintillating fiber HCAL has the advantages of very high resolution for electrons and photons, speed, uniform coverage and hermeticity, good resolution for hadron jets, and a deeper calorimeter to filter out hadrons within a given radius. Figure 2.4-4 shows a side elevation view of the BAF + HCAL system.

Table 2.4-2 Liquid Argon Calorimeter Parameters

Rapidity Coverage	$\|\eta\| \leq 3.$
Segmentation	
EM	$\Delta\eta = \Delta\phi = 0.04$
Hadronic	$\Delta\eta = \Delta\phi = 0.08$
Depth Segmentation	
EM	3 (1 may be preradiator)
Hadronic	4
Total Depth	
$\eta = 0$	12 λ
$\eta = 3$	14 λ
Total Weight (t)	2100
Number of Channels	80,000

Although the BaF_2 EM section is non-compensating, a GEANT simulation predicts good jet resolution with a small constant term can be obtained by using an HCAL section with an average e /π response $\approx$ 1.0. This is illustrated in figure 2.4-5, a GEANT simulation (which correctly predicts the $< e/\pi >$ ratio), where the optimal weighting of the energy deposited in the BaF_2 and in the HCAL is used to reconstruct the total jet energy.

The resulting GEANT prediction of jet response is linear, with Gaussian resolution functions and no resolution tails, and the fitted constant term is 1.4 $\pm$ 0.2%. The dependence of the resolution on the e/π of the HCAL behind the BaF_2 is shown in figure 2.4-6 for jets between 100 and 1000 GeV.

2.4.4.1 High Precision BaF_2 Electromagnetic Calorimeter

2.4.4.1.1 BaF_2 Detector Features.

The high sensitivity of the BaF_2 detector to new physics is the result of the following features: high speed (gating the signal in 16 ns), very high energy resolution, $\sigma_E/E = (2.0/\sqrt{E} \oplus 0.5\%)$, good position resolution (Δx and $\Delta y \approx$ 1 mm for EM showers), excellent e/π, γ/jet, and e/jet separation ($\sim 10^{-4}$), and good potential radiation resistance ($\geq 10^7$ rads demonstrated in small crystals).

2.4.4.1.2 BaF_2 Detector Concept.

The conceptual design of the BaF_2 calorimeter shown in figure 2.4-7 illustrates a central barrel calorimeter with an inner radius of 75 cm and an outer radius of 140 cm, covering a rapidity rangeof $|\eta| \leq 1.32$ ($30° \leq \theta \leq 150°$); and two endcaps, located at $z = \pm$ 164 cm, covering a rapidity range of $1.32 \leq |\eta| \leq 2.5$ ($9.4° \leq \theta \leq 30°$ and $150° \leq \theta \leq 170.6°$).

The BaF_2 calorimeter follows the proven uniform and extremely light structural design used in the BGO calorimeter, which has allowed L3 to achieve the very high resolution. Each crystal is housed in a precisely dimensioned, thin-walled (300 μm) carbon fiber-epoxy composite cavity, and is

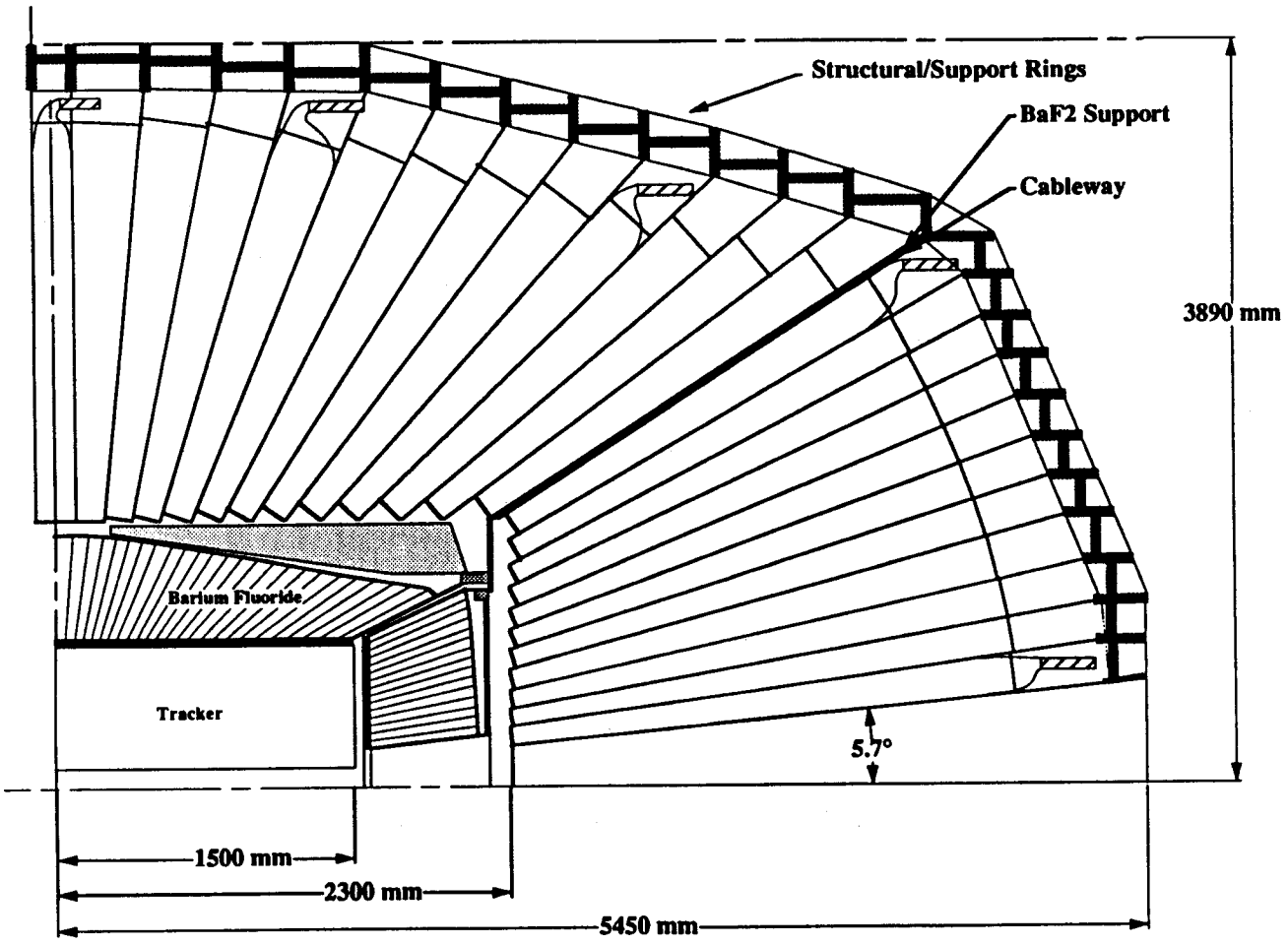

Figure 2.4-4 Side view of the GEM BaF_2 and Scintillating Fiber Hadron Calorimeter System

compressed by small fixtures mounted in each cavity against an inner core consisting of carbon fiber skins surrounding acrylic foam. A complete finite element analysis at ORNL has shown that in spite of its thinness, the structure is stable against the tensile and torsional loads provided by crystal weight and compression, with a large safety factor.

Table 2.4-3 shows the basic parameters of the GEM BaF_2 calorimeter.

Table 2.4-3 Features of the BaF_2 Calorimeter

Detector	Barrel	Two Endcaps
Rapidity Coverage	$\|\eta\| \leq 1.32$	$1.32 \leq \|\eta\| \leq 2.5$
Crystal Front/ Rear Face (cm^2)	3.1×3.1 / 5.1×5.1	2.3×2.3 / 3.1×3.1
Crystal Length (cm)	50	50
Crystal Number	10,880	4144
Crystal Volume (m^3)	8.4	2.2
Crystal Weight (t)	41.1	10.7

2.4.4.1.3 BAF Calorimeter Performance.

The performance of the BaF_2 calorimeter was computed with a GEANT simulation, including the effects of the carbon fiber walls, shower leakage due to summing (3 × 3) crystals, and 0.30 X_0 dead material representing the beam pipe, tracker, and mechanical support. The results are summarized in table 2.4-4. The intercalibration precision of 0.4% assumed in the table has been demonstrated with the RFQ calibration system developed by Caltech.

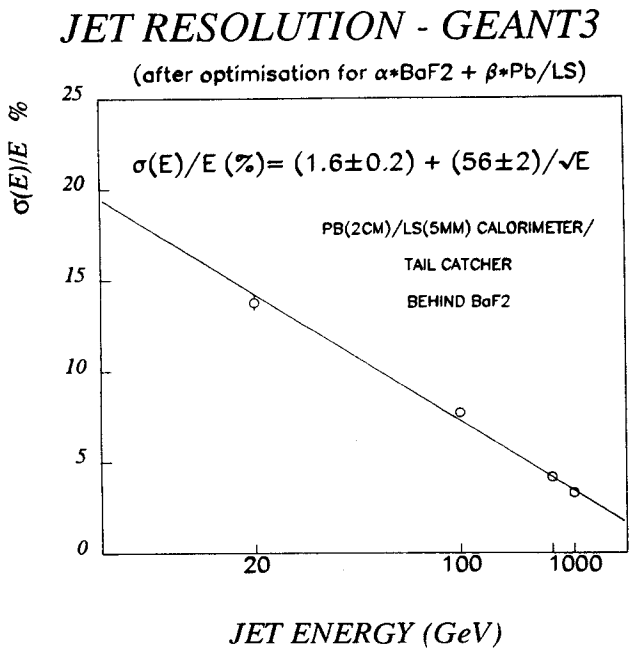

Figure 2.4-5 Jet Energy Resolution for the GEM BaF_2 and Scintillating Fiber Hadron Calorimeter System (20-1000 GeV)

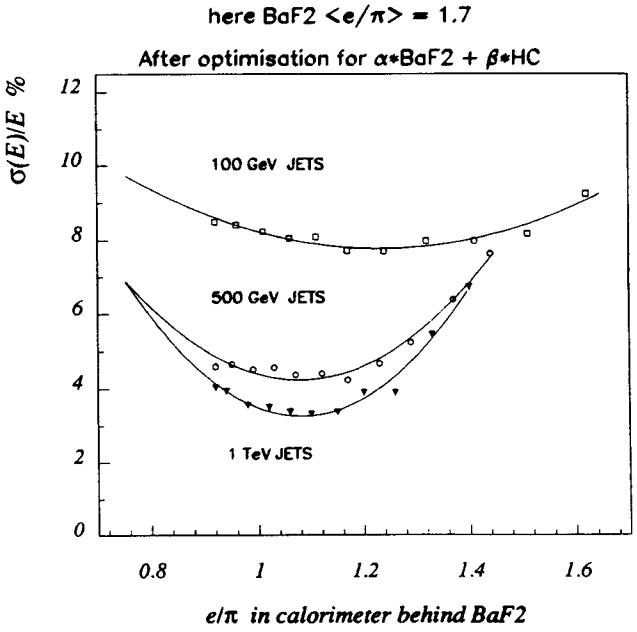

Figure 2.4-6 Dependence of the Energy Resolution on the <e/π> Ratio in the Scintillator Hadron Calorimeter Behind the BaF_2 EM Section

Table 2.4-4 Energy Resolution (%)

E(GeV)	5	10	100	500
Electrical Noise	0.4	0.2	0.02	0.004
Photoelectrons	0.2	0.14	0.045	0.02
GEANT	0.67	0.56	0.42	0.36
Intercalibration	0.40	0.40	0.40	0.40
Total	0.90	0.73	0.58	0.54

As shown in 2.4-8b, the resolution can be parametrized as $2\%/\sqrt{E} \oplus 0.5\%$. For comparison, figure 2.4-8a shows the energy resolution measured with 4000 L3 BGO crystals in a CERN test beam [12]. It can also be parametrized as $2\% \sqrt{E} \oplus 0.5\%$.

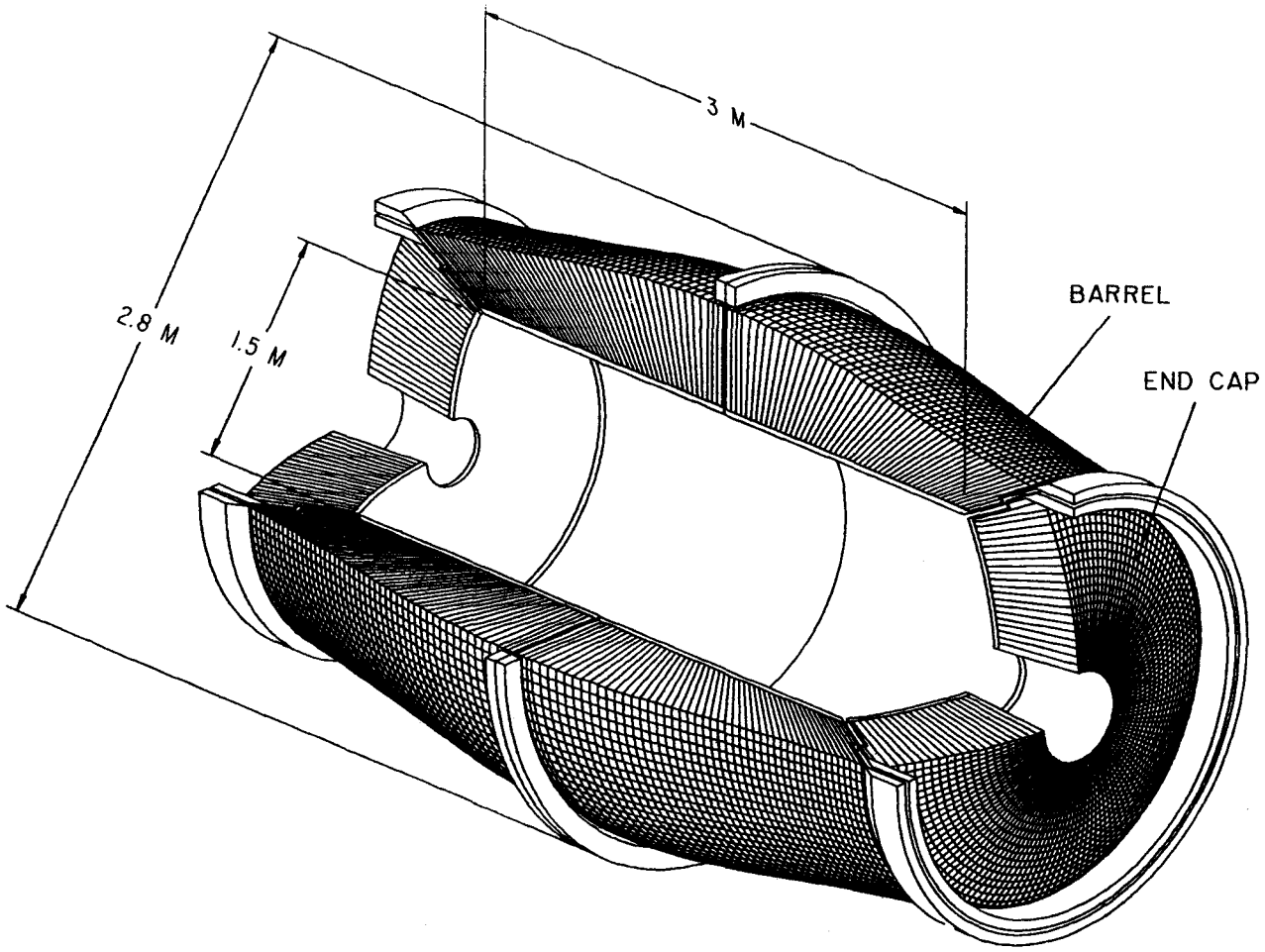

Figure 2.4-7 Conceptual View of the Barium Fluoride Calorimeter

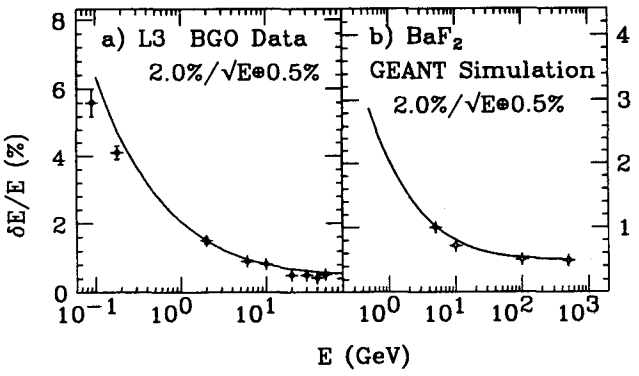

Figure 2.4-8 Energy Resolution of (a) L3 4000 crystal BGO calorimeter, measured at CERN, and (b) BaF2 calorimeter, calculated with GEANT simulation. The solid curves show 2% / $\sqrt{E}$ ⊕ 0.5%

2.4.4.1.4 R &D Progress in 1991 [13]

During 1991, SIC (Shanghai) and BGRI (Beijing) have established a production facility for large BaF_2 crystals, with major Chinese funding. The capacity is currently 140 twenty-five cm crystal pieces (tower-halves) per month (18% of full GEM rate requirements.) The first 98 crystal pieces and spares were delivered to Caltech by May, 1991. A Memorandum of Understanding was signed with SIC and BGRI management for production of rad-hard crystals at $2.5/cc.

The 49 crystal (50 cm long) prototype matrix was constructed by Caltech and UCSD, and is now in a test beam at Fermilab (T-849). The matrix is instrumented by Hamamatsu UV-selective K-Cs-Te R4406 phototriodes, which suppress the slow component and operate in 1T fields. (Thin UV-selective proximity focused photodiodes and UV-selective solid state devices with sharp cutoffs are under development.) Full suppression of the slow component is completed by fast preamp and shaping circuits developed by ORNL. A high transmittance, rad-hard RTV (KE-103) bonds the two crystal pieces of each calorimeter element. Light collection uniformity is $\sim \pm 7\%$, with typically 50 p.e./MeV. The tests of the crystal matrix with muons, electrons and pions will yield results on the resolution, e/π response, e/π separation algorithms and calibration with minimum ionizing particles by December, 1991.

A systematic series of radiation damage studies (up to 20 mrads of Co^{60} γ's, 10^{14} neutrons/cm^2 in some tests) have shown in small samples that: (a) the damage saturates at 10 - 100 krads, with no further damage to beyond 10 mrads; (b) there is no spontaneous annealing at room temperature; and (c) there is no permanent damage from γ or neutron radiation; complete recovery can be achieved by annealing at 500°C, or by a UV lamp. The radiation damage appears impurity or defect related and large crystals have not shown the same characteristics as small crystals. A systematic program to identify and eliminate the key impurities is underway, in collaboration with Optovac and the ORNL Solid State Division in the U.S., as well as with SIC and BGRI in China.

A GaAs preamp with risetime ~1 ns has been developed by Princeton, and tested with a vacuum phototriode on a large BaF_2 crystal using electrons up to 50 GeV. A gated integrator and 60 MHz digital readout pipeline is being developed at Princeton. Los Alamos is developing a GaAs amplifier based on MESFET transistor arrays with rad hardness to 10^{15} neutrons/cm^2 and 10^8 rads.

A structural analysis of the full GEM calorimeter has been completed at ORNL. The engineering and detailed design of the second prototype array including a carbon fiber structure which matches the full detector near $\eta = 0$ has been completed, and is ready for manufacture.

A UV laser and quartz fiber light monitoring system is under development at CMU. The L3 RFQ system completed at AccSys Inc. has been tested with a neutral beam on target and has been shipped to CERN. This will provide information on the calibration precision obtainable *in situ* in L3 during the 1992 LEP run.

2.4.4.1.5 R&D Program for 1992.

The most critical issue for the BaF_2 calorimeter is production of radiation hard, full size crystals. An expert panel has been commissioned to evaluate the risk of proceeding with an R&D program aimed at beginning mass production of radiation hard crystals by 1993. After reviewing current understanding of radiation damage in BaF_2, the panel will assess the prospects for this program. If sufficient promise appears, the extensive R&D program [13] being carried out at 13 institutions in the U.S., China and India will proceed for 1992 to

complete the development and engineering design of the BaF_2 calorimeter in 1992. If completed, this R&D program will culminate in the construction of the first production-quality BaF_2 crystal matrix composed of 81 full-sized crystal elements, integrated with a carbon fiber structure, and full speed front end electronics (gated integrator or fast shaper). The R&D program includes: BaF_2 crystal mass production, radiation damage tests, engineering design of the final prototype and full scale calorimeter, electronics readout development and testing, UV performance monitoring development, rad hard electronics readout development, beam and cosmic ray tests, BaF_2 crystal matrix assembly, and RFQ calibration facility funded under a DOE SBIR grant.

2.4.4.2 Scintillating Fiber Hadron Calorimeter

2.4.4.2.1 Baseline Design.

A scintillating fiber hadron calorimeter has been selected to complement the precision BaF_2 EM calorimeter option. A scintillating fiber hadron calorimeter combines high speed, compensation, compactness, and radiation resistance with a high degree of uniformity and hermeticity in a projective geometry. It also provides design flexibility in the choice of fiber diameter, fiber filling fraction, and lateral readout segmentation, thus allowing for optimal cost/performance trade-offs. Some longitudinal segmentation is possible through the separate readout of fibers terminating at different depths within the calorimeter, at a modest increase in readout channel count and cost.

The SPACAL collaboration has demonstrated the performance achievable with a scintillating fiber calorimeter in resolution, compensation, particle identification, speed, and radiation hardness [14]. The SSCintCAL collaboration has complemented this effort by developing cost-effective methods for calorimeter construction and engineering on the scale required for GEM [15]. Separate optimization of EM and hadronic calorimetry leads to different design decisions for such parameters as fiber diameter and filling fraction.

Figure 2.4-9 illustrates the baseline design of a scintillating fiber hadron calorimeter module for GEM. This design is based on 3 mm diameter fibers cast within an absorber matrix of lead and lead/bismuth alloy. The feasibility of casting 1-ton projective towers has been demonstrated by the SSCintCAL group, which has constructed several 1-ton prototypes prepared for a FNAL beam test. The absorber consists of a 60% / 40% mixture of fine lead shot and eutectic lead/bismuth alloy, where low melting-point alloy is percolated through a previously assembled fiber matrix/lead shot mixture within a mold. The resultant casting has higher density and lower cost than is achievable by casting fibers within eutectic alloy alone, while providing comparable structural integrity and dimensional control. Stress/strain measurements have shown that the resultant towers will be self-supporting under forces indicated by a finite-element analysis of a GEM scintillating fiber hadron calorimeter.

While efficient construction may argue for simultaneous casting of 4 physics towers as a modular "supertower", a single physics tower has been shown in figure 2.4-9 for simplicity. The lateral segmentation into physics towers is matched

with that of the EM calorimeter to .08 (η) × .08 (ϕ), with the option remaining for a future upgrade

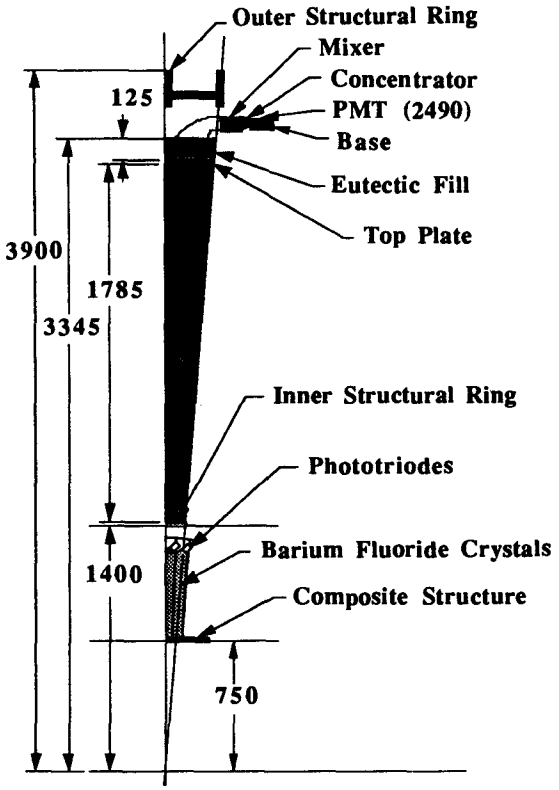

Figure 2.4-9 GEM Scintillating Fiber Hadron Calorimeter

increasing the transverse segmentation. The active depth of the hadron calorimeter alone is 9 λ at η = 0, increasing to 12 λ at η = 3, and it should be noted that the BaF_2 EM calorimeter provides an additional 1.7 λ of material upstream. Readout is accomplished through a mass-fiber splice between 3 mm fibers within the calorimeter module and 1 mm clear readout fibers, providing a flexible and compact method for aligning mesh dynode photomultipliers with the magnetic field.

2.4.4.2.2 Beam Test of the BaF_2+ Scintillator HCAL System in 1992

The primary objective of the FY92 R & D effort will be to construct a fully hadronic shower-containing set of scintillating fiber prototype towers embodying GEM's baseline design. The prototypes will be characterized in beam tests to measure detector performance and subsequently to assess alternative manufacturing techniques, to establish the mechanical integrity of the calorimeter system design, and to refine cost projections. The primary objective of the FY92 engineering effort will be to extrapolate from experience with prototype modules to the full GEM calorimeter, in particular addressing issues of mechanical tolerances, assembly and access, support structures, readout systems and cables, and optimized production techniques.

Prior experience with the infrastructure that developed in producing the first generation of cast fiber supertowers has raised confidence that a large fully containing prototype can be produced in a timely and efficient manner. The prototype will be tested and calibrated using high energy electron, pion and muon beams at CERN, together with the BaF_2 EM calorimeter prototype. The test will focus on resolution and effective compensation, e/π separation, and MIP calibration.

2.4.5 Forward Calorimetry

Physics with a forward calorimeter covers a range of topics and imposes a number of requirements. Foremost among these is the measurement of the p_T of particles close to the beam pipe in order to make the best estimate of global event p_T and therefore missing p_T due to neutrinos and other weakly interacting particles. Thus the forward calorimeter is an important ingredient in the construction of a hermetic detector. Missing p_T signatures that will be sought at the SSC will be of order 100 to 200 GeV/c or greater. A modest

measurement of the p_T of jets in the forward direction will be sufficient to ensure that the background due to mismeasurement will be small. The most critical parameter seems to be the range of coverage, i.e., how high in η can adequate p_T resolution be maintained.

Further study of forward calorimetry is needed. One option for the forward calorimeter is provided by a compromise between the best coverage and cost. This is a small forward calorimeter as close to the interaction region as possible. For the baseline design, the front face of the forward calorimeter is 6.5 m from the interaction region. Using Tungsten with a small sampling fraction gives the densest calorimeter possible and therefore the optimal transverse containment of hadronic showers. Depth segmentation would allow accurate position determination in the first segment with adequate energy determination in the sum over segments. A premium would be placed on extending the sensitive volume of the calorimeter as close to the beam pipe as possible, perhaps as close as 2 cm from the beam centerline.

Several technologies are under consideration for the forward calorimeter. Work on liquid Argon / Tungsten plate geometry, liquid scintillating spaghetti and high pressure gas tubes is proceeding in parallel. All three technologies are believed to perform adequately even in the very high radiation fields predicted at this close distance and at the higher luminosities projected for later years of running. A rough estimate of neutron albedo in the central tracking region suggests that the forward calorimeters contribute about the same amount as the rest of the detector.

Table 2.4-5 lists some parameters of the close-in forward calorimeter. Further study is underway to evaluate this configuration.

Table 2.4-5 Forward Calorimeter Parameters

Hadronic coverage (full resolution)	$3.0 < \eta < 5.0$
Hadronic resolution	$\Delta p_T / p_T \approx 10\%$
Distance (front face to IP)	6.5m
Depth	1.06 m
Mean radius	80 cm
Weight	40 t (each)
Electronic channels	1070 (each)

2.4.6 Calorimetry R&D Summary

The R&D program for the GEM calorimeter will advance the two systems selected to achieve the GEM goal of the best possible electromagnetic calorimetry: the liquid argon with accordion EM and BaF_2 with a scintillating fiber hadron calorimeter. The objective of the R&D plan is to prepare for a comparison of the two systems during FY92, so that a choice is made and further engineered for the Technical Proposal in November, 1992.

R&D on the liquid argon approach will emphasize the accordion concept, developing improved electromagnetic resolution with thinner radiator plates (1 mm) and testing liquid krypton in place of liquid argon with 2 mm plates. R&D on liquid argon hadron calorimetry (plates) will be limited.

R&D on BaF_2 will emphasize developing the fabrication process for large radiation hard crystals. An expert panel will review the prospects

for this achievement before FY92 R&D proceeds. In addition the first production-prototype system consisting of 81 full-sized crystals will be prepared with full speed electronics.

The R&D for the scintillating fiber hadron calorimeter will advance the technique of eutectic alloy/fine lead shot module fabrication and will include construction of a fully hadronic shower containing set of GEM towers for beam test in FY92. This test will combine the BaF_2 production-prototype with the scintillating fiber hadron calorimeter for evaluation as the GEM calorimeter system.

R&D on the forward calorimetry will proceed on liquid argon, liquid scintillator and high pressure gas tubes. A silicon strip preradiator prototype will be tested.

---

[1] B. Aubert *et al.*, "Performance of a Liquid Argon Electromagnetic Calorimeter with an "Accordion" Geometry," CERN-PPE-91 - 73, 1991 (Submitted on Nucl. Instr. and Meth.)

[2] H. Burkhardt *et al.*, Nucl. Instr. and Meth. A 268, 116 (1988).

[3] GEM Collaboration, SSC-EOI-0020, An Expression of Interst to Construct a Major SSC Detector, July 1991.

[4] CERN Green Book, "ECFA Workshop on LEP 200", Aachen, September, 1986.

[5] R. Y. Zhu, GEM Internal Note.

[6] H. Benson and T. Sjostrand, "A Manual to the Lund Monte Carlo for Hadronic Processes", PYTHIA version 5.5, June, 1991.

[7] J. Brau *et al.*, "GEM Preradiator", GEM -TN-91-18.

[8] R. Y. Zhu, Proceedings of ECFA LHC Workshop, Aachen, October 1990, Vol. III, 411.

[9] F.E. Paige and E. M. Wang, Proceedings of the Workshop on Calorimetry for the Supercollider, Mar. 13-17, 1989, U. of Alabama, Tuscaloosa, Alabama, World Scientific, p. 99.

[10] See for example, H.A. Gordon, Symposium on Detector Research and Development for the SSC, Oct. 15-18, 1990, World Scientific, p. 100.

[11] J. Colas, Proceedings of the Workshop on Calorimetry for the Supercollider, Mar. 13-17, 1989, U. of Alabama, Tuscaloosa, Alabama, World Scientific, p. 553

[12] B. Adeva *et al.*, Nucl. Instr. and Methods, A289 (1990), 35-102; J. Bakken *et al.*, Nucl. Instr. and Methods A275 (1989) 81.

[13] BaF_2 Collaboration, "A Precision BaF_2 Crystal Calorimetewr for the SSC," R&D Proposal and Progress Report Submitted to the SSCL, Sep., 1991.

[14] D. Acosta *et al.*, NIM A 305, 55 (1991); D. Acosta *et al.*, NIM A 302, 36 (1991); D. Acosta *et al.*, NIM A 294, 193 (1990); R. DeSalvo *et al.*, NIM A 279, 467 (1989); D. Acosta *et al.*, NIM A 308, 481 (1991); D. Acosta *et al.*, NIM A 309, 143 (1991); D. Acosta *et al.*, CERN-PPE/91-45 to be pub NIM B; D. Acosta *et al.*, CERN-PPE/91-195 to be pub NIM A.

[15] D. Brown *et al.*, IEEE Trans. Nucl. Sci. (1991); W. Worstell *et al.*, IEEE Trans. Nucl. Sci. (1990).

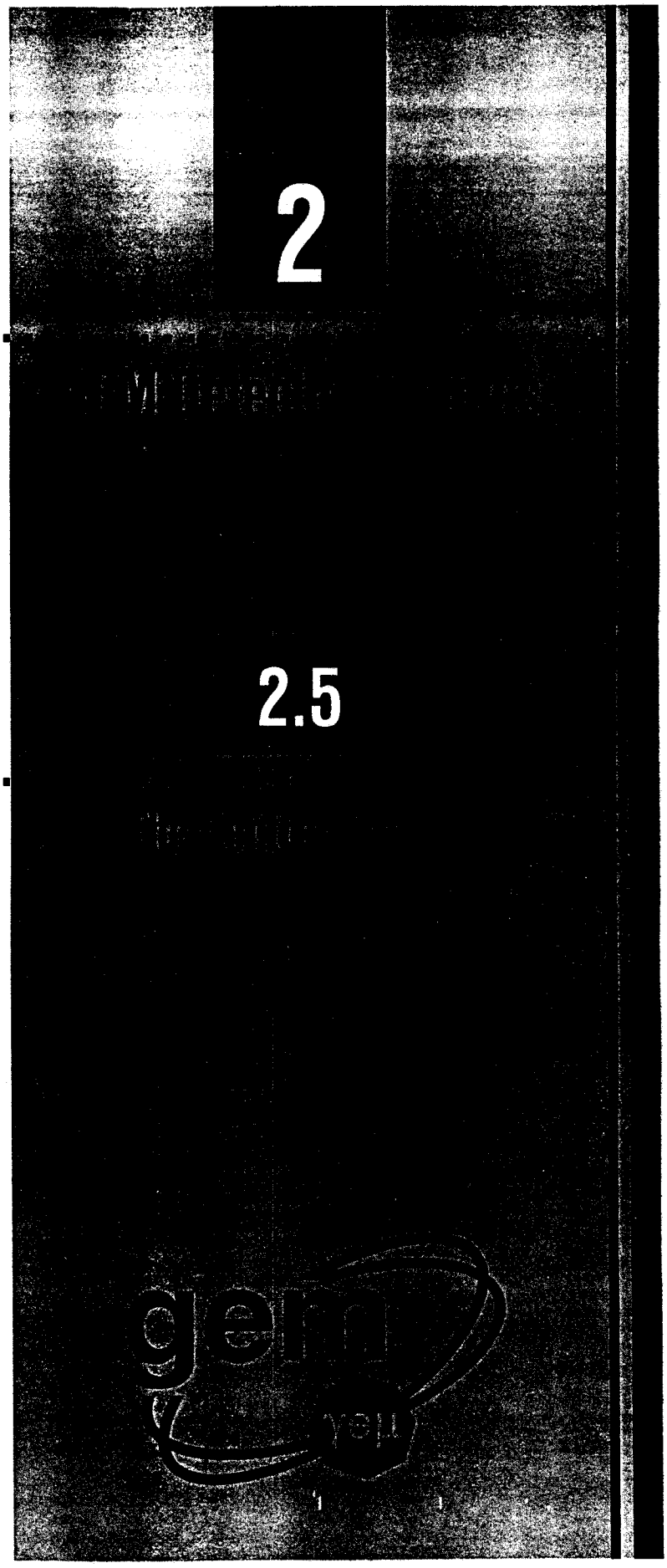
2
2.5

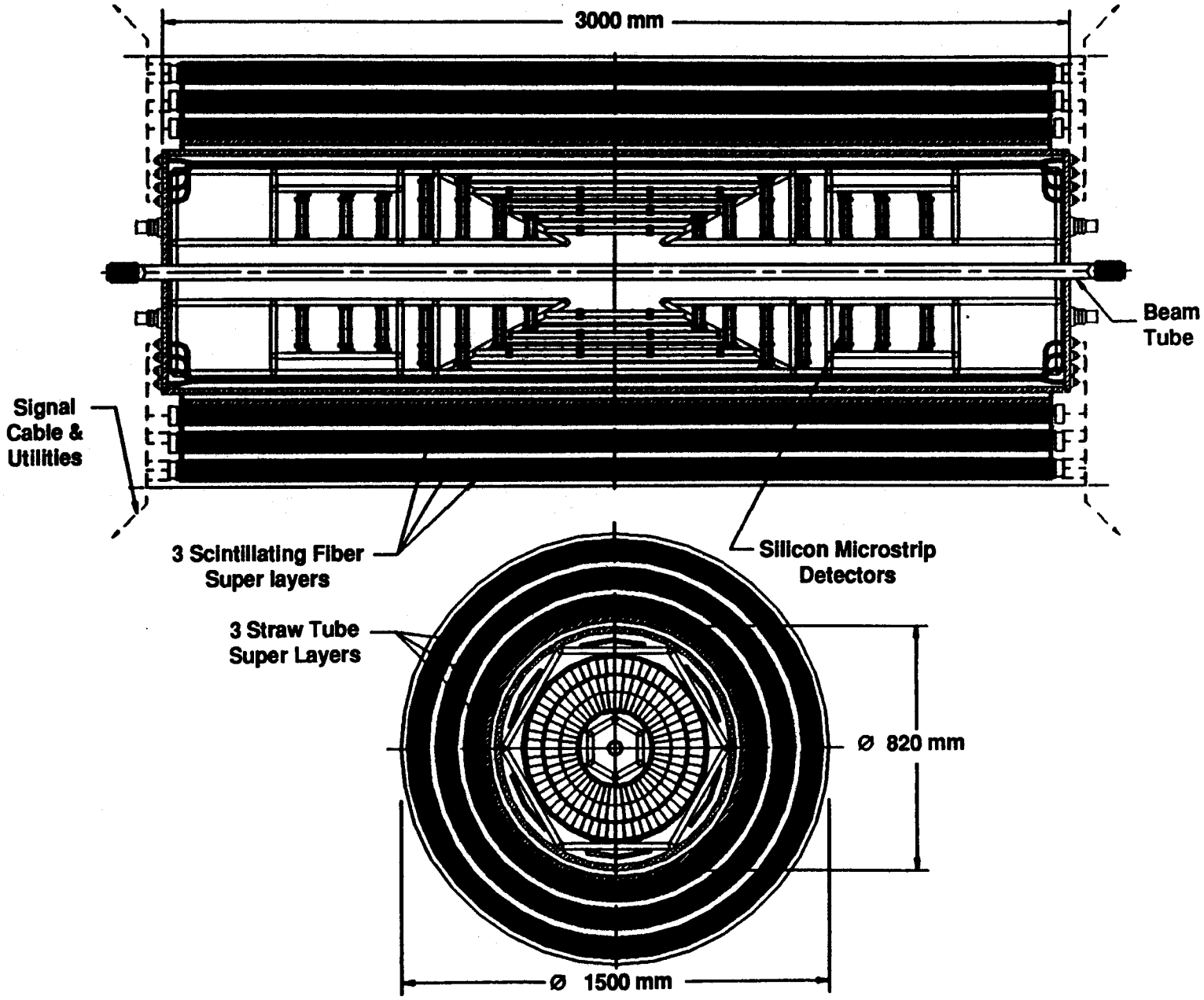

BASELINE CENTRAL TRACKER

2.5 The Central Tracker

The Central Tracker in the GEM detector will operate in the 0.8 T magnetic field of the large GEM superconducting solenoid. The tracker is compact, with a 75 cm outer radius and a total length of 300 cm. It covers a pseudorapidity of ± 2.5. At present there are two options under consideration for the design of this device. The first uses a silicon microstrip inner tracker surrounded by an outer tracker of straw tubes and scintillating fibers arranged in layers. This design was presented in the Expression of Interest [1] and the cost estimates in this Letter of Intent are based on this design. An alternate design, employing a somewhat smaller silicon microstrip inner detector surrounded by Interpolating Cathode Pad Chambers is being considered because its lower occupancy would enable the detector to operate well at luminosities of $10^{34}\,cm^{-2}s^{-1}$. One of the criteria for this alternate design is to keep its cost at or below the cost estimate presented for the EOI design.

2.5.1 Physics Goals and Design Parameters

The physics goals for the central tracking in GEM can be divided into two categories. The first are those features that are required to support the primary objectives of GEM, namely the detection of gammas, electrons and muons at high p_T. Some examples of these are:

- Identify the primary vertex of an event of interest, so that it can be separated from other pileup events in the memory time of the detector.
- Separate electrons and gammas using the presence or absence of a charged track pointing to an electromagnetic shower in the calorimeter.
- Provide track information for e, μ or γ isolation cuts, and to help with rejection of conversions and Dalitz pairs.
- Help with electron-hadron separation by providing a momentum measurement that can be compared with the energy deposition in the calorimeter.
- Help with rejection of background by matching the muon momentum measured in the central tracker with the momentum measured in the muon chambers.
- Determine the electron sign up to 400 GeV/c.

The tracker should be able to fulfill these goals well at the design luminosity of $10^{33}\,cm^{-2}s^{-1}$. These capabilities should also survive to luminosities up to $10^{34}\,cm^{-2}s^{-1}$. These minimum goals do not require full pattern recognition, but can be met by looking for hits in the tracker in a specific road extrapolated from the calorimeter or the muon system.

The second category of physics goals are more ambitious:

- Full reconstruction of the charged tracks in the event.
- Secondary vertex finding.
- Tracking at low momenta.

These features would enhance GEM's ability to address issues such as b and Top physics. They

are more demanding in that they require pattern, recognition capabilities and very good vertex resolution. It is expected that these more ambitious goals can be met at luminosities up to $10^{33}\,cm^{-2}s^{-1}$, but probably not much higher. This, however, seems satisfactory since the physics topics requiring these more ambitious features have relatively large crossections and can thus be studied at luminosities of $10^{33}cm^{-2}s^{-1}$ or below.

The parameters for the central tracker that will satisfy the goals outlined above are summarized in table 2.5-1.

Table 2.5-1 Design Parameters for GEM Central Tracking

Outer Radius	70 cm
Length	±150 cm
Rapidity Coverage	$\|\eta\| \leq 2.5$
Magnetic Field	0.8T
Occupancy	
at $\mathcal{L} = 10^{33}cm^{-2}s^{-1}$	$\leq 1\%$
at $\mathcal{L} = 10^{34}cm^{-2}s^{-1}$	~ 3%
2σ charge separation	$p \lesssim 400$ GeV/c
Momentum Resolution at 90°	
at high momenta (measurement limited)	$\Delta p/p^2 \sim$ (1 to 3) × 10^{-3} $(GeV/c)^{-1}$
at low momenta (multiple scattering limited)	$\Delta p/p \sim 2$ to 4%
Vertex Resolution	
along beam direction	$\delta z \sim 1$ mm
impact parameter	$\delta b \sim 20\ \mu$m above 10 GeV/c

2.5.2 Silicon Microstrip, Straw Tube and Scintillating Fiber Option

The baseline tracker design, shown on the section divider has evolved from the GEM EOI design [1]. The tracker is designed with two distinct systems: the inner silicon tracker and the outer straw tube drift chambers with scintillating fibers. The inner silicon tracker provides a precise vertex measurement and a fine grain track measurement. The outer tracker provides the outer measurement for the momentum determination. It also provides many layers for good pattern recognition and track finding.

2.5.2.1 Baseline Silicon Inner Tracker

The silicon tracker (ST) has undergone minor revisions since the GEM EOI. The dominant change affects the placement of the silicon ladders to provide full coverage everywhere in the pseudorapidity range ± 2.5.

The ST consists of six layers of silicon strip ladders. Each ladder is composed of two back-to-back single sided silicon sensors with a 5 mrad stereo angle between the two sensors. Each sensor is 300 μm thick with a strip pitch of 50 μm. Each pair of sensors provides a space point with a resolution of 10 μm in the r-ϕ plane and 3 mm in the r-z projection. The six layers of ladders are organized into three superlayers, each of which provides a track stub to a track finding algorithm. In the forward region the silicon sensors are mounted into disks with the strips projecting radially inward toward the beam axis. The ST is ~2.5 m long and extends to a radius of 40 cm.

2.5.2.2 *Straw/Fiber Outer Tracker*

The outer tracker is little changed from the EOI design [1]. It consists of three superlayers of straw drift tubes and scintillating fibers. Each superlayer is composed of 16 layers of 4 mm straw tubes along the z direction and four layers of 1 mm fibers placed in a ZZUV arrangement with a $\pm 10^{o}$ stereo angle for the UV layers. Each superlayer will provide a track stub measurement with a 25 μm r-ϕ accuracy and a 300 μm r-z accuracy.

2.5.3 Silicon Microstrip and Interpolating Pad Chamber Option

Some of the reasons for considering an alternate design to the "Baseline Design" described in the previous section are as follows:

- The calculated occupancy in the straw tubes of the Baseline Design is well in excess of 10% at the luminosity of $10^{33}\,cm^{-2}s^{-1}$. Since backgrounds in real life are likely to be worse than calculated, this technology is marginal at $10^{33}\,cm^{-2}s^{-1}$ and not useful at $10^{34}\,cm^{-2}s^{-1}$. With the Interpolating Pad Chambers (IPC's), considerably lower occupancy is possible, even at $10^{34}\,cm^{-2}s^{-1}$.
- Both the straw tubes and the scintillating fibers of the Baseline Design are stereo devices, i.e. all of the tracks in the tracker are projected onto a plane at the end of the device. In the high multiplicity and high luminosity environment of the SSC, tracking and pattern recognition would be much easier and more robust with a "3-D" device.
- The Baseline Design consists of three different technologies (silicon, straws, and fibers). It would be an advantage to reduce the tracker to two technologies.

The above considerations seem sufficiently weighty to cause serious consideration of an alternate design consisting of silicon microstrips and Interpolating Pad Chambers. A general schematic drawing of this design is shown in figure 2.5-1.

2.5.3.1 *The Silicon Inner Tracker*

The details of this silicon inner tracker are similar to those described in the Baseline Design of the previous section. However, the outer radius is reduced to 35 cm, and the overall length to 200 cm.

2.5.3.2 *The Interpolating Pad Chamber Outer Tracker*

The outer tracker consists of 9 layers of pad chambers both in the barrel region at radii between 35 and 70 cm, and in the forward region which extends from 20 to 70 cm in radius. The 9 layers are arranged in 3 superlayers with 3 layers each. Each barrel layer will consist of 16 chambers, each covering 24° in azimuth, with the largest chamber being 32 cm wide × 200 cm long. The forward layers will be divided into trapezoidal chambers about 50 cm × 50 cm each. The IPC's in this system will be very similar in concept and performance to chambers with chevron shaped cathode pads which have been constructed and are now taking data in experiment E-814 at Brookhaven AGS [2]. These chambers have various sizes up to 50 cm × 200 cm and have obtained a resolution of ~50 μm, or ~1% of the pad size.

Each of the chambers will be tilted in azimuth by the Lorentz angle of the gas (~6 to 9°) so that the $E \times B$ effect in the 0.8 T field does not degrade the resolution. This tilt also allows the chambers to be overlapped, eliminating dead regions due to electronics and structural elements (figure 2.5-1b).

The direction of good resolution in these chevron pad chambers is along the anode wire. Thus the wires in the barrel chambers will run across the chambers, in the "ϕ direction", keeping the wire length between 15 and 32 cm. In the forward chambers the wires will also run in the "ϕ direction," with wire length between 10 and 40 cm.

In the present design pad sizes are a uniform $\Delta\eta \times \Delta\phi = 0.001$ in all parts of the tracker. This results in a total of just under 300,000 pads for the entire device.

The anode wires will be spaced at about 2.5 mm intervals. To obtain precision better than the pad size in the "θ direction", readout of the anode wires is expected in at least one layer in each superlayer. A digital readout would provide a precision of ~700 μm in this direction. This precision in each of the superlayers will provide the required $\delta z \sim 1$ mm to separate event vertices at a luminosity of $10^{34}\,cm^{-2}s^{-1}$, when the silicon tracker is expected to be out of operation. This would require about 60,000 wires to be readout, which will be multiplexed at a level that satisfies the occupancy requirements.

The IPC readout electronics for each pad include a fast front end amplifier and shaper feeding into an analog pipeline which is multiplexed at the output by a factor of 256, giving a total of 1200 channels. The present design calls for the multiplexed analog outputs to be input to Mach-Zehnder electro-optic modulators, each of which is connected by a fiber optic cable to a remote 9 bit flash ADC system. The readout of the IPC wires can be accomplished with a simple comparator on each of the instrumented wires, followed by a multiplexed digital pipeline.

2.5.3.3 Engineering Design

The main concern of the engineering design of the central tracker is to:

- Guarantee sufficient rigidity and temporal stability so that systematic alignment errors can be kept below 10 μm within the silicon tracker and below 25 μm in the IPC system, in the relevant dimensions.
- Keep the entire system extremely light to achieve an acceptably small fraction of a radiation length (between 10 and 20%) in order to keep both multiple scattering and secondary interactions at a tolerable level.

Due in part to the work done in the Silicon Subsystem R&D effort [3], the engineering design of the silicon tracker is well advanced. The design of the IPC's is just beginning. The present thinking is to build each superlayer of 3 pad planes as a single mechanical unit, as shown in figure 2.5-2.

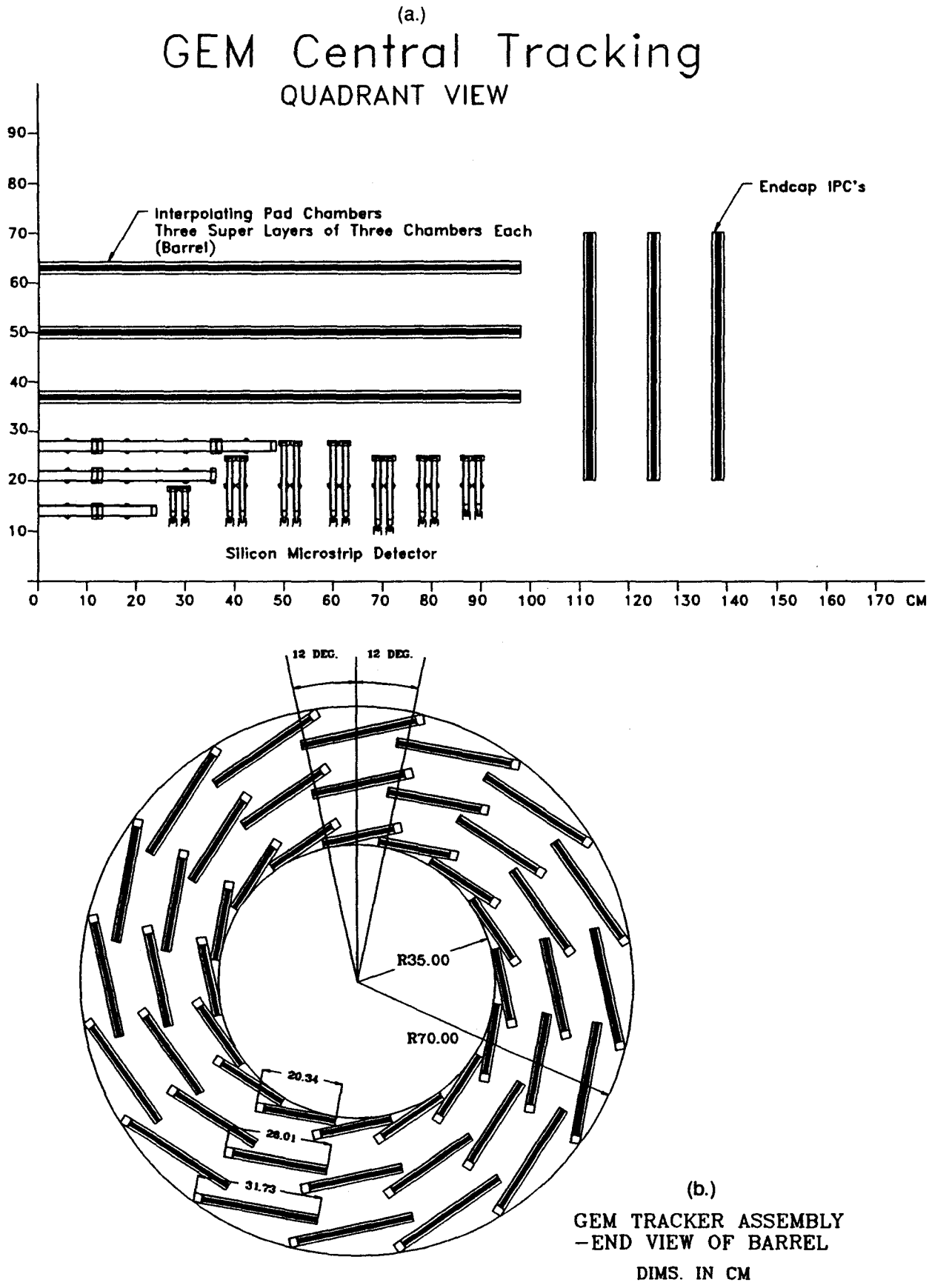

Figure 2.5-1 GEM Silicon Microstrip and Interpolating Pad Chamber Option

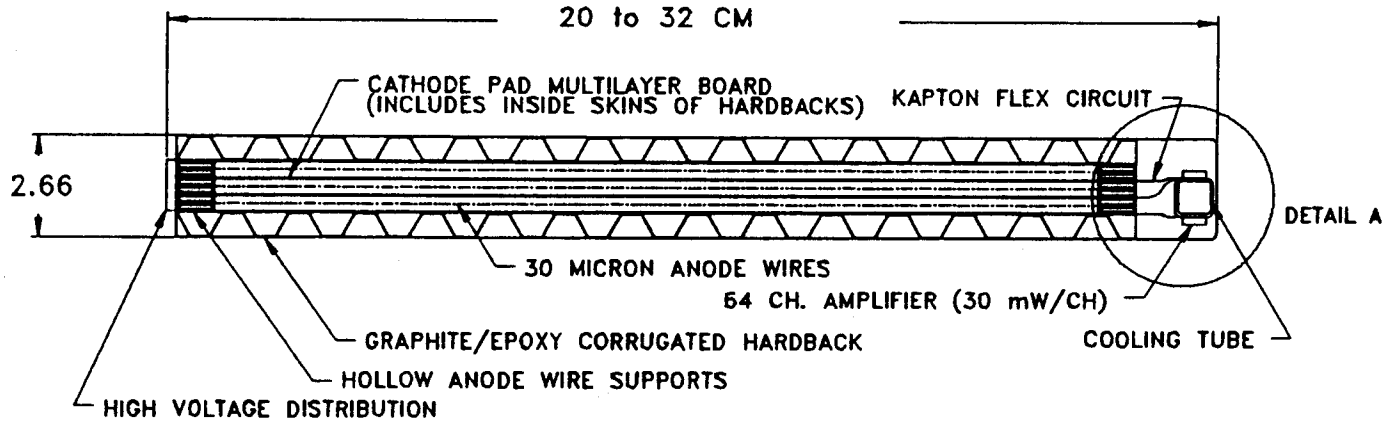

SECTIONAL OF TYPICAL BARREL MODULE

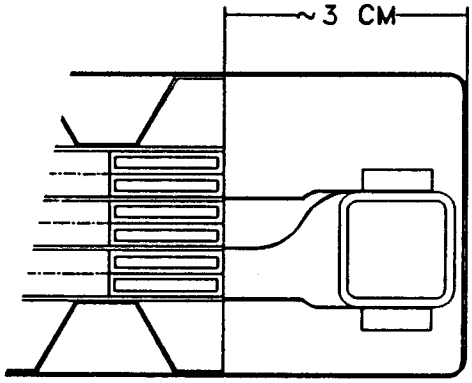

DETAIL A: SECTIONAL OF ELECTRONICS/COOLING LOCATION

Figure 2.5-2 GEM IPC Detail of Superlayer Module with Cathode Pad Amplifiers

2.5.3.4 Detector Performance

Initial calculations indicate that the silicon microstrip plus IPC tracker can meet all of the design criteria summarized in table 2.5-1. Detailed computer simulations of the momentum resolution of the tracker at high momenta (neglecting multiple scattering, which is negligible above 50 GeV/c) have been carried out. The resolution as a function rapidity is shown in figure 2.5-3. Sign selection can be obtained at the two sigma level up to 400 GeV/c. A detailed simulation code based on GEANT in which the geometry and the amount of material in the tracker are faithfully described is in progress. This program will be used to carry out the optimization of the tracker design.

2.5.4 Central Tracker R&D Plan

Of the four technologies being considered for GEM central tracking, only two, silicon and IPC's, are supported in the R&D program. While there are still many unanswered questions about straw tubes and scintillating fibers, the SDC tracking group is leading extensive R&D studies in both these areas, and members of the GEM tracking team are participating in some of this work. The limited resources available for R&D must be

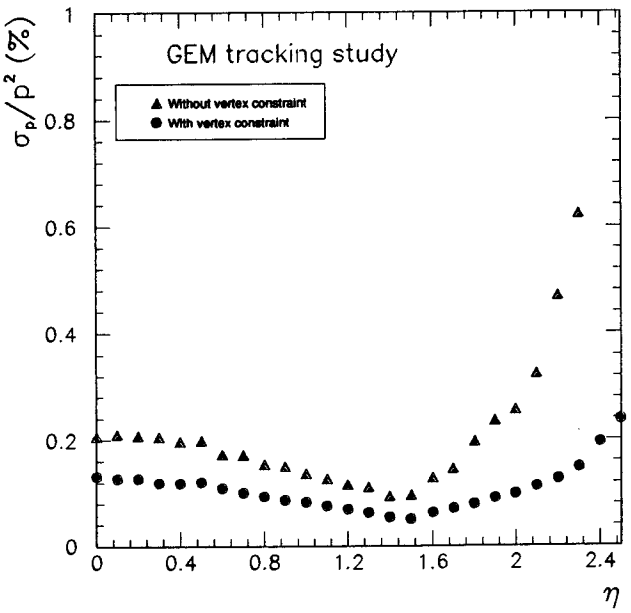

Figure 2.5-3 Tracker resolution in the momentum regime where multiple scattering may be neglected

devoted to providing answers to questions that are crucial to the program and that are unaddressed at present.

The R&D program for the GEM Central Tracker in FY92 has three major objectives with the overall goal of determining a final central tracker configuration by mid 1992, and producing a preliminary engineering design by the last quarter of 1992. The objectives of the R&D program are:

- Fully evaluate the capabilities of interpolating pad chambers for use as the outer detector in the central tracker.
- Construct Proof of Principle readout and trigger electronics for both silicon and IPC's.
- Resolve critical mechanical design issues.

What follows is an outline of the critical issues which will be addressed for silicon and IPC's in order to achieve the objectives in FY92.

2.5.4.1 Silicon Microstrip Inner Tracker

For the silicon inner tracker the primary R&D effort will be on the front end electronics design. Mechanical engineering must also continue on the support and cooling systems and on assembly and alignment. The major issues to be addressed in the electronics R&D will be the radiation resistance of rad hard bipolar electronics, their power levels and speed, design of a digital pipe line and multiplexer, 1st and 2nd level channel readout, and cabling and power distribution requirements. The mechanical engineering and R&D study will include the design and analysis of an electronics cooling system, design of the silicon ladder bridge, developing specifications for a double sided wafer and developing an in-situ alignment technique.

2.5.4.2 Interpolating Pad Chambers

A vigorous R&D program is required during the next year to demonstrate the viability of IPC's in the GEM central tracker environment. A key issue is the design and cost of rad-hard front end electronics. The radiation resistance of the IPC's at the gas gains needed to obtain 1% position resolution accuracy must be demonstrated using a gas with both the required drift speed and low Lorentz angle. It must also be demonstrated that the chambers can operate at the required speed without degrading the resolution. A mechanical design which minimizes the material thickness of the chambers must be developed in conjunction with engineering work on the support system,

cathode design and fabrication, electronics cooling, and gas and power distribution and alignment.

2.5.4.3 Other Technologies

The benefits of devices which provide "3-D" readout are also attractive to consider for the inner tracker. Both Silicon Pixels and Silicon Drift carry this potential and have been considered for use in GEM. At present, however, both suffer from a low level of technological maturity and the development of either for use in this detector requires greater resources than are available. Interest in these technologies remains very high, and any advances which might put these devices within range would be welcome.

---

[1] GEM Collaboration, "An Expression of Interest to Construct a Major SSC Detector", SSC-EOI0020, July 8, 1991.

[2] B. Yu *et al.*, "Investigation of Chevron Cathode Pads for Position Encoding in Very High Rate, Gas Proportional Chambers", BNL 44748, October 1990.

[3] W. O. Miller *et al.*, "Superconducting Super Collider Silicon Tracking Subsystem Research and Development", LA-12029, December 1990.

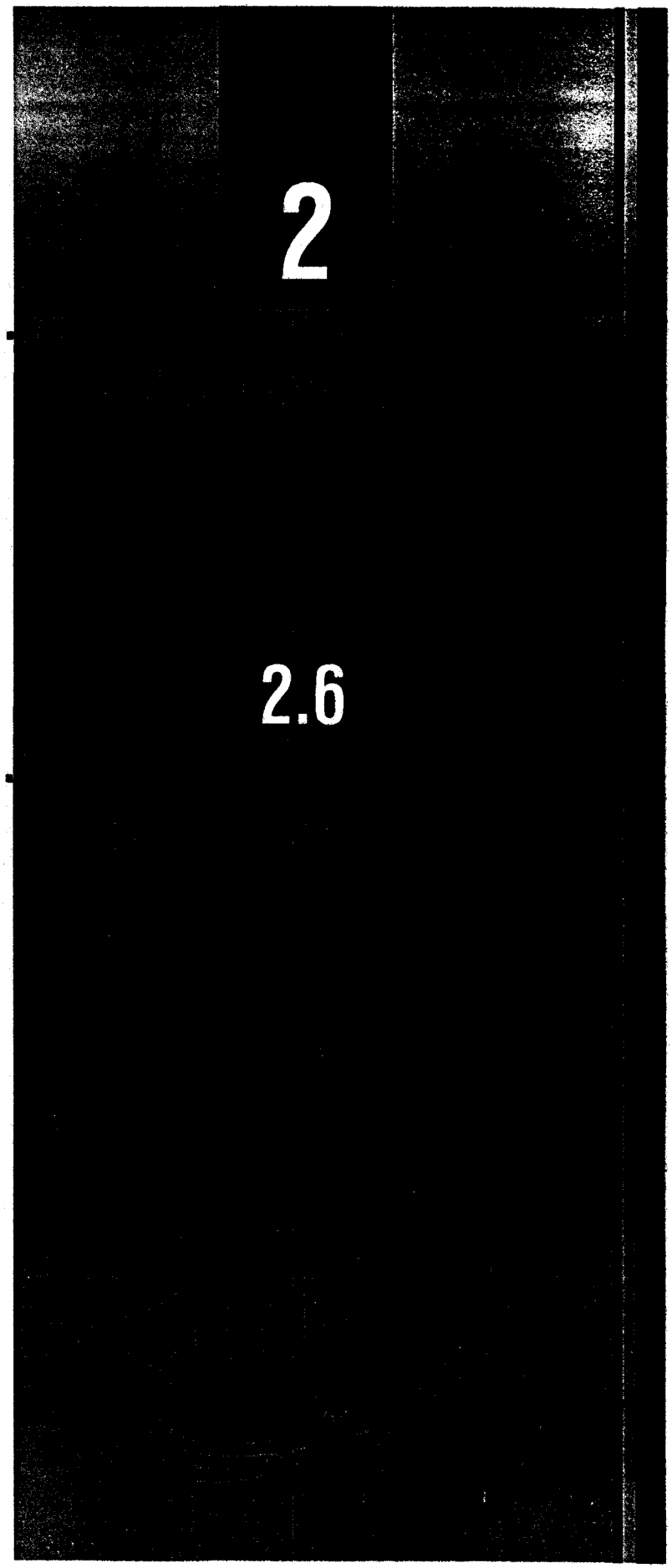
2
2.6

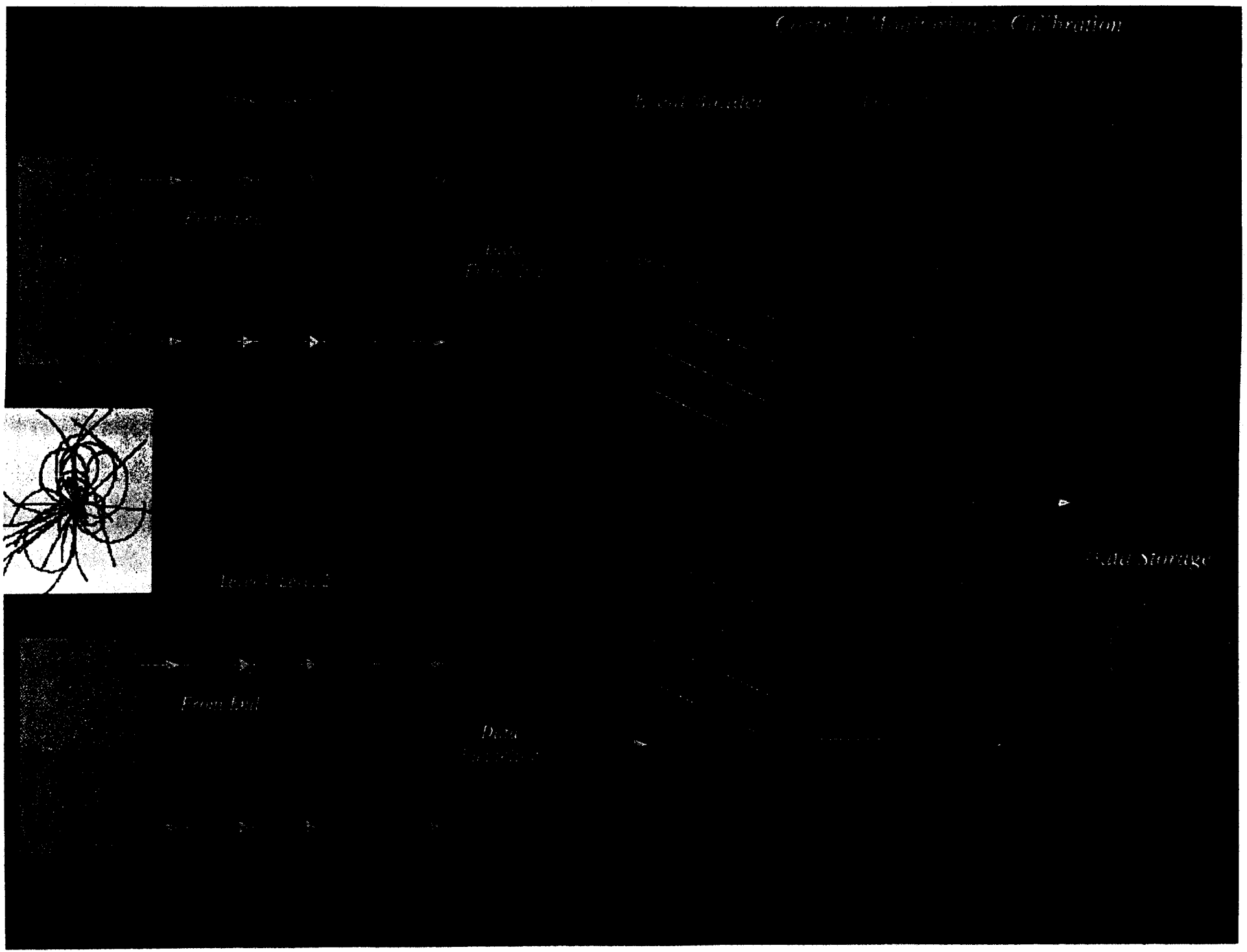

2.6 Trigger and Data Acquisition

The first two parts of this section describe general features of the trigger and data acquisition (DAQ), while the third presents specific trigger strategies along with sample rate estimates.

2.6.1 Trigger System

The trigger/DAQ system, shown in figure 2.6-1, will follow a conventional three-level approach: Level 1 is synchronous and pipelined; Level 2 is asynchronous, but monotonic; and Level 3 is a processor ranch. Event rates and latency times are summarized in table 2.6-1. The second column in table 2.6-1 specifies the maximum *average* input rate that can be sustained at each Level. To avoid overlapping events it may also be necessary to "throttle" the Level 1 accepts—i.e. it may be necessary to suppress Level 1 accepts spaced by less than ~ 1 μs. The rate handling capability of each level will be ten times greater than the design goal for the output rate of the preceding level. Although this presents a challenge, such an approach is essential to ensure reliable operation at $\mathcal{L} = 10^{33}\,\mathrm{cm}^{-2}\mathrm{s}^{-1}$ and to leave room for running at $\mathcal{L} = 10^{34}\,\mathrm{cm}^{-2}\mathrm{s}^{-1}$.

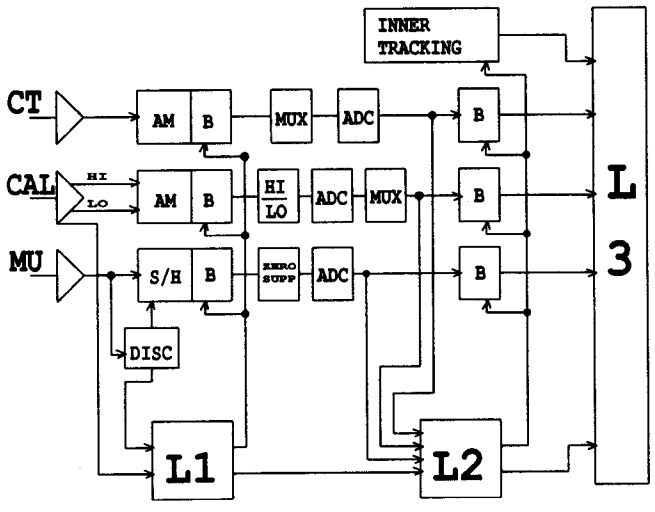

Figure 2.6-1 Block diagram of GEM trigger/DAQ system.

Table 2.6-1 Design goals for the GEM Trigger/DAQ System. Output rates are for operation at $\mathcal{L} = 10^{33}\,\mathrm{cm}^{-2}\mathrm{s}^{-1}$

GEM Trigger/DAQ Design Goals				
Lvl.	Max Av. Rate In	Rate Out	Latency	Comments
1	62 MHz	10 kHz	3 μs	Synchronous, Pipelined
2	100 kHz	300 Hz	100 μs	Asynchronous, Monotonic
3	3 kHz	10 Hz	—	CPU Ranch

2.6.1.1 Level 1

The Level 1 trigger decision will be based on a reduced set of calorimeter and muon system signals, encoded to a minimum number of bits, here called primitives. Specifically, trigger towers will be formed from electromagnetic (EMC) and hadronic (HCAL) calorimeter regions of size $\Delta\eta \times \Delta\phi = 0.2 \times 0.2$. Analog sums of the calorimeter elements comprising each tower will be flash encoded and compared to preset digital thresholds. Photon and electron triggers will be defined as energy depositions in EMC-towers accompanied by corresponding HCAL-tower depositions satisfying $E_{HCAL}/E_{EMC} < 1/10$. Jet triggers will be formed from local sums. Digitally formed global sums of trigger towers will allow for total transverse (and missing transverse) energy triggers.

Muon trigger primitives will be generated using hit patterns produced through discrimination of the

muon chamber signals, which will be projected onto look-up tables to define high-p_T candidates.

A Level 1 trigger decision will be formed for each bunch crossing from the *global* pattern of trigger primitives. It will be possible to trigger on single high-p_T electrons, photons, muons, or jets; on pairs of lower p_T leptons; or on any other combination of interest. Definition of a suitable set of Level 1 primitives is under study.

To simplify the system design and to avoid sampling more bunch crossings than necessary, the trigger signals from the Level 1 subsystems will tag the bunch crossing of the event. This imposes constraints on the design of the calorimeter trigger pickoffs and the design of the muon system.

2.6.1.2 Level 2

The Level 2 trigger is a distributed, pipelined digital-processor system designed around general data-driven principles. It will use digitized data from the calorimeter, muon, and central-tracking systems to refine trigger candidates identified by Level 1.

Calorimeter data with high precision and full granularity will be used to apply shower-shape and isolation cuts to electron and photon candidates. Electron candidates will be further refined by requiring stiff (p_T > 10 GeV/c) spatially-matched tracks in the central tracker. Investigation is currently underway to determine whether this is best done in the inner silicon tracker or in the outer tracker. Finally, digitized muon information will allow a precise determination of muon momenta.

2.6.1.3 Level 3

Level 3 will be a "ranch" of processors having access to information from the entire detector. See section 2.7.

2.6.2 Data Acquisition

The data acquisition system must provide deadtimeless operation at rates up to 100 kHz while taking into account the Level 1 trigger latency time of 3 μs. The architectures for the different components are described below and shown schematically in figure 2.6-1.

2.6.2.1 Calorimeter

After preamplifiers, shapers, and fast trigger pick-offs, the calorimeter signals will be sampled every bunch crossing with the samples stored in analog memories (AM). (A digital pipeline approach is also being investigated.) Seventeen bits of dynamic range will be achieved by splitting the input into high-gain and low-gain channels.

Upon receipt of a Level 1 trigger, up to 5 samples per signal will be transferred to a Level 2 derandomizing buffer. The buffered samples will be digitized with fast (≥ 1 MHz) 12-bit ADC's. The data will then be sent bit-serially to Level 2 after an approximate 10:1 multiplexing to reduce the cable count.

The ADC will be a custom device, or a commercial product, if one with reasonable cost and power consumption can be found.

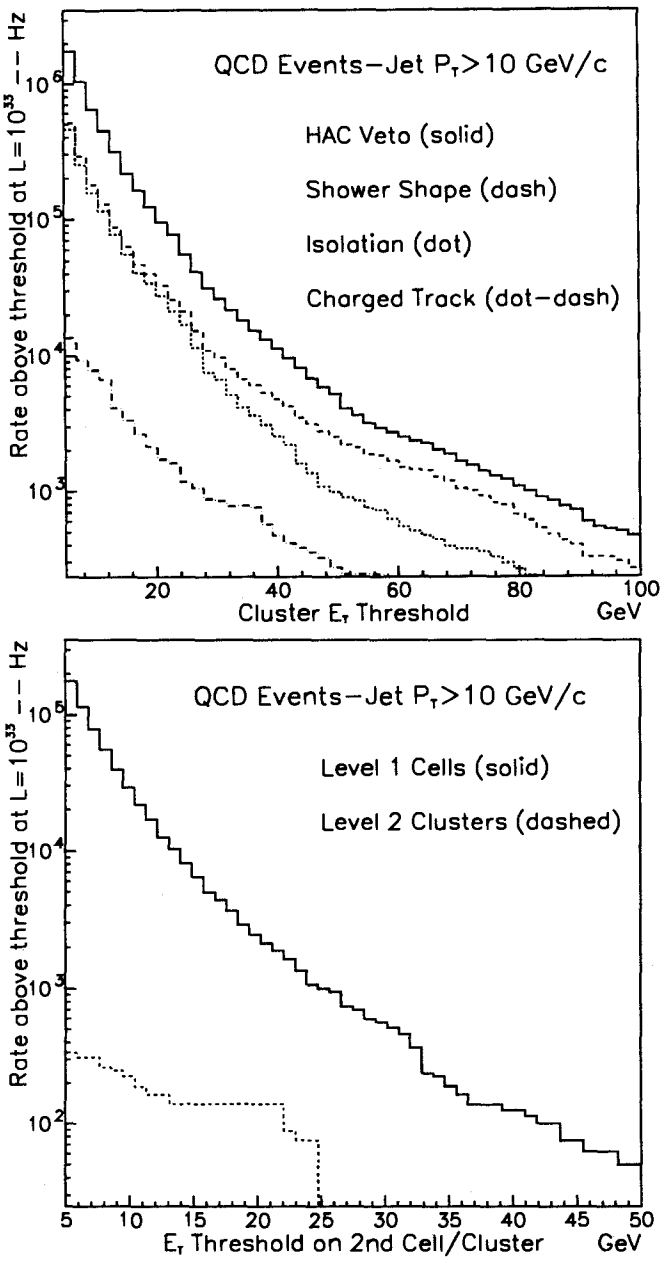

Figure 2.6-2 (a) Rates for single γ/e⁺ triggers, (b) rates as a function of the second highest energy γ/e⁺ cluster or cell in the event

2.6.2.2 Muon Pads

Low occupancy will allow the pipeline delay principal to be replaced by a simpler discriminator (DISC) driven sample-and-hold circuit (S/H), plus an analog derandomizing buffer. Upon receipt of a Level 1 trigger, the stored samples will be routed through an analog multiplexer to a 9-bit FADC. Although many (256 or more) channels will be serviced by a single MUX/FADC combination, the readout time will be greatly reduced by using the delayed discriminator bits to perform a selective scan of only the channels of interest. Digitized charge and address data will be sent bit-serially to Level 2.

2.6.2.3 Muon Drift-Wires

Circuits providing time-stamped leading-edge information with 1 ns resolution and multi-hit capability are already commercially available. With straightforward changes in readout architecture these circuits will be suitable for use in GEM.

2.6.2.4 Silicon Tracker

The front end of the silicon strip readout is composed of a bipolar amplifier/discriminator chip and a hardened CMOS pipeline chip. The pipeline is split into a Level 1 section, which operates at the bunch crossing frequency (62.5 MHz) and a Level 2 section, which operates at speeds up to 100 kHz. Upon receipt of a Level 2 accept, data will be read out via a serialized transmission of 640-channel - wide chip-level data registers. This data will be further multiplexed outside the main calorimetry and transmitted optically to the counting house, where DSP's will be used to zero suppress the incoming data. After suppression the expected event size is (assuming 5 M channels and 2 k hits/event) of order 50 kbits.

The trigger data from the silicon strip detector consists of a logical OR of 16 neighboring strips. This data is transmitted off-detector, on receipt of

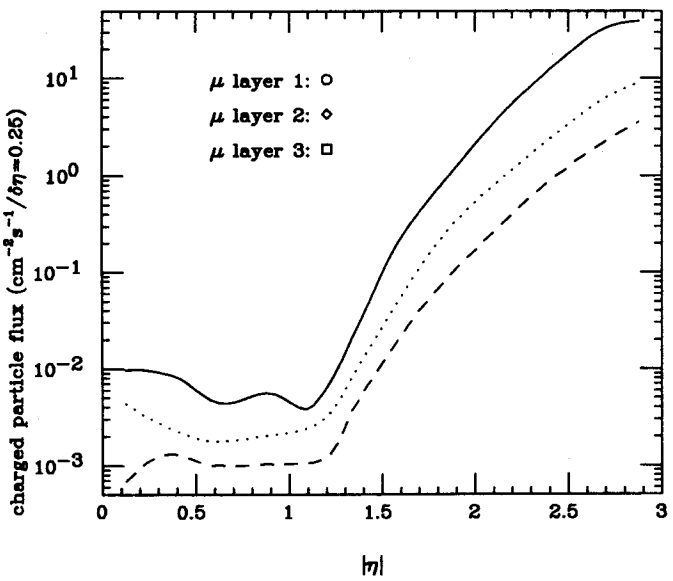

Figure 2.6-3 Charged particle rates versus |η| in the muon system

the Level 1 accept signal, via serial links operating at bit rates of 4MHz. Trigger processors located outside the calorimetry take the data and form coincidences between the layers, which provide a 14 GeV p_T cut-off (by assuming a 500 μm error on the beam position). Sectors with candidate tracks are then further processed to reconstruct the r - z direction of the candidate.

2.6.2.5 Central Tracker Pads

The Level 1 delay for the pad chambers will be achieved using SCA's in a manner similar to the calorimeter readout. In the case of pads, a single scale with nine bits of dynamic range will suffice. However, the pad electronics will be chamber-mounted and will need to be radiation tolerant. Analog outputs from the SCA will be combined on-chamber via analog multiplexers so as to reduce the bulk of cables needed to transmit the information from the tracker volume. One possibility for high-bandwidth analog links is fibers driven by electro-optic modulators [2].

Information for the Level 2 trigger can be extracted quickly by a selective scan of pads along roads defined by the calorimeter-defined electron candidate(s).

2.6.2.6 Dataflow and Event Building

Subsequent to a Level 2 trigger decision, data must be moved from buffers near the detector to the Level 3 ranch and be assembled into events in the process. Preliminary estimates of event sizes yield 300–400 kbytes, but in view of the uncertainties in these estimates a size of of 1 Mbyte/event is assumed, for a total data rate of 3 Gbyte/s.

These data will likely be carried over fiber links, since such links are compact, less prone to ground-loop problems, and capable of high transmission rates (systems operating at 125 Mbyte/s are now in use). In principle only a few dozen parallel links will be needed, but practical considerations, such as uneven loading induced by the natural divisions between detector subsystems, may require additional links.

The event builder accepts sub-event data from the parallel data paths, assembles the sub-events into full events, and then directs the full events to one of the processors in the Level 3 ranch. Event builders of varying levels of complexity are currently the subject of R&D [3]. Within GEM, those options will be investigated along with approaches such as using dual-port memory with interconnections to both the Level 2 data collection paths and the Level 3 ranch.

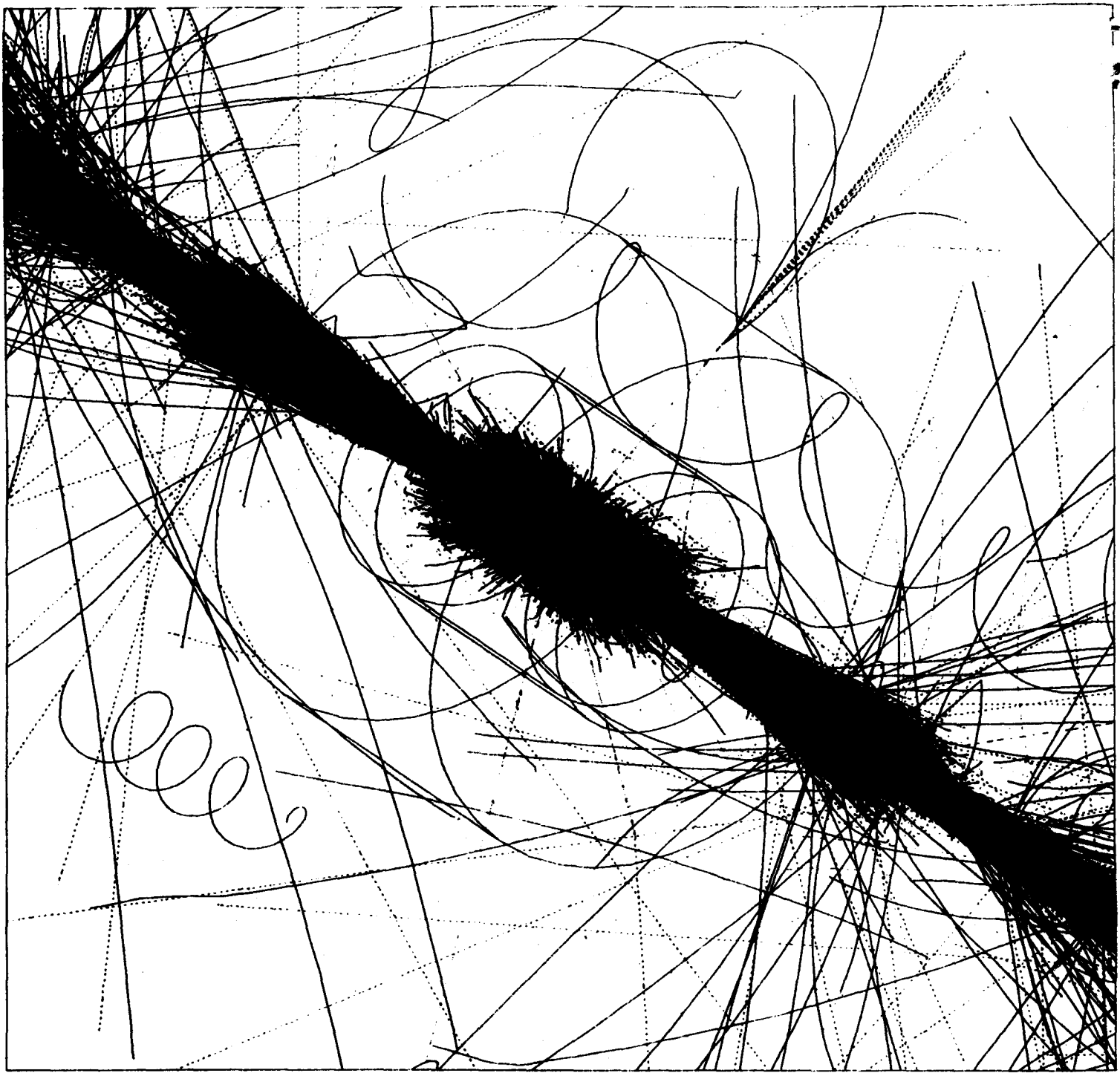

An 800 GeV Higgs decaying via Z^0Z^0 into $\mu^+\mu^-\mu^+\mu^-$ in a single beam crossing at a luminosity of 10^{34}. Outlines of the barrel regions of electromagnetic and hadronic calorimeters shown. In this simulation the forward calorimeters (not shown) are inside the magnetic field volume.

FRONT COVER: View of the GEM magnet